The Durability and Functionality Assessment of SHM Systems in Multi-functional Composites

RMIT University

A dissertation submitted in total fulfilment of the requirements for the degree of

Doctor of Philosophy

by

Mohammad Mehdizadeh

M Eng. By Research Mechanical Engineering
B.Sc. Mechanical Engineering

School of Aerospace, Mechanical & Manufacturing Engineering
College of Science, Engineering and Health

RMIT University
March 2014

Dedicated to …

First and foremost I will thank Almighty GOD, the Compassionate, the Merciful, who kindly helped me to complete my thesis.

My Parents, Ahmad and Marzyeh, who continue to learn, grow and develop, and who have been a source of encouragement and inspiration to me throughout my life. A very special thank you for providing me with this wonderful opportunity, and for the myriad of ways in which, throughout my life, you have actively supported me in my determination to find and realise my potential, and make this contribution to our world.

The Great Soul of My Grandmother who taught me the power of generosity.

My Brother and Sister, Ali and Melika who have supported me in each step of my academic journey.

And finally, to all My Friends, who have been there for each step of the way.

Declaration

I certify that, except where due acknowledgement has been made, this work is that of the author alone; the work has not been previously submitted, in whole or in part, to qualify for any other academic award; the content of the thesis is the result of work which has been carried out since the official commencement date of the approved research program. In addition, any editorial work, paid or unpaid, carried out by a third party, is acknowledged.

Mohammad Mehdizadeh

Acknowledgement

First I wish to express my deepest appreciation to my first supervisor, Professor Sabu John of RMIT University for his invaluable help and support from the first day of this project as well as his technical guidance, endless forbearance, and constant encouragement.

I wish to thank my second supervisor, Professor Chun Wang of RMIT University, School of Aerospace Mechanical and Manufacturing Engineering, for his priceless assistance, support and suggestions during the time of this research project.

I also wish to thank the following:

- Dr. Paul Callus of DSTO (Defence Science and Technology Organization) for his invaluable assistance, support, and suggestions during different stages of this research.

- Dr. Mark Hodge, the CEO of DMTC, for his valuable suggestions at different stages of this research and his kind support of this project

- Associate Professor Kamran Ghorbani of RMIT University School of Electrical and Computer Engineering for his valuable assistance and support throughout the different stages of this research.

- Dr. Wayne Rowe of RMIT University School of Electrical and Computer Engineering for his valuable assistance, support and suggestions during different stages of this research.

- Mr. Peter Tkatchyk of RMIT University for his technical support and assistance in the fatigue testing.

Abstract

The next-generation of composite structures, known as Multifunctional (MF) composites, involves combining various functions, such as structural and electrical, through multiple subsystems blended within a structural housing. The performance of MF composites can be affected by the degradation of any of these subsystems. Structural Health Monitoring Systems (SHMS) have emerged as a feasible method with which to improve the reliability of MF structures. However, the reliability of an SHMS can be affected by erroneous information from its sub-components such as transducers. Improving reliability requires a new capability to delineate failures associated with transducers and the transducer network from actual damage in the structure being monitored.

This study investigated the reliability of piezo-fibre-based transducers, such as MFC (Macro Fibre Composite), in both actuation and sensing modes. Scanning Electron Microscopy (SEM) was used to study the modes of damage within the MFC piezo-fibres. The measurement of key electrical properties, such as capacitance, confirmed that transducer damage may start prior to the structural damage and it may cause 'false positive' readings from the transducer. An assessment was carried out to delineate MFC damage from structural damage using three different techniques.

With the first technique, the $\Delta_{structure}$ parameter showed significant sensitivity, even to small (6%) strain changes caused by structural fatigue damage, while the Δ_{sensor} parameter performed well in detecting MFC strain changes of only 4%, which resulted from fatigue loading. With the second technique, it was discovered that the real impedance is a suitable parameter with which to detect structural damage, while the imaginary impedance can reliably detect pure actuator damage. The imaginary admittance parameter proved to be capable of extracting measurable responses from a degraded actuator to detect structural damage. In addition, the real admittance performed well when it came to the detection of actuator damage when the responses were already degraded due to structural damage. The third technique was based on the sensitivity of MFC to electromagnetic interference. The S_{11} parameter exhibited a 60% increase of return loss for a damaged transducer, while only a 2% loss was observed for structural damage. This difference was employed as an indicator to detect transducer damage. A complex Finite Element Analysis (FEA) of the MFC transducer is proposed. The accuracy of the (FEM) simulation was approximately 90% for both sensing and actuation modes of the degraded MFC compared to accuracies of approximately 20% for simplified simulations reported in the literature.

The second technique exhibited better performance of delineating various transducer-structure damage scenarios from each other. The third technique proved to be very sensitive to transducer damage. It is envisaged that by using these techniques, the determination of damage in the structure, transducer or the network will be possible.

Table of Contents

List of Figures

21

List of Table

Abbreviations and Acronyms

ANN	Artificial Neural Network
CAD	Computer Aided Design
CAE	Computer Aided Engineering
CDA	Central Difference Approximation
EMI	Electromagnetic Interference
EM	Electromechanical
DOF	Degree of Freedom
FEA	Finite Element Analysis
FEM	Finite Element Method
FMSECR	Flexural Modal Strain Energy Change Ratio
FRF	Frequency Response Function
GAs	Genetic Algorithms
ICA	Independent Component Analysis
IRR	Implicit Redundant Representation
LHS	Latin hypercube sampling
MB	Model-Based
MMCs	Metal Matrix Composites
MP	Mega Pascal
NDT	Non-Destructive Test
ODS	Operational Defection Shape
PMC	Polymer Matrix Composite
RMS	Route Mean Square
RTM	Resin Transfer Molding
MFC	Macro Fiber Composite
SHM	Structural Health Monitoring
SHMS	Structural Health Monitoring System
PFC	Piezo-Fibre Composite
WPT	Wavelet packet transforms
MFS	Multifunctional Structure
UAV	Unmanned Aerial Vehicle

List of Symbols

EI(x)	N.m^2	Bending stiffness distribution of the beam
Z	Ω	Impedance
F	N	Applied force input to the structure
λ_E	m	Bragg wavelength
RG	Ω (Ohm)	Resistance of the undeformed gauge
ϵ		Strain
GF		Gauge factor
a	m	Unit cell width, centre-to-centre spacing of interdigitated electrodes
A (.)		Arbitrary parametric smooth curve in the complex plane intersects *B (.)*
An	m^2	Discrete area element of interdigitated electrode
α		Vertex number
arg	degree	Phase of a complex number, interpreted as a vector angle
B (.)		Arbitrary parametric smooth curve in the complex plane, intersects *A (.)*
C	Farad	Capacitance
d	m	½ interdigitated electrode width
d_{31}	m/V	Indirect piezoelectric constant, electrical field perpendicular to mech. field
d_{33}	m/V	Direct piezoelectric constant, electrical field aligned with mechanical field
D	Coulombs/m2	Electrical displacement field
E (.)	V/m	Complex electrical field solution
E	V/m	Electrical field
Eu	V/m	Partial derivative of electrical field with respect to *u*
Ev	V/m	Partial derivative of electrical field with respect to *v*
Ey	V/m	Partial derivative of electrical field with respect to *y*
Ξ(.)	Vm	Electric flux function
f (.)		Complex function

f-1(.)		Inverse complex function
F (.)		Incomplete elliptic integral of the first kind, elliptic function of the first kind
g (.)		Inverse complex function
γ		Real constant that characterises an angle direction change
h	m	Unit cell height, half of the height of a piezoceramic fibre
h (.)		Real composition function that is harmonic
i		Imaginary number, $(-1)^{1/2}$
j		Imaginary number, $(-1)^{1/2}$
π		Pi= 3.141…..
Φ(.)		Real potential function
Q	Coulomb (c)	Charge
ρ	Coulomb (c)	Total charge contained in a system
t	m	Length of unit cell electrodes
θ	degree	Angle of intersection of two smooth curves in the complex plane
u(.)		Real function constituting the real part of a complex function
ux		Partial derivative of *u(.)* with respect to *x*
uy		Partial derivative of *u(.)* with respect to *y*
V_o	Volts	Constant voltage differential
v(.)		Real function constituting the imaginary part of a complex function
V	Volts	Voltage, potential solution
R	Ohm (Ω)	Resistance
L	Henry (H)	Inductance
X	Ohm (Ω)	Reactance
B	Siemens	Susceptance
G	Siemens	Conductance
S_{11}	dB	Port 1 reflection coefficient
S_{21}	dB	Port 1 to Port 2 transmission coefficient
S_{22}	dB	Port 2 reflection coefficient
S_{12}	dB	Port 2 to Port 1 transmission coefficient

CHAPTER 1 Introduction

1.1.   Background and Rationale

Composite structures have enabled great weight savings, increased efficiency and improved performance for a wide range of industries, such as the production of aerospace vehicles. However, these structures are still based on traditional structural design philosophies, whereby composites perform only the principal task of load bearing. The next-generation design of structural components involves a combination of multiple functions. The goal of these Multi-Functional Structures (MFS) is to incorporate various tasks and functions, such as structural, electrical and thermal features, within a structural housing. Multi-functionality seeks to integrate functions usually performed by different subsystems. The blending of multiple subsystems into a single material or structure reduces overall system mass and size, while simultaneously increasing system performance and functionality. However, the performance and behavioural characteristics of the multi-functional structures can be affected by degradation of any of the sub-components. This can be caused by sustained use, as well as exposure to severe environmental conditions or damage resulting from external conditions such as loading abrasion, operator abuse or neglect. These factors can have serious consequences on safety, cost, and operational capability. As a result, major concerns in the operating environment include the timely and accurate detection, characterisation and monitoring of cracking, corrosion, delamination, material degradation and other types of damage in any of these sub-components, as well as in the structure itself.

Recent times have seen the emergence of Structural Health Monitoring (SHM) as a feasible method with which to improve the safety and reliability of structures, thereby reducing their operational cost. SHM technology is perceived as a revolutionary method for determining the integrity of structures and involves the use of multidisciplinary fields including sensors, materials, signal processing, system integration and signal interpretation. However, as the application of SHM systems to monitor the status of the MFS becomes increasingly common, it will be even more important to determine the durability, reliability, and reparability of the SHM system itself. In this context, the transducers or the transducers network must possess sufficient reliability so that they do not require replacement at intervals less than the economic lifetime of the components they are monitoring. For safety-critical structures, such as primary aircraft structures, it is imperative for SHM systems to demonstrate a probability of failure lower than that of the host structure. To

achieve this very challenging goal, new technologies are needed to distinguish transducer failure from structural damage. The ability of diagnosing transducer failure is important if false positive or false negative responses from such transducers are to be avoided.

1.2. Aim of the proposed research

The aim of this research project was to identify and address one of the main gaps in the certification of structural health monitoring technologies. Indeed, addressing said gap is essential when it comes to enabling the industry to implement this technology. Indeed, there is a lack of standards, procedures, and methodologies with which to certify the reliability, durability and functionality of the host structure (body), SHM systems and their components during the lifetime of the structure. These components include transducers, batteries, etc. In fact, existing standards mainly focus on the structure rather than the SHM system. Furthermore, the assumption in most of these standards is that the SHM system is intact and free of any damage, which is clearly not the case in real-life conditions. In other words, the SHM system, which has the task of monitoring the status of the host structure, is also subject to failure or gradual degradation. This failure/degradation would change the integrity of the SHM system and therefore modify the electromechanical properties of its components, which are normally used to monitor the status of the host structure. Hence, the responses of the degraded or failed SHM system would no longer be reliable as these responses may not be a sign of structural damage but rather a false negative indication caused by the damage within the SHM system itself. Of course, the failed SHM system would not generate any responses and, as such, the main challenge arises when the SHM system becomes degraded due to fatigue.

The above statement clearly illustrates that the functionality of SHM systems in monitoring structural damage relies on the proper understanding of their behaviour, particularly in terms of detecting possible structural damage while the SHM system itself is degraded. In fact, the key point in this understanding is the ability to delineate SHM-related damage from structural damage. This ability enables us to characterise the degraded SHM system responses in order to monitor the status, not only of the structure, but also of the SHM system itself. This also makes it possible to utilise a practical SHM technique with the ability to diagnose damage occurring in different parts of the system, such as transducers, their network and the host structure. The questions which this research project seeks to answer are presented below:

1. Which technique is capable of delineating structural damage from damage within the transducer in sensing and actuation modes?

2. Which deterministic method can be employed to detect structural damage resulting from measurement by sensors which may concurrently incur damage and degradation?

3. What is the effect of electromagnetic interference on the piezo-fibre-based transducers?

4. What is the impact of sensor damage/degradation on its internal component?

5. How do changes in the damaged transducer's electrical properties relate to the damage within its internal components such as fibre breakage?

6. Which FEA approach is capable of accurately evaluating the performance of the bonded MFC transducer?

1.3. Methodology

During the initial stages of this study, an appropriate literature review was conducted, which involved gathering resources related to Structural Health Monitoring (SHM), Multifunctional Structures (MFS) and embedded systems, as well as various damage detection techniques. The literature was sourced from a diverse range of databases, thus making it possible to understand the background of this work and investigate future possibilities. The aim was to find two kinds of databases: firstly, the articles related to the background of relevant fields such as SHM, MFS and embedded systems; secondly, those related to the research, studies, methods, experiments, and techniques carried out in this field. This was essential when it came to determining the existing gap in research related to the functionality and reliability of embedded systems. The relevant information from these databases was gathered and studied to determine a proper methodology with which to address the identified gaps. The main goal of this literature review was to identify experimental modelling and appropriate analytical modelling techniques. This comprehensive search revealed the need for a delineation technique that is capable of distinguishing structural damage from damage in the SHM system and its components, such as transducers. Indeed, it became evident that this represented one of the major issues in the certification of SHM systems.

Following this stage, the required experiments were modelled based on the gaps identified during the literature review. Generally speaking, there are three steps involved in the completion of an experimental process: formulating the appropriate samples according to desired specifications, setting up the proper test rig, and conducting the experiments on these samples to acquire the results. The first step involved the manufacturing of carbon/epoxy composite plates with bonded Piezoelectric Fibre Composite (PFC) or Macro Fibre Composite (MFC) transducers. The structures were made of carbon fibre and epoxy resin and had a [0/90] lay-up with a total of eight layers. Each layer measured 0.2 mm in thickness whilst the total thickness was 1.8 mm. Each plate

had a width of 140 mm and a length of 250 mm. During the manufacturing, Teflon tapes were used to simulate damage in different locations of four carbon/epoxy plates. Furthermore, damage was induced in five of the MFC transducers prior to bonding. The total number of six samples were manufactured from which five samples (bonded transducer on carbon/epoxy plate) had various forms of damage in the structure and/or transducer. The remaining samples were kept free from damage for comparison purposes. As a result of the manufacturing process, certain errors, such as misalignments, shifts and gaps, may be found in the samples. With this in mind, all samples were scanned using a C-Scan test machine. In this process, the C-Scan machine scanned all of the samples' soft and rough surfaces to determine whether any shifts or manufacturing errors existed in the samples and also to confirm the existence of induced damage (Teflon) at the designated location of relevant plates. Fortunately, it was confirmed that errors were not significant and all samples were suitable for testing. The last step involved testing the samples to obtain the data required to delineate damage in the transducer from structural damage. First, the fatigue performances of MFC/PFC transducers, as well as carbon/epoxy plates, were explored using a 3-point-bend loading configuration. The fatigue cyclic loading was applied to the samples. The LCR meter and an A/D data logger were used to continuously measure the electrical properties of the transducer. SEM and C-Scans were used to visually inspect the transducer and the structure once a change was observed in the measured electrical properties. The aim was to identify the proper parameter needed to distinguish transducer damage from structural damage. Following this, a strain gauge was applied to measure the strain level of the structure under fatigue loading using a Vishay strain recorder. The MFC strain reading and strain gauge reading were gathered using the strain-based delineation technique.

The next step of the project was to find the appropriate computational modelling technique with which to validate the experimental results. For this purpose, an FEM software package known as ABAQUS was selected due to its diverse material library and special piezoelectric material features. The MFC transducers bonded onto carbon/epoxy composite plates were modelled and simulated using similar loading and boundary conditions in both active and passive modes. In addition, the damage that was intentionally inflicted onto the structure and/or the transducer was also simulated in ABAQUS.

Up to this point, all of the experiments were performed using the transducer in passive mode (sensor) as the mechanical excitation caused the MFC transducer to generate electrical output (voltage). However, the active form of the MFC transducer (actuator) was used for the electromechanical impedance-based delineation technique. An AD5933 impedance analyser was used to activate the MFC bonded to the carbon/epoxy structure and to simultaneously measure the

electromechanical impedance responses of the MFC actuator. The electromechanical impedance, including resistance and reactance, was experimentally measured and admittance components, such as susceptance and conductance, were calculated. These parameters are compared for six samples with various structural-transducer damage situations in order to delineate transducer damage from structural damage.

During the fatigue test experiments, it was incidentally observed that the electromagnetic field generated by the electric engine of the test machine interfered with the output voltage of the MFC transducer. To identify the main recipient of this interference, a series of shielding and insulation tests were conducted, which illustrated that the MFC transducer itself is subject to electromagnetic interference (EMI). Therefore, the scattering parameters of the normal and damaged transducers were measured using the network analyser while the horn antenna transmitted the electromagnetic waves to the transducer. The aim was to investigate the possibility of using the MFC transducer's sensitivity to EMI as a tool with which to detect damage in the transducer itself. After the experimental and computational results were gathered, they were analysed and compared to each other for validation purposes. This comparison and discussion helped in determining the optimum delineation technique.

1.4.   Thesis Outline

Chapter 1: Introduction

This chapter presents the background of the proposed research, as well as the rationale for this project, the methodology, and the thesis outline.

Chapter 2: Literature Review

This chapter includes a wide-range Literature Review of relevant fields, such as SHM and Multifunctional Composite structures and their applications. In addition, different types of Structural Health Monitoring/Non-Destructive Techniques and their backgrounds are briefly introduced. The background of piezoelectric transducers and the new generation of piezo-fibre-based transducers are also investigated.

Chapter 3: Manufacturing and Experiments

This chapter outlines the process behind the manufacturing of carbon/epoxy samples as well as the bonding of PFC and MFC transducers to these plates. The process consists of layering

carbon/epoxy plates and placing Teflon in relevant locations, curing the laminate, cutting the laminate into designated dimensions and bonding the transducer to the structure.

Next, the experimental modelling procedure performed in the present research is explained. The manufacturing process is first described and explored, following which the experimental procedure for each proposed technique as well as the data acquisition instruments and processes are discussed.

Chapter 4: Finite Element Analysis

In this chapter, the Finite Element Method software package known as ABAQUS is used for computational modelling. The sample consists of an MFC transducer bonded onto a carbon/epoxy plate, which is modelled and simulated. Loading and boundary conditions identical to those in the experiments are defined and the model is analysed using the ABAQUS/Solver. The MFC transducer is simulated in both active and passive modes. The comparison of FEM results and experimental results is discussed accordingly in the relevant chapter.

Chapter 5: The Fatigue Performance of Degraded Piezo-Fibre-based Transducer

This chapter investigates the performance of healthy and damaged transducers under fatigue loading through the continuous monitoring of their electrical properties and voltage responses. The controlled fatigue cyclic loading is applied to the sample and the status of the structure whilst the transducer is also periodically observed. The aim of this chapter is to investigate the fatigue behaviour of piezo-fibre-based transducers and the impact of transducer damage, as well as structural damage, on their electrical properties. The status of the structure is inspected using the C-SCAN test, whilst Scanning Electron Microscopy (SEM) imaging is used to inspect the impact of transducer damage on its internal components, such as piezo-fibres and electrodes. The changes in the local properties of the transducer are also explored through SEM and local capacitance measurement.

Chapter 6: The Strain-based Delineation Technique

This chapter examines how the comparison of MFC strain readings with the strain gauge measurements and theoretical strain calculations (FEM results) can be used to delineate possible damage in the transducer from that in the host structure.

Chapter 7: Electromechanical Impedance-based Technique

This chapter proposes a delineation technique based on the active behaviour of the MFC transducer. The electromechanical coupling between the bonded MFC and composite structure is used as the basis for this proposed technique. The electromechanical impedance components of the MFC transducer, such as Real or Imaginary, are measured for samples with various damage scenarios. The admittance values are also calculated from the impedance measurements. These parameters are compared for all six samples to find the proper parameter for each damage situation, such as pure structural damage, pure transducer damage or damage in both the structure and the transducer.

Chapter 8: Electromagnetic Interference Effect on the MFC transducer

In this chapter, the effect of electromagnetic interference on the MFC transducer output is investigated using two approaches. With the first approach, shielding techniques are used to eliminate noise caused by EMI. It is also observed that the main recipient of interference in the test rig is the MFC transducer itself. With the second approach, the horn antenna is used to transmit the electromagnetic waves generated by the network analyser to damaged or intact MFC transducers, thus enabling a comparison between the scattering parameters measured by the network analyser and the selected frequency range for both.

Chapter 9: Conclusion

After gathering all experimental results from this research project and comparing them with some FEM and computational results, a summary of the research findings is presented.

References

This chapter presents all of the referenced databases including catalogues, journals, and electronic resources.

1.5. List of Publications

Journal Papers

1. M. Mehdizadeh, S. John, C.H. Wang, V. Verijenko, and P.J. Callus, "Delineation of Structural Damage from Piezo-fibre-based Sensor Degradation.", International Journal of Engineering Science and Technology, 247-264, 2012

2. M. Mehdizadeh, S. John, C. H. Wang, V Verijenko, and P. J. Callus. "Characterization of Piezo Fibre-Based Sensors Responses in Multifunctional Composites." Advanced Materials Research, 633-638, 2012

Peer-reviewed Conference Papers

3. M. Mehdizadeh, S. John, C. H. Wang, "Electromechanical Behavior of Degraded Piezo-Fibre-Based Transducer to Detect Damage in Carbon-Fibre Composite Structures." Proceeding of ASME 2014 Conference on Smart Materials, Adaptive Structures and Intelligent Systems, Rhode Island, Prtland USA, 8-10 September 2014.

4. M. Mehdizadeh, S. John, C. H. Wang, K. Ghorbani, and W. Rowe. "Distinguishing the Degradation of the Interdigital Piezoelectric Fibre Transducers from Structural Damage in Multifunctional Composites." In ASME 2012 Conference on Smart Materials, Adaptive Structures and Intelligent Systems, pp. 869-877. American Society of Mechanical Engineers, 2012.

5. M. Mehdizadeh, S. John, C. H. Wang, V. Verijenko, P. J. Callus, W. Rowe, A. Galehdar , K. Ghorbani "Characterization of Structural Damage from Piezo fibre-based Damaged in Multifunctional Composite" ASME 2011 Conference on Smart Materials, Adaptive Structures and Intelligent Systems SMASIS2011, Scottsdale, Arizona, USA, September 18-21, 2011.

6. M. Mehdizadeh, S. John, C. H. Wang, V. Verijenko, W. Rowe, K. Ghorbani, A. Galehdar, and P. J. Callus "Differentiating Structural Damage From Piezo-Fibre-Based Sensor Damage in Multifunctional Composites." In ASME 2011 Conference on Smart Materials, Adaptive Structures and Intelligent Systems, pp. 119-128. American Society of Mechanical Engineers, 2011.

7. M. Mehdizadeh, S. John, C. H. Wang, M. Bannister, and V. Verijenko. "Degradation of Sensor Systems in Multifunctional Composites." In ASME 2010 Conference on Smart Materials, Adaptive Structures and Intelligent Systems, pp. 115-124. American Society of Mechanical Engineers, 2010.

CHAPTER 2 Literature Review

2.1. Introduction

Composite structures have enabled great weight savings, efficiency and performance for advance structures such as aerospace vehicles. However, these structures are still based on traditional structural design philosophy whereby composites perform only one task, namely that of loading bearing structures. In contrast, the next-generation design of structural components involves combining multiple functions, and thus making the structure a multi-functional unit. This type of structure was first investigated by Chamis et al. (1987, 2001). The goal of such multifunctional structures (MFS) is to incorporate various tasks and functions such as structural, electrical and thermal within a structural housing. According to Inman et al. (2007), multifunctionality refers to reducing the physical distance between subsystems and coupling the functions different subsystems perform." The blending of multiple subsystems into a single material or structure reduces overall system mass and size while simultaneously increasing system performance and functionality.

However, the performance and behavioural characteristics of the multifunctional structures can be affected by degradation of any of the sub-components such as sensor, actuator, structure (body), battery etc. This can be caused by sustained use as well as exposure to severe environmental conditions or damage resulting from external conditions such as loading abrasion, operator abuse, or neglect. These factors can have serious consequences on the in-service structures as it relates to safety, cost, and operational capability. In light of this, major concerns in the operational environment include the timely and accurate detection, characterisation and monitoring of structural cracking, corrosion, delamination, material degradation and other types of damage (Kessler et al., 2002).

This calls for Structural Health Monitoring (SHM) as a possible method with which the safety and reliability of structures can be improved, thereby also reducing their operational cost. Structural health monitoring technology is perceived as a revolutionary method for determining the integrity of structures and involves the use of multidisciplinary fields including sensors, materials; signal processing, system integration and signal interpretation (Wicklie et al., 2000). However, as the application of SHM systems to monitor the status of the MFS becomes increasingly common, it

will be important to define standardised procedures with which to test the durability, reliability, and longevity of the systems. In addition, while no formal standard regulates these criteria for SHM devices, to achieve condition-based maintenance in a cost effective manner, the sensors themselves must be reliable enough with sufficient MTF meaning that they do not require replacement at intervals less than the economic lifetime of the components they are monitoring.

Shaio et al. (1993) put forth two requirements which they felt were critical to establishing such a multifunctional structure which can be performed properly in real life. The first requirement related to the effective use of available resources, whilst the second pertained to formal methods to quantify the current integrity of a specific structure and subsequent reliable evaluation of its future integrity. This dissertation will cover various topics regarding the functionality and durability of transducers, as one of the more vulnerable parts of SHM systems, within the M.F composites. This will include the design of multifunctional composites, existing standards for SHM systems, state-of-the-art transducer systems etc.

2.2. Composites and their application

Advance composite materials have been extensively used in structural applications, due to their advantageous characteristics, such as high stiffness and strength to weight ratio, improved fatigue resistance, and superior damage tolerance capability compared to the metallic structure. Carbon/epoxy composites (Figure 2.6) have higher stiffness and strength properties than other composites, and particularly the commonly used E-glass/epoxy composites. These advantageous properties have led to the use of carbon/epoxy composites in structures which withstand higher stresses, such as aircraft and aerospace structures (Kedward, 2007). However, carbon/epoxy composites laminates, like any composite material or structure, are susceptible to defects such as fibre breakage, matrix cracking, deboning between the fibres and matrix, and delamination. The defect can significantly reduce the strength of structures and may result in failure of the structure. When failure occurs, it is often catastrophic, not only in terms of human life or monetary losses, but also with regard to the potentially devastating effects on the psychological state of the public.

2.3. Multifunctional composites

There have been numerous advances in materials and structural technology over the last few decades. Indeed, there are widespread efforts in the aerospace industries to replace metallic structures with high performance composite structures. The composite structures have enabled great weight savings, efficiency and performance for aerospace vehicles. These advanced structures using composites are still based on traditional structural design philosophy, whereby composites perform only one task, namely that of load bearing structures. Furthermore, over the

past decade, the expectations of aeronautical systems have continued to demand significant increases in flight time, service life, and adaptability for multi-phase missions without sacrificing payload capacity, additional structural weight, or reliability. Such expectations drive technological advances in the area of composites and multifunctional materials. Multifunctionality, according to Matic (2003), "is about reducing the physical distance between subsystems and coupling the functions different subsystems perform." The blending of multiple subsystems into a single material or structure reduces overall system mass and size while simultaneously increasing system performance and functionality. The goal of such multifunctional structures (MFS) is to incorporate various tasks within a structural housing. An example of a multifunctional composite structure would be to combine structural, electrical and thermal functions. The avionics in aircraft or spacecraft comprise various separate supporting components such as electrical housing, supporting walls, cables, interconnects, spacers, dampers and other parts. Avionics can account for anywhere between 20 to 40% of the weight of a spacecraft or a UAV. Roberts (2009) demonstrated a working prototype of MFS for the spacecraft avionics housing. The MFS was designed to replace the conventional avionics housing, wall support, thermal management units, interconnects and wirings. This was a novel approach to reducing the weight by a substantial amount. There were many challenges involving the integration of multiple functionalities. The use of novel thermal dissipating materials with the assistance of heat pipes was shown as one of the options. The multi-chip module with copper interconnect flex circuit board was used to embed avionics on top of a load-bearing composite structural unit. There are a number of other ideas for integrating electronics and structures. One such idea involves integrating structural and battery components for small scale UAVs. The lithium polymer battery is used to power the UAV flight as well as acting as a structural component. This is an increasingly common practice in small and mid-scaled UAV designs, where increasing payload capacity and reducing volume are the primary goals. Nevertheless, most of the existing techniques are still laboratory-scale and are not capable of being performed in real-life environments.

Such expectations drive technological advances in the area of composites and multifunctional materials. Indeed blending multiple subsystems into a single material or structure reduces overall system mass and size while simultaneously increasing system performance and functionality. Such trends propel the drive behind technological advances in multifunctional materials. Matic (2003) provided 3 classes of multifunctionality, designating them as Types I, II, and III.

Type I multifunctionality involves the addition of subsystems to provide additional performance enhancement to a primary or critical function. Most smart structures would be considered Type I multifunctional systems. Type II multifunctionality is the union or co-location of functions

embedded within a system component. Type III multifunctionality is the integration of functions shared in a volume of material. The progression from Type I to Type II to Type III multifunctionality also represents the desired technological track in the overall design course of multifunctional structures. For example, surface mounting a structural health monitoring system to an airfoil would be a Type I, whereas a load bearing, health monitoring sensory skin shaped as an airfoil would be a Type III. A summary of the characteristics of Types I, II, and III multifunctionality is given in Table 2-1.

For over a decade now, the International Society for Optical Engineering (SPIE) has sponsored a multifunctional materials segment as part of their Smart Structures and Materials conferences. In the more recent literature, researchers have been focussing on the transition between Type I and Type II systems to the Type III systems. At the Naval Research Laboratory, Thomas et al. (2002) focussed their research efforts on extending the flight time of a DARPA sponsored unmanned autonomous vehicle (UAV). One concept pursued by Thomas et al. (2003) was the development of structure battery materials. In brief, commercially available plastic-lithium-ion batteries which come in thin (~0.5 mm thick) flexible sheets were combined with other structural materials to create a load bearing wing which also doubled as the power supply for the electric propulsion system. Their work also serves as a prime example of extending a Type I multifunctionality (the plastic-lithium-ion battery) to a Type III system (using the battery as a load-bearing support structure). Another area of research is the use of structural materials as consumable propellants, sometimes referred to as autophagous materials. Qidwai, Thomas & Matic (2003) also discussed the concept of structure battery design. Joshi et al. (2003) designed structural polymer composite materials which can be converted into combustible fuels once in orbit.

Table 2-1: A Summary of Characteristics of Types I, II, and III Multifunctionality

Type l Multifunctionality - Added Subsystems	• Subsystem addition to provide additional performance • Connectivity of links between subsystems • Increased physical or informational coupling between subsystems
Type וו Multifunctionality Co-located components	• Component co-location to provide packaing integration • Reduced dimensionality and complexity of final system • Physical distances between susbsystems are reduced
Type III Multifunctionality Integrated Materials	• Material selection based on a set of properties to satisfy more than one subsystem function • Physical volumes of subsystems are combined • Reduced volume and mass of final multifunctional subsystem

It is also important to recognise that multifunctionality can occur on different scales. Material scientists and engineers have been trying to construct new polymers and ceramics which exhibit desirable traits in the macro-world by layering materials at the nano-level atomic scale. For example, in 1989, a multifunctional materials symposium of the Materials Research Society outlined the design of ceramic composites, silica optics, and piezoelectric composites at the nano-level. Similarly & Maruo et al. (2008) discussed the design of MEMS- and NEMS-based smart chips with embedded carbon nanotube technology to impart superior structural, electronic and surface quality properties. The current state-of-the-art MNT sensors examined here come primarily from the field of smart materials and structures. In addition, the Australian Government has funded a 7 year program aimed at developing indigenous expertise in the design and development of multifunctional materials and structures at the Defence Materials Technology Centre (DMTC).

2.4.   Piezoelectric Direct and Converse Effects

For piezoelectrics, the poling process is used to align the domain of piezoelectric ceramic. In this process, the piezoelectric ceramic placed in a strong DC electric field and with a temperature less than its curie temperature. The poled piezoelectric ceramic can become electrically polarised and generates electric charge on its surface when it is under mechanical excitation (strain). The electrodes on the surface of piezoelectric material collect the generated charges and apply electric field to the piezoelectric element. This is called the direct piezoelectric effect and used in sensing applications. In the other hand, the poled piezoelectric ceramic generates mechanical strain once it gets excited by an electric filed. This is called the converse piezoelectric effect and used in actuation applications. Figure 2-1 shows the direct and converse piezoelectric effect.

Hence, a piezoelectric material can be used as a transducer with the ability to convert mechanical to electrical or electrical to mechanical energy. For electrical to mechanical energy conversion, it is called a piezo-motor or in more common term piezo-actuator. The piezo-generator or piezo-sensor is called a piezoelectric material which converts mechanical energy. The performance of the piezoelectric material in sensing and actuating modes depend on various parameters such as charge coefficient (d_{31} and d_{33}), coupling coefficient (k_{31} and k_{33}) and the polarisation direction. Figure 2-2, in the form of block diagrams, shows the transducer characteristics of the piezoelectric materials.
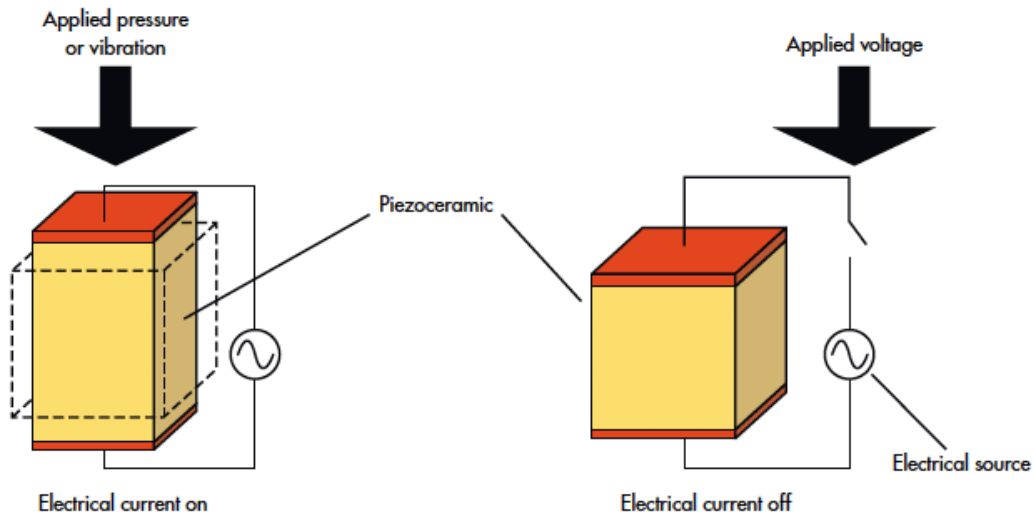
Figure 2-1: Piezoelectric material (Dirjish, 2012)

Direct Effect

| Mechanical Energy | ⟷ | Piezoelectric Material | ⟷ | Electrical Energy |
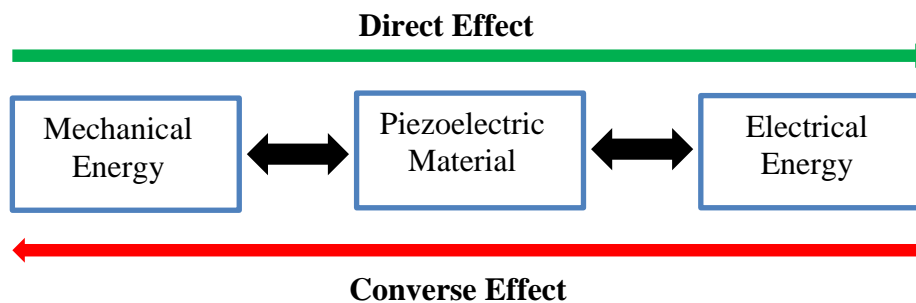
Converse Effect

Figure 2-2: Piezoelectric material direct and inverse effects

2.4.1. Piezoelectric Material Components

There are various types of piezoelectric materials such as lead titanate, lead lanthanum zirconate titanate, polyvinyl fluoride (PVF), polyvinyl fluoride (PVF). Some of the typical piezoelectric materials, quartz, lead zirconate titanate (PZT), lead lanthanum zirconate titanate, barium titanate, lead titanate, cadmium sulphide etc. The piezoelectric materials in ceramic form show better electromechanical performance as compared to their polymer form. However, the ceramic form is extremely brittle. In following sections, a brief introduction to some of the typical types of piezoelectric materials such as piezo-polymers, piezo-composites, single crystal materials and piezo-ceramics are provided.

2.4.1.1.   Single Crystals

Single crystals are normally used for frequency stabilised oscillators and surface acoustic devices applications. They are anisotropic and their properties depend on the cut of the materials and

direction of wave propagation in the material. Quartz, lithium nibonate (LiNbO3), and lithium tantalite (LiTaO3) are some of the most popular single crystals materials (Schwartz, 2009).

2.4.1.2. Piezo-ceramics

Piezoelectric ceramics have a perovskite structure which is an ideal structure for scientists as it can be easily tailored for applications by incorporating various captions into the perovskite structure. This specification makes the piezoelectric ceramics a suitable material for many applications.
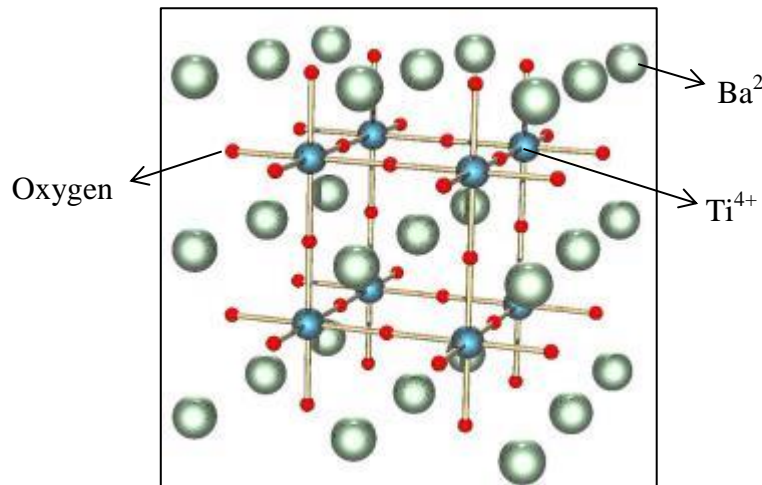
Figure 2-3: Crystalline structure of a Barium Titanate (Perovskite structure) (Konka H.P., 2010)

One of the common examples of perovskite piezoelectric ceramic material is Barium Titanate ceramic. As it is shown in Figure 2-3, the large caption at the corner of the structure is Ba^2, the smaller caption in the body centre is Ti^4 and the Oxygen (O) is in the centre of the face. (Moheimani et. al., 2006 and Schwartz, 2009)

2.4.1.3. Piezo-polymers

Polymers are known as one of the materials which have piezoelectric properties. However, these properties are only strong and effective in polyvinylidene fluoride (PVDF or PVF2) and PVDF copolymers. The PVDF is one of the common piezoelectric materials, especially for the application where the low-cost piezoelectric material is required. The piezoelectric polymers are mostly used for directional microphones and ultrasonic hydrophones applications (Konka H.P., 2010).

2.4.1.4. Piezo-composites

Piezo-composites are one of the most common types of piezoelectric material used in various applications. Due to their composite nature, they have excellent tailored properties. These materials are flexible and have high coupling factors and low acoustic impedance. Some of their common applications are underwater sonar and medical diagnostic ultrasonic tests (Konka H.P., 2010).

2.4.2. Piezoelectric Constitutive Equations

In order to describe the behaviour of piezoelectric material when excited by whether mechanical strain or electric charge, the constitutive equations are widely used. The assumption for deriving constitutive equations is that the total strain in the piezoelectric material can be calculated by adding the mechanical strain induced by mechanical stress to the actuation strain caused by the applied electric voltage. The general from of constitute equations for a linear piezoelectric material in actuation mode is presented in Equation 2-1 (Moheimani et al., 2006):

Equation 2-1

$$\epsilon_i = S_{ij}^E \sigma_j + d_{mi} E_m$$

$$D_m = d_{mi} \sigma_i + \xi_{ij}^\sigma E_k$$

This can also be written for sensing application as shown in Equation 2-2 (Konka H.P., 2010).

Equation 2-2

$$\epsilon_i = S_{ij}^D \sigma_j + g_{mi} D_m$$

$$E_i = g_{mi} \sigma_i + \beta_{ij}^\sigma D_k$$

Where σ is the stress vector (N/m^2), ϵ is the strain vector, E is the applied electric field vector (V/m), D is the electric displacement matrix (C/m^2), d is the piezoelectric strain constant in matrix from (m/V), S is the compliance coefficient matrix (m^2/N), g is the piezoelectric constants matrix (m^2/N), ξ is permittivity (F/m) and β is the impermittivity components (m/F). Superscripts D, E and σ show the measurements under constant electric displacement, constant electric field and contact stress respectively. Subscripts m and k are represent directions and indexes i, j=1, 2… 6.

2.4.3. Piezoelectric Coefficients

The terminologies of various piezoelectric coefficients such as d_{ij}, g_{ij}, S_{ij}, k_{ij}, and e_{ij} are presented in previous section. However, due to the importance of these coefficients in explaining the performance of piezoelectric material, further information on their physical meaning are provided here.

- **Piezoelectric Constant (d_{ij})**

Assuming that the strain is in j-axis and electric field is in i-axis, their ratio is defined through piezoelectric constant as d_{ij}. For instance, the ratio of strain along axis 1 to the electric field applied along axis 3 is called d_{31}.

- **Piezoelectric Constant (g_{ij})**

When the strain is developing along j-axis and the electric charge is stored on electrodes which are perpendicular to the i-axis. The ratio of developed strain to the stored charge is called g_{ij}.

- **Elastic Compliance (E_{ij})**

Assuming that the stress is only in j-direction, the ratio of the strain in the i-direction to the stress is shown as E_{ij}.

- **Dielectric Coefficient, (e_{ij})**

The dielectric coefficient (e_{ij}) show the generated charge per unit area in the i-axis caused by an electric field applied to the j-axis.

- **Piezoelectric Coupling Coefficient (k_{ij})**

This is one of the more important coefficients of piezoelectric materials as it can indicate the strength of a piezoelectric material in term of converting mechanical energy to electrical energy of vice versa. The k_{ij} is representing a situation where the input energy (stress or strain) is in the j-direction and the piezoelectric electrodes are perpendicular to the i-axis. The coupling coefficient has a relationship with piezoelectric constants as shown in Equation 2-3:

Equation 2-3

$$K_{ij}^{2} = g_{ij} d_{ij} E_p$$

2.4.4. Piezoelectric Sensor

As it was mentioned before, the piezoelectric sensor refers to a transducer which produces electrical charge when mechanically excited. The piezoelectric sensors are widely used in various applications due to their excellent signal to noise ratio, compactness and ability to bond or embed to a structure. The aim of this section is to formulate the performance of piezoelectric sensor in terms of generating voltage due to the mechanical deformation. The generic form of a piezoelectric sensor is provided in Figure 2-4.
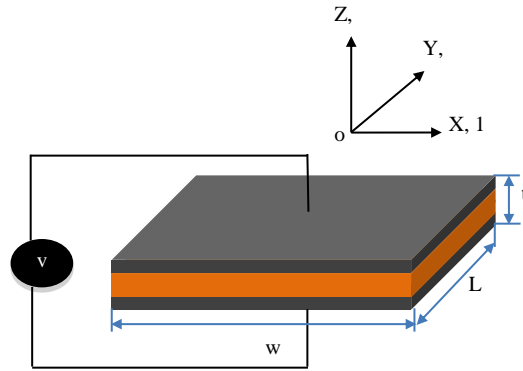
Figure 2-4: Piezoelectric transducer

Equation 2-4 shows the relation between the applied stress field (S) and the generated electric displacement (D in the piezoelectric sensor, assuming that there is no applied electric field (E=0) (Moheimani et al., 2006; Konka H.P., 2010).As mentioned earlier, d is the coupling vector.

Equation 2-4

$$Ds = dS$$

Therefore, the matrix from of electric displacement and stress field are as below:

$$D = \begin{bmatrix} D_1 \\ D_2 \\ D_3 \end{bmatrix}$$

D_1, D_2, and D_3: Electric displacements in the directions 1, 2, and 3 respectively.

$$S = \begin{bmatrix} S_1 \\ S_2 \\ S_3 \\ S_{23} \\ S_{31} \\ S_{12} \end{bmatrix} \begin{bmatrix} 0 & 0 & 0 & 0 & d_{15} & 0 \\ 0 & 0 & 0 & d_{15} & 0 & 0 \\ d_{31} & d_{31} & d_{33} & 0 & 0 & 0 \end{bmatrix}$$

Preumont, 2011 derived the generated charge (q) as shown in Equation 2-5:

46

Equation 2-5

$$q = \iiint [D1 \quad D2 \quad D3] \begin{bmatrix} dA_1 \\ dA_2 \\ dA_3 \end{bmatrix}$$

In this equation, dA_1, dA_2 and dA_3 are the areas of the differential electrodes in (2-3), (1-3), and (1-2) planes, respectively. In the other hand, the general equation of generated voltage based on the capacitance of the piezoelectric material (C) and generates charge (Q), is written as Equation 2-6 (Preumont, 2011):

Equation 2-6

$$V = \frac{q}{C}$$

By replacing the relationship for q into Equation 2-6 and Equation 2-7 can be presented as below:

Equation 2-7

$$V = \frac{E d_{3x} \varepsilon_{3x} dA}{C}$$

It can be deduced from above equation that the generated voltage in the piezoelectric sensor due to mechanical deformation, is directly proportional to the applied strain and has inverse relationship with the capacitance of the piezoelectric transducer. It also has direct relationship with the material properties such as Young's modulus and piezoelectric charge coefficient.

2.4.5. Piezoelectric Actuator

In previous section, the performance and formulation of piezoelectric transducer in sensing mode (piezoelectric actuator) was discussed. However, the actuation properties of piezoelectric materials are also play a very important role in many applications and need to be discussed. The capabilities of piezoelectric actuators are widely used in various fields of technology. Among all, piezoelectric bimorph configuration gets a lot of attention from researchers and industries when it comes to converting mechanical to electrical and electrical to mechanical energy. Two main types of piezoelectric bimorphs are heterogeneous bimorphs and homogeneous bimorphs. The difference between these two types is based on their ability to serve different functions such as electric and elastic. In a heterogeneous bimorph one element serves only an elastic function whilst the other

serves two functions, namely electric and elastic. In the other hand, in homogeneous bimorphs both the elements serve both functions, electric and elastic.

According to (El Sayed, 2013), the bending moment generated by the heterogeneous bimorph can be defined as a function of the thickness ratio of the piezoelectric layer and elastic layer. Cunningham et al. (1997) derived the equation to determine the effective bending moment and stress for a heterogeneous piezoelectric bimorph configuration based on following assumptions:

- The composite structure is assumed to be very thin
- Linear strain distribution across the thickness of the composite structure.
- The piezoelectric layer covered the whole elastic layer.
- The constant electric field
- The perfect bonding (thickness of bonding layer is zero)

Figure 2-5 shows the structure of a heterogeneous piezoelectric bimorph configuration where D represents the distance between neutral axis and bottom of the elastic layer. This parameter, D, can be calculated from Equation 2-8 according to Cunningham et al., 1997.
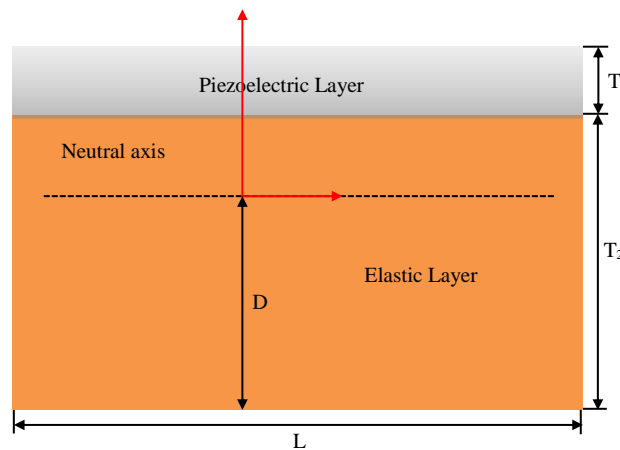
Figure 2-5: Piezoelectric layer bonded to the elastic layer

Equation 2-8

$$D = \frac{Te(1 + 2ET + ET^2)}{2(1 + ET)}$$

Where, T I the thickness ratio and is equal to thickness of piezoelectric layer (Tp)/ thickness of elastic layer (Te).

Furthermore, the relationship between the stress and strain for a piezoelectric actuator can be determined by Equation 2-9 (Cunningham et al., 1997).

Equation 2-9

$$\sigma_p = E_p\big(\epsilon_p - \Lambda\big)$$

$$= E\frac{\sigma}{Te}(Y + D) - E_p\Lambda$$

$$\Lambda = \left(\frac{V}{T_p}\right) * d_{31} \ \& \ E = \frac{E_p}{Ee}$$

The stress-strain relation of elastic layer can also be gained from Equation 2-10.

Equation 2-10

$$\sigma_e = E_e\epsilon_e$$

$$= E\frac{\sigma}{Te}(Y + D) - E_p\Lambda$$

$$\Lambda = \left(\frac{V}{T_p}\right) * d_{31} \ \& \ E = E_p/E_e$$

Therefore, this relation can be presented as shown in Equation 2-11(Cunningham et al., 1997).

Equation 2-11

$$\sigma_e = E_e\epsilon_e$$

$$= \sigma(Y + D)/T_e$$

In order to find the interface stress relation, the moment equilibrium formulation is derived about the neutral axis as shown in Equation 2-12.

Equation 2-12

$$\int_{elastic} \sigma_e dA + \int_{Piezo} \sigma_p dA = 0$$

Therefore, the stress at interface (σ) can be presented as Equation 2-13: (Konka H.P., 2010).

Equation 2-13

$$\sigma = E_P \frac{\frac{\Lambda}{2}\left[-\mathrm{T} - 2\mathrm{T} + 2\mathrm{T}\frac{\mathrm{D}}{\mathrm{Te}}\right]}{\frac{Te}{3}\left[1 - 3\frac{D}{Te} + 3\left(\frac{D}{Te}\right)^2\right] + E\left(T^3 + 3T^2(1 - \frac{D}{Te} + 3T(1 - \frac{2D}{tb} + \frac{D^2}{Te^2})\right) + \frac{D}{2}\left[ET\left(\frac{2D}{Te} - T - 2\right) + \left(\frac{2d}{Te} - 1\right)\right]}$$

The piezoelectric layer applies a bending moment to the elastic layer due to the electrical excitation. The effective bending moment can be calculated from Equation 2-14 (Konka H.P., 2010):

Equation 2-14

$$M = W.\frac{Te^2\sigma}{6}$$

By inserting the bending moment from Equation 2-13 into Equation 2-14, it can be discussed that both effective bending moment and interface stress are functions of D, T and young's modulus ratio E (Ep/Ee). However, D itself is a function of T and E, as mentioned before. Therefore, it is concluded that the effective bending moment as well as interface stress are functions of T and E only. In other words, the performance of heterogeneous piezoelectric bimorph configuration is depending on the optimisation of T and E values.

2.4.6. Applications of Piezoelectric Materials

Since the discovery of piezoelectricity phenomenon, it has been numerous researches and developments on the piezoelectric materials and how to employ them in the variety of applications. In fact, one of the first major applications of these materials was as an ultrasound submarine detector during World War I. Nowadays, the piezoelectric materials are used in different applications such as ultrasonic transducers, microphones, piezo-ignition systems. (Konka H.P., 2010)

One of the significant applications of piezoelectric materials is in vibration control of aircrafts, satellites. Also, some of the sport-related companies have been using the piezoelectric materials to improve the performance of their products such as composite tennis rackets and cricket bat. These sport equipment are mainly equipped with a piezoelectric transducer to reduce the vibration and increase their comfort and handling (Moheimani & Fleming, 2006).

The most advanced applications of piezoelectric materials are in aerospace devices and instrumentations, structural health monitoring, vibration control, and energy harvesting. Some of the examples for the application of piezoelectric Martials in aerospace structures are in helicopter rotor blades, morphing wings and telecommunication satellites. Furthermore, the noise controlling application of piezoelectric materials such as acoustic transmission reduction panels, and active antenna structures are among the important application of these materials. The aim of researchers who work on the development of piezoelectric materials are to design high-performance and light-weight piezoelectric transducers to be used in aerospace and structural health monitoring applications. (Konka H. P., 2010)

The piezoelectric materials have also a wide range of applications as actuators. For instance, the piezoelectric actuators can be used to reduce the buffeting loads on the tail of the fighter aircraft in attacking position. In Figure 2-6 , the active vertical tail model which contains an embedded Macro Fibre Composite actuators built at NASA-Langley is shown (Konka H.P., 2010).
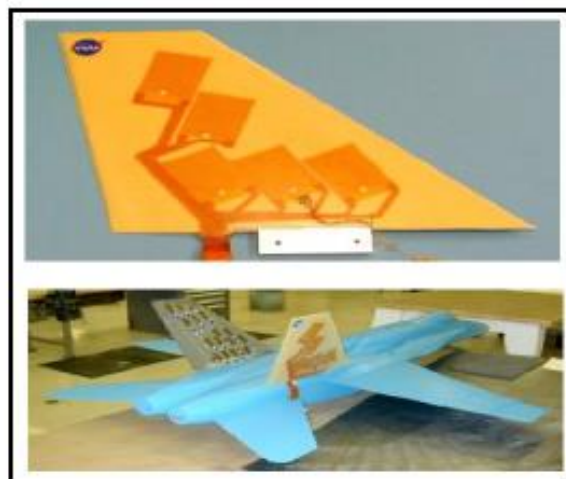
Figure 2-6: 1/6th scale of MFC buffet load alleviation
Wind tunnel model (Wilkie et al., 2000)

As it was mentioned before, energy harvesting is another important application of piezoelectric materials. In Figure 2-7, a concept design of a shoe energy harvester system is presented. In this design, the PVDF films are used to recovers the power which generates during walking.
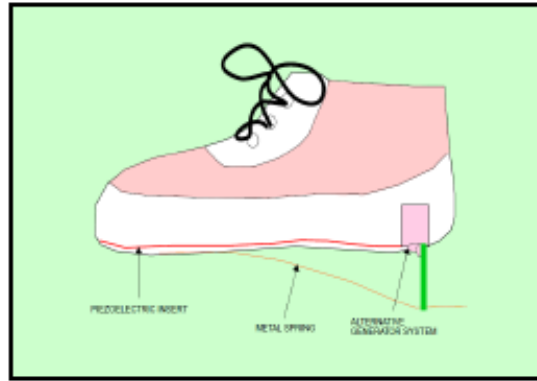
Figure 2-7: Shoe energy harvesting systems (Starner, 1996)

Another concept design is shown in Figure 2-8. In this design, a magic backpack is presented which has embedded PVDF films. It was found that carrying 45 kg backpack while waling at the speed of 4-5 km/h can generate 45.6 mW of power. This is an enough power to run an iPad, iPhone or head-mounted flashlight applications. (Sodano et al., 2007).

Figure 2-8: Magic backpack straps power generator (Sodano et al., 2007)

The piezoelectric linear motors/actuators and z-axis nanopositioning stages are among other examples of the application of piezoelectric actuators as shown in Figure 2-9. Figure 2-10 shows one of the examples of piezoelectric materials for structural health monitoring which is to evaluate the level of wear in wheels.

Figure 2-9: (a) N 215 linear piezoelectric motor (Pyhsik Instruments), (b) P-611 piezoelectric Z-axis nano-positioning stage (Pyhsik Instruments)
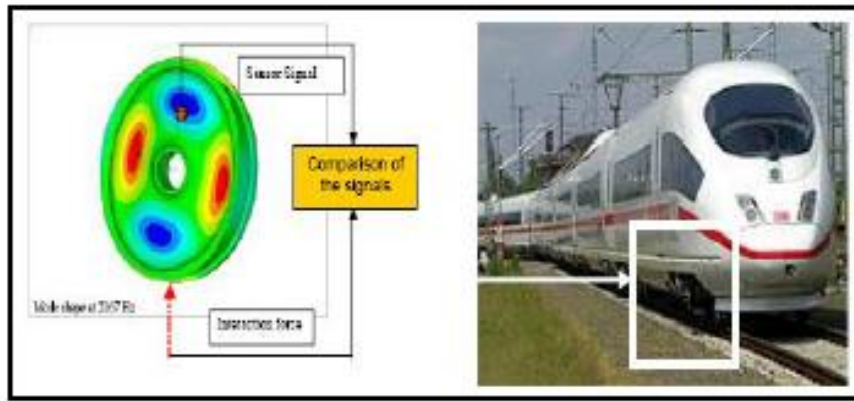
Figure 2-10: The proposed method for the assessment of the roughness of the wheel (Nuffer & Bein, 2006)

2.5. FE Dynamic Analysis

Finite element analysis (FEA) is a computer simulation technique used in a variety of science and engineering analyses. This analysis uses a numerical method known as the finite element method (FEM). This method is commonly embedded into different software packages in order to make them more user-friendly. These software packages are developed for various applications from medical to aerospace fields. Development of the finite element method in structural mechanics is usually based on an energy principle such as the virtual work principle or the minimum total potential energy principle The principle of this method is to represent the system or object with a geometrically similar model consisting of multiple, linked, simplified representations of discrete regions—i.e., finite elements on an unstructured grid (Zampelis et al., 2010). In order to analyse this system, the equations of equilibrium along with all the required physical boundaries and constitutive relations should apply to each element. Considering all the elements, a system of simultaneous equations is constructed. Depending on the nature of analysis i.e. linear or non-linear, the system of equations is solved for unknown values.

As the FEM is based on the calculations of each element, increasing the number of elements can improve the accuracy of the analysis. The act of dividing the system or structure into elements is called meshing. A common use of FEA is for the determination of stresses and displacements in mechanical objects and systems. However, it is also routinely used in the analysis of many other types of problems, including those in solid state diffusion, electromechanical and electromagnetism. This method will be discussed more thoroughly in the following sections.

2.5.1. FEM CAD

The application of computer software in engineering to analyse and simulate structures and components is called Computer-aided engineering (CAE). It encompasses simulation, validation,

and optimisation of products and manufacturing tools (Kolgiri et al., 2013). The CAE is widely used in engineering and science fields such as civil, mechanical, aerospace, and electronic engineering. In these fields, the CAE is used along with FEA to perform all kinds of engineering tasks. The following steps are common for all the FEA software packages:

- Pre-processing

- Analysis solver

- Post-processing

2.5.1.1. Pre-Processing

The first step in any Finite Element Analysis is the pre-processing which is called to the process of constructing the finite element model of the designated structure. For this step, the geometry of the structure as well as topological description are required. The goal of pre-processing is to realistically replicate the characteristics of the real model. To achieve this goal, all the available information such as pre-existing digital blueprints, design files and CAD models should be imported into the FEA environment. Upon the completion of this step, the generated model should be meshed which break up the model into small elements. The mesh network includes the geometric arrangement of elements and nodes. FEA packages such as ABAQUS and ANSYS use node numbers as a tool to identify the viewing solutions in structures such as deflections. Elements are bound by sets of nodes and contain the properties of the model such as mass and stiffness.

2.5.1.2. Analysis Solver

The next stage of the FEA process is to analyse the generated model in previous step. In this step, the FEM applies the designated loading and boundary conditions as well as properties of the elements to the model and conducts a series of computational procedures based on the selected analysis type which produce a model solution. This structural analysis solves the model and makes the calculation of various parameters such as deformations, strains, and stresses possible (Kolgiri et al., 2013).

2.5.1.3. Post-processing

The outcome of previous step can be observed and tabulated in the post-processing step. There are various numerical and graphical tools to identify the required data.

2.6.   Structural Health Monitoring/NDT

The process of implementing a damage detection strategy for aerospace, civil, and mechanical engineering infrastructure is referred to as Structural Health Monitoring (SHM) (Casciati, 2005). The aim is to quantify the inputs to and replications of a structure afore damage so that regression analysis can be acclimated to prognosticate the onset of damage and deterioration in the structural condition. A number of strategies are utilised to estimate the remaining functional life of the system such as the coupling of information from SHM, current environmental and operational conditions, precedent component and system level testing, and numerical modelling.

The SHM process involves the observation of a system over time utilising periodically sampled dynamic replication quantifications from an array of sensors, the extraction of damage-sensitive features from these quantifications, and the statistical analysis of these features to determine the current state of the system's health. For long-term SHM, the output of this process is periodically updated information regarding the ability of the structure to perform its intended function, namely that of identifying aging and degradation resulting from operational environments (Ren & Du, 2013). After extreme events, SHM is utilised for rapid condition screening and aims to provide, in near authentic time, reliable information regarding the integrity of the structure.

In recent years, the application of non-destructive examination (NDE) method to detect the damage status of structures has expanded significantly. The researchers have been developing new NDE techniques to be used in various industries such as such as aviation, space conveyance, power plant equipment and mechanical manufacture. In general, the structural damage detection can be categorised into local and global damage detection techniques.   The local-damage detection techniques are strong in detecting local damages and therefore mainly used to determine the existence and location of the damage. Examples of this type of damage detection are CT scanning and ultrasonic (Figure 2-11). Furthermore, the local damage detection method is based on the obtained information from damaged structure. In other words, it does not consider the baseline or theoretical calculations. The local damage detection technique is practical for small and regular structures. However, for complex structures in invisible or closed environments, it won`t be possible to detect possible structural damages based on the local damage detection logic. In other words, the local damage detection method can only be used to detect certain special components of a structure. In order to detect damage throughout the whole structure, especially for complex structures, a methodology called global damage detection has been widely used among researchers.

(a)   (b)

Figure 2-11: Local damage detection facilities: (a) C-SCAN, (b) Ultrasonic (Yan et al., 2007)

2.7.   Ultrasonic NDT Techniques

Ultrasonic Testing (UT) is one of the most important techniques and has many applications in a variety of fields. The principle of UT is to employ high frequency sound energy to conduct examinations and take measurements. Ultrasonic inspection can be used for flaw detection/evaluation, dimensional measurements, material characterisation, and more. To illustrate the general inspection principle, a typical pulse/echo inspection configuration, as illustrated in Figure 2-12, will be used.
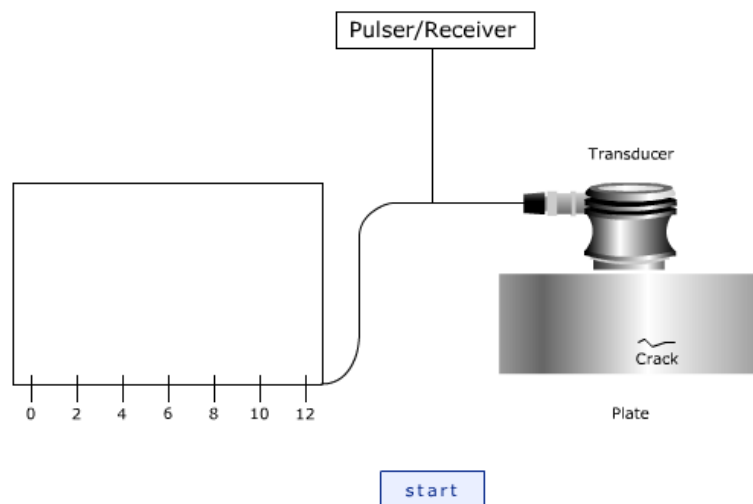
Figure 2-12: a typical pulse/echo inspection configuration (Courtesy: www.ndt-ed.org)

2.7.1. Conventional Ultrasonic Methods

An ultrasonic A, B or C scan involves the generation of an ultrasonic plot of the structure under study. The plot is generated by scanning the complete structure at regular intervals with a

piezoelectric transducer. In the A-Scan procedure, output signal amplitudes are displayed against a time scale and the depths of various defect locations are judged from the position of the signal peaks on the time sweep. The B-Scan procedure scans the top and the bottom surfaces of a flaw, while the C-Scan procedure displays the plan view of the defect boundaries in the material. In order to conduct the scan, two sensor configurations, namely the Through Transmission Method and the Pulse Echo Method, can be used. Conversely, this technique is time intense, as it involves line scanning of the entire structure, and also needs access to the complete structure under study, which is hard to achieve in the majority of cases (Bray & McBride, 1992; Shull, 2002).

2.7.2. Acoustic Emissions

The ASTM defined Acoustic Emission as the generation of transient elastic waves during the rapid release of energy from localised sources within a material (Figure 2-13). The source of these emissions in metals is proximately associated with the dislocation kineticism accompanying plastic deformation and the initiation and extension of cracks in a structure under stress. Other sources of Acoustic Emission include: melting, phase transformation, thermal stresses, cools down cracking and stress build up. The Acoustic Emission NDT technique is predicated on the detection and conversion of these high frequency elastic waves to electrical signals. This is accomplished by directly coupling piezoelectric transducers on the surface of the structure under study and loading the structure. Sensors are coupled with the structure by betokens of a fluid coolant and are secured with tape, adhesive bonds or magnetic hold downs. The output of each piezoelectric sensor (during structure loading) is amplified through a low-noise preamplifier, filtered to abstract any extraneous noise and further processed by opportune electronic equipment. The instrumentation of Acoustic Emission must provide some measure of the total quantity of detected emission for correlation with time and/or load. The Schematic process is shown in Figure 2-13 (ASTM Standard 2012).
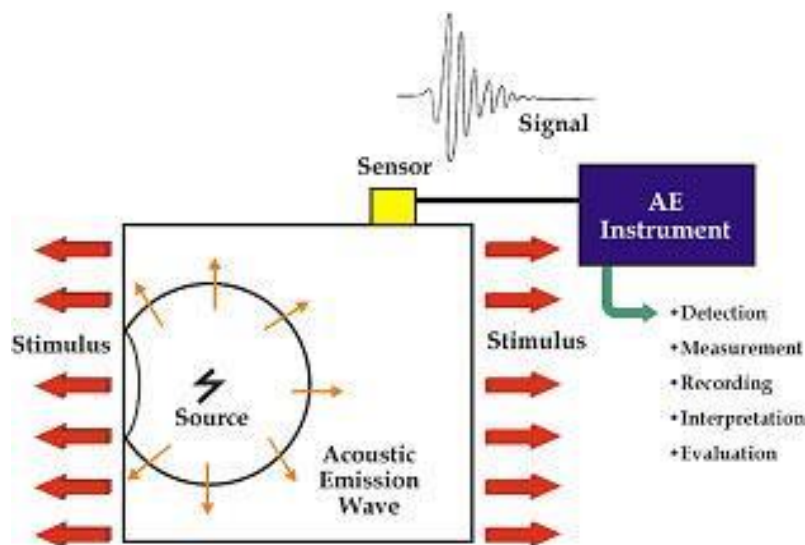
Figure 2-13: Acoustic Emission Process (ASTM E610-52)

Compared to conventional inspection methods the advantages of the Acoustic Emission technique are:

- High sensitivity.
- Early and rapid detection of defects, flaws, cracks etc.
- Real-time monitoring.
- Cost Reduction.
- Defective area location: only critical defects provide sustainable Acoustic Emission sources
- Minimisation of plant downtime for inspection: no need to scan the entire structural surface
- Minor disturbance of insulation.
- Application of Artificial Intelligence (AI) and Technological Packages: Expert systems for evaluating the condition of metallic pressure systems and tank bottoms based on the acquired experience of a huge number of tests are used worldwide.

2.8. Structural Dynamic-based Damage Detection Technique

Structural health monitoring (SHM) is one of the most important tools when it comes to maintaining the safety and integrity of structures, such as aerospace, automotive, machinery, and civil structures. Reliable non-destructive damage identification and assessment is essential for the development of such monitoring systems, since undetected or untreated damage may grow and lead to structural failure. The challenge is to interpret the changes of the response parameters due to damage and correlate them with the corresponding measured parameters. Specifying the relationship between the damage and characteristic parameters provides the foundation of identification and assessment algorithm required for the SHM system. Furthermore, the anisotropy of material, along with the fact that much of the damage in composites occurs beneath the surface of laminates increase the complexity of damage assessment in composite structures (Mehdizadeh et al., 2009). This research project focusses primarily on developing the relationship between the dynamic characteristics and the damage as a substratum of the damage identification method for composite structures. With this technique, it is assumed that the dynamic parameters such as natural frequencies, mode shapes, transfer functions, or frequency response functions (FRFs) are functions of the physical properties of the structures. As such, any change in these dynamic characteristics can be used to locate and assess damages. The experimentally quantified data from the surface-bonded sensors provide subsidiary information regarding the structural health without the need for costly structure dismantling procedures. Through the continuous comparison of structural dynamic characteristics with the baseline information gathered from the intact structure, damage locations and corresponding magnitudes can be identified. The steps of the Vibrational-based damage detection technique are shown in Figure 2-14.
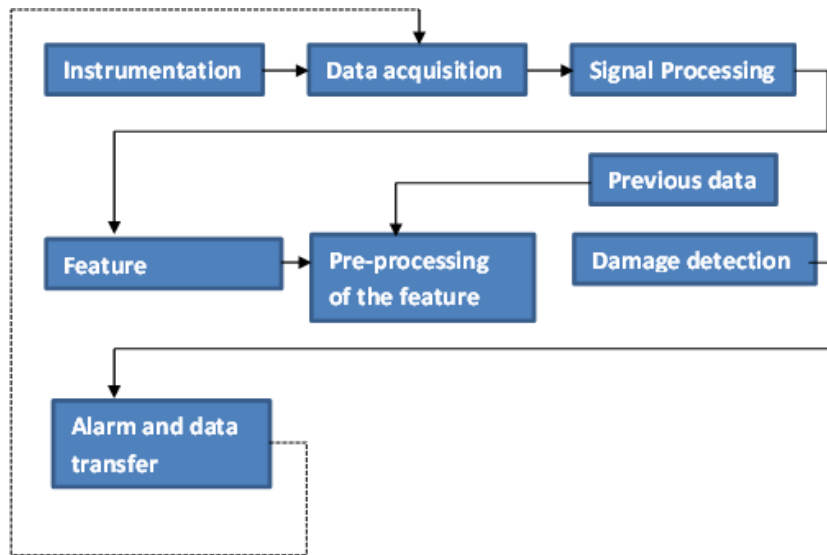
Figure 2-14: Vibration-based damage detection technique

2.8.1. Model-based Damage Detection Methods

The model-based (MB) methods undertake analysis of structural models and are usually implemented by Finite element analysis. Damage is simulated by modifying the models. Experimental data can then be compared with the analytical data to determine the location and extent of the damage. The effectiveness of all MB techniques, however, is dependent on the accuracy of the structural model and these methods may encounter difficulties when applied to complex structures (Lestari et al., 2006). With the model, various response characteristics of the structure such as time response, frequency response and impedance response can be extracted and analysed. These response characteristics are described in the following sections.

2.8.1.1. Frequency Domain

Damage may only be detected using the frequency response of the structure. The foundation of this group of methods is that damage produces a decrease in structural stiffness, which, in turn, produces decreases in natural frequencies (Zheng et al. 2012). The location of the defect can be estimated from the degree of change in natural frequency, which in turn depends on the position of the defect for a particular mode of vibration. In other words, local or distributed changes in stiffness produce changes in natural frequencies, which affect each mode differently depending on the damage location. This is because the damage event is a local phenomenon in most cases. It has been suggested that resonant frequency is a better indicator of defects than frequencies because it can change more significantly than frequencies do when properties change. The current frequency domain methods either use lower frequencies to provide global information regarding structures or

59

higher frequencies to provide local information regarding structures. None of these can provide sufficient information for the detection of both small and large defects (Annamdas et al., 2010).

2.8.1.2. Time Domain

All methods in this category are essentially related because they use time history. While these methods could be independent of modal information, they are usually combined with frequency domain methods (Murthy et al., 2009). Damage is estimated using time histories of the structure's input and vibration responses. Indeed, it is essential to use time response over a long period while simultaneously taking into account the information in several modes. This means that the damage evaluation is not dependent on any particular mode, and could be sensitive to any. The most notable advantage of the methods in this group is that they can detect damage situations both globally and locally by changing the input frequencies.

2.8.1.3. Impedance Domain

Damage is detected through measuring the changes of impedance in the structure. The basis of this technique is that each part of the structure contributes, to some extent, to the structure's impedance. Any variation in the structure integrity will generally result in changes in the impedance, i.e., the impedance will change with changes in the stiffness. This group of techniques models the defect as a spring and assumes that it is clamped around the edges of the defect. The spring stiffness is given by the stiffness of the layers above the defect. In the absence of a defect, the spring stiffness is infinite. The damage detection process, therefore, becomes that of inspecting the change of stiffness and location of the spring within the structure. There are two groups of techniques in this domain. The first one is mechanical impedance, while the other is electrical impedance. Mechanical impedance techniques are based on the measurement of the impedance, Z, at a point of a structure. The impedance is defined as $Z"F/v$, where F is the applied force input to the structure, and v is the resultant velocity of the structure at the same point. Similar to the mechanical impedance, electrical impedance techniques measure changes in electrical impedance which is defined as the ratio of the applied voltage to the resulting current of the structure. The elastic admittance of the collocated sensor/actuator is assumed to be functionally equivalent to its mechanical impedance (Annamdas et al., 2010). This group of methods is capable of multi-location and real-time health monitoring.

2.9. Applications of Sensors in Structural Health Monitoring

There are various types of sensor which are used in SHM systems. The most frequently used sensors include: Optical fibres, piezoelectric sensors, strain gauges, shape memory alloys, and

Scanning Laser Vibrometer (SLV) systems. The operation principles of some of these sensors, along with their relevancy to this project, are described in the following sections:

2.9.1. Piezoelectric Sensors

Piezoelectricity was discovered by Pierre and Jacques Curie in 1880. In recent years, the use of piezoelectricity has been significantly increased for various fields and applications. Two general types of effect are considered for Piezoelectricity, namely direct and indirect effects. The direct piezoelectricity involves a situation where a piezoelectric material generates electric charge on its surface due to mechanical stress. In contrast, with in-direct piezoelectricity, the piezoelectric material produces mechanical displacement due to an electric field. These effects are visually explained in Figure 2-15. This type of material is called piezoelectric material.
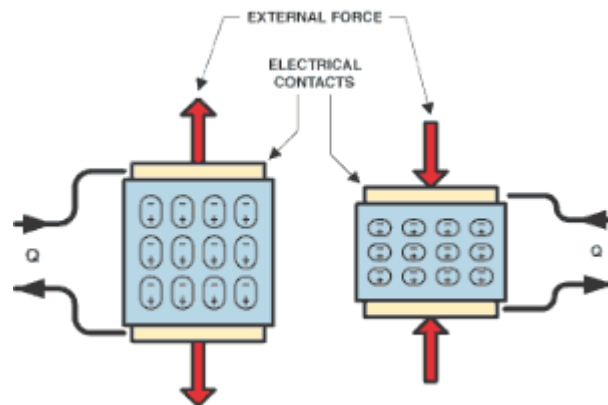
Figure 2-15: Piezoelectric material (Ramsden, 2006)

For the direct piezoelectric effect, a high electrical field is applied to the piezoelectric material, in a particular direction, which causes the ferroelectric domains within the material to align in the direction of the electric field (poling). The common types of piezoelectric material include: quartz, barium titanate, cadmium sulphide, and lead zirconium titanate (PZT) which are mostly ceramic and brittle in nature (Vepa, 2010). This makes it difficult to embed them within the layers of composite structures. In order to address this issue, piezoelectric polymers such as Polyvinyl Chloride (PVC), Polyvinylidene Fluoride (PVDF) and polymer films are increasingly used as sensors. The advantage of piezoelectric material is that it can be formed into different shapes and generates a coupling between electrical and mechanical energies. This can be widely used for a variety of applications such as SHM, gas ignition etc.

2.9.2. Strain Gauges

Strain gauges are the most commonly used devices for the measurement of strain. The frequently used strain gauge, an example of which is the bonded metallic strain gauge, consists of a flexible backing which supports a metallic foil pattern etched on to said backing. The strain gauge is bonded onto a structure through the use of epoxy adhesive. The working principle of the strain gauge is based on the piezo-resistive effect. The resistance of the foil changes when the foil is deformed (Hanna R. L. et al., 1992). The working concept of the strain gauge can be visualised with a beam under extreme bending as shown in Figure 2-16. A Wheatstone bridge circuit is then used to calculate the strain, from the resistance change. Different types of Wheatstone bridge circuits can be used for this purpose including: Full bridge circuit, half bridge circuit and the quarter bridge circuit.
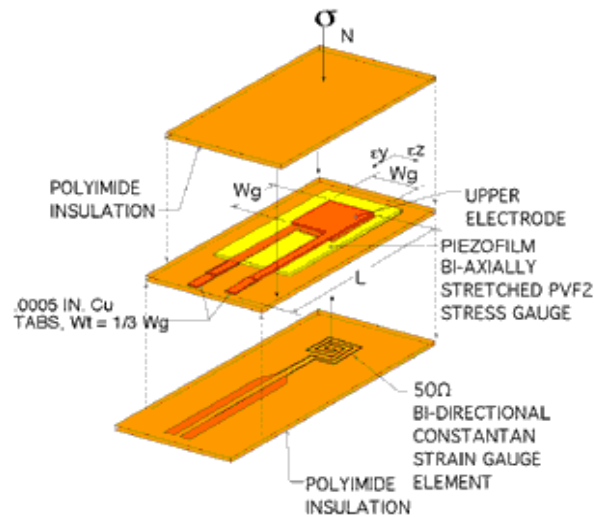
Figure 2-16: Visualisation of the working concept behind the strain gauge under exaggerated bending (Courtesy: Dynasen Inc.)

A parameter known as "gauge factor" is used to show the sensitivity of a strain gauge (Hanna R. L. et al., 1992). It can be calculated from Equation 2-15:

Equation 2-15

$$GF = \frac{\frac{\Delta R}{R_G}}{\varepsilon}$$

Where:

GF: is the gauge factor

R_G: is the resistance of the unreformed gauge

ΔR: is the change in resistance caused by strain

ε: is strain

2.10. Advanced Sensing Technologies for Structural Health Monitoring

New sensor technology should be developed to address some of the fundamental limitations associated with the current structural monitoring paradigm (Loh, 2008). In fact, various new sensing technologies have been proposed over the past few years for SHM applications. This new generation of sensors includes mainly wireless sensors, radio frequency and identification (RFID), ultrasonic and micro-electromechanical systems. Although each of these sensors has improved SHM technology, none of them have provided a practical and reliable solution to address the issues associated with SHM. This calls for a new wave of sensing systems with the ability to perform in a real-time environment. Most of the current studies in this field are focussed on active materials i.e. piezoelectric transducers and especially their new generation which is piezo-fibre-based piezoceramic transducers. This type of material is explained and discussed in the following section.

2.10.1. Active Materials and Piezoceramic

The incomparable capabilities of active materials such as piezoelectric material have prompted studies to put a great deal of effort into establishing the new types of active material and developing their availability and affordability for academic and commercial purposes. These efforts are designed to overcome the existing challenges and gaps. Each type of active material, whether it is shape-memory alloys, electro-active polymers, magnetorheological fluids or piezo-ceramics, receives one type of input field as an input and generates another field as an output. For instance, an electro-active polymer generates a displacement field output in response to an electrical field input. However, this input-output relationship can sometimes be reversible (i.e. an electrical input creates a mechanical output and a mechanical input creates an electrical output). These special characteristics of active materials make them a perfect choice for both sensing and actuation applications. Engineering topics like vibration, structural control, automation and data-acquisition all benefit from smart materials application and especially this reversible interaction. Furthermore, active materials have opened many new doors for engineers to generate new technologies and address the existing problems accordingly. This is especially useful for modern research on structural health monitoring, power harvesting and sensing/actuation.

Piezoelectric materials are one of the earliest known active materials. However, characterisation work conducted by different studies around the globe eventually led to the first piezoelectric ceramic called Barium Titanate, in 1940. The piezoceramics exhibit extremely strong electromechanical coupling and mechanical properties similar to other ceramic materials (Lloyd, 2004). In the following years, a new generation of piezoceramics with stronger piezoelectric effects was developed, thus leading to the most common modern piezoceramics, such as lead zirconate titanate (PZT) and lead metaniobate (PMN).

The induced strain in the piezoceramics due to electrical excitation is relatively small (around 0.1%) although their force outputs can be very large, which can result in high energy density. The fact that the piezoceramic response time to the excitation is fairly short makes them a good choice for high frequency applications. In addition, they are very sensitive to mechanical deformation or excitation and can produce measurable charges for very small applied mechanical excitation. In light of this, they have a wide range of applications in the field of sensing. The properties of certain PZT materials are presented in Table 2-2.

Table 2-2: Selected material properties of three common piezoceramic materials. PMN-PT is a single-crystal piezoceramic material (Lloyd JM., 2004).

Material	K_3^T	k_{33}	d_{33}	d_{32}	ρ	s_{33}^E	s_{11}^E	s_{23}^E	s_{44}^E
Unit	KHz	-	pm/V	pm/V	g/cm^3	-	-	-	-
PZT-5A	1900	0.72	390	-190	7.8	18.8	16.4	-7.22	47.5
PZT-5H	3800	0.75	650	-320	7.8	20.7	16.5	-9.1	43.5
PMN-PT	7151	0.91	2285	-1063	8.05	86.5	59.7	-45.3	14.4

In order to use the piezoceramic material for sensing and actuation purposes, they need to be reformed to shapes called monolithic wafers (Schulz et al., 2000). The term monolithic refers to a single, contiguous piece of piezoceramic, free from added materials. As most of the sensing and actuation applications are in-plane i.e. induced stresses and strains parallel to the structure's surfaces, piezoceramic wafers mostly operate through the d_{31} effect, where the electric field is perpendicular to the poling direction (Bystricky, 2012). Under this technique, in-plane structural strains are conveniently induced and measured with an affixed piezoceramic monolith. Another advantage of monolithic piezoceramic wafers is the fact that they can be mounted on any type of material and can be applied rather simply in terms of sensing and actuation applications.

However, the properties of piezoceramics are still similar to other ceramics in that they are brittle and weak when it comes to generating strain under external loading. Furthermore, the electromechanical coupling between the monolithic piezoelectric actuators and host structure is weak when the electrodes are uniform. Moreover, the strain output as well as energy density is significantly weaker for d_{31} compared to the d_{33} piezoelectric effect, where electric fields applied parallel to the direction of piezoelectric poling induce large strains in the same direction. These limitations raise a concern for researchers in terms of using monolithic piezoelectric wafers for irregular shaped surfaces and structural control (Bystricky, 2012).

2.10.2.   Active-Fibre Composites

In order to overcome the issues associated with monolithic piezoceramics, Bent et al. (1997) developed the first generation of piezocomposite actuators. Additional inactive components in a specific structure are added to piezoceramic material to form the piezocomposite sensor/actuators. Like any other composite, the advantages of piezoceramics and other structural material are superimposed in the piezocomposite actuator, which improves their performance significantly. These types of actuators are normally called Active Fibre Composites (AFC). Considering their advantages, recent years have seen many studies focus on improving the geometry, construction and composition of AFCs.

The piezoelectric fibre composite (PFC) is one of the improved versions of AFC, and was designed to address the conformability issues of standard piezoceramic monoliths. This task is accomplished by employing surrounding round, extruded piezoceramic fibres with a network of epoxy matrices which protect the fibres from brittle fracture and improve the conformability and mechanical properties. Moreover, to address the issues with low strain generation, a dual integrated electrode (IDE) design is used instead of the traditionally used conventional electrodes. Unlike the conventional electrodes, where the electric field is perpendicular to the direction of the fibre poling, IDE generates an electric field roughly parallel to the direction of fibre poling (Willkie et al., 2000). This phenomenon has a strong d_{33} effect on PDC which therefore increases the strain output and energy density significantly. According to Lloyd (2013), the strain output for PFC is almost doubled. The structure of the generic piezoceramic fibre composite is provided in Figure 2-17. The operation principles of PFC are also presented in Figure 2-18.
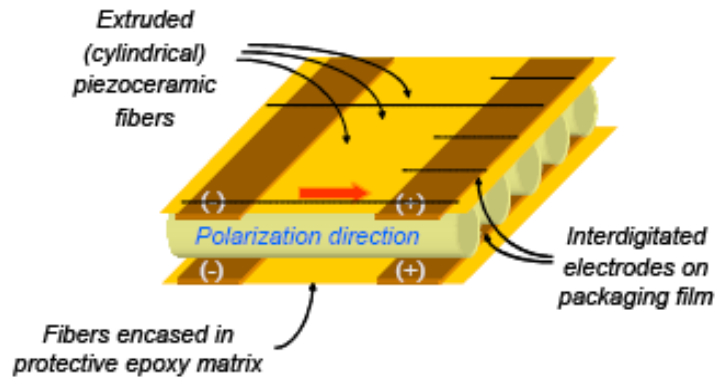
Figure 2-17: Section illustration of the structure of a generic piezoceramic fibre composite (Willkie et al., 2000)
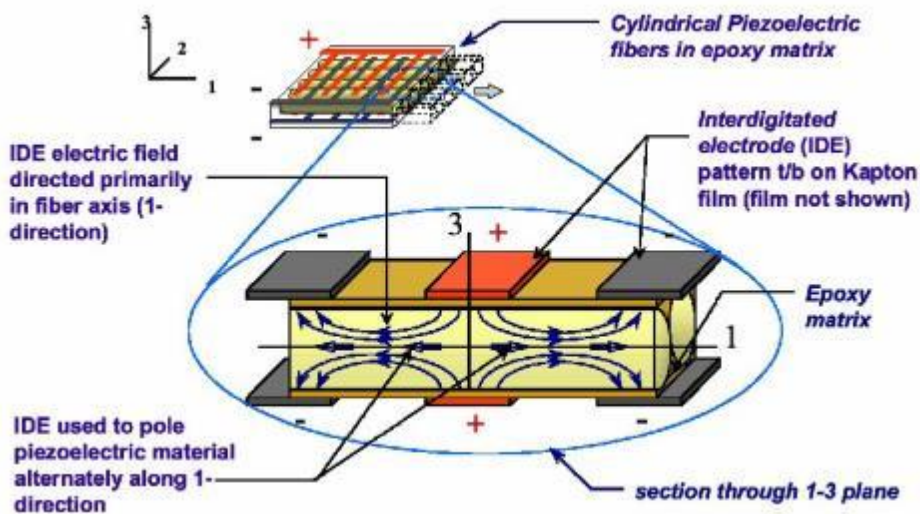
Figure 2-18: Section illustration explaining the operating principle of a generic PFC (Lloyd et al., 2004)).

The design and development of AFC and PFC sensors/actuators makes a significant contribution to the sensing and actuation body of knowledge. However, there remain certain issues in regard to the performance of AFCs which must be properly addressed. The challenge of maintaining sufficient contact between the interdigitated electrodes and cylindrical piezo-fibres, which significantly affect the performance of AFC and PFC, is one of the main issues. In addition, the repeatability issues of the AFC and PFC structures, which result from the manual manufacturing process, represent another major issue as they vary the performance of each manufactured AFC from one to another. These challenges and obstacles have prompted researchers to come up with an improved version of PFC which will be described in the following section.

2.10.3. The Macro-Fibre Composite

Piezoceramic fibre composite (PFC) actuators and sensors offer many advantages over conventional monolithic piezoceramic devices. Conformable, durable and, when equipped with

interdigitated electrodes (IDEs), more responsive than regular monolithic devices, PFCs promise to revolutionise the application of piezoelectric materials. Developed by the NASA-Langley Research Centre, the Macro-Fibre Composite (MFC) actuator and sensor is the most sophisticated PFC device ever invented (Willkie et al., 2000). With superior qualities among PFCs in performance, behaviour repeatability and manufacturability, the MFC has spawned great interest in the commercial and academic community as a tool in multitudinous engineering applications. Like the AFC (and PFC as the next generation), the MFC actuator package employs piezoceramic fibres locked in an epoxy matrix and sandwiched between two arrays of interdigitated electrodes (Sodano, 2003). In contrast with the round fibre geometry of the PFC, however, the piezoelectric fibres in MFCs have rectangular cross sections and are assembled in the MFC package with regular spacing and precise parallel alignment. Manufacturing considerations have necessitated the rectangular form of the MFC fibres, which is much more cost-effective to construct and handle in mass-production environments. The production of rectangular fibres instead of round fibres has enabled the use of commercially available piezoceramic materials in raw form, which are diced into smaller piezoelectric fibres through a repeatable, cheap manufacturing process. Thus, MFC active layer geometry serves to standardise the performance of mass-produced MFCs while lowering production costs. Due to these substantial manufacturing advantages, the MFC has realised actual commercial licensing and mass-production; a feat never achieved by the PFC. (Lloyd et al., 2004).

Additionally, the rectangular fibre geometry of the MFC guarantees consistent, appreciable contact between the IDEs and piezoceramic fibres, thus reducing attenuation of the IDE electric field due to the low dielectric constant of the epoxy matrix. Because of the improved electrical contact, MFC strain performance exceeds AFC strain performance by up to 150% (Wilkie et al., 2000). Due to the in-situ poling scheme used in manufacturing, the poling direction of the MFC's piezoceramic fibres aligns with the electric field produced by the MFC's interdigitated electrodes, thus enabling the high strain output of the MFC.

Currently manufactured by the Smart Material Corporation, MFCs are categorised as layered composite materials. Every MFC contains an orthotropic piezo-fibre/epoxy layer at its centre, which is then sandwiched between two layers of homogenous epoxy to add structural reinforcement. Laminated to the bottom and top of the epoxy/piezo-fibre layers are two more orthotropic layers of IDEs, running perpendicular to the piezoceramic fibres and encapsulated in Kapton. Figure 2-19 illustrates the MFC structure.
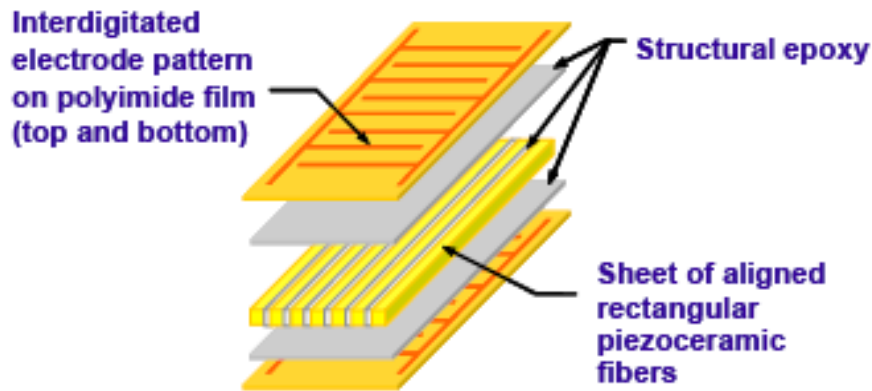
Figure 2-19: Diagram of the layered construction of a typical MFC (Wilkie et al., 2000)

2.10.3.1. MFC-related Researches

In general, the MFC-related studies can be categorised into two independent branches: characterisation research and applications development. Based on existing literature, the body of information for the second branch is considerably larger. This is mainly due to the superior performance of MFC as a sensor/actuator, thus resulting in the MFC being employed in a wide range of applications in the fields of structural control, vibration suppression and structural monitoring projects. In addition, the fact that the MFC does not introduce significant mass or stiffness to the host structure, due to high flexibility and low mass, has resulted in extensive research regarding the use of MFC for the dynamic analysis and control of membranes and inflatable, thin-walled structures (Matveenko et al., 2012).

One of the early advanced applications of MFC was achieved by Park et al. (2002) who used MFC excels to excite the vibratory nodes of thin-walled structures. Following on from this, Ruggiero et al. (2002) showed the capability of MFC as a sensor of vibrations in inflatable membrane structures through MIMO modal testing of an inflatable torus satellite. Another example of these advancements was put forth by Jha et al. (2003) who proved that the MFC can be used as an actuator in structural control schemes. This work was then improved by other studies focussing on vibration control of active structures using smart materials and application of MFC in SHM technology (Preumont, 2011).

The second branch of MFC research was on MFC characterisation, which focusses on the quantification, explanation and prediction of MFC behaviour and properties. This aspect of MFC research has not been properly investigated due to the empirical design of MFC which brings complexity and difficulty to the determination of the mechanical properties, electronic properties,

and actuation and sensing capabilities of the MFC. However, this remains one of the main challenges faced by researchers wishing to certify the performance of MFC. To address this issue, a proper understanding of the performance of MFC is required in order to analytically simulate MFC. An accurate and practical analysis is the key point in characterising the performance of MFC in SHM technology.

2.10.3.2. MFC Analytical and Numerical Modelling

There have been various attempts to achieve accurate models of the electric behaviour and electromechanical coupling of the MFC and similar PFCs (AFC). These attempts have focussed heavily on finite element formulations and other numerical models. The primary obstacle in explaining and modelling MFC behaviour lies with the complex electrical interaction between the dual IDEs and the electromechanically coupled piezoelectric fibres constituting the active layer (Lloyd et al., 2004). Efforts by Beckert et al. (2003) to model the electric field of the IDE structure with ANSYS strove to predict the strain behaviour of IDE equipped MFCs based on actuator geometry. Analysing the micro-scale behaviour of the AFC, Warminski et al. (2011) developed a nonlinear model to calculate the local stress distributions using active elements. Trindaded et al. (2012) suggested a parametric analysis of the MFC transducer. Other FEA formulations considered a more global perspective of MFC implementation, modelling the MFC laminated to its host structure to predict the frequency response of the overall structure (Azzouz et al., 2012).

Generally speaking, all modelling efforts pertaining to the electromechanical behaviour of the MFC assume that FEA models provide the only possible approach to obtaining solutions. Some MFC studies go so far as to specifically declare that analytical solutions to the electric field produced by the dual-IDE structure are impossible. Despite these claims, exact or even simplified analytical models of MFC response phenomena remain desirable for their explanatory value and computational efficiency. With this same motivation, scientists have administered unrelated studies to derive analytical expressions modelling the electric behaviour of the IDE structure for the sake of other devices (Lloyd et al., 2004). Purely mathematical studies of the electric field of the IDE structure directly relate to MFC development, despite the fact that certain treatments first appeared several decades ago. Nevertheless, most of the existing analytical works fail to consider the actual operation and characteristics of MFC when it comes to simulation and analysis. The FEA-based analytical approach which is provided in this research project has brought into consideration the micro-scale structure of MFC as well the multi IDEs` interaction.

2.11. Developing SHM Standards

Recent years have seen sensor optimisation become the centre of attention in SHM-related research and publications; however, only a few studies have been carried out regarding the characterisation and certification of SHM systems (Kessler, 2005). Topics relating to the durability, reliability, and longevity of these systems have not been sufficiently addressed. For example, whilst the standard for manufacturing and integration of components in the aircraft industry is well presented, there is only limited information available regarding the certification of SHM systems used in this industry.

As the application of SHM systems increases, further work must be done on the certification and commercialisation of these systems. In fact, there are currently no established standards for durability testing or certification of SHM systems for commercial or military aerospace structures. This certification should involve installation, credit validation, and instruction for perpetuated airworthiness. The Federal Aviation Administration (FAA) has recently developed certification guidance for health usage monitoring systems (HUMS) in rotorcraft as a part of Advisory Circular (AC) 29-3C. However, no documentation has been provided regarding the utilisation of SHM systems in various structures i.e. aircraft/spacecraft, which is one of the main gaps in the field of SHM. To address this important gap, recent times have seen the formation of a group known as the Structural Health Monitoring – Aerospace Industry Steering Committee (SHM-AISC). This committee has representatives from industry (Airbus, BAE Systems, Boeing, EADS, Embraer, Honeywell), aircraft regulatory agencies (EASA, FAA), US government agencies (DoD, NASA), and a subset of the SHM community developing the sensors (Sandia National Labs, Stanford University). The aim of this committee is to provide the SHM community with a standardised integration and certification procedure (Kessler, 2005). Moreover, a research project is currently under way at the Defence Materials Technology Centre (DMTC) with a focus on functionality, durability and reliability assessment of SHM systems in multifunctional composites (Mehdizadeh et al., 2012).

The certification of an SHM system has different aspects such as reliability, durability, longevity and repairability. The reliability and durability of SHM systems can be broken down into two aspects which must be considered in parallel. The first aspect is to ensure that the SHM system is intact and able to detect any possible damage/degradation not only in the structure but also within itself. This approach, which is extremely important for the commercialisation of the SHM system, is widely investigated in the current research project. The second aspect is to develop a durability standard for SHM systems. A practical approach to preparing such a standard would be to develop

existing standards in order to recognise that the SHM system is both a sensor and a structure (Chambers et al., 2007).

Existing standards used to form the foundation of the environmental SHM test matrix here include: RTCA/DO-160E, MIL-STD-810F (environmental testing), and MIL-STD 310 (global climatic data). Both military and commercial structural standards exist or are evolving to meet certification requirements (e.g., FARs) for both metal and composite structures (e.g., ASTM, MIL-STD, and industry proprietary standards). The main focus in certifying the SHMS is currently on the overlaps shown in Figure 2-20 between the SHM durability and the structural design standards and the SHM durability and the environmental standards. The central overlap is important for SHM systems but is unexplored when compared with the other two regions (Kessler, 2005).
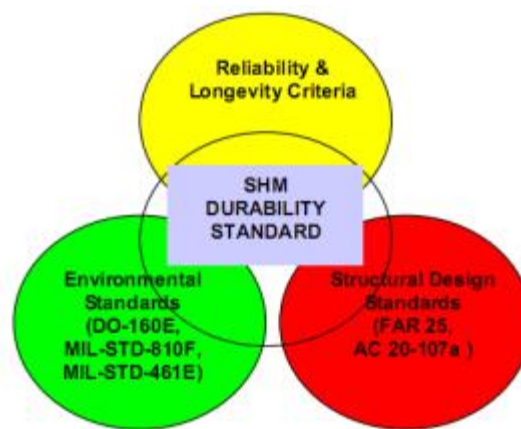
Figure 2-20: Framework for identifying SHM or smart structure durability standard.

2.11.1. Durability and Reliability Criteria for SHM Systems

Three relevant standards are currently in place for durability certification, namely:

- RCTA/DO-160E, Environmental Conditions and Test Procedures for Airborne Equipment

- MIL-STD-810, Department of Defence Test Method Standard for Environmental Engineering Considerations and Laboratory Tests

- MIL-STD-461E, Department of Defence Interface Standard Requirements for the Control of Electromagnetic Interference Characteristics of Subsystems and Equipment

The tests within these standards can be divided into three categories: environmental susceptibility, electromagnetic interference and electromechanical testing (Kessler, 2005). Each standard provides the requirement for the test, detailed setup information and often some criteria with which to determine whether or not the component has passed the test.

With the first standard, the DO-160 document is recommended by the US Federal Aviation Regulations AC21-16D as an acceptable means for any environmental qualification. This document defines procedures and criteria for testing airborne equipment aircraft ranging from light aircraft to large commercial jets and supersonic transport aircraft. In addition, it is recognised by the International Organization for Standardization (ISO) as de facto international standard ISO-7137. The second standard provides information on how to certify the structure against shock and vibration conditions. This third standard is related to the Electromagnetic Interference (EMI) testing. The requirements specified in this standard contain a detailed series of tests to measure both conducted and radiated emissions from electronic components, as well as to quantify their susceptibility to electromagnetic interference.

The certification of the SHM system as well as its structure under environmental and loading conditions requires clear test instructions. These tests are designed to ensure that the system is capable of operating within the expectations in the harsh environment. Some of these tests include: temperature, pressure, moisture, fluid susceptibility, vibration, acceleration, electromagnetic interference and combined loading. The details on vibration and EM effect which are more relevant to this research project are presented in the following sections.

2.11.1.1. Vibration

Two vibration tests require investigation: stress and acoustic. For normal vibration, a sinusoidal sweep is applied to the specimen for 1 hour per axis while continuously testing performance (Chamber, 2006). The sweep should range from 5Hz with amplitude of 2.5mm peak-to-peak through 2000Hz with amplitude of 2.5µm peak-to-peak. Following this, acoustic noise is tested in a reverberation chamber using an overall sound pressure level of 160dB for 30 minutes, with random frequencies up to 10,000Hz.

2.11.1.2. Electromagnetic Effects

There are 10 separate tests contained within the various standards relating to electromagnetic testing. The first 5, described in MIL-STD-461E, specify measurements of susceptibility and emissions conducted through external cables. These are followed by 2 similar tests for radiated susceptibility and emissions suitable for both wired and wireless sensors. Following this, the DO-160E further recommends tests for the effects of voltage spikes both through the main power bus and through electro-static-discharge (Kessler, 2005). Lastly, there is also a section on the direct (power spike) and indirect effects (heating, acoustic wave) of lightning strikes.

2.11.1.3. Combined Loading

One of the areas in desperate need of further investigation is combined loading testing. SHM dictates combined temperature, pressure, moisture and vibration testing. Tests should be designed to simulate real probable environments, such as high temperature and moisture with vibration for take-off, or low temperature and pressure with vibration for cruise.

2.11.2.   Reliability and Longevity issues of SHM Systems

Reliability and longevity of the SHM systems are two of more important issues which need further investigations. Reliability describes the probability of a monitoring system failing to perform its function within a certain expected lifetime. This can be due to manufacturing variability, level of quality control, installation conditions or procedures, and robustness of error handling in firmware and software design.

Longevity relates to the ageing of components over time; a "natural" degradation due to a combination of repetitive environmental and mechanical factors wearing away at parts. Longevity is typically used to define a safe-hours-of-usage or mean-time-to-failure (MTF) figure, so that devices can be retired prior to reaching an uncertain state of functionality. While often difficult to quantify, these phenomena are essential when considering an SHM system to reduce life-cycle costs (Santoni, 2010). Again, while no formal standard regulates these criteria for SHM devices, to achieve condition-based maintenance in a cost-effective manner, the sensors themselves must be reliable enough with sufficient MTF, meaning that they do not require replacement at intervals less than the economic lifetime of the components they are monitoring.

2.12. Gaps in the Body of Knowledge

The gap in the SHM body of knowledge exists mainly because of a lack of standards, procedures and methodologies with which to certify the reliability, durability and functionality of the host structure (body), SHM systems and their components i.e. transducers, batteries etc. in multifunctional structures. In fact, the existing standards are mainly focussed on the structure rather than the SHM system. Furthermore, the assumption with regard to most of these standards is that the SHM system is intact and free of any damage, which is clearly not the case in real-life conditions. In other words, the SHM system, which has the task of monitoring the status of the host structure, is also subject to failure or gradual degradation. This failure/degradation would change the integrity of the SHM system and therefore modify the electromechanical properties of its components such as transducers. Hence, the responses of the degraded or failed SHM system will no longer be reliable as they may not be a sign of structural damage but rather a false negative

indication caused by the damage within the SHM system itself. Of course, the failed SHM system will not generate any or considerable responses and therefore the main challenge is when the SHM system is degraded due to fatigue.

The above statement clearly illustrates that the functionality of SHM systems in monitoring the structural damages relies on a proper understanding of their behaviour, in terms of detecting possible structural damages, while the SHM system itself is degraded. In fact, the key-point in this understanding is the ability to delineate the SHM-related damage from structural damage. This ability helps us to establish when the SHM system becomes degraded and characterise the degraded SHM system responses in order to monitor the status not only of the structure but also of the SHM system itself. This also makes it possible to utilise a practical SHM technique with the ability to diagnose damage occurring in different parts of the multifunctional composites i.e. transducer, host structure.

2.13. Research Plan and Methodology

The existing body of knowledge in the fields relevant to this research project has been extensively discussed in previous sections. However, in order to achieve the objectives of the project, and as mentioned in the previous chapter, a research plan is designed at the beginning of this project. This plan is prepared to ensure that the required steps to achieve the aims of this research are well defined and followed. These steps and selected methodology are put forth in the present section.

The first step in any research project, including this study, is to obtain a proper literature review which contains the background, theory and previous work carried out in the field of interest. The way in which this was achieved is shown in the present chapter. The collected literature review helps us to identify the fields which are not properly addressed and need further investigation. The next step in the research plan is to conduct the required experiments to investigate the gaps identified during the literature review. In order to conduct an experiment, a sample must be designed and manufactured. The type and material of the sample is based on the nature of the project. In this research, the carbon/epoxy composite plates with bonded Piezoelectric Fibre Composite (PFC) or Macro Fibre Composite (MFC) transducers are designed and manufactured. The instruments and tools used to carry out the experiment should also be identified. Furthermore, the loading and boundary conditions of the test should be selected according to the operation environment of the selected transducer and the structure. Once the experimental procedure is determined, a test is run and the results gathered for further analysis. The aim is to identify the proper parameter with distinguishable sensitivity to transducer and structural damages.

The next step is to employ a theoretical or numerical model of the sample under conditions similar to those found in the experiments so as to validate the experimental measurements. For this stage, the FEM software package known as ABAQUS is chosen to simulate the sample under loading and boundary conditions similar to those in the experiments. Following this, they are validated accordingly. At this juncture, the baseline for the proposed research project will be available for further investigation. Indeed, the aim of this research is to propose a damage detection technique, with the ability to identify and diagnose damage not only in the structure but also in the transducer itself, and as such various delineation techniques are tested. The key point in this step of the research is to identify the suitable techniques which are capable of delineating structural damage from transducer damage.

The strain-based technique, which is based on the passive mode of the transducer (sensor), is initially explored. The experimental results should be compared and validated with help from the FEM simulation results. Up to this point, all experiments have used the transducer in its passive mode (sensor) as the mechanical excitation causes the MFC transducer to generate electrical output (voltage). However, the active form of the MFC transducer (actuator) is used for the electromechanical impedance-based delineation technique. With this technique, a proper experimental modelling must be initially carried out as the previous experiments were based on the sensor behaviour of MFC. Once the experiment is conducted, various electromechanical impedance components such as real and imaginary impedance, conductance, susceptance etc. should be collected and analysed to find the suitable parameters for different structure-transducer damage situations.

Finally, the effect of electromagnetic interference on the performance of piezo-fibre-based transducers, which was accidentally observed during the tests, should be explored. This effect is first used to identify the main recipient of this interference, with a series of shielding and insulations carried out. To clarify these issues, an experiment is conducted to establish whether or not the difference in the responses of the healthy and intact transducer can be used as a damage detector parameter for the transducer itself.

2.14. Summary

In this chapter, the basics and background of the proposed research are provided. Discussion will focus on the background of composite materials, multifunctional composites and piezoelectric materials, as well as the various applications of these materials. The wide ranges of applications shown in this chapter illustrate the popularity of these types of materials in various fields. In addition, the smart structures and the function of piezoelectric materials in smart structures are

discussed. Furthermore, there will also be a review of the recent advances in functionality assessment of embedded systems in multifunctional composites and current uncertainties in the performance of SHM systems. Discussion also focusses on the gap within the SHM durability standards, which is one of the main obstacles standing in the way of commercialising SHM devices. The SHM system must able to perform in a way which means it does not need to be replaced within the economic lifetime of the structure which it is meant to monitor.

CHAPTER 3 Manufacturing and Experiments

3.1. Introduction

The aim of this chapter is to explain the experimental modelling and procedure used in this research project. An explanation is also provided of the manufacturing steps and processes of carbon/epoxy plates as well as the bonding of PFC and MFC transducers on these plates. This is followed by a description of the electrical properties measurement setup and test rig. The 3-point-bend test configuration used for fatigue investigation is also described. The Scanning Electron Microscopy (SEM) imaging techniques as well as the SEM sample preparation are comprehended in this chapter. The test procedure and configuration are also discussed for strain-based experimentations, electromechanical impedance experimentations and electromagnetic interference tests. The devices used for these experiments include AD5933 impedance analyser, Network analyser, Digital Oscilloscope, strain indicator and recorder, NI USB 6009 DAQ. The characteristics and specification of these devices are also provided along with the data analysis technique.

3.2. Manufacturing Process

3.2.1. Carbon/Epoxy Composite Plates

The purpose of this manufacturing process is to prepare the composite structure used in various experiments in this project. During this process, samples with the induced damage in various locations of the structure are manufactured, as is the sensor. The structural damage is induced using a Teflon tape as a delamination whilst the sensor damage is induced by locating an identical point on every sensor under the optical microscope and inducing the damage using a needle drilled into the specified point of the sensor. Carbon fibre reinforced epoxy unidirectional (UD) prepregs, each measuring 0.2 mm in thickness, are used to make the composite plates along with Teflon impregnated glass film (~60 μm) which is inserted as artificial delamination.

The specimens are made of carbon fibre and epoxy resins and have a total [0/90] lay-up of 8 layers, with each layer measuring 0.2 mm in thickness and a total thickness of 1.6 mm. Each specimen has a width of 250 mm and a length of 250 mm (Figure 3-1).
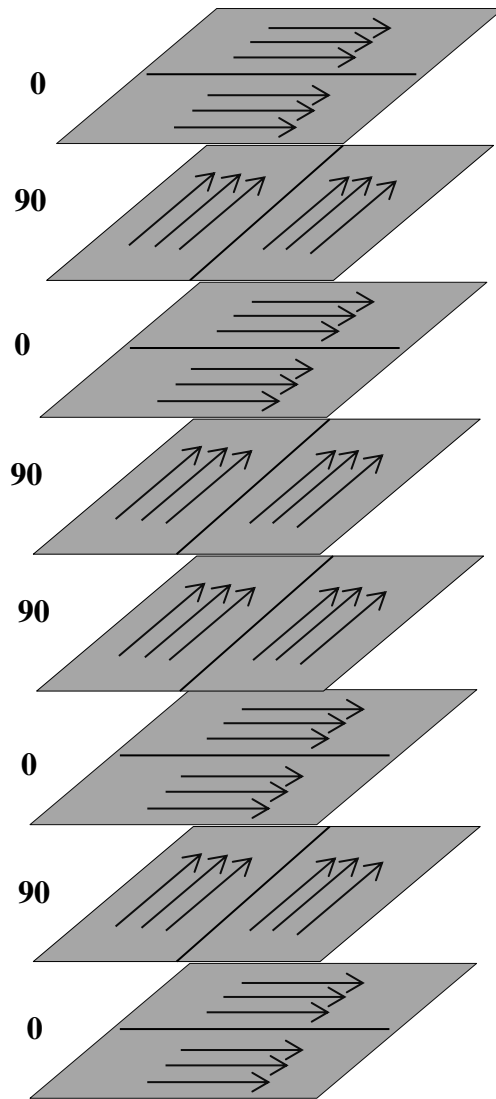
Figure 3-1: lay-up used for the manufacturing of carbon/epoxy plates

During the manufacturing, 4 Teflon layers are placed as delaminations in 2 of the specimens in various locations (2 for each specimen) while the remaining specimen is considered healthy (healthy structure). The locations of the Teflon tapes are presented in Figure 3-2.
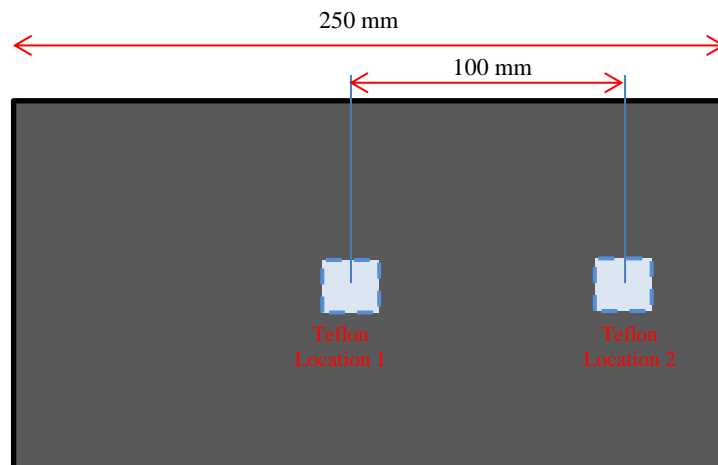
Figure 3-2: Location of Teflon tapes in carbon/epoxy plate

A total of 8 plies are cut and arranged into 250 mm × 250 mm rectangles before being stacked using the hand layup technique with a hand roller onto a steel plate in a Quasi Isotropic & Symmetric layup [(0 90)s]n ; n=6. During stacking, each ply is rolled to ensure no air is trapped in between the layers. This process is shown in Figure 3-3.

Figure 3-3: Lay-up process of carbon/epoxy laminate

In addition, the Teflon impregnated glass film is introduced between layers to simulate delamination. During the manufacturing, the aim is to make the samples as accurate as possible although manufacturing errors i.e. bubbles, gaps, shifts are inevitable. A total of 3 laminates are manufactured with embedded artificial delamination in various locations. After the layup process, carbon/epoxy laminate is ready for the next step, namely that of curing. However, a clamping method needs to be used to hold the laminate in place. Vacuum bagging is used in this experiment as shown in Figure 3-4. The air under the bag is extracted by vacuum pump and up to one atmosphere of pressure can be applied to the laminate. This compression under the vacuum helps remove the air, voids, etc. For hand lay-up, it is recommended to apply pressure and vacuum prior to the application of heat in the curing process.

Figure 3-4: Vacuum bagging process

There is an overlap on each side of the laminate to ensure that the final edges are completely straight and accurate. The steel plate is polished several times and a sheet of release paper is placed on the sheet before the laminates are stacked onto it. A release film is also placed on the surface of the uppermost laminate. A layer of breather-bleeder combination is placed over this surface. The laminate is then covered with a flexible bag, all ends of which are sealed to the plate. The release film prevents the cured laminate from sticking to the plate. The breather enables the uniform distribution of the applied vacuum and permits the uniform flow of the resin during the curing process. The uniform pressure applied also helps to remove excess trapped air. Autoclave curing is the most extensively used method when it comes to producing high-quality laminates within the Marin/Aerospace industry. Autoclaves are extremely resourceful pieces of equipment (Mallick, 1988; Schwartz, 1996; Barbero, 1998). Since the gas pressure is applied iso-statically to the part, almost any shape can be cured in an autoclave. The only limitation is the size of the autoclave and the large initial capital investment needed to purchase and install an autoclave. The resin is normally held at this cure temperature for 4 to 6 hours, thus allowing time for the cross linking process to be completed. Figure 3-5 shows the curing process in an Autoclave.
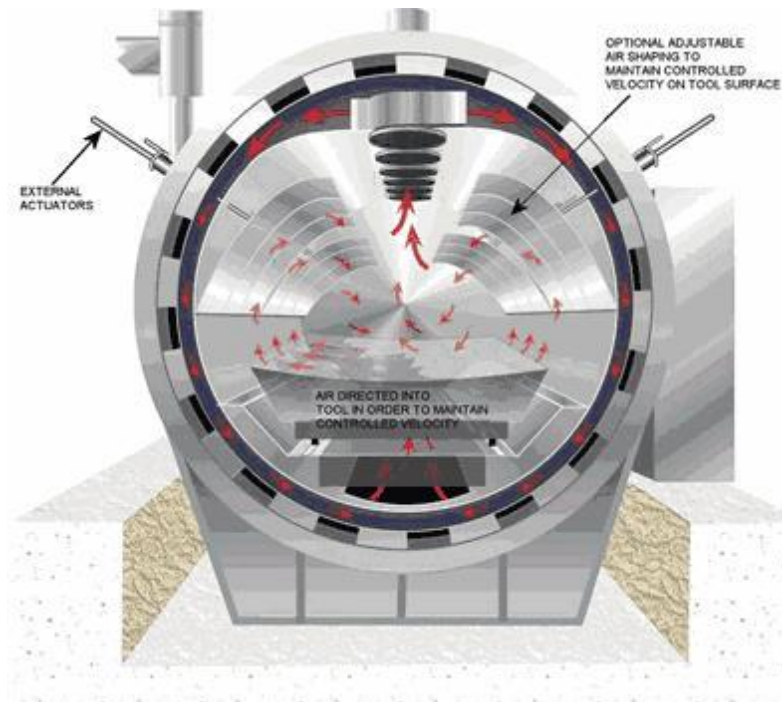
Figure 3-5: Curing process using autoclave (Aeroform Ltd., 2010)

After the over-laminate is fully cured, the composite is ready to be machined to make the required specimens for testing. The composite laminate is cut into 10 plates. Each plate has a length of 250 mm, a width of 140 mm and a thickness of 1.6 mm. As previously mentioned, 4 out of 10 plates have delamination in different locations and 6 of the remaining plates are kept as healthy samples. The 4 damaged samples and 2 undamaged samples are used for the electromechanical impedance technique and electromagnetic interference investigations. 2 remaining healthy samples are used for the strain-based delineation technique and investigations into the electrical properties of the bonded transducer. The cutting procedure is shown in Figure 3-6.

3.2.2. Bonding the Transducer

Once the samples are cured and cut into designated dimensions, the transducers are bonded onto the surface of the samples. The MFC or PFC transducers (depending on the relevant experiment) are placed identically and at the centre of all the samples for further comparisons. Araldite 420 A/B, which is a room temperature curing paste adhesive of high strength and toughness, is used for the bonding process. This adhesive is suitable for a wide variety of metal, honeycomb and fibre reinforced composite bonding applications. It has very high shear strength even at temperatures up to 70°C and good peel strength. The bonding layer is cured under the firm pressure and at room temperature for 8 hours to make the bonding layers as strong and homogenised as possible. This process is separately shown for the PFC and MFC transducer in Figure 3-7.

Figure 3-6: Cutting Process
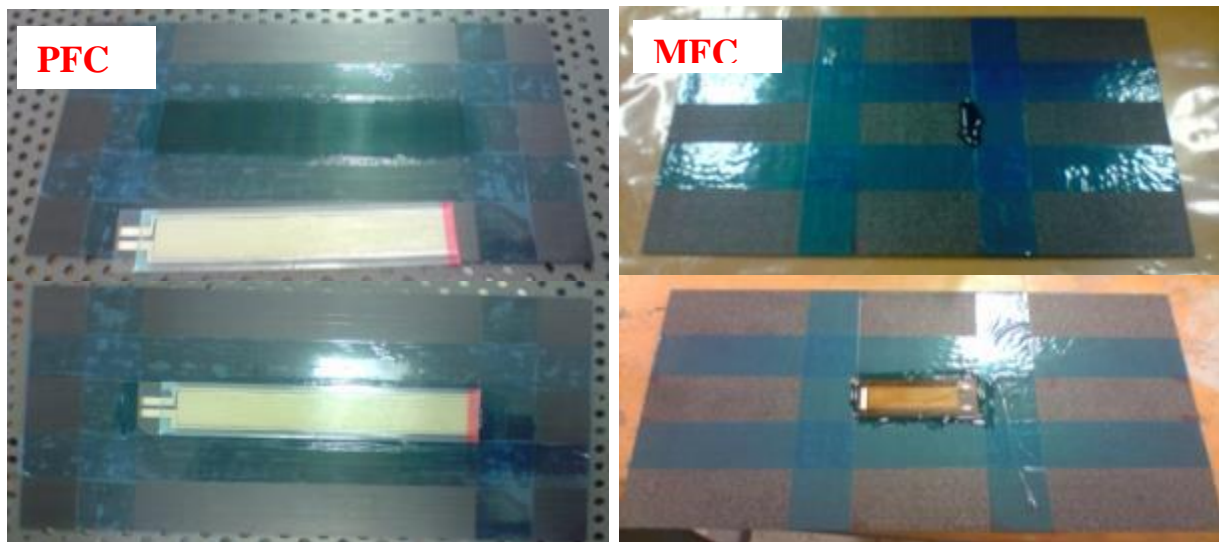
Figure 3-7: Bonding process for PFC and MFC transducers

3.2.3. Inducing damage in MFC transducer

The composite structures with and without artificial delamination have been manufactured in previous sections. The next step is to induce damage in the transducer on designated structures. The aim here is to prepare 6 samples (bonded MFC transducer on carbon/epoxy plate) for electromechanical and electromagnetic investigations (Figure 3-11). The sensitivity of the transducer and the fact that the induced damage should be identical, urges extreme caution when

inducing the damage in the transducers. To satisfy this, the selected transducers for damage induction are placed under the optical microscope prior to the bonding process and an identical location at the exact centre of the each transducer is highlighted. Following this, a rectangle-shape glass with the same dimensions as the transducer is drawn on a piece of flat glass and a hole measuring 0.1 mm in diameter is drilled through it at its exact centre. Finally, the glass plate is placed on each transducer and after matching the dimensions of the transducer with those on the glass, a drill with low torque is placed on top of the glass hole and drilled into the transducer to make a hole with the same diameter as the glass hole in the transducer. This process is shown in Figure 3-8.

Figure 3-8: Damage induction in MFC transducer

This process is repeated for 4 out of 6 transducers as 2 of them should remain healthy for comparison purposes. The above procedures lead to the manufacturing of 6 samples with various damage statuses in the structural and/or transducer. These 6 samples are visually shown in Figure 3-10. Once the samples are prepared, identical cables in terms of length and type are soldered to each transducer. Prior to the soldering procedure the electrode leads are cleaned so as to remove any particles or dust which might affect the soldering process. The soldering time and temperature should be controlled to avoid the electrodes being completely dissolved in the solder. However, the soldering time should not exceed 2-3 seconds, in order to minimise heat transfer to the transducer and thus avoid the risk of depolarising the PZT fibres. A small amount of soldering material is melted at the tip of the soldering iron. The soldering iron is held at the electrode surface for approximately 1 second. More soldering material is applied to form a small circular soldering

material spot. The pre-soldered wire is placed on top of the circular soldering material spot and then soldered to said spot. This process is shown in Figure 3-9.
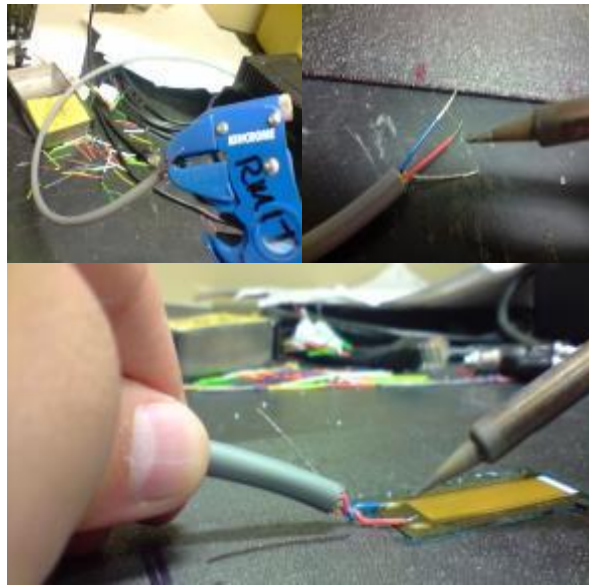
Figure 3-9: Soldering process
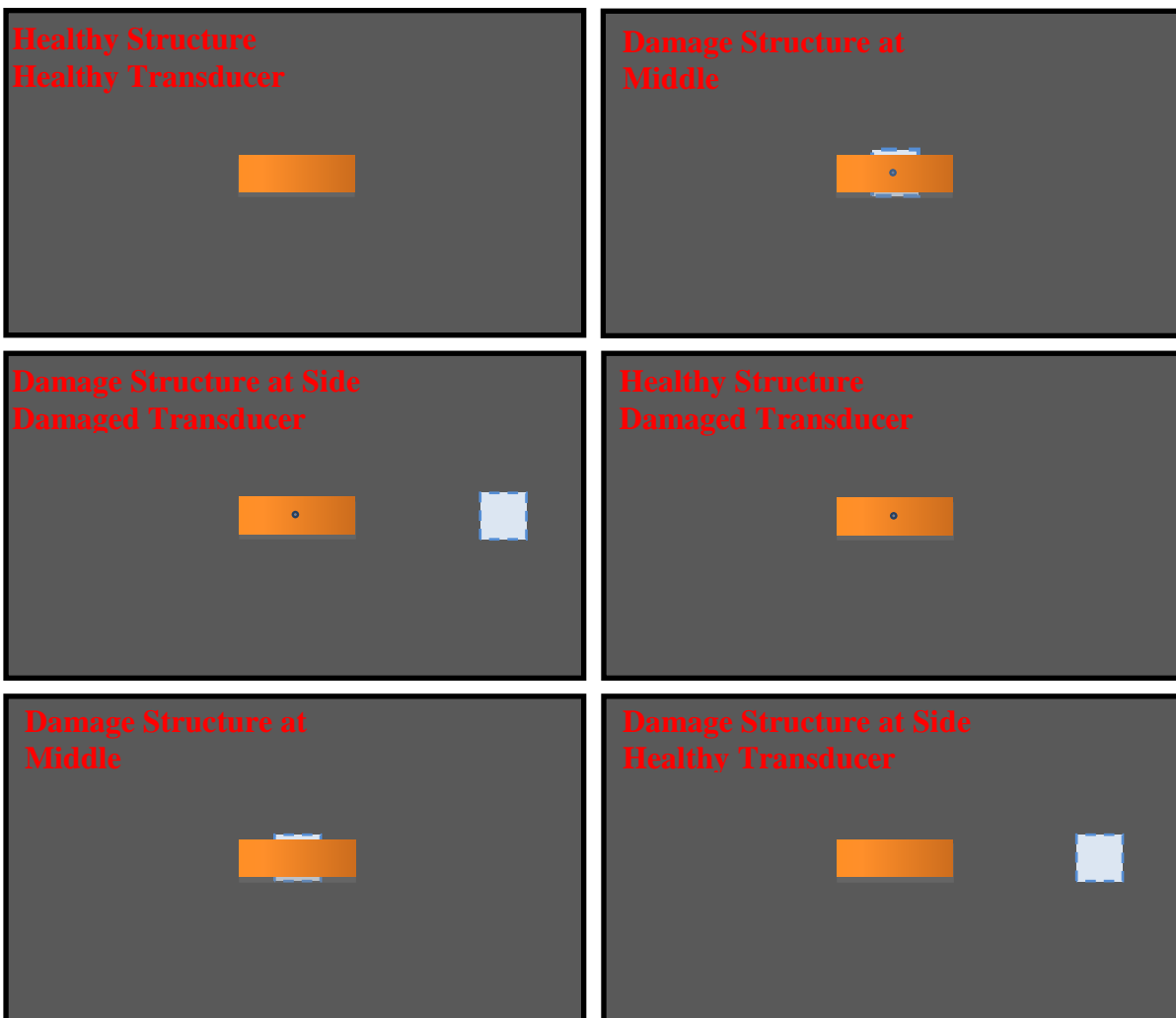
Figure 3-10: Six manufactured samples
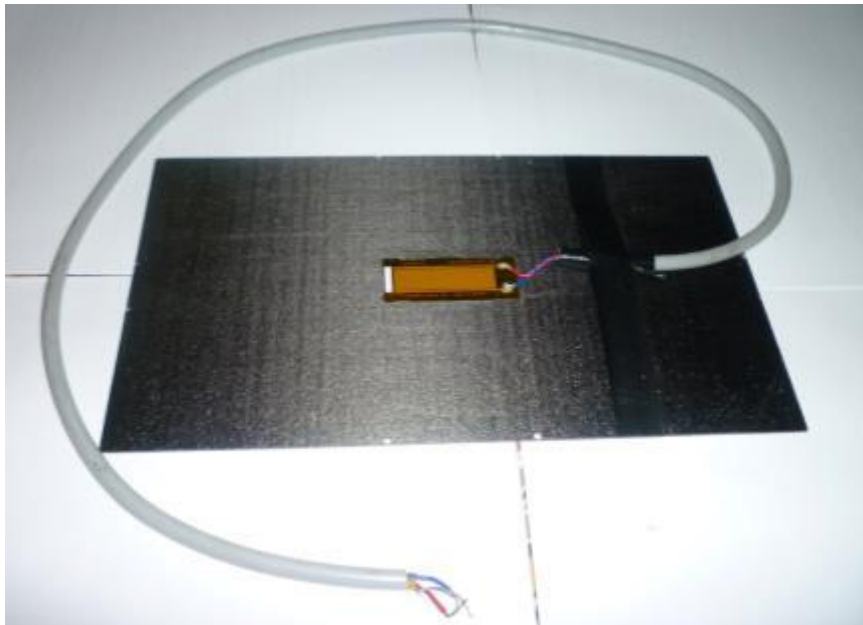
Figure 3-11: Complete manufactured sample

3.3. Experimental Process

3.3.1. Three-point-bend Test Configuration

The INSTRON$^{\circledR}$ Machine is used for the 3-point-bend test under displacement control, at an increment of 0.5 mm per minute. The load is measured up to the breakage. The fatigue load range is then calculated according to the ASTM E399-90. The ultimate load is measured as 1795.5 N when the carbon/epoxy sample fails at 20 mm of displacement (Figure 3-12). The load range of 14 N and 140 N is selected based on the previous results and the initial frequency of f = 5 Hz is applied to the test. The test is under displacement control throughout to ensure that the possible delamination is under control. The displacement range is defined as -1.804 mm to -0.411 mm.

The 3-point-bending flexural test provides values for the modulus of elasticity in bending, flexural stress, flexural strain and the flexural stress-strain response of the material. The main advantage of a 3-point-flexural test is the ease of the specimen preparation and testing. However, the loading geometry and strain rate should be defined properly in order to record reliable results. The carbon/epoxy composite plate with bonded transducer is placed in the test setup and the electrode leads are attached to the required data acquisition instruments i.e. oscilloscope, LCR meter etc. In order to avoid any further damage to the transducer, a gap is introduced to the spin which applies load on top of the sample (Figure 3-12).
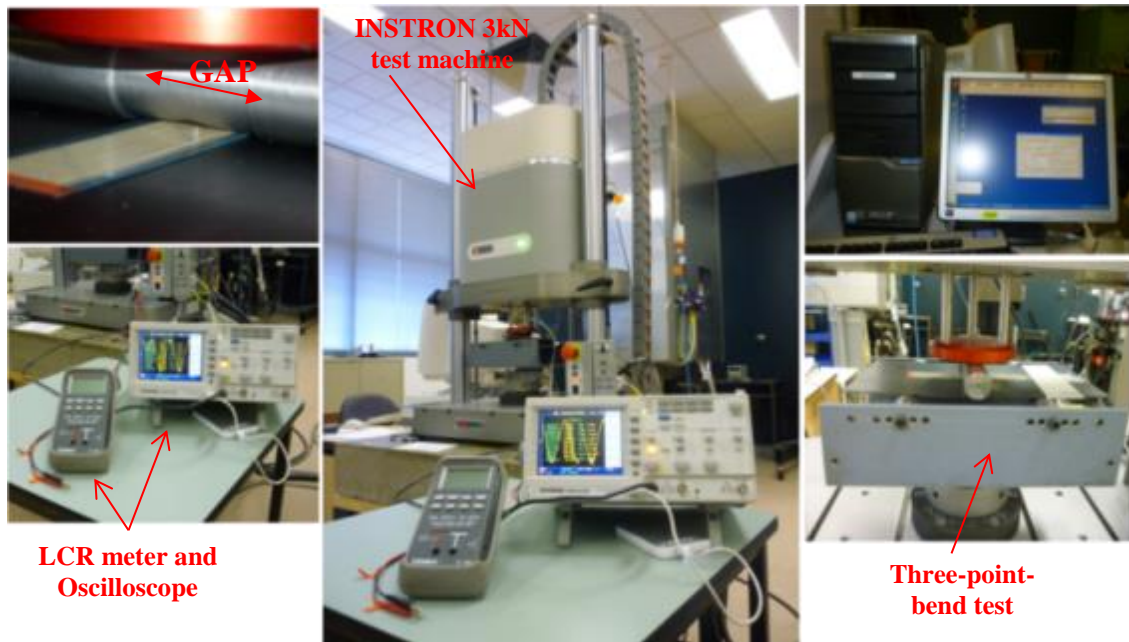
Figure 3-12: The experimental setup for fatigue test

3.3.2. Electrical Properties Measurement of MFC/PFC Transducer

The test rig, as shown in Figure 3-13, is used to measure the electrical properties of the MFC/PFC sensor. There are various parameters which can be measured. However, some of the electrical properties are more sensitive to the degradation of the sensor such as Capacitance, Resistance, Inductance, Electrical Impedance etc. The transducer leads are connected to the LCR meter to measure capacitance, inductance and resistance values. The digital oscilloscope, which has the data recording capability, is also used to measure the output voltage of the transducer. The data is collected prior to bonding and after bonding to ensure that the bonding process does not affect the integrity of the transducer.
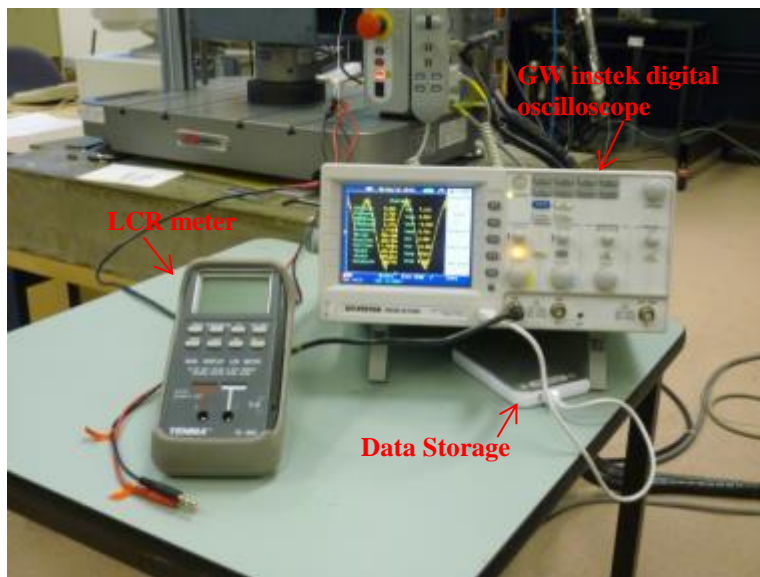
Figure 3-13: Transducer electrical properties measurement

3.3.3. Strain Measurements Procedure

In order to measure the strain level of the samples, the strain gauge, which is one of the most common tools for strain measurement, is used. The description of strain gauges is provided in Chapter 1. The Araldite 420 A/B, which is a 2 component room temperature curing paste adhesive boasting high strength and toughness, is used to bond the strain gauge to the carbon/epoxy composite plate. The strain gauge is bonded to the X, Y coordinates of the transducer but on the back of the plate. In addition, the strain gauge should be bonded in the same direction as the transducer fibres to provide us with strain level in the piezo-fibres direction (Figure 3-14).

In order to measure and record the strain readings of the strain gauge, the digital data logger used to Measure strain from strain gauges is the Vishay Micro- Measurements™ strain indicator and recorder (Model P3™). This is a portable, battery-operated instrument capable of simultaneously accepting 4 inputs from quarter-, half-, and full-bridge strain-gauge circuits, including strain-gauge-based transducers (Figure 6.13) (Vishay, 2011). This recorder is connected to the bonded strain gauge and to a laptop which is used to record the strain readings of all channels as shown in Figure 3-15.
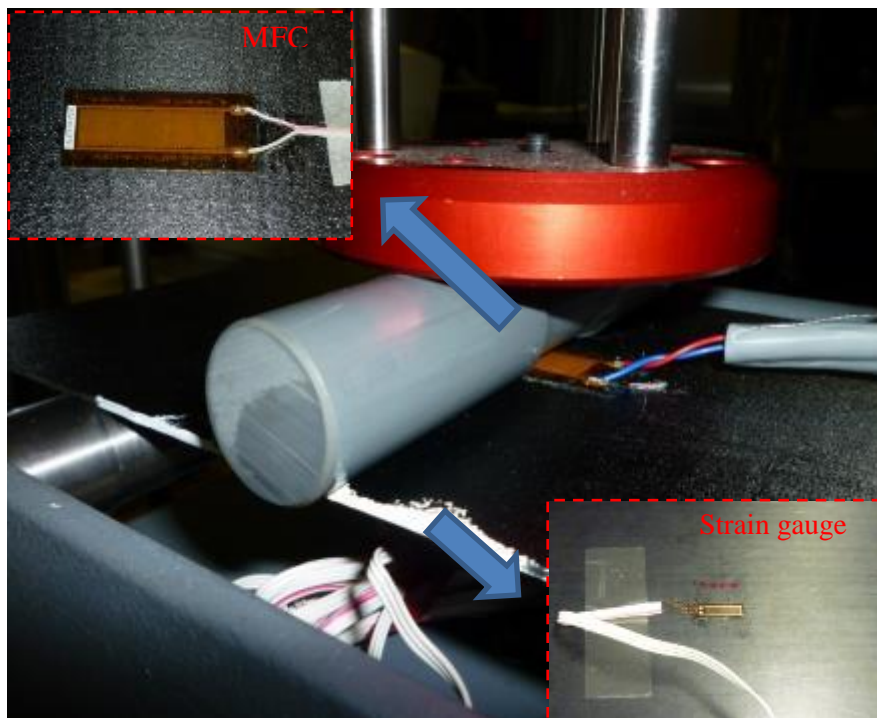
Figure 3-14: Figure 3 13: Strain gauge and MFC bonded on composite plate

To obtain an accurate strain measurement, it is important to calibrate the strain recorded based on the gauge factor (GF) of the strain gauge. This factor is provided by the manufacturer for each type of strain gauge. The strain gauge used in this experiment has a gauge factor of 2.
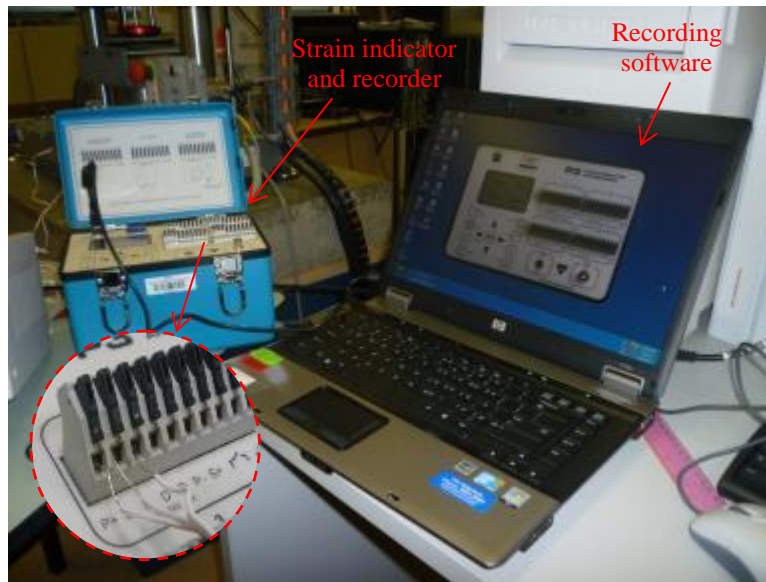
Figure 3-15: Strain measurement test rig

3.3.4. Electromechanical Impedance Experimentation

One of the important experiments in this research involves the measuring and analysis of the MFC transducer's electromechanical impedance. To measure this parameter, the impedance analyser excites the piezoelectric transducer bonded to a structure with a sinusoidal signal. This electrical excitation generates the mechanical excitation in the transducer due to its direct effect. The bonding layer transfers the mechanical excitation to the structure which affects its structural dynamics through mechanical impedance relations. As the transducer is bonded to the structure, any change in the dynamics of the structure also affects the transducer. As such, the change in the mechanical impedance of the structure causes a strain on the transducer. The direct effect of the transducer converts this mechanical strain to a current output in the piezoelectric transducer. The ratio between the initial voltage induced to the transducer and the final output current applied to the transducer is generally called electromechanical impedance, and is measured by the impedance analyser connected to the transducer electrodes. The measured electromechanical impedance is normally presented versus a designated frequency range. The impedance analyser determines the FRF (Frequency Response Function) of the structure and measures it over the designated bandwidth.

It is observed in this project that at very low frequencies (less than 10 kHz), the MFC transducer excitation is not sufficient to couple the electrical properties of the transducer to the mechanical properties of the structure and the measured electrical impedance is only valid to detect possible damage or degradation in the transducer itself. It should be also noted that the impedance

measurements at extremely low frequencies (less than 300Hz) are subject to various noise levels and should be avoided. Generally speaking, the frequency range of 10-400 kHz, based on the nature of the test, is used for impedance-based SHM using piezoelectric transducers such as MFC. Of course, the measurement of the electromechanical impedance over the whole range will significantly decrease the sensitivity of the readings and therefore only a portion of this bandwidth is used for any application. Nevertheless, the whole bandwidth range of 0.1-100 kHz is used in this research project based on the size of the structure as well as the MFC transducer and induced damage and also to investigate the quality of electro-mechanical coupling between the transducer and the structure at low and high frequencies. There is no standard to determine the appropriate frequency range for an SHM application. However, it is suggested by researchers such as Park et al., (2003) that choosing the high frequency range makes the transducer more sensitive to small and local damage and also eliminates the impact of the bonding layer and environmental noise and vibration.

3.3.4.1. AD5933 impedance analyser characteristics and operation

Analog Devices, Inc. has recently developed two new single chip impedance measurement devices. The chip under consideration is the AD5933 (AD Application Note, 2005). This chip has a 1 mega sample per second (MSPS) sampling rate and costs around $10 AuD (Australian dollar) per chip. An evaluation board for the AD5933 can also be purchased from Analog Devices for 190.00 AuD. The board comes with software which controls the parameters of the chip via a USB interface. The general operation of the chip can be outlined as follows. A 24-bit direct digital synthesis (DDS) core produces a digitised sine wave of the desired interrogation frequency. The excitation signal is then passed through a programmable gain stage and output passes into the device of interest. The current output from the device caused by the excitation signal is then passed through a current-to-voltage amplifier, which features a user-selectable feedback resistor in order to vary the amplifier gain.

The amplifier feedback resistor must be sized appropriately in order to ensure that the signal remains in the linear range of the analog-to-digital converter (ADC). The resulting real and imaginary values as well as the impedance magnitude and absolute value are sent to the software for further analysis. At this point, it is important to note that the AD5933 does not directly give out real and imaginary values proportional to the real and imaginary values of the impedance. In reality, by looking over the operation of the impedance chip, it is possible to see that it is actually giving out real and imaginary DFT values corresponding to the current output from the device. For

this reason, it is necessary to use the following formula (Equation 3-1) to calculate the impedance measurement at any given frequency point (AD Application Note, 2005).

Equation 3-1

$$|Impedance| = \frac{1}{GF \times \sqrt{Real_{register}^2 + Imaginary_{register}^2}}$$

The "GF" variable is referred to as the "Gain Factor," which is simply a calibration factor. The magnitude squared of the real and imaginary registers is used in order to avoid complications involved with negative and positive values. This factor is calculated using the software which is provided by the manufacturer. As the phase of pure resistance is zero, a known resistor is placed between terminals of AD5933. In addition, the calibration resistor which is used to calibrate and measure the impedance analyser is placed in the evaluation board as shown in Figure 3-16.
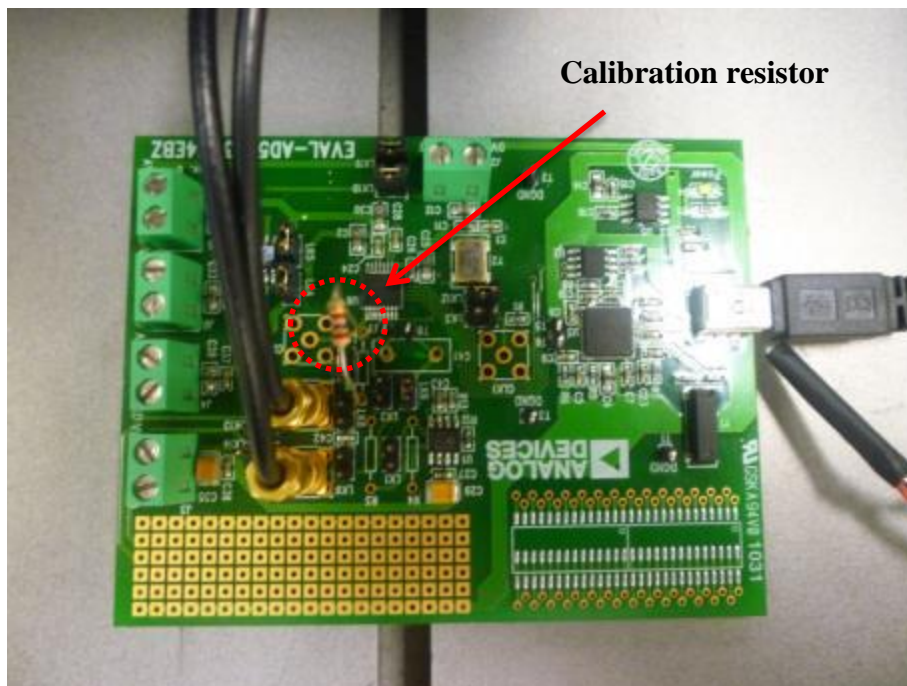
Figure 3-16: AD5933 Evaluation Board

The software automatically calculates the Gain Factor based on the selected settings and calibration resistor value. The board can be calibrated based on the mid-point frequency. However, as a wide frequency range is used in this experiment, the multiple-point frequency is more suitable for calibration. The signal is then swept into the board and passes the known resistor. The software measures the impedance magnitude and phase. For the 2KΩ resistor which is used in this instance, the magnitude should be shown as 2KΩ due to the fact that the impedance

of a pure resistor is equal to its resistance value. Moreover, the phase should be zero as the resistor does not cause a phase delay between induced voltage and measured current. Figure 3-17 shows that the calibrated board measures the impedance magnitude and phase of 2KΩ resistor as per expectations.
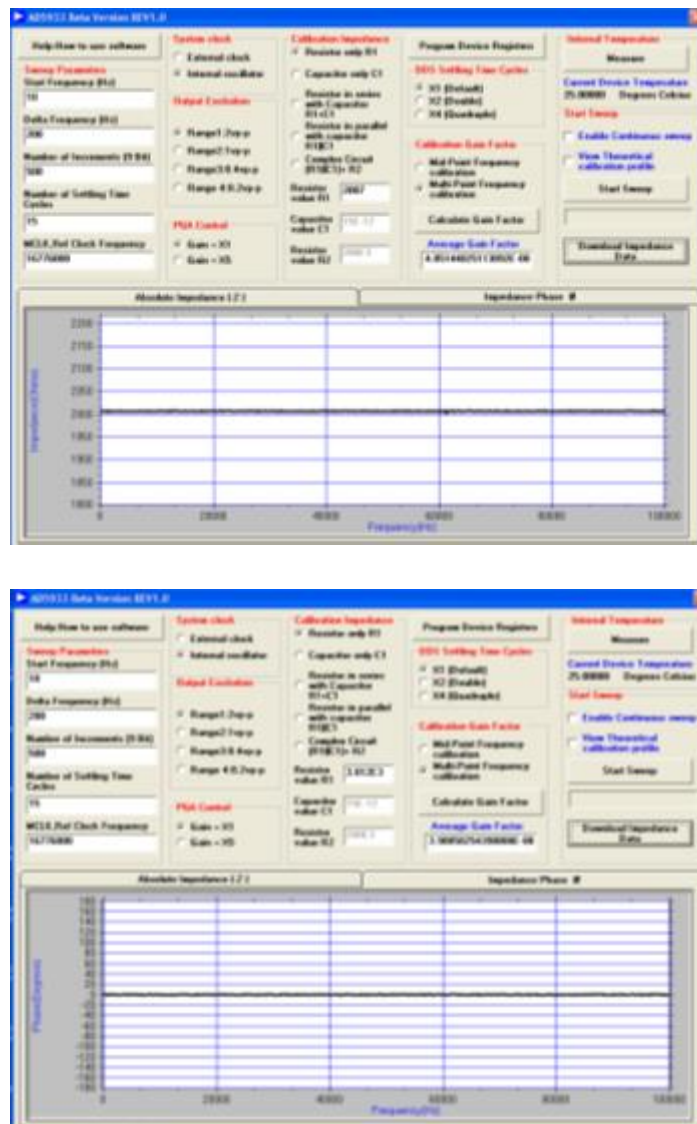
Figure 3-17: AD5933 evaluation board software

3.3.4.1.1. Phase Calibration of the AD5933 Impedance Analyser

In order to accurately measure the impedance of the MFC transducer, the AD5933 evaluation board needs to be calibrated prior to any measurement range. This is to make sure that the impedance of internal components of the board does not have any effect on output impedance. This process can be achieved through a component with known impedance i.e. resistor, capacitor. The phase measured by the software accounts for the phase shift introduced to the DDS output signal as it passes through the internal amplifiers on the transmit and receive side of the AD5933

along with the low-pass filter and also the impedance connected between the VOUT and VIN pins of the AD5933 (Figure 3-18).
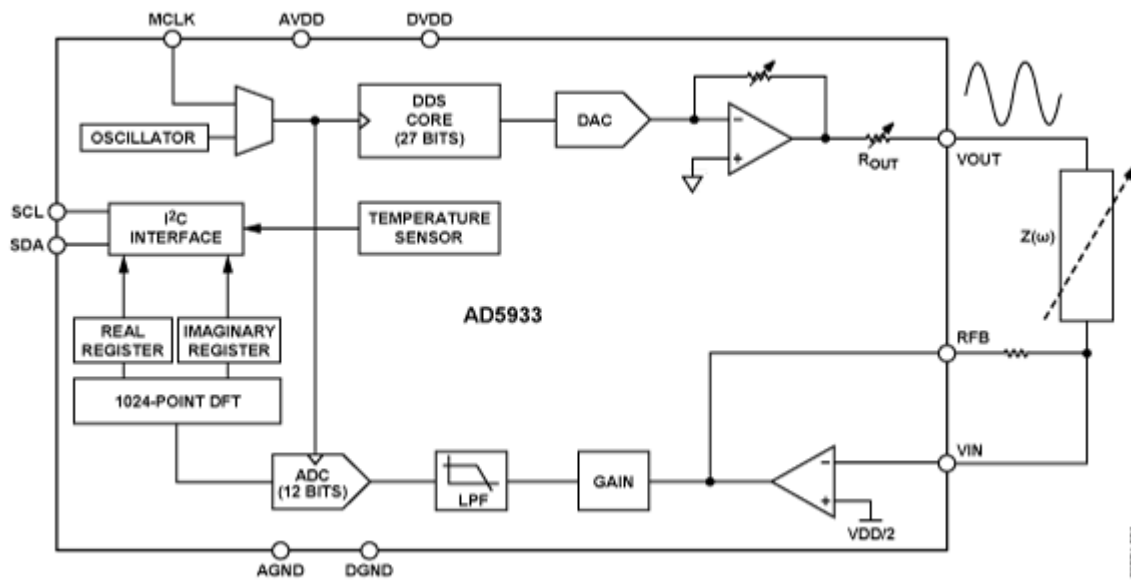
Figure 3-18: Functional block diagram for AD5933 (AD Application Note, 2005)

The parameters of interest here are the magnitude of the impedance (|ZUNKNOWN|) and the impedance phase (ZØ). However, the measurement of the impedance phase (ZØ) is a 2-step process. The first step, as previously mentioned, involves calculating the AD5933 system phase. The AD5933 system phase can be calculated by placing a resistor across the V_{IN} and V_{OUT} pins of the AD5933 and calculating the phase after each measurement point in the sweep. By placing a resistor across the V_{IN} and V_{OUT} pins, there is no additional phase lead or lag introduced to the AD5933 signal path and the resulting phase is due entirely to the internal poles of the AD5933, that is, the system phase.

Once the system phase has been calibrated using a resistor, the second step involves calculating the phase of any unknown impedance by inserting the unknown impedance between the V_{IN} and V_{OUT} terminals of the AD5933 and recalculating the new phase (including the phase due to the impedance) using the same formula. The phase of the unknown impedance (ZØ) is given by Equation 3-2.

Equation 3-2

$$Z\emptyset = \Phi_{unkown} - \nabla_{system}$$

Where ∇_{system} is the phase of the system with a calibration resistor connected between V_{IN} and V_{OUT}, Φ *unknown* is the phase of the system with the unknown impedance connected between V_{IN} and V_{OUT} and *Z*Ø is the phase due to the impedance, that is, the impedance phase.

It is also possible to calculate the gain factor and to calibrate the system phase using the same real and imaginary component values when a resistor is connected between the V_{IN} and V_{OUT} pins of the AD5933, for example, measuring the impedance phase (ZØ) of a capacitor. The excitation signal current leads the excitation signal voltage across a capacitor by −90 degrees. Therefore, an approximate −90 degree phase difference exists between the system phase responses measured with a resistor and that of the system phase responses measured with capacitive impedance. To determine the phase angle of capacitive impedance (ZØ), we need to determine the system phase response and subtract this from the phase calculated with the capacitor connected between V_{IN} and V_{OUT} (Φ unknown).

3.3.4.1.2. Highlights of AD5933 impedance analyser

As previously stated, the AD5933 provides SHM researchers with many advantages, although it is still apparent that the performance of the bulky and expensive impedance analysers such as Agilent 4294A is superior to the performance of the AD5933, except in the areas of cost, size, and power supply, as shown in Table 3-1. It should be noted, however, that many of the superior features of the Agilent 4294A are not utilised in SHM applications (Mascarenas et al., 2006). For example, most SHM impedance measurements are made between 10 kHz and 200 kHz, meaning that the majority of the Agilent 4294A bandwidth is not used in SHM applications. In contrast, the entire frequency range of the AD5933 is usable for SHM applications. SHM applications typically require a large array of sensor nodes distributed across a structure. Wide scale deployment requires that the sensor nodes be low cost, as well as small and lightweight. The Agilent 4294A does not satisfy either requirement, but the AD5933 at $10 with a chip footprint of 6 mm×5 mm, addresses both cost and size constraints. Furthermore, sensor nodes are often applied to a structure after the design and construction phases are complete. Adding the hard-wired 120 V AC connections required for an Agilent 4294A based sensor node, after construction is complete, is often prohibitively expensive. In contrast, a sensor node utilising the AD5933 could be powered by conventional batteries since the normal operation current draw is only 10 mA. Clearly, the AD5933 provides enough advantages for structural health monitoring when compared to typical bulky and expensive impedance analysers even though they have more options and better resolution.

Table 3-1: Comparison of AD5933 and typical impedance analyser (Mascarenas et al., 2006)

Parameter	Typical impedance analyser	AD5933	Unit
Dimensions	50000	Eval. Board 190, Chip 10	$
Frequency range	500×225×425	100×75×15	Mm
Max points/sweep	801	512	Points
ADC sampling rate	Around 200	1	MSPS
ADC resolution	N/A	12	Bit
Power supply voltage	120 AC	3.3. DC	V

3.3.4.2. Experimental Procedure

After the manufacturing process, 6 samples are prepared with the induced damage in the structures and sensors. The proper study of the behaviour of these samples under loading condition can provide us with valuable information regarding the effect of sensor damage and the structural damage on the responses of the bonded sensor, as well as the dependency of the sensor responses to the location of the damage in the structure. Furthermore, the functionality of the sensor itself after damage, as one of the major concerns in the SHM, can be evaluated. These 6 samples consist of: Sample with Healthy Sensor and Healthy Structure (HSEN_HST), Sample with Damage Sensor and Healthy Structure (DSEN_HST), Sample with Healthy Sensor and Damaged Structure with the damage at the side of the plate (HSEN_DST_SIDE), Sample with Healthy Sensor and Damaged Structure with the damage at the middle of the plate (HSEN_DST_MIDDLE), Sample with Damaged Sensor and Damaged Structure with the damage at the middle of the plate (DSEN_DST_MIDDLE), Sample with Damaged Sensor and Damaged Structure with the damage at the side of the plate (DSEN_DST_SIDE). As mentioned earlier, all the damage in the structure is identical in terms of severity while all the damage in the sensors is identical in terms of location as well as severity. In order to collect the sensor responses, identical cables are soldered to the sensors` leads and the electrical properties of the sensor, including capacitance, are measured before and after the soldering to make sure that the heat does not cause any further damage to the sensor. The electrode leads of the MFC transducer are connected between the V_{IN} and V_{OUT} of the AD5933 impedance analyser. The impedance analyser is also connected through a USB cable to the software which calculates and records impedance components. The test rig is shown in Figure 3-19. The impedance analyser sends the excitation voltage in the frequency range of 0.2-100KHz to the MFC via its electrode leads and measures back the generated current. Following this, the AD5933 evaluation software calculates the impedance magnitude, impedance phase as

well as the real and imaginary impedance of the system based on the ration of V/I and the phase difference between these two parameters. Upon the completion of sweep, the data can be exported into Excel for further analysis. The data is tabulated versus designated frequency range and can be plotted accordingly.

Figure 3-19: E/M impedance measurement test setup

The above setup is used to measure the impedance components which will also be used to calculate the admittance values. These components are then compared before and after the occurrence of damage in the structure and/or transducer in order to make the delineation of transducer damage from structural damage possible. This logic is presented in Figure 3-20.
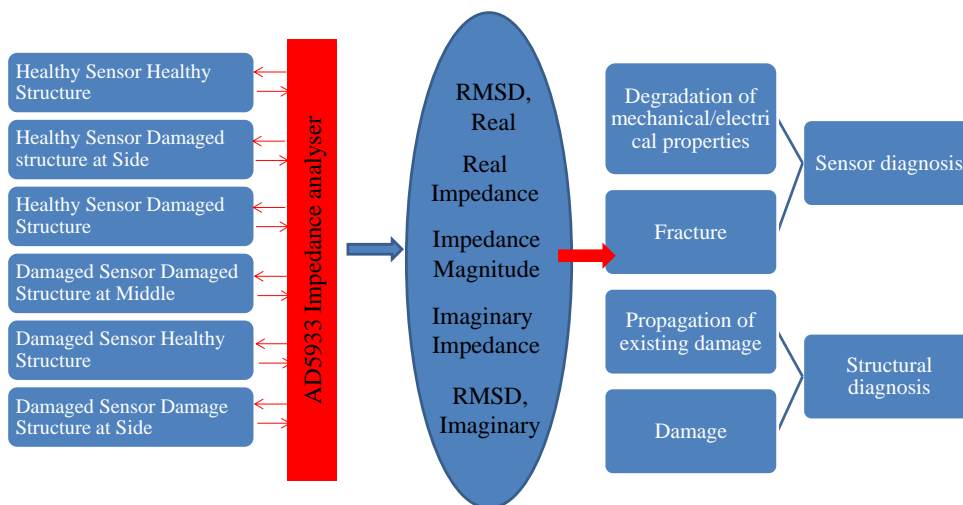
Figure 3-20: E/M impedance methodology

3.3.5. Scanning Electron Microscopy (SEM)

SEM imaging is used to inspect the impact of damage on the internal components of PFC and the MFC transducer. The appropriate samples are prepared prior to the imaging as stated below. The damaged transducer is debonded from the host structure and cut into damaged and undamaged sections, following which these sections are gold-coated for the SEM process.

3.3.5.1. Transducer Removal and SEM Sample Preparation

The bonded transducer, which is damaged during fatigue cyclic loading, is carefully removed from the carbon/epoxy plate. The oven is used to apply 80°C temperature for approximately 30 minutes to soften the bonding layer. The transducer is then carefully detached from the structure. It is important to detach the transducer directly after the sample is removed from the oven as the bonding layer becomes rigid again after a few seconds. The properties of the transducer are measured before and after the debonding process to make sure it does not induce any further damage to the transducer. Upon removal of the transducer, it is cut into various damaged and undamaged sections under the optical microscope for SEM imaging. The preparation process is shown in Figure 3-21.

Figure 3-21: The transducer detaching process and sample preparation

3.3.5.2. Gold Coating Process

As the outer surfaces of MFC and PFC transducers are non-conductive, they need to be gold coated prior to any SEM imaging. In order to prepare the sections of both transducers for the coating process, the surfaces should be cleaned of dust and any particles using ethanol before being dried thoroughly. Following this, the samples are mounted on an aluminium SEM stub of appropriate size using carbon tape. These stubs are used to place the sample in the coating chamber as well as in the Philips SEM machine. The SPI® Supplies Sputter Coater (Figure 3-22) is used to gold coat the prepared samples. The SPI-Sputter Coater with Etch Mode Module is a sputtering power supply generating more than 1000 volts DC and a diode magnetron sputtering head with a high voltage cable with and is a 3Mil gold (1 mil=0.001 inch).

The power is switched to the VACUUM CONTROL BASE and the SPUTTER COATER MODULE. With the gas leak needle valve closed after 10 to 15 seconds, the fall in pressure within the work chamber will register on the vacuum gauge on the front of the VACUUM CONTROL BASE. As the pressure falls below 600-400 millitorr, the vacuum safety interlock is triggered and the power and ready lamps will come on. This interlock will close and operations cease whenever the pressure rises above 1000 millitorr. The unit should be left running for at least one hour or until the gauge indicates 80 millitorr or less. The test button is then depressed and the gas leak valve slowly opened while observing the plasma current. It should begin to rise as the current is set for 18ma and the test button is released. The timer is then set at 10 seconds and the start button depressed again. The plasma current will be somewhat more than 18 ma. Although it will proceed to decrease and stabilise at 18 ma or lower, the gas leak valve may be used to set whatever current is desirable. After 10 seconds the discharge will cease, and a small deposition of gold may be observed. Depressing the start button again will give another 10 seconds, or the timer can be set for a longer time.

After sputtering both power switches are turned off, the gas leak valve closed and air admitted to the chamber by opening the vent valve on the top of the sputter head. The samples (sections of MFC and PFC transducers) are mounted on an aluminium SEM stub of appropriate size using carbon tape. The sample mounts are then secured to the holder by the set screws. It should be approximately 50 mm from the bottom of the sputter head. The glass work chamber is replaced and the sputters head placed on top of the chamber. The timer is then set to 120 seconds and the leak valve is fully closed. The argon pressure is set to 5 PSI as per instruction. Both power switches are turned on which starts the rotary pump and the vacuum process. As soon as the pressure falls to approximately 400-500 millitorr, the "Ready" button goes on. This is the

appropriate pressure for gold coating, which makes the coating consistent and homogenised. The gas leak is then partially opened to flush the work chamber with argon for approximately 10-15 seconds. Following this, the leak valve is closed and leaves the chamber to pump down to approximately 80 millitorr. Once the chamber reaches this pressure, the gas leak is opened until the pressure begins to rise and by intermittently depressing the test button and adjusting the leak valve, the plasma current is set to the 18 ma as per requirement. A visible discharge should be observed in the chamber at this stage. Finally, the start button is depressed and gold is sputtered onto the samples for the set time (120 seconds). The plasma is automatically stopped at the end of this period.
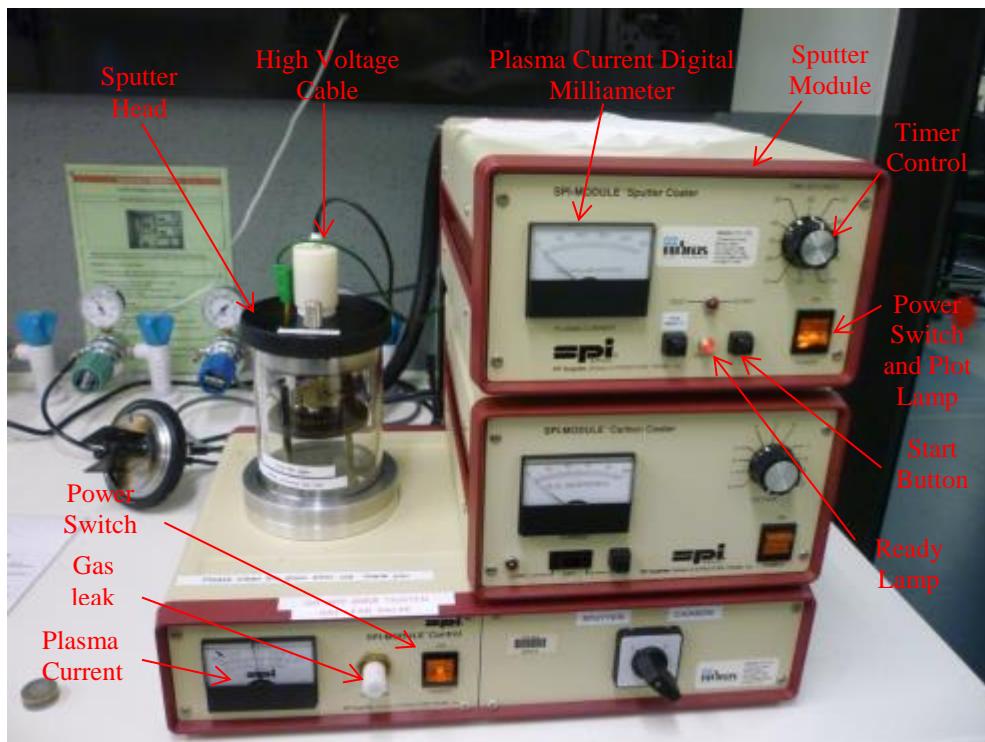
Figure 3-22: The SPI Sputter Coater

The thickness of coating is dependent on the type of coating as well as the gas used to vacuum the chamber. Generally, a gold film thickness between 100 and 300 angstroms is used for investigations. The experimentally determined thickness can be obtained from Equation 3-3.

Equation 3-3

$$d = KIVt$$

Where d is the thickness of coating in angstrom units. K is the constant calculated from experiment based on the gas type, coating material and distance to the target, I is the plasma current, V is applied voltage (KV) and t is the sputtering duration (sec). In this experiment, gold is used as

sputtering metal along with argon gas and therefore the "K" is approximately 0.17. The plasma current was also set to 18 mA and the duration of sputtering was 120 s. Hence, the expected thickness can be calculated as below:

$$d = KIVt = 0.17 \times 18 \times 1 \times 120 = 367 \text{ angstroms}$$

This shows that the average value for this process is approximately 3 angstroms per second. It should be noted that the cleanness of the chamber may change the required "d". The gold-coating process is shown in Figure 3-23.
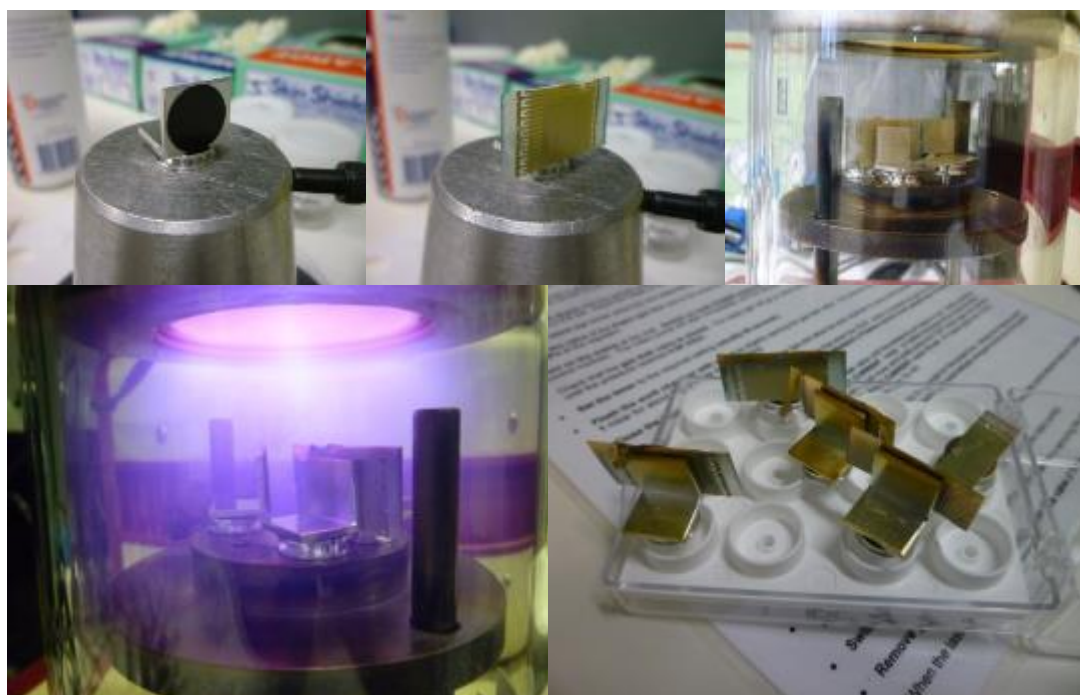
Figure 3-23: The gold-coating process

3.3.5.3.   XL30 SEM

The XL30 Conventional Scanning Electron Microscope (CSEM) manufactured by Philips Electron Optics is used for surface observations of a wide range of conductive or non-conductive solid state samples (Figure 3-24). A guaranteed point resolution of 3.5 nm at 30 kV and 30 nm at 1 kV is achieved; the continuously variable accelerating voltage covers the range from 0.2 kV to 30 kV and the magnification range changes from 10x to 400.000x. Scan modes are either full frame, reduced raster (beam scans in a limited area), horizontal line scan or spot mode. The Energy Dispersive X-ray Spectrometer (EDXS) manufactured by Oxford Instruments, and fully integrated with the SEM XL30, offers qualitative and quantitative elemental analysis of all elements down to boron (Z = 5). Images, spectra and X-ray maps from analysed micro-areas can

be acquired. Two data correction procedures are available on the EDX LINK ISIS such as ZAF and PhiRoZet. The first procedure yields excellent results for elements Z>11, while the second is used especially for the light elements at low electron beam energies. The X-ray Si (Li) Pentafet detector with energy resolution of 138 eV operates with Super Ultra-Thin Window (SUTW) for the ultimate in light elements performance.
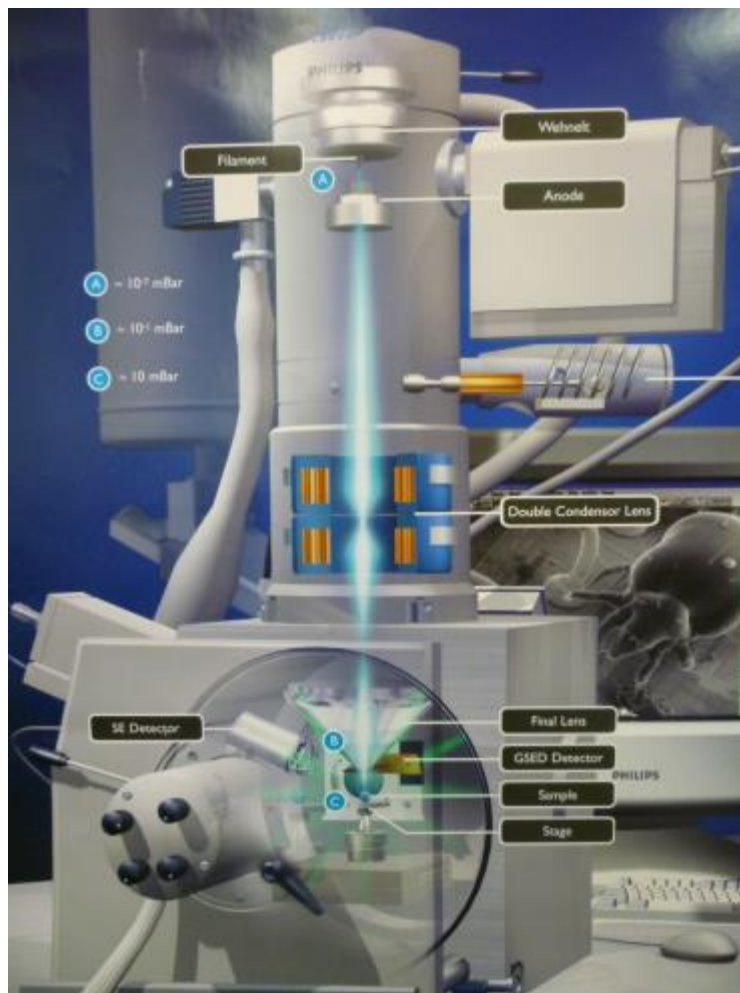
Figure 3-24: The XL30 SEM machine

Scanning Electron Microscopy (SEM) is one of the most frequently used characterising tools within material research because of a whole range of different research information which can be obtained from macro down to Nano scale. During an SEM study, a focussed electron beam is scanned upon the surface of the material under study and generates different signals (SE, BSE, and X-rays, light...) which can be picked up by different detectors to build images, maps and/or spectra.

Nowadays, a variety of detectors are available to obtain besides the classical imaging modes (SE: Secondary Electrons and BSE: Back Scattering Electrons). There is also an abundance of information relating to the chemical compositions (EDX: Energy Dispersive X-ray detection), the

crystal structure (EBSD: Electron Back Scatter Diffraction) and the presence of defects (EBIC: Electron Beam Induced Current) etc. The lateral resolution of the SEM technique in imaging mode can be in order of 1 nm in SE mode. Nowadays, SEMs are also operational in 3 vacuum modes (high vacuum, low vacuum and ESEM (environmental SEMI) to accommodate the widest range of sample. The digitised SEM allows continuous imaging to perform in-situ SEM studies of dynamical processes. Due to its versatility, Scanning Electron Microscopy can be used in many research domains. Depending on the information to be gathered, studies are carried out in a non-destructive or destructive way. Some typical examples include: inspection of microelectronic devices at the surface and in cross-section, evaluation of coating, corrosion study, and failure analysis. The steps for SEM imaging are explained below and shown in Figure 3-25:

3.3.5.3.1. Inserting the sample

Following this, the gold-coated samples are placed in the SEM machine for the imaging process. The Vent Button is pressed first and once the vacuum panel reads idle, the sample is inserted into the chamber using the stub holding tweezers. The height gauge should be used to check the sample height prior to closing the door and lower if necessary using the z knob on the chamber door. The chamber door is then closed carefully and held closed while the Pump button is pressed.

3.3.5.3.2. Initial set-up

Once the samples are placed into the chamber, it is imperative to wait until Vac OK. Following this the high voltage is turned on by pressing the kV button on the beam page. The Link Z to FWD (Free Working Distance) dialog box will open. Following this, the contrast and brightness is roughly adjusted so as the element which requires focus can be seen.

We focus on the image at low magnification by holding down the right mouse button and dragging it from side to side. Now we can zoom in to 1000X and focus the image as well as possible and click Ok to link Z to the FWD window. The microscope now knows where the top of the sample is and we can safely change the working distance i.e. change the Z to 10,000 mm.

3.3.5.3.3. Imaging

The imaging process is relatively easy as the previous steps are properly defined. The contrast, brightness and focus should be adjusted. In addition, the reduced area scan is used to focus on finer details. We can also adjust other properties such as HV or spot size of the beam can also be

adjusted to obtain the best clarity and details.
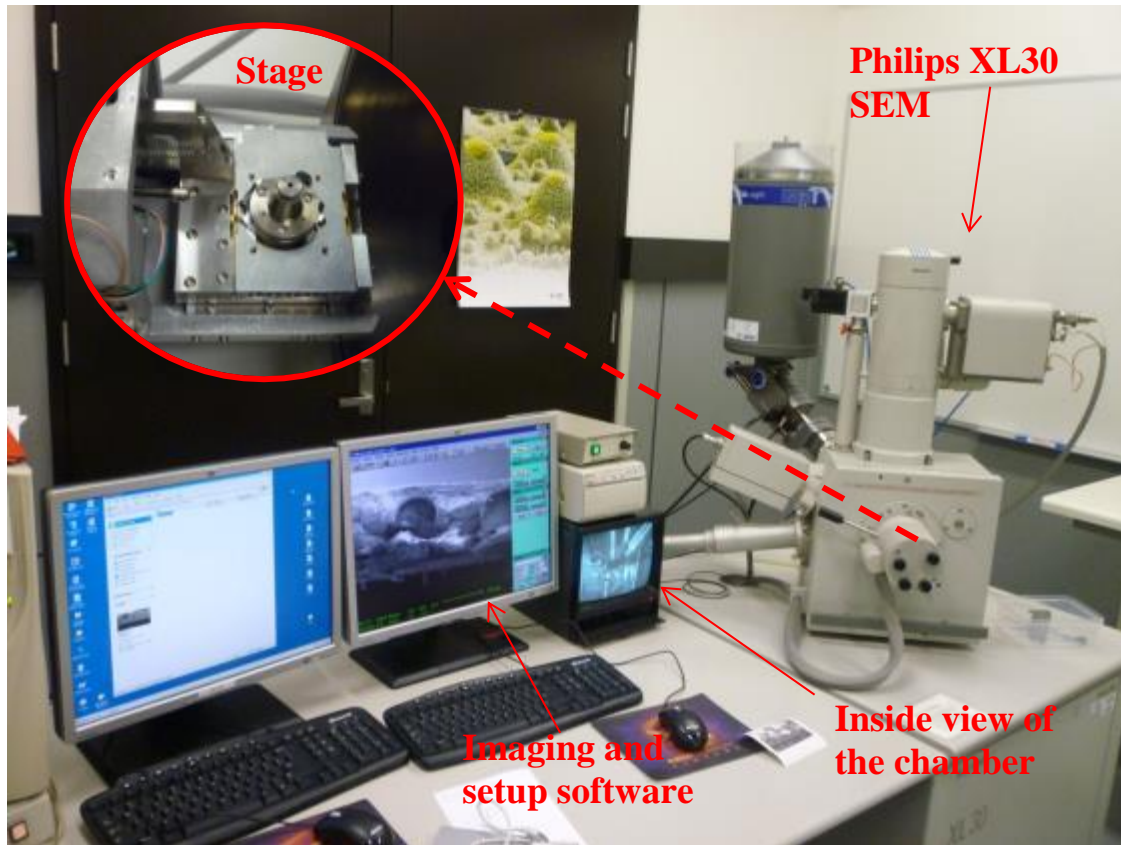
Figure 3-25: The SEM setup and process

3.4. Summary

In this chapter, the design and manufacturing process of the samples which are used in this project are explained. Moreover, the experimental setup and preparation are visually presented and the details of the experimental procedure such as test conditions, instrumentations etc. are discussed. In this chapter, the electrical properties of the free and bonded PFC (Piezoelectric Fibre Composite) and MFC (Macro Fibre Composite) are successfully measured using the LCR meter and Oscilloscope. The measurements are repeated to ensure that the measuring process is reliable and devices are calibrated. The process of bonding PFC and MFC transducers on the surface of carbon/epoxy plates is also proved through the measurement of their properties before and after the bonding, thus ensuring that they are consistent and repeatable. One of the important experiments in this research involves the proper measurement and analysis of the MFC transducer's electromechanical impedance. The accuracy and repeatability of this measurement are as important as the impedance-based technique, which will be presented in the next chapters and is based on the continuous comparison of the MFC's electromechanical impedance measurements. This chapter outlines the operation principle of the Analog Device AD5933 impedance analyser,

as a miniaturised solution for the cost-effective, light-weight and energy efficient impedance-based technique. The calibration process is presented and the sample measurements after calibration show an accurate setup for AD5933. The principle and methodology of the electromechanical impedance-based technique is also presented and required test samples are visually shown and described. The debonding procedure of the MFC and PFC transducers from carbon/epoxy plates, after observing the damage in the structure or the transducer, are presented. The debonding procedure, in terms of the required temperature and time, is selected in a certain way so as to ensure it has a minimum effect on the transducer or the structure. The sample preparation for the SEM (Scanning Electron Microscopy) imaging used to observe the micro-structure of the damaged and intact transducers is also illustrated. This step is achieved under an optical microscope due to the required size of the samples. The prepared samples are carefully placed in the SEM machine as discussed in this chapter.

CHAPTER 4 Finite Element Analysis

4.1. Introduction

The aim of this chapter is to use the Finite Element Method (FEM) to numerically simulate and analyse the transducers as well as the structure used in the experimental section of this project in order to validate the measurements. Upon validation of this simulation, it can also be employed to predict the behaviour of the transducer as well as the structure under various conditions. Moreover, an additional attempt is made to improve their reliability and functionality. In this chapter, the commercial FEM simulation software package ABAQUS^{TM} is used for the modelling and analysis. The PZT and MFC transducers are simulated in both the bonded and free conditions. The boundary and loading conditions are identical to those in the experiments for comparison purposes.

In this project, the MFC transducer, as one of the most advanced and commercially available transducers, is used for experimentation. In fact, the simulation of the MFC is intricate and time-consuming due to the complex structure of MFC which needs the piezo-fibres, interdigitated electrodes and epoxy layers within the MFC to be separately modelled. Indeed, the complexity lies with the fact that the relevant properties and the connections between subcomponents should also be properly simulated. In light of this, most of the existing simulations of MFC are simplified and either models the MFC as a macro structure like PZT or use an equivalent volume to represent the whole transducer. However, the accurate investigation of MFC behaviour, especially after the generation of damage in the MFC itself, requires the full and detailed simulation of MFC and its components. In order to illustrate this statement, a simplified PZT-like transducer, which has a macro-scale and simple structure, with the same specifications as MFC is also simulated in this chapter and the results are compared to detailed simulation results which is based on the actual structure of the MFC.

4.2. Background

The FEM has become a strong and accurate tool with which to numerically simulate and analyse complicated procedures and provide us with reliable conclusions. Due to the accuracy of this method, it has been successfully turned into software packages such as ANSYS^{TM}, ABAQUS^{TM} etc. for general applications as well as specialised applications. This computer-based simulation

packages offer the advantage of checking the procedure and outcome at the preliminary stage of design.

4.3. ABAQUS^{TM}

In this chapter, the commercial FEM simulation software package ABAQUS/CAE version 6.11 is used for the modelling and analysis (Hirsch C., 2007). ABAQUS^{TM} is a set of finite element analytical programs originally developed by Hibbitt, Karlsson & Sorensen, Inc. (Hassan J.M., 2011). It is currently maintained by SIMULIA Corp. ABAQUS/CAE is the complete ABAQUS environment which includes capabilities for creating ABAQUS models, interactively submitting and monitoring ABAQUS jobs and evaluating results. In this chapter, the ABAQUS/CAE is used as the pre-processor (Part, Property, Assembly, Step, Interaction, Load, Mesh, Job modules) and postprocessor (Visualisation module). ABAQUS/CAE is capable of simulating simple linear 2D analysis up to complex nonlinear 3D simulations. It has 2 main modules: ABAQUS/Standard and ABAQUS/Explicit.

ABAQUS contains an extensive library of elements which can model virtually any geometry. It has an equally extensive list of material models which can simulate the behaviour of most typical engineering materials including metals, polymers, composites, reinforced concrete etc. (Hassan J.M., 2011). Designed as a general-purpose simulation tool, ABAQUS can be used to study more than just structural (stress/displacement) problems. It can simulate problems in such diverse areas as heat transfer, electromechanical (coupled electrical-mechanical analysis), mass diffusion, thermal management of electrical components (coupled thermal-electrical analyses), acoustics, piezoelectric analysis and electromagnetic analysis. ABAQUS offers a wide range of capabilities for the simulation of linear and nonlinear applications. Problems with multiple components are modelled by associating the geometry defining each component with the appropriate material models and specifying component interactions.

4.3.1. The ABAQUS Products

ABAQUS consists of 3 main products: ABAQUS/Standard, ABAQUS/Explicit and ABAQUS/CAE. While ABAQUS/Standard and ABAQUS/Explicit perform analysis, ABAQUS/CAE provides a graphical environment for pre- and post-processing. The ABAQUS/Standard is a general-purpose analysis program used to solve linear, nonlinear, static and dynamic problems. ABAQUS/Explicit is a special-purpose analysis program which uses an explicit dynamic finite element formulation. It is suitable for modelling brief, transient dynamic events, such as impact and blast problems (ABAQUS, 2008a). Moreover, several add-on analysis

options are available to further extend the capabilities of ABAQUS/Standard and ABAQUS/Explicit (ANSYS Manual, 2011). Some of these add-on analysers are listed below:

- ABAQUS/Aqua option works with ABAQUS/Standard and ABAQUS/Explicit.
- ABAQUS/Design and ABAQUS/AMS options work with ABAQUS/Standard.
- ABAQUS/Foundation is an optional subset of ABAQUS/Standard.

The definition and application of the main product and add-on are presented in the following sections (Svensk K AB, 2010).

4.3.1.1. ABAQUS/Standard

ABAQUS/Standard is a general-purpose analysis product which can solve a wide range of linear and nonlinear problems involving the static, dynamic, thermal, electrical, and electromagnetic response of components. The ABAQUS/Standard solves a system of equations implicitly at each solution "increment." In contrast, ABAQUS/Explicit marches a solution forward through time in small time increments without solving a coupled system of equations at each increment (or even forming a global stiffness matrix).

4.3.1.2. ABAQUS/Explicit

ABAQUS/Explicit is a special-purpose analysis product which uses an explicit dynamic finite element formulation. It is suitable for modelling brief, transient dynamic events, such as impact and blast problems, and is also very efficient for highly nonlinear problems involving changing contact conditions, such as forming simulations.

4.3.1.3. ABAQUS/CFD

ABAQUS/CFD is a computational fluid dynamics analysis product. It can solve a broad class of incompressible flow problems including laminar and turbulent flow, thermal convective flow, and deforming mesh problems.

4.3.1.4. ABAQUS/CAE

ABAQUS/CAE (Complete ABAQUS Environment) is an interactive, graphical environment for ABAQUS. It allows models to be created quickly and easily by producing or importing the geometry of the structure to be analysed and decomposing the geometry into meshable regions. Physical and material properties can be assigned to the geometry, together with loads and boundary conditions. ABAQUS/Viewer is a subset of ABAQUS/CAE which includes only the

functionality. ABAQUS also provides translators which convert geometry from third-party CAD systems to models for ABAQUS/CAE, convert entities from third-party pre-processors to input for ABAQUS analyses, and convert output from ABAQUS analyses to entities for third-party postprocessors. In this research, ABAQUS/Standard and ABAQUS/CAE are used for structural analysis. Generally speaking, a complete ABAQUS simulation consists of 3 distinct stages: preprocessing, simulation and postprocessing, as shown in Figure 4-1.

```
┌─────────────────────┐
│   Preprocessing     │
│   ABSQUS CAE        │
└─────────────────────┘
          ↓
      ╭─────────╮
     │ Input file  │
     │  Job.inp    │
      ╰─────────╯
          ↓
┌─────────────────────┐
│   Simulation        │
│   Abaqus/Standard   │
│   (or) Abaqus/Explicit │
└─────────────────────┘
          ↓
      ╭─────────╮
     │ Output files │
     │ Job.odb, Job.dat │
      ╰─────────╯
          ↓
┌─────────────────────┐
│   Postprocessing    │
│   Abaqus/CAE        │
└─────────────────────┘
```
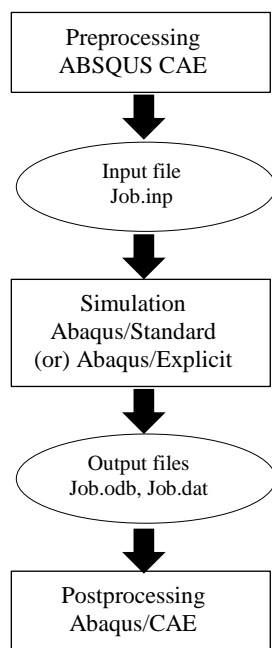
Figure 4-1: ABAQUS Simulation Stages (Bicak, 2013)

4.4. FEA using ABAQUS/CAE

As mentioned in the previous sections, Finite Element Analysis (FEA) is a suitable tool with which to predict the behaviour of a system or a structure in a specific condition. It can also reduce the cost and time of experiments by analysing the performance of this system under experimental test conditions and verifying the experimental results. From various FEA packages, ABAQUS/CAE is selected for this research project due its ability to simulate the required materials such as carbon-fibre composite and piezoelectric materials, as well as its ability to perform both structural and electromechanical analysis. Of course, this software is only capable of simulating and analysing the designated structure with bonded piezoelectric transducer and generating the electrical responses of the piezoelectric transducer as well as mechanical responses of the composite structure. Further calculations must be done on these results using the electromechanical impedance relations in order to calculate the electromechanical impedance components and to compare them with experimental measurements. These calculations can be done with MATLAB or any other numerical computing environment. Details of the experimental setup and test conditions simulated in this chapter can be

found in Chapter 3. The simplified and detailed simulation of the MFC transducer is presented using ABAQUS software. The MFC is bonded onto the carbon/epoxy composite plate in both simulations. The same material properties and test configurations are used in FEA modelling in order to make further comparisons possible.

4.4.1. Element types

The MFC transducer is modelled using the C3D8E element to simulate the piezoelectricity characteristics. This element is from the piezoelectric family of elements in ABAQUS used to model the piezoelectric structures. All of the PZT transducers as well as the piezo-fibres within the MFC transducer are modelled with this element. However, the composite structure is modelled using the C3D8R element. This element can be used for all types of structural analysis. The specifications of these element types are provided in the following sections.

4.4.1.1.   8-node brick element (C3D8)

This is a general purpose linear brick element, fully integrated (2x2x2 integration points). The node numbering follows the convention of Figure 4 2 and the integration points are also numbered according to Figure 4 2. This element is normally followed by another letter which shows the specific field to use this element. The elements used for modelling in this project both belong to this family of elements, although they have different functionalities as described above.

4.4.1.2.   8-node brick element with reduced integration (C3D8R)

This is a general purpose linear brick element, with reduced integration (1integration point). The node numbering follows the convention, whilst the integration point is also shown in Figure 4 2. The integration point of the C3D8R element is located in the middle of the element. Thus, small elements are required to capture a stress concentration at the boundary of a structure.
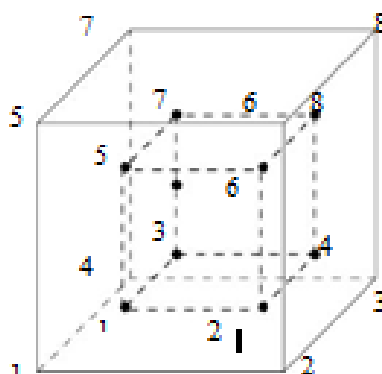
Figure 4-2: 2x2x2 integration point scheme in hexahedral element (Abaqus Analysis User's Manual, 2010)

4.4.1.3.   8-node linear piezoelectric brick element (C3D8E)

C3D8E is an 8-node linear piezoelectric brick element. This is a solid 3-dimensional general-purpose continuum element. The geometry of the continuum element is shown in Figure 4-3.
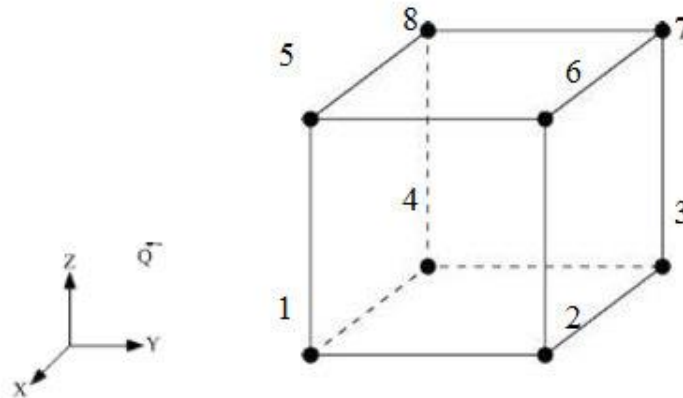
Figure 4-3: C3D8E element geometry and coordinate system

(Abaqus Analysis User's Manual, 2010)

4.5.   ABAQUS Modelling

The first step in the ABAQUS simulation is to create the parts of the model. The exact dimensions of the transducer as well as the structure are required for this step. The following sections provide further information on modelling the transducer and the structure.

4.5.1. Carbon/Epoxy Composite Modelling

As the transducer is bonded on a carbon/epoxy plate in the experiments, the structure is also created with the same dimensions as the carbon/epoxy plate as shown in Figure 4-4. The structure is an 8 ply carbon/epoxy plate with the same lay-up and orientation as the experimental sample which is shown in Figure 4-5.
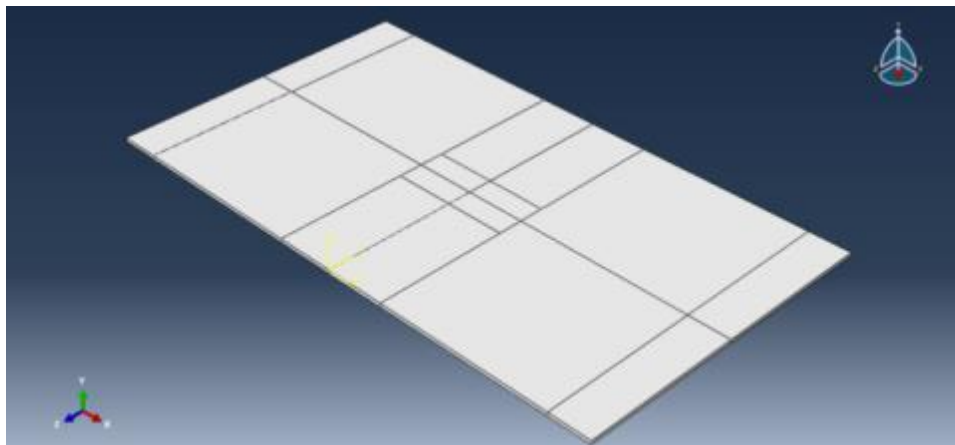
Figure 4-4: The structure modelled by ABAQUS
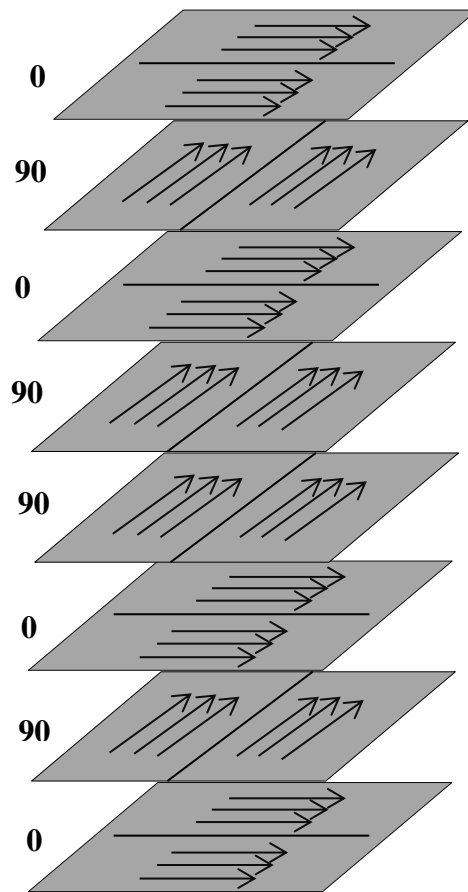
Figure 4-5: Carbon/Epoxy structure layup

4.5.2. Simplified MFC modelling

The simplified modelling of the MFC transducer is relatively simple when compared to the detailed MFC modelling which is based on its actual micro-structure. In the simplified model, the MFC piezoceramic fibres were replaced by a solid layer of piezoceramic and the rectangular epoxy separators are neglected. Unlike the detailed MFC model, the simplified model does not have the micro-scale sub-components. Therefore, a solid plate is created with the same dimension as MFC using ABAQUS and the properties of the MFC transducer are assigned to the solid plate (Figure 4-6).
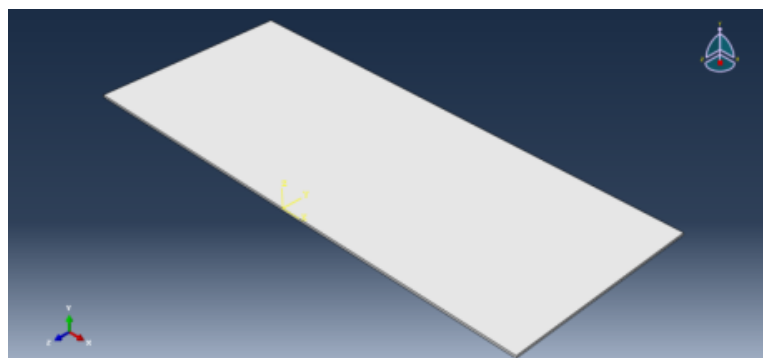
Figure 4-6: The PZT transducer modelled by ABAQUS

The relevant properties and element type are then assigned to both parts. The properties, including density, dielectric, elasticity and piezoelectric should be defined for the simplified MFC model to simulate the transducers as used in experiments. Moreover, the elasticity and damping are defined for structure. It should be noted that ABAQUS has no inherent set of units and it is the user`s responsibility to use a consistent set of units. In our modelling, the SI units are used for all the inputs. The interaction between the transducer and the host structure is another important issue which is dealt with after the previous step. The bottom surface of the transducer should be tied properly to the centre of the carbon/epoxy plate. In reality, the transducer is bonded to the carbon/epoxy structure using an adhesive as described in the manufacturing chapter. The bonding layer between the transducer and the host structure in the experimental work is found to be strong and consistent enough under the designated loading conditions. Therefore, the transducer is considered to be ideally tied to the structure in FEA modelling as well.

However, further research can and should be carried out on the integrity of the bonding layer itself using the same modelling and removing the tie at some of the bonding surfaces in the model. The loading and boundary conditions must also be defined. The assembly is subjected to a 3-point bend configuration similar to the physical tests. The maximum displacement at the centre of the plate is from the initial point of -0.411 mm to -1.804 mm with the increment of 2×10^{-5} mm. The periodic loading must also be defined using the Fourier series in Equation 4-1:

Equation 4-1

$$a = A_0 + [A_m \cos n\omega(t - t_0) + B_n \sin n\omega(t - t_0)] \quad for\ t \geq t_0$$

$$a = A_0 \quad for\ t \leq t_0$$

Where t_0, N, ω, A_o, A_n and B_n are user defined constants and n=1, 2,…, N.

The values for the constants are defined based on the loading conditions of the simulation. The Fourier series can be simplified for this modelling based on the periodic loading used here, as seen in Equation 4-2:

Equation 4-2

$$a = A\cos n\omega(t) \quad A=0.006965 \quad \omega=6.28$$

The time increment of 2×10^{-5} (sec) is applied to the above equation to define the periodic loading of the model. Furthermore, the electrical boundary condition should be applied to the modelled transducer in order to make its poling and electric field the same as MFC transducer used in experiments (Figure 4-7).

The meshing is also a very important step in any FEA software package including ABAQUS. The quality of meshing directly affects the accuracy of the results. The partitioning process is used to optimise the meshing of the transducer as well as the structure. In terms of the partitioning process, the part is partitioned into smaller rectangular shapes and each partition is meshed separately with similar meshing specifications. As a result, the meshed elements become more regular and conformal. This process is shown in Figure 4-18. While the large meshing size would considerably reduce the accuracy of the results, overly small meshing size would increase the simulation time significantly. Therefore, the meshing size should be selected based on the structure of the model and complexity of the simulation. Moreover, in case of two parts with different materials and element type tied to each other, the size of the meshing on each part should be selected according to the other part. The defined element types for transducer and the structure are used to mesh the relevant part accordingly.
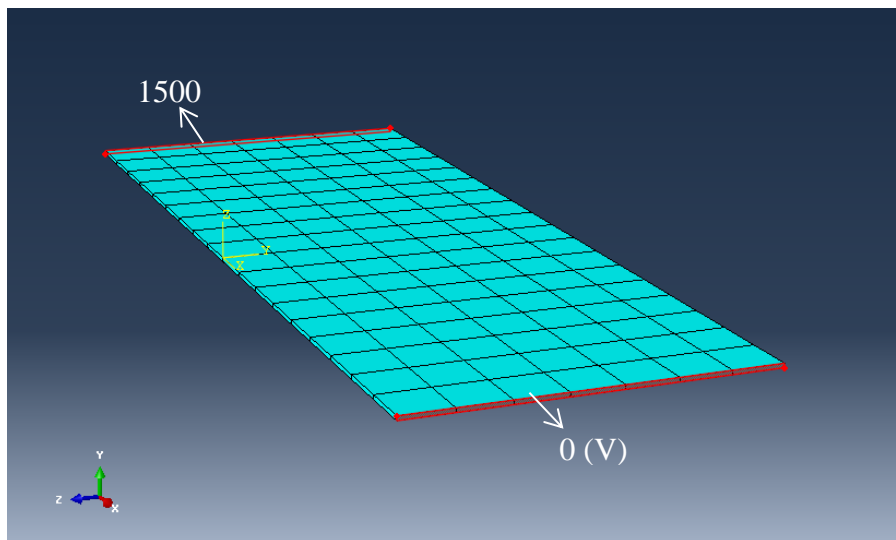
Figure 4-7: electrical boundary conditions of simplified model of MFC transducer

The structure of the simplified model is relatively simple. As such, the meshing size to be used for simplified model does not need to be as small as the one for detailed MFC modelling. However, as the purpose of modelling MFC transducer through simplified approach is to compare its results with detailed MFC simulation results, the same meshing quality used for both modellings. The meshing configuration of the transducer and the composite structure is shown in Figure 4-8.

The meshed assembly is then submitted to the FEA solver of ABAQUS while the mechanical parameters i.e. stress, strain as well as the electrical parameters such as electrical potential are derived at each stage. Due to the loading conditions and the dynamics of the assembly, the model is initially submitted to the standard analyser and then propagated to the dynamic/implicit analyser to simulate the cyclic movement of the model. As two parts are tied to each other, the order in which the two surfaces are specified on the "CONTACT PAIR" option is critical because of the manner in which surface interactions are discretised. For each node on the first surface (the "slave" surface) ABAQUS/Standard attempts to find the closest point on the second surface (the "master" surface) of the contact pair where the master surface's normal passes through the node on the slave surface. The interaction is then discretised between the point on the master surface and the slave node. The composite plate is used as the Master surface and the transducer as the slave surface in this simulation.
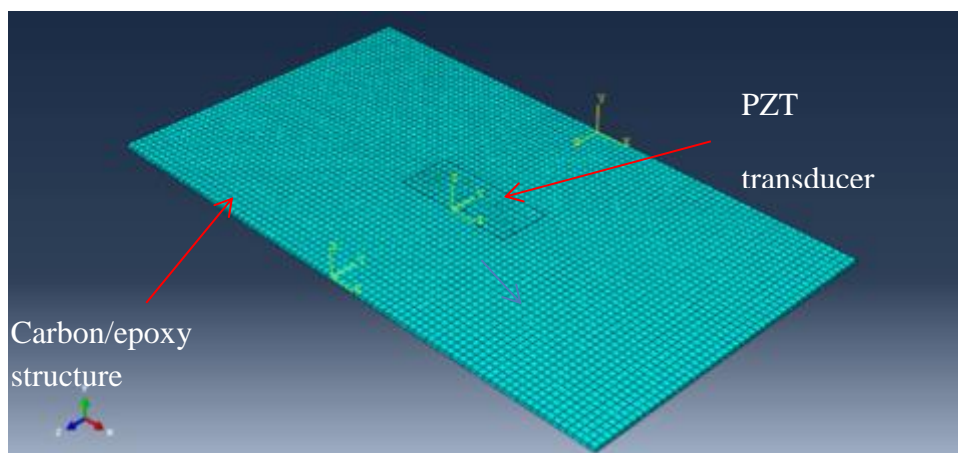
Figure 4-8: meshing configuration of simplified model of MFC transducer bonded on carbon/epoxy plate

The ABAQUS solver collects all the defined properties as well as boundary and loading conditions before applying them to the model. This step is very important as all the required information must be properly defined in order for the model to be solved properly. In addition, the submitted job can take from a few minutes up to a few days to solve based on the complexity of the simulation. For simplified model, the solving time is not as much as for detailed MFC model due to the more complex structure of detailed MFC modelling. While the processing time for simplified MFC model took 3 hours to complete using the personal laptop, the simulation of detailed MFC model took approximately 72 hours using the High Performance Cluster (HPC) service of RMIT University, as explained in the following sections.

To solve the simulation based on the analysis steps which are defined for the software, ABAQUS automatically subdivides a large time step into several smaller `increments' if it finds that the

solution is nonlinear. This process is completely automatic and ABAQUS will always take the largest possible time increments that will reach the end of the step and still give an accurate, convergent solution. Upon the completion of analysis, the status of submitted job changes from "Running" to "Completed" and the values for each increment are tabulated as shown in Figure 4-9. By default, ABAQUS/CAE writes the results of the analysis to the output database (*.odb) file. When the steps are created, ABAQUS/CAE generates a default output request for each step. A list of the selected variables written to the output database is given in Figure 4-10 and Figure 4-11.
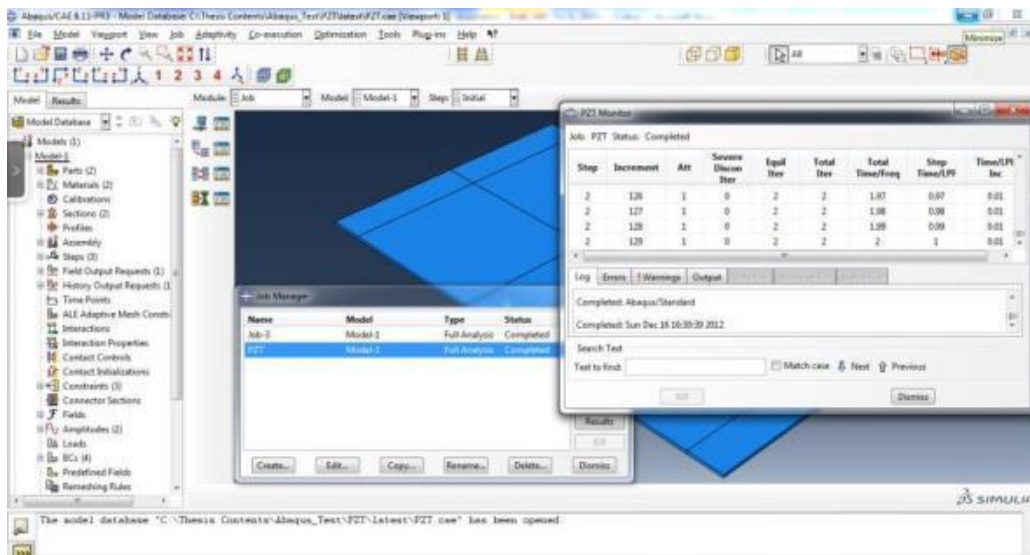
Figure 4-9: The solving process of bonded MFC (simplified model) on carbon/epoxy plate

Field Output Requests Manager is used to request the output of variables that should be written at relatively low frequencies to the output database from the entire model or from a large portion of the model. The History Output Requests Manager is also used to request output of variables which should be written to the output database at a high frequency form a small portion of the model.
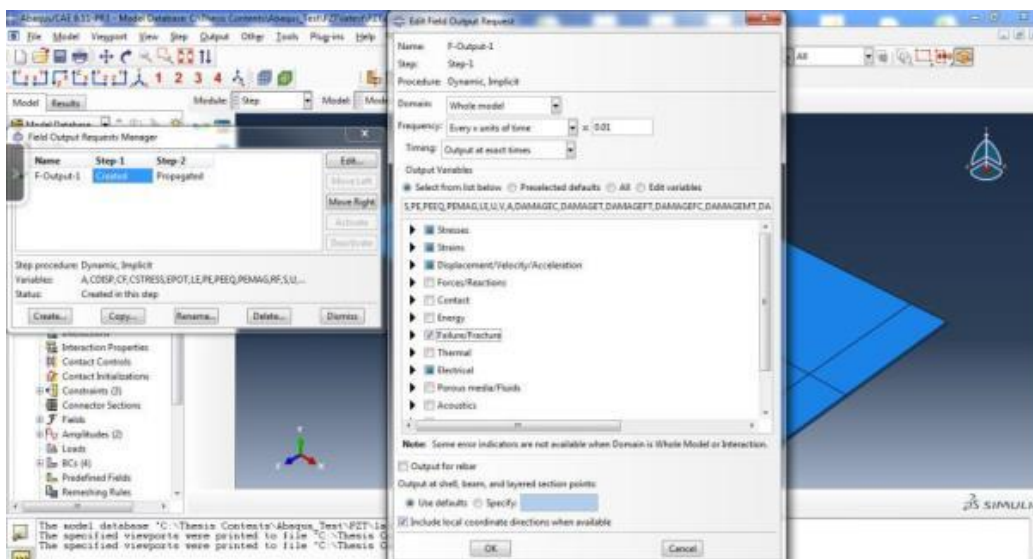
Figure 4-10: Defined field outputs
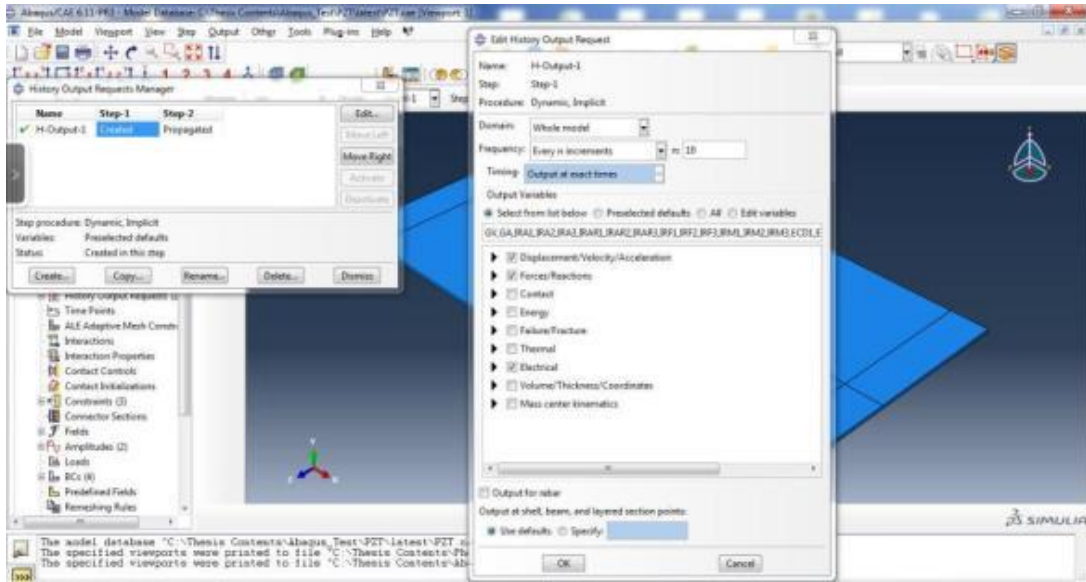
Figure 4-11: Defined history output

Upon completion of the submitted job, the calculated values for selected outputs are tabulated in the output file. Moreover, these outputs can be investigated through visualisation, which is done using the Abaqus/Viewer. Figure 4-12 shows the strain distribution in the assembly. The corresponding contour of the electric potential of bonded MFC (simplified model) is also shown in Figure 4-13.
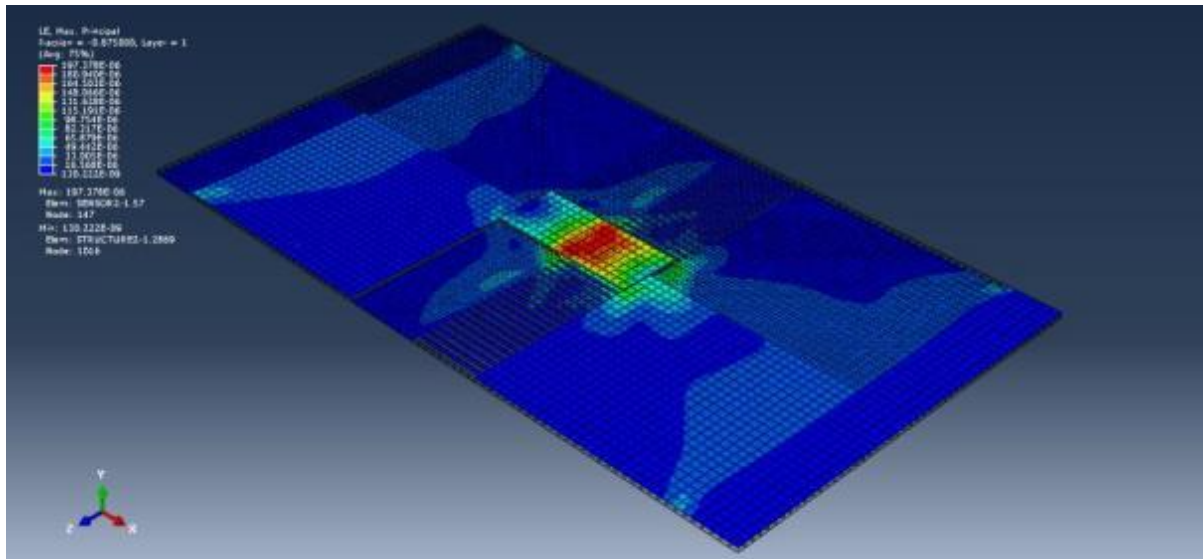
Figure 4-12: Logarithmic strain components at integration points
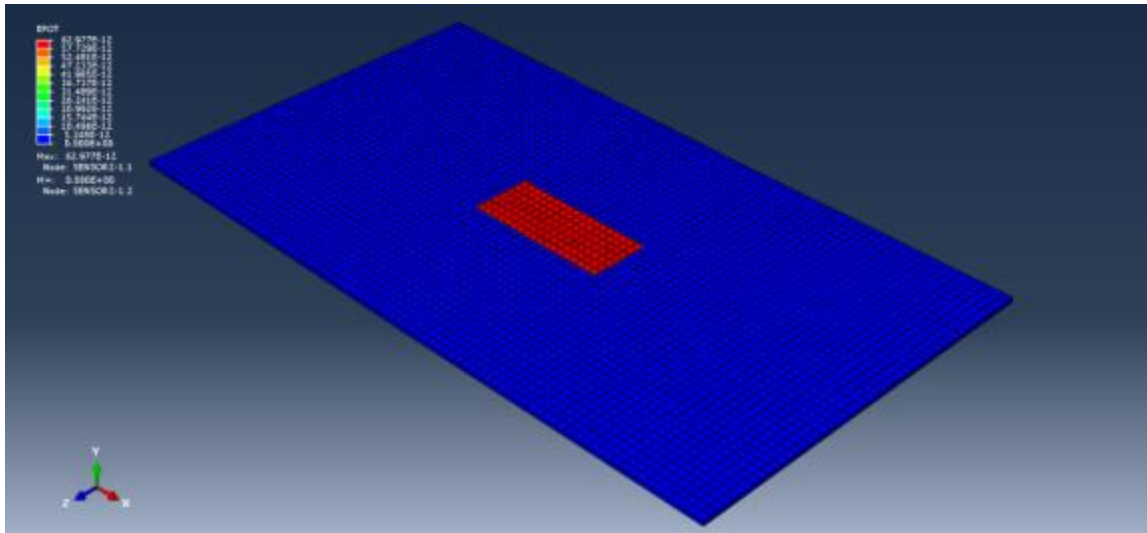
Figure 4-13: Electrical potential at nodes

4.5.3. Detailed MFC Sensor Modelling

The detailed MFC modelling process in both sensing and actuation modes are discussed in the next two sections. As previously mentioned, the main transducer used in this project is the Macro Fibre Composite (MFC) due to its various advantages over the traditional PZT transducers. Unlike simplified modelling, he detailed model of MFC has a complex structure with interdigitated electrodes and piezoelectric fibres attached to an epoxy layer as shown in Figure 4-14. As previously mentioned, the d_{33} MFC is used in this project. In d_{33} MFC, the poling direction follows a complex non uniform distribution according to the disposition of the interdigitated positive and negative electrodes aiming to yield an equivalent macroscopic poling direction parallel to the fibre length, so that longitudinal extension of the fibres can be obtained through the d_{33} constant.
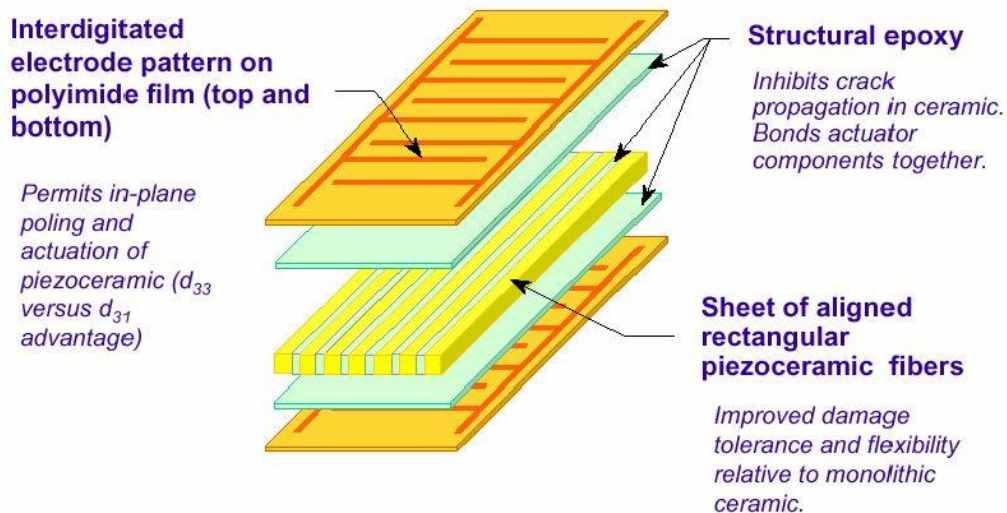
Figure 4-14: Schematic representation of longitudinal "d_{33}" Macro-Fibre Composite (Courtesy: www.smart-material.com)

In order to model this transducer, the piezoelectric fibres, interdigitated electrodes as well as the structural epoxy layers should be separately designed and appropriate material and element types should be assigned to each one of them. Finally, these parts should be tied to each other to represent the MFC transducer. The host structure to which the MFC transducer is bonded is identical to the one in simplified MFC modelling. However, extra properties were used for detailed MFC model due to its different structure. These properties are shown in Table 4-1.

Table 4-1: MFC Parts Geometric Properties

Part	Dimension	Unit
Kapton Thickness	25.40	µm
Acrylic Thickness	12.70	µm
Copper Thickness	17.78	µm
Fibre Thickness	127.00	µm
Fibre Width	355.60	µm
Copper Fibre Width	101.60	µm
MFC Thickness	250	µm

The main difficulty in modelling the MFC, as an alternative to monolithic piezoceramic patches, is that their behaviour may be much more complex since they are made of several different materials (piezoceramic fibres, epoxy matrix, electrode layers and protective layers). In light of this, it is necessary to understand and model their behaviour to be able to quantify or characterise their effective material properties and, thus, their effectiveness as distributed sensors and actuators. This requires a good understanding of their performance in actual testing, which is achieved from experimental work, and the use of this understanding to model the MFC parts and their interaction with each other in a way to simulate its actual behaviour. The piezo-fibres within the MFC generate electrical charge when the MFC undertakes mechanical strain. This electrical charge is then collected by interdigitated electrodes throughout the transducer and sent to the negative and positive leads accordingly. In cases where MFC is used as an actuator, the piezo-fibres are subject to induced electrical charge and generate the mechanical strain on MFC due to the converse effect of piezoelectric material. These interactions must also be properly addressed in the FEA modelling.

According to manufacturer data and actual measurements the active area for M4010-P1, which is the type of MFC used in the experimentation, is 40×10 mm^2 out of the total area of 54×22 mm^2. The active area of the MFC model is highlighted in Figure 4-15. Each part of MFC is first modelled and relevant properties as provided before being assigned to each part. The dimensions of each part are provided in Table 4-2. The ABAQUS model of piezo-fibres is provided in Figure 4-16. It can be seen from this figure that the fibres have a rectangular shape, which differs in MFC compared to the previous generation of piezo-fibre-based transducers such as PFC (piezoelectric fibre composite) with round-shape fibres.

Table 4-2: The dimensions of MFC components

Component	Dimension	Unit
MFC active area	$40\times10\times0.25$	mm
Kaptan thickness	25.4	µm
Acrylic thickness	12.7	µm
PZT fibre width	355.60	µm
PZT thickness	12.7	µm
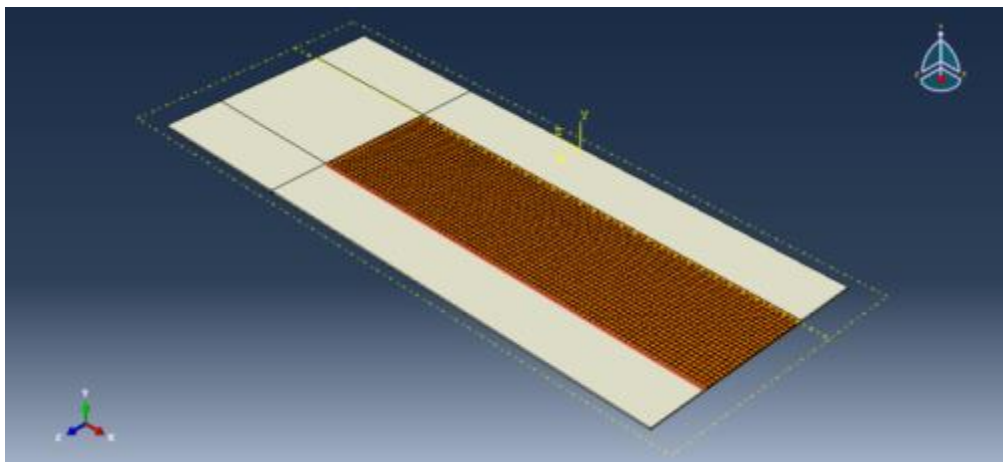
Figure 4-15: The active area of MFC transducer is shown in colour

The next important characteristic of MFC is its interdigitated electrodes. The interdigitated electrodes allow the electrical potential to form along the length of the fibre, therefore capitalising on the higher d33 piezoelectric coupling coefficient. As can be seen in Figure 4-17, one figure is set as a negative electrode whilst another figure is set as a positive electrode. In order to model the

electrode leads, the equation constraint is used to nominate 2 points as positive and negative leads on the model. These points represent the total charge on the positive and negative parts of the interdigitated electrodes respectively.
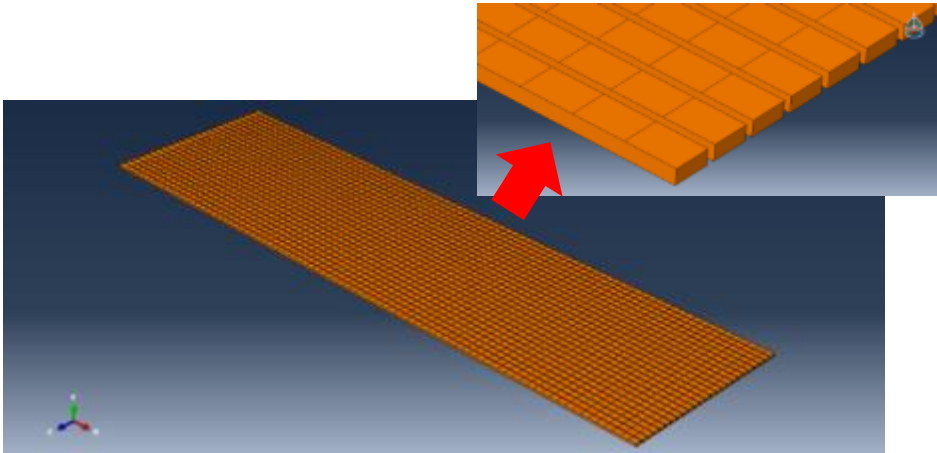
Figure 4-16: Piezoceramic fibres of MFC transducer modelled in ABAQUS

Once the model is completed, the relevant properties as well as element type are assigned to each part. The C3D8E element, which has piezoelectric characteristics, is assigned to piezo-fibres and the C3D8R element is assigned to other parts of the transducer. The meshing step in detailed MFC modelling is more complex and time consuming than the simplified model. This is due to the micro-scale structure of MFC. As there are various materials and element types within the MFC, the global meshing is not accurate enough to mesh the entire model. Therefore, the MFC geometry is divided into smaller regions using a partition toolset to refine the meshing. The comparison between the meshing before and after the refinement is provided in Figure 4-18.
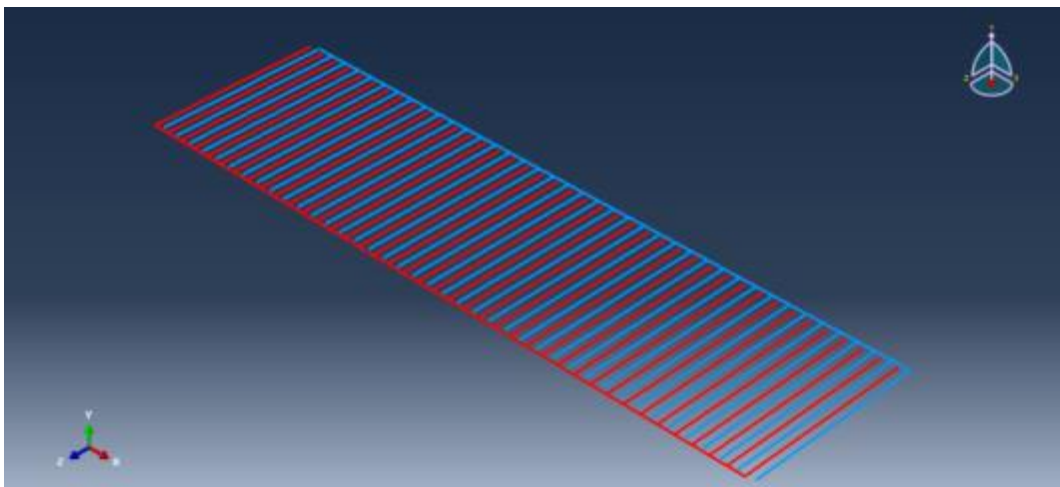
Figure 4-17: Interdigitated electrodes of MFC

119
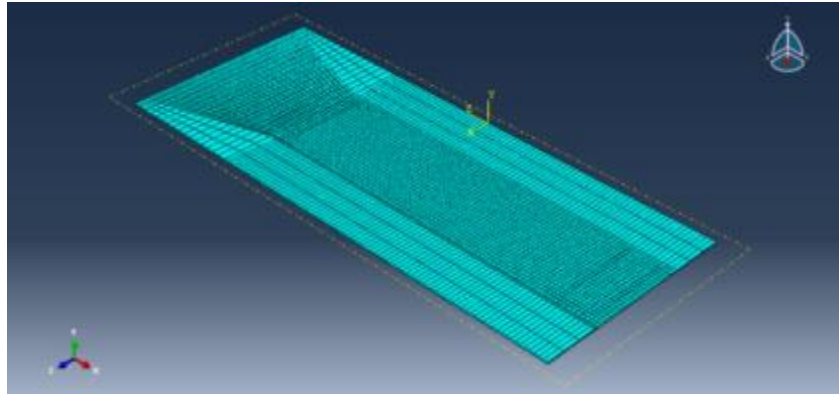
(a)
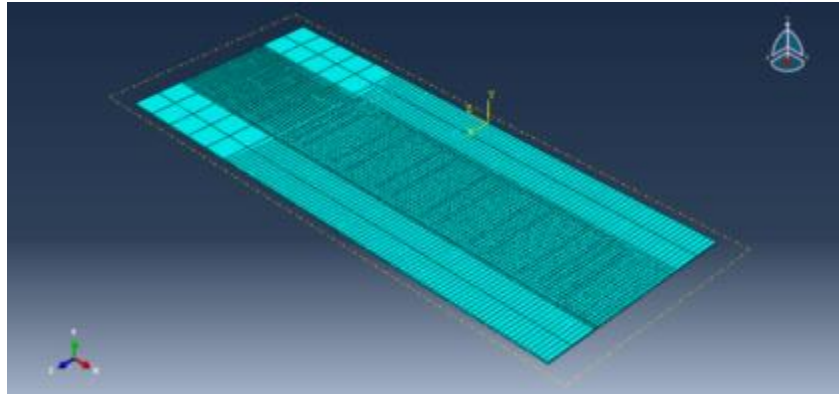
(b)

Figure 4-18: MFC Meshing; (a) before partitioning, (b) after partitioning

Following this, the MFC part is 'glued' to the master structure using the TIE constraints method, which results in joining the appropriate DOF of both bodies. In order to obtain correct and valid results, the mechanical impedance of the structure, including things such as the dynamics of the structure, should be coupled properly with the electrical impedance of the transducer. The electromechanical coupling factor, K_{33}, is used. This factor is 0.72 according to the manufacturer's datasheet. The mechanical boundary conditions are the same as the simplified MFC model and the same 3-point-bend loading configuration is applied to the assembly.

The constitutive equation of piezoelectric material is used by ABAQUS to simulate the behaviour of any piezoelectric transducer including MFC. As mentioned in previous sections, this set of equations is based on the assumption that the total strain in the piezoelectric transducer is due to the strain caused by the mechanical strain as well as the strain caused by the applied electric voltage. In other words, this equation describes the interaction of both mechanical and electrical phenomena. The constitutive equation can be written in different forms based on the application, although in FEM where the displacement is a primary factor, the so called force based formation is frequently used as shown in Equation 4-3.

Equation 4-3

$$\sigma = C^E \varepsilon + e^T E$$

$$D = e\varepsilon + \xi^\varepsilon E$$

where σ is the stress vector, C^E is the elastic stiffness matrix at the constant electric field (m^2/N), ε is the strain vector, e is the piezoelectric stress coefficient matrix (C/m^2) (T denotes matrix transposition), E is the electric field matrix (V/m), D is the vector of electric displacement (C/m^2) and ξ^ε is the matrix of dielectric permittivity coefficient (F/m) at a constant strain.

It can also be written in a displacement formulation where the stress is the primary factor. Two matrices of piezoelectric coefficients, d and e, are related to each other by a material constant matrix, as shown in Equation 4-4:

Equation 4-4

$$d = eS^E$$

The d and e coefficients are determined at not only the constant electric field and strain or stress respectively, but also at a constant temperature. However, in most of the applications it is assumed that the influence of temperature on the piezoelectric coefficient and other properties is negligible. The expansion of the above system of the equation in general form can be written as Equation 4-5:

Equation 4-5

$$
\begin{bmatrix} \varepsilon_1 \\ \varepsilon_2 \\ \varepsilon_3 \\ \varepsilon_4 \\ \varepsilon_5 \\ \varepsilon_6 \\ D_1 \\ D_2 \\ D_3 \end{bmatrix} =
\begin{bmatrix}
S_{11} & S_{12} & S_{13} & S_{14} & S_{15} & S_{16} & d_{11} & d_{21} & d_{31} \\
S_{21} & S_{22} & S_{23} & S_{24} & S_{25} & S_{26} & d_{12} & d_{22} & d_{32} \\
S_{31} & S_{32} & S_{33} & S_{34} & S_{35} & S_{36} & d_{13} & d_{23} & d_{33} \\
S_{41} & S_{42} & S_{43} & S_{44} & S_{45} & S_{46} & d_{14} & d_{24} & d_{34} \\
S_{51} & S_{52} & S_{53} & S_{54} & S_{55} & S_{56} & d_{15} & d_{25} & d_{35} \\
S_{61} & S_{62} & S_{63} & S_{64} & S_{65} & S_{66} & d_{16} & d_{26} & d_{36} \\
d_{11} & d_{12} & d_{13} & d_{14} & d_{15} & d_{16} & \xi_{11} & \xi_{12} & \xi_{13} \\
d_{21} & d_{22} & d_{23} & d_{24} & d_{25} & d_{26} & \xi_{21} & \xi_{22} & \xi_{23} \\
d_{31} & d_{32} & d_{33} & d_{34} & d_{35} & d_{36} & \xi_{31} & \xi_{32} & \xi_{33}
\end{bmatrix}
\begin{bmatrix} \sigma_1 \\ \sigma_2 \\ \sigma_3 \\ \sigma_4 \\ \sigma_5 \\ \sigma_6 \\ E_1 \\ E_2 \\ E_3 \end{bmatrix}
$$

The factors on the main diagonal represent mechanical and electrical effects which are related to each other through the parameters outside the main diagonal (d_{ij}). These values are used to couple the mechanical and electrical characteristics in various situations. However, the above system equation can be significantly simplified for materials with a 4mm crystalline class such as PZT and MFC (Wiley et al., 2007). This is related to the symmetry of elastic, electric, and electro- mechanic

properties. In addition, as the d_{33} MFC is used in this research project the ANSI IEEE 176 standard states that the device is poled along the three axes and that the piezoelectric material is transversely isotropic. Therefore the constitutive equation can be simplified, as shown in Equation 4-6:

It should be noted that all of the data given by the manufacturer are for single couple of electrodes and should be multiplied by the number of sections in order to obtain the effective value. The properties used to model the MFC transducer in ABAQUS are provided in Table 4-3.

Equation 4-6

$$
\begin{bmatrix} \varepsilon_1 \\ \varepsilon_2 \\ \varepsilon_3 \\ \varepsilon_4 \\ \varepsilon_5 \\ \varepsilon_6 \\ D_1 \\ D_2 \\ D_3 \end{bmatrix} = \begin{bmatrix} S_{11} & S_{12} & S_{13} & 0 & 0 & 0 & 0 & 0 & d_{31} \\ S_{21} & S_{11} & S_{13} & 0 & 0 & 0 & 0 & 0 & d_{31} \\ S_{31} & S_{31} & S_{33} & 0 & 0 & 0 & 0 & 0 & d_{33} \\ 0 & 0 & 0 & S_{55} & 0 & 0 & 0 & d_{15} & 0 \\ 0 & 0 & 0 & 0 & S_{55} & 0 & d_{15} & 0 & 0 \\ 0 & 0 & 0 & 0 & 0 & 2(S_{11}-S_{12}) & 0 & 0 & 0 \\ 0 & 0 & 0 & 0 & d_{15} & 0 & \xi_{11} & 0 & 0 \\ 0 & 0 & 0 & d_{15} & 0 & 0 & 0 & \xi_{22} & 0 \\ d_{13} & d_{13} & d_{33} & 0 & 0 & 0 & 0 & 0 & \xi_{33} \end{bmatrix} \begin{bmatrix} \sigma_1 \\ \sigma_2 \\ \sigma_3 \\ \sigma_4 \\ \sigma_5 \\ \sigma_6 \\ E_1 \\ E_2 \\ E_3 \end{bmatrix}
$$

The assembly of MFC bonded to a composite structure with assigned elements and material properties is finally meshed and submitted to the FEA analyser for processing. Due to the complex nature of MFC, which requires a very fine meshing as well as a much smaller increment compared to PZT, the RMIT High Performance Computer Cluster (RMIT-HPC) is used to analyse the assembly. In order to export the ABAQUS model into a cluster, a code needs to be written using Linux, as set out below:

```
#!/bin/bash
#PBS -l nodes=8:ppn=8
#PBS -l walltime=72:00:00
#PBS -N MFC
#PBS -j oe
#PBS -m abe
cd $PBS_O_WORKDIR
. /etc/profile
module load abaqus
abaqus job=MFC input=MFCT.cae double cpus=64 standard_parallel=all mp_mode=mpi
interactive
```

Table 4-3: The MFC properties

Parameter	Value
MFC piezoelectric constant, d_{33}	3.74E-10 C/N
MFC piezoelectric constant, d_{31}	1.70E-10 C/N
MFC dielectric constant	1.58E-8 F/m
MFC density	7500 Kg/m^3
Epoxy elastic constant	E=0.1GPa, ν=0.38
Epoxy density	2200Kg/m^3
MFC elastic constants	E_1=30.34GPa, E_3=15.86 GPa, ν_{13}=0.31, G_{13}=5.52GPa
Voltage constant g_{33}	2.55E-2 Vm/N
Coupling factor K_{33}	0.72

This code defines the input file for the cluster, and it also allocates the number of required nodes and processors as well as the maximum duration of analysis. For this simulation, the name of the defined job is "MFC", and MFCT.inp is imported into the cluster along with the above codes. In addition, a total number of 64 cpus are booked to run the job in parallel, for the maximum duration of 72 hours.
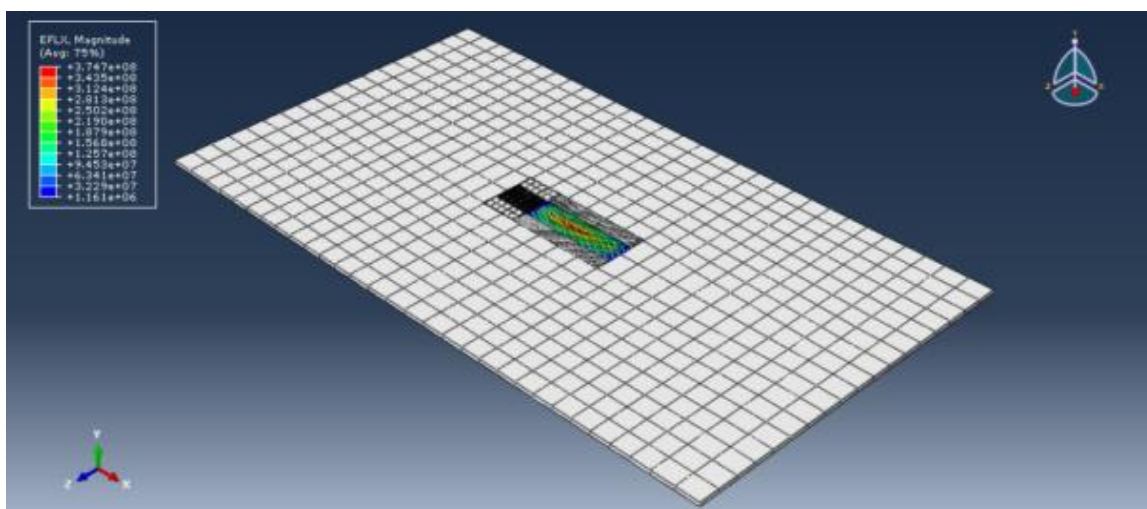
Figure 4-19: Strain contribution of MFC

This code is then imported into an SSH software program such as PUTTY along with the input file of the model which is created in ABAQUS. The .inp file contains all the required details of the model for the processing stage. After complete analysis of the submitted job, the result is provided as a .cae file in PUTTY, which is then exported to ABAQUS for post-processing and visualisation. Moreover, full details regarding the processing of the submitted job and possible errors and

warnings are saved in a .log file, which is stored in the cluster and can be viewed at any time during the process. In addition, the status of the submitted job can be continuously checked via the ID number which is provided for each submitted job. The strain distribution in the assembly is shown in Figure 4-19. The corresponding contour of electric potential is also shown in Figure 4-20.
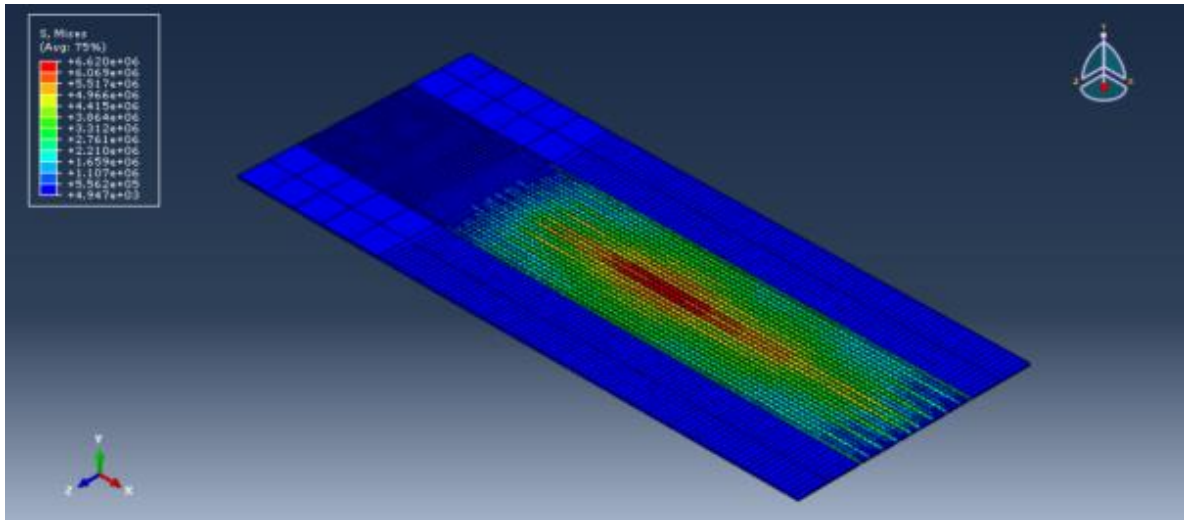
Figure 4-20: The corresponding contour of electric potential

4.5.4. Comparison of Simplified and Detailed FEM Simulation of MFC

As previously mentioned, one of the main reasons to model the MFC through both simplified and detailed approaches is to clarify the necessity of going through the complex micro-scale modelling of MFC instead of the simplified analysis which is currently available in the literature. The FEM simulation is one of the main tools which can be used to evaluate the performance of MFC transduce, especially when it becomes degraded. Therefore, it is extremely important that the FEM simulation of MFC has the same characteristics and responses as actual MFC. Furthermore, the existing assumption in most of the existing MFC simulations is to simplify the complex structure of MFC components such as interdigitated electrodes and piezo-fibres. Also, the load bearing parts of MFC such as Kapton layers, Acrylic layers and epoxy separators between the piezo-fibres are mainly eliminated from current MFC simulations. Although these simplifying assumptions reduce possible errors caused by the complexity of the simulation, they significantly reduce the accuracy of the simulation when compared to actual MFC performance.

The initial comparison of the strain distribution and contour of electric potential for simplified and detailed MFC simulations confirms their difference under similar loading and boundary conditions. As shown in Figure 4-21, the strain calculation by a detailed MFC sensor simulation approach shows around a 90% magnitude match with experimental results, while the simplified

approach has less than 20% of the experimental measurements. Also, the detailed MFC simulation has over a 90% match of voltage with experimental measurements, while the simplified simulation has around 60% of relevancy. This comparison is shown in Figure 4-22.
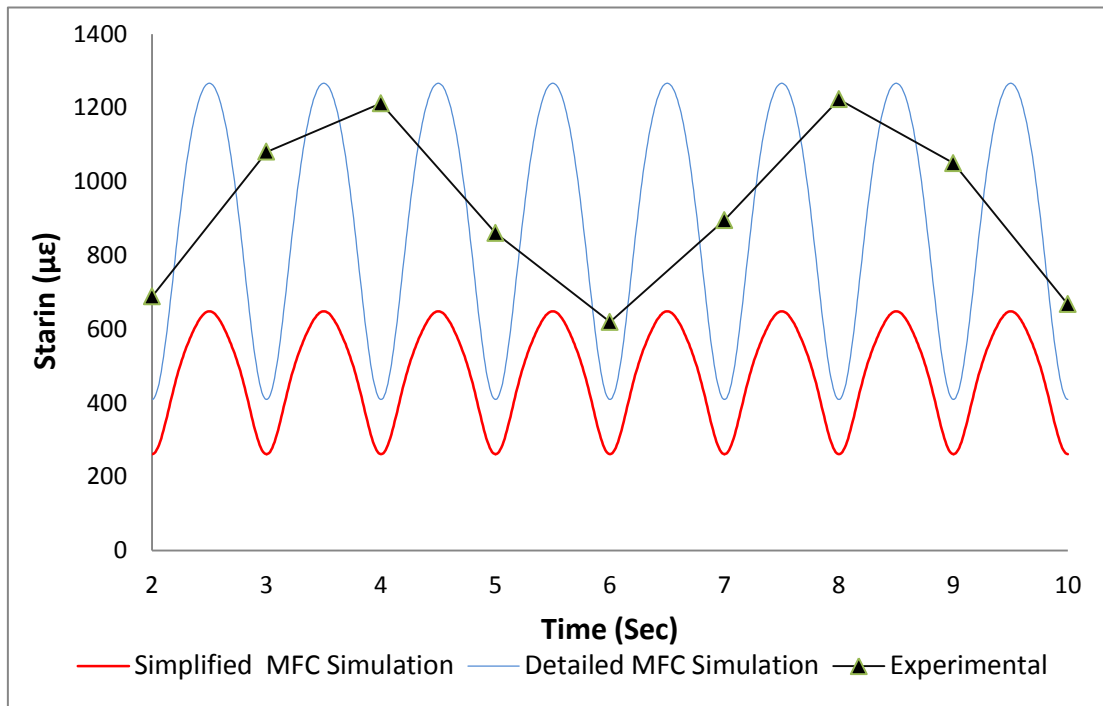
Figure 4-21: Comparison of strain calculations by simplified and detailed MFC simulations
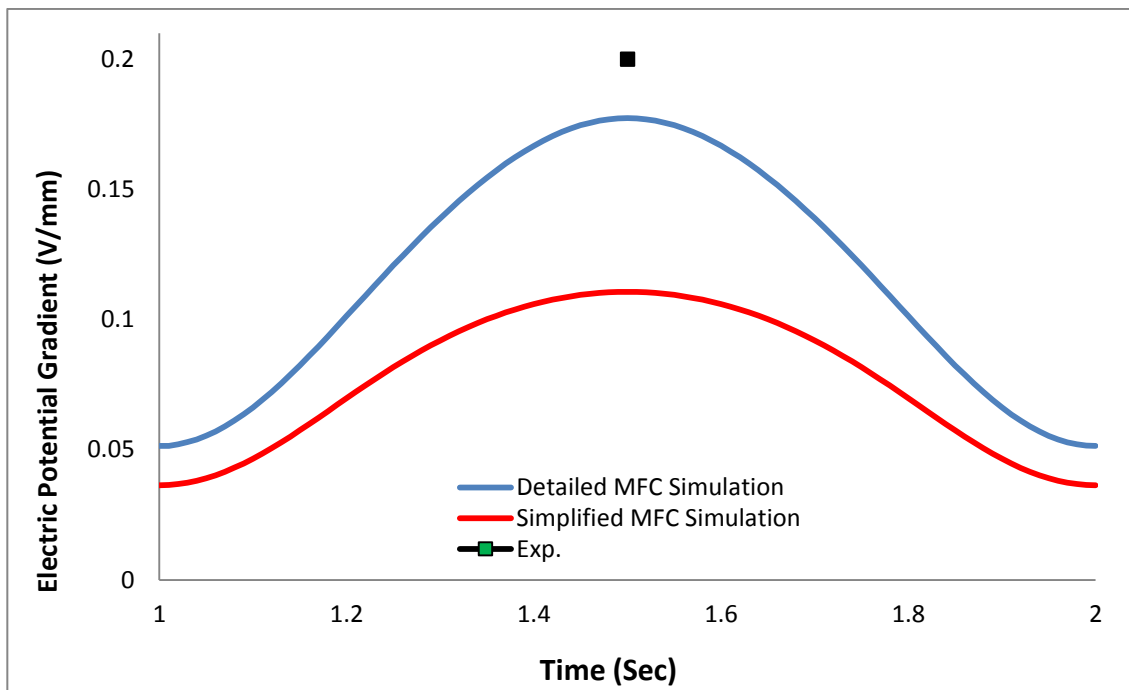
Figure 4-22: Comparison of electric potential calculations by simplified and detailed MFC simulations

4.5.5. MFC Actuator Modelling

The next approach to the performance of the MFC transducer is when the MFC is activated with an induced excitation voltage. In terms of FEM simulation, the same modelling procedure as previously explained can be used to model the active MFC transducer (actuator) bonded to the carbon/epoxy structure. However, the loading and boundary conditions and the analysis procedure need to be changed, as described below.

The coupled-field feature of ABAQUS software is used for this purpose. This feature was initially applicable to thermo-elasto-dynamic analysis only. However, due to the advantages of this feature, it was later developed for more complex coupled-filed situations where the elastic, dynamic and electrical fields are coupled which is the case for piezoelectric devices. The new capabilities of couple-field feature are currently embedded in software packages like ABAQUS and ANSYS. The aim of this section is to illustrate the application of FEM coupled-filed feature to determine the electromechanical impedance characteristics of MFC transducer and evaluate the experimental measurements accordingly. First, the MFC transducer is modelled through coupled-field FEM approach and voltage constraints are applied to the interdigitated electrodes. The time-harmonic analysis is run and the electrical charge output field is calculated in accordance with frequency. In the harmonic analysis, excitation sinusoidal voltage is applied to the nodes of interdigitated electrodes of MFC. This signal then sweeps the designated frequency range to the MFC electrodes. This is similar to the operation of impedance analyser in measuring electromechanical impedance. Once the MFC got excited via induced voltage (electrical DOF), the relevant current flows through the nodes defined on the MFC interdigitated electrodes. The nodes at positive and negative electrodes have their voltage DOF coupled to a common master node in order to simulate the existence of electrode leads. The electric current is then calculated from the electric charge data. The electromechanical impedance of MFC transducer, Z (w), is essentially the ratio V (voltage)/I (current) and therefore the ratio of voltage constraint of MFC model to the current, which is calculated from the electric charge, can be used to numerically calculate the electromechanical impedance. A comparison of the simulated E/M impedance results with the measured experimental data is also provided.

One of the important requirements for coupled-filed analysis is selecting appropriate coupled-filed element which can deal with both fields. In this research, the selected element should have both mechanical and electrical features. In other words, the stress field should be coupled with the electric field in each element in a way that the change in one filed cause the change in another field. For this purpose, the 3-D brick element which is a coupled-filed element and has 8 nodes

with up to 6 degrees of freedom at each node is selected. This element is suitable for mechanical-electrical analysis. Furthermore, this element may have one extra degree of freedom which corresponds to electric field. To represent the actuation mode, there is a reaction force for each degree of freedom. These reaction forces are F_X, F_y, and Fz for X, Y, Z DOFs, respectively. Also, the electrical reaction which is related to the voltage DOF is called electric charge (Q). The electrical reaction Q is applied to represent electrical charge on the MFC electrodes. To determine the electrical impedance Z, the current and voltage are calculated. The current I is calculated as $I=j\omega\sum Q$, where ω is the operating frequency, j is $\sqrt{-1}$, and $\sum Q$ is the sum of electrical reaction load at nodes and the electrical DOF is used to apply the electric voltage (V) to the coupled-filed elements. The modelling of MFC bonded to the composite structure is useful when it comes to understanding the electromechanical coupling between the mechanical responses of the structure and the complex electrical response of the transducer.

The excitation of MFC may cause the resonances in the forms of electromechanical or mechanical to become fairly large. While the mechanical resonances are similar to the ones for any elastic structures, the electromechanical resonances are specific to piezoelectric materials. In fact, the electromechanical resonances occur when the mechanical and electrical properties of a piezoelectric material are coupled under electric excitation. This excitation generates the electromechanical responses (mechanical vibration and a change in the electric admittance and impedance). The electromechanical coupling between the MFC and the host structure caused the electrical resonances of MFC to be associated with the mechanical impedance of the structure. In piezoelectric transducer, the mechanical responses at electrical resonances are very large due to the fact that the mechanical resonances transfer energy from an electrical into a mechanical response.

As the purpose of this research is to delineate the structural damage from transducer damage, all 6 samples with various damage conditions which were manufactured and tested before must be simulated whilst the results should be compared with experimental measurements. With this in mind, the existing MFC model is modified and relevant damage is also simulated in each sample. The schematic overview of the damage scenarios in all 6 samples is provided in the "Manufacturing Chapter." There are two types of damage in the sample: the first is a 2×2 cm^2 Teflon plate which is embedded during the manufacturing process to represent delamination in the structure. This Teflon is placed either at the centre of the carbon/epoxy plate or 100 mm from the centre of the structure. In addition, a 2 mm hole is induced at the centre of the MFC during the manufacturing process to represent the transducer damage. The schematic overview of these damage types is shown in Figure 4-23.
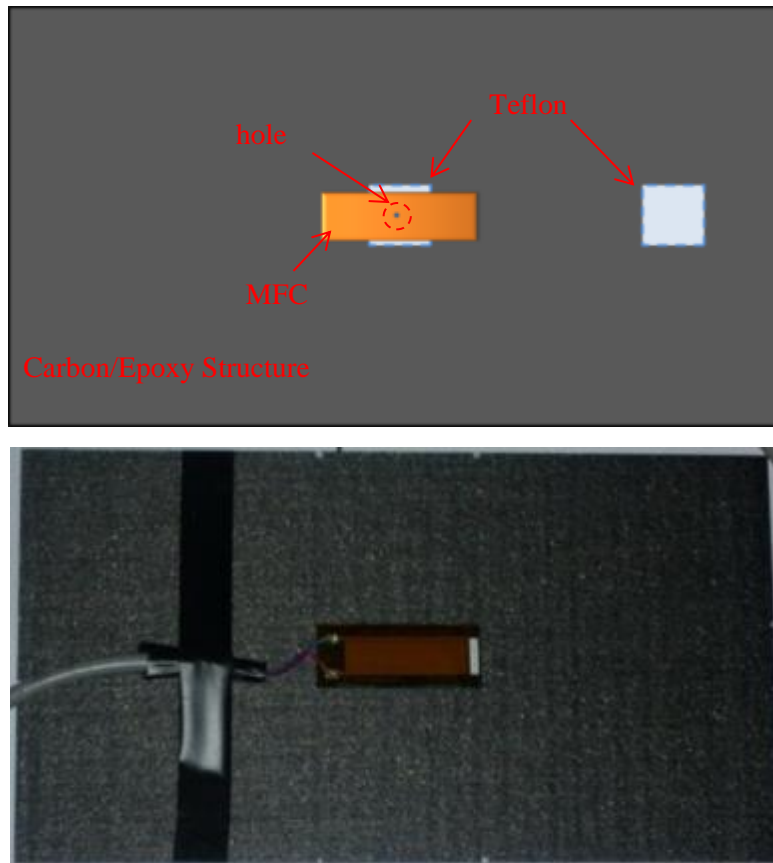
Figure 4-23: Structural and Transducer damages

4.6. Simulation of the Structural Damage

In order to introduce damage to the sample, a feature called "XFEM" in ABAQUS software is used to define the crack, as explained in the following section:

4.6.1. eXtended Finite Element Method (XFEM)

The eXtended Finite Element Method is a partition of the unity based method in which the classical finite element approximation is enhanced by means of enrichment functions. The XFEM method was first introduced by Belytsckho et al. (1999). Their work presented a method for enriching finite element approximation in such a way that crack growth problems can be solved with minimal re-meshing. It represents a milestone in XFEM history. Many improvements have been introduced over recent years which make the XFEM a well suited technique for 3 dimensional crack modelling. However, there remain a few limitations due to the shortage of commercial codes which have implemented this method. Nevertheless, seeing the enormous capabilities provided by the XFEM implementation, among which the most important is undoubtedly that the mesh need not conform exactly to the crack surfaces, several attempts have been made throughout the years to include them in both stand-alone codes and multi-purpose commercial FEM software (Gigliotti, 2012).

ABAQUS was the first software system to have this functionality, and it still has one of the most complete user-ready versions of XFEM which is used in this research. The XFEM implementation in Abaqus/Standard is based on the phantom nodes method. This method is based on the superposition of phantom nodes to the standard ones to reproduce the presence of the discontinuity. Roughly speaking, phantom nodes are tied to their corresponding real nodes when the enriched element is intact. This situation holds until the element is not cut by a crack; as soon as the element is cracked, it is divided into two separate parts, each of which includes both real and phantom nodes (Figure 4-24).
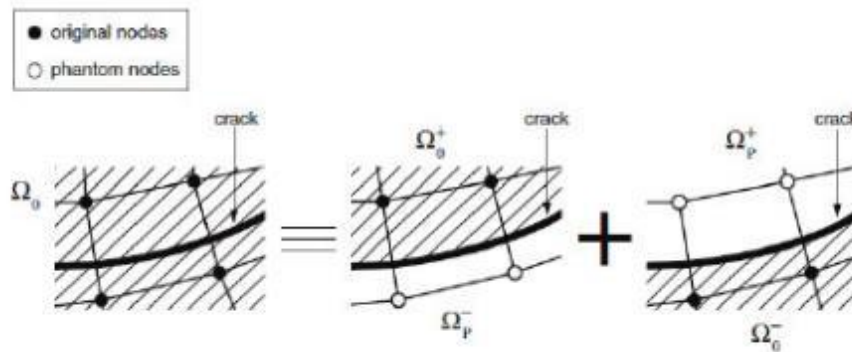
Figure 4-24: Phantom nodes method (Ke et al., 2012)

In particular, the separation procedure occurs when the equivalent strain energy release rate exceeds the critical strain energy release rate at the crack tip in an enriched element. Once this condition has been satisfied, each phantom node is no longer restrained to its corresponding real one, and therefore, they can freely move apart.

The first step in simulating damage in the structure is to create the damaged part with identical specifications to those of the experimentally induced damage. For this purpose, the shell base feature is used to create a rectangle with the same dimensions as the Teflon. This part is then translated to the centre of the structure or the side of the structure according to the experimental modelling details. Finally, using the XFEM feature which is available in the "Special menu" of ABAQUS, the created rectangle is defined as a crack location and the structure is defined as a crack domain. The structural damage at the middle and side of the structure is highlighted in Figure 4-25 and Figure 4-26 respectively.
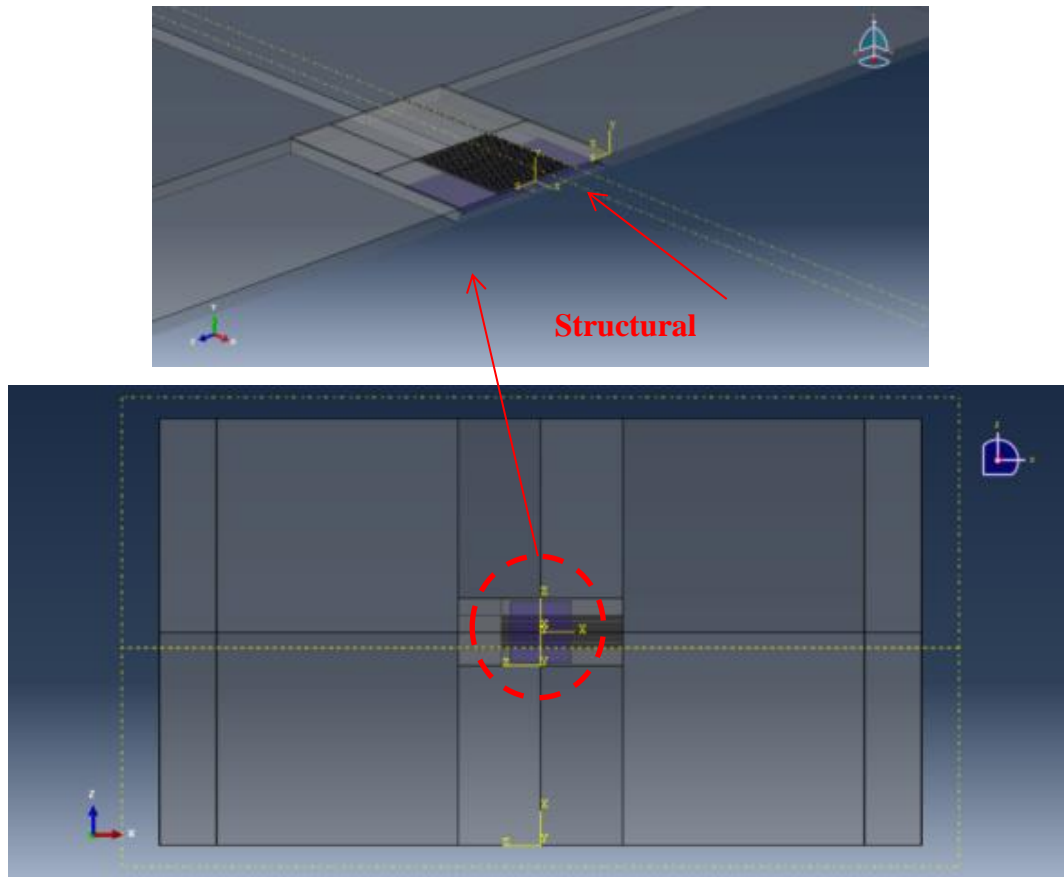
Figure 4-25: Simulated structural damage at the middle of structure
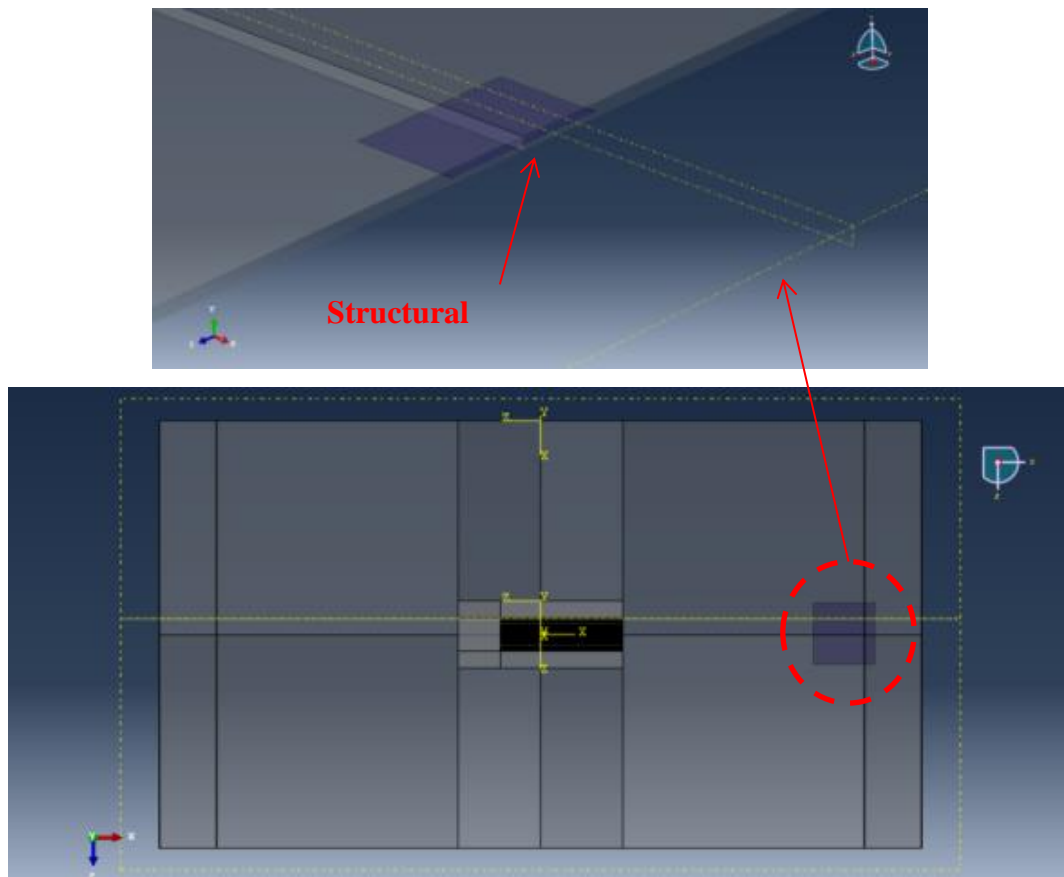
Figure 4-26: Simulated structural damage at the side of structure

To make sure that the introduction of damage to the structure does not modify other steps of simulation, all of these steps and the loading and boundary conditions are reviewed prior to the submission of the job for analysis.

4.7. Simulation of Transducer Damage

Unlike the structural damage, the induced damage in the transducer cannot be simulated through the XFEM feature due to the limitations of this feature. The XFEM is still limited to specific element types, and it is observed in our investigations that the simulation of damage in the transducer via XFEM generates considerable error. With this in mind, an alternative method is used to simulate the damage in the transducer model. This method is based on the traditional way of introducing damage, which is to use a gap with identical dimensions to represent the crack or delamination. As the induced damage in the MFC transducer is essentially a hole with a diameter of 2 mm and a depth of 0.1 mm, a cylinder with similar dimensions is created and translated to the centre of the transducer. This cylinder is then subtracted from the transducer using part tools, which generates a transducer part with a gap at its centre. Upon the completion of this step, all of the defined properties are re-allocated to the transducer and it is re-meshed. The transducer with induced damage is highlighted in Figure 4-27.
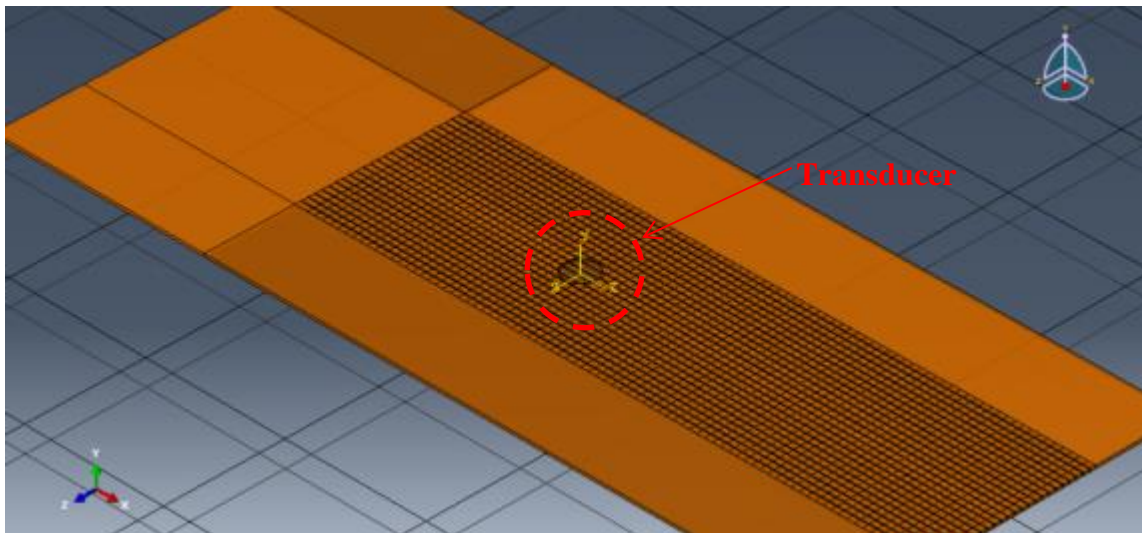
Figure 4-27: Simulated transducer damage

Finally, these damage types are introduced to the structure and/or transducer to represent all 6 samples used in experiments as listed below:

- **HSEN_HST:** Healthy Sensor is bonded to the healthy structure
- **HSEN_DST_MIDDLE:** Healthy sensor is bonded to the damaged structure where damage is at the middle of the plate (close to sensor)

131

- **HSEN_DST_SIDE:** Healthy sensor is bonded to damaged structure where damage is at the side of the plate (far from sensor)
- **DSEN_HST:** Damaged sensor is bonded to healthy structure
- **DSEN_DST_MIDDLE:** Damaged sensor is bonded to damaged structure where damage is at the middle of the plate (close to sensor)
- **DSEN_DST_SIDE:** Damaged sensor is bonded to damaged structure where damage is at the side of the plate (far from sensor)

The excitation voltage is introduced to the master nodes which represent negative and positive electrode leads. As previously mentioned the electromechanical impedance is a frequency dependent parameter and must be calculated in a frequency range. Therefore, the harmonic analysis is used to define excitation voltage whilst the same frequency range as the experiments, 20-100 KHz, is defined as a new analysis step (Figure 4-28).
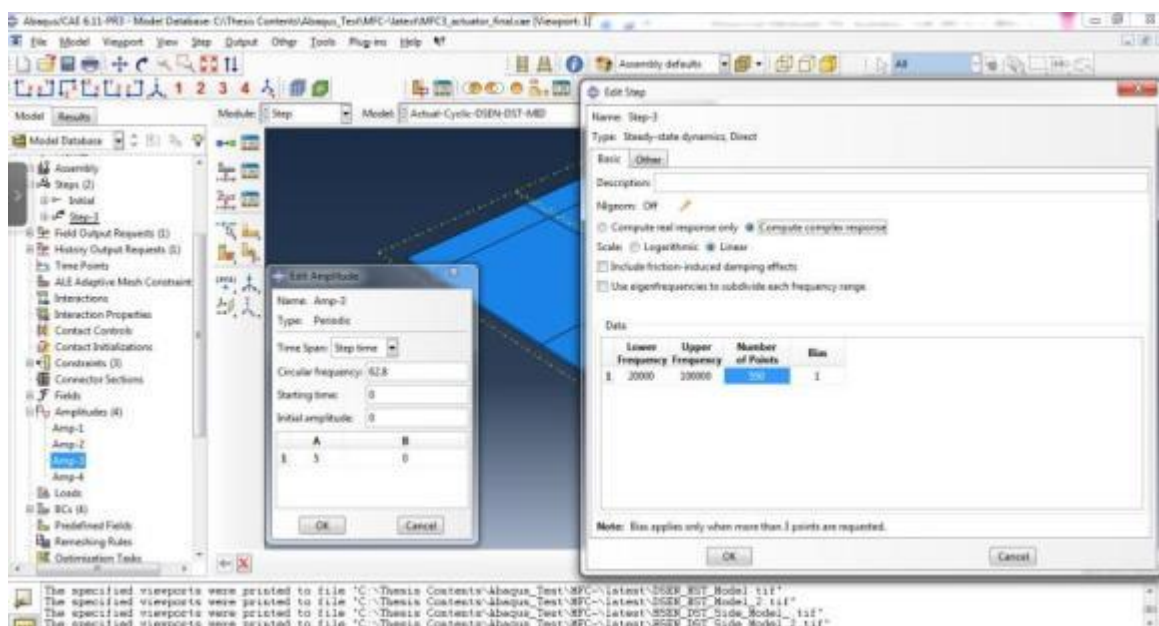
Figure 4-28: The analysis setup for MFC actuator

Furthermore, 3 field outputs need be calculated by the ABAQUS Solver, namely CECHG (Concentrated electrical nodal charge at nodes), EPOT (Electrical potential at nodes), and RCHG (Reactive electrical nodal charge at nodes). These parameters are then used to calculate the electromechanical impedance as described previously. Once the job is completed the plot contours of each field output can be observed, as shown in Figure 4-29 and Figure 4-30. However, as the main objective in this FEM simulation is to confirm the validity of our experimental results, the XY data tool is used to tabulate the calculated parameters against the designated frequency range.

These data are then exported to excel using the ABAQUS export plugin, and the relevant equations (refer to MFC actuator section) are used to plot the electromechanical impedance of MFC in the frequency range of 20-100 KHz.
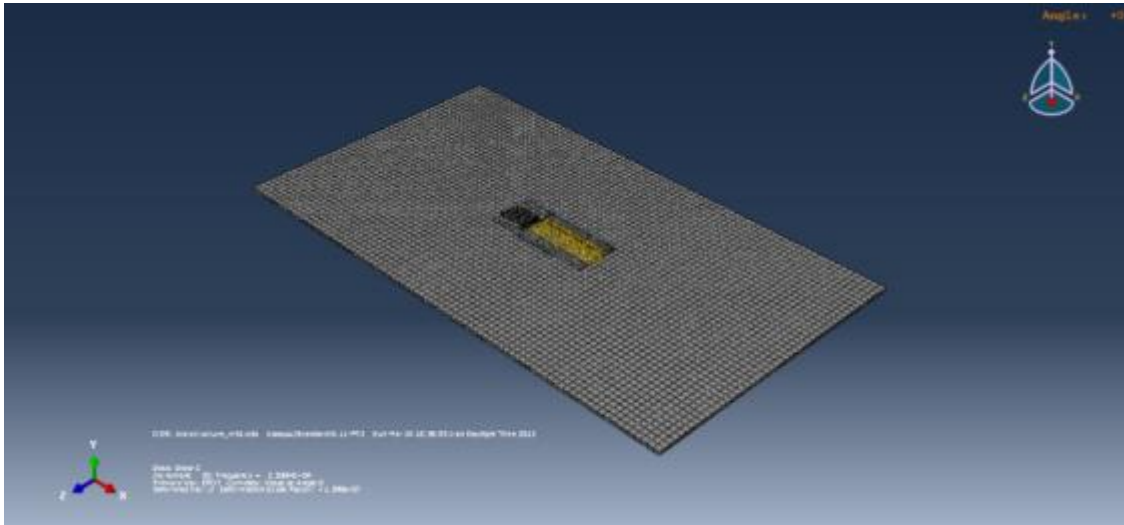
Figure 4-29: EPOT of DSEN_HST sample
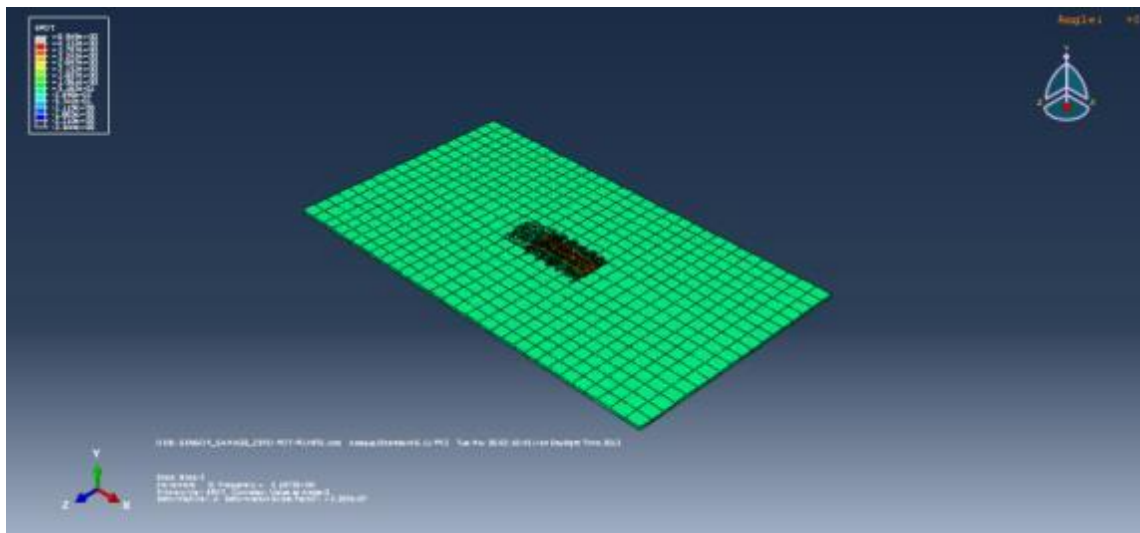
Figure 4-30: EPOT of HSEN_DST_MIDDLE sample

These plots and the comparison between the experimental measurements and FEM calculations of the MFC electromechanical impedance are provided in Chapter 7.

4.8. Summary

In this chapter, the passive (sensor) and active (actuator) behaviour of a bonded Macro Fibre Composite (MFC) transducer on a carbon/epoxy composite structure is numerically investigated using the FEM software package, ABAQUS. In order to confirm the requirement for a detailed and accurate simulation of MFC, which is complex and in micro-scale, a simplified simulation

approach is also investigated In the simplified approach, the MFC structure is simulated by assuming that the electrodes are solid plates at two sides of the MFC transducer, and that the piezoceramic fibres are a solid plate at the middle. This is very similar to the structure of the PZT transducer and is very common across most of the studies previously conducted on the numerical simulation of MFC. Using a detailed approach, the MFC is modelled and simulated based on the actual structure of its components such as interdigitated electrodes and piezoceramic fibres etc. The simulation of MFC in this approach is relatively complex in terms of modelling the components, accurate meshing and defining the proper interaction between IDEs and piezo-fibres. While the solving process of the model in the first approach takes a few minutes to complete using a high performance university PC, the accurate model of MFC (second approach) is solved using the High Performance Cluster (HPC) service of RMIT University and takes 72 hours to complete. The comparison of the results of these two approaches shows a clear difference which is investigated in this chapter. To identify the most reliable approach, the strain outputs and electric potential of both models are compared with the strain measurements. This comparison showed more than a 90% match between detailed MFC simulations results and experimental measurements while this number is only around 60% for the simplified approach. Therefore, the focuses for the remaining chapters is on the detailed simulation approach.

For the MFC sensor, the identical loading and boundary conditions are defined with a similar 3-point-bend configuration using ABAQUS. For MFC actuator modelling, a relatively new feature of ABAQUS called coupled-field is used to simulate the interaction between elastic, dynamic, and electrical fields which takes place in the MFC actuator. The nodal charge (Q) and applied voltage (V) of the model are set to be calculated as the Q can be used to calculate current (I) and V/I is equal to the electrical impedance which will be used to validate the experimental results in Chapter 7. In order to investigate the behaviour of the MFC transducer and carbon/epoxy structure when they are damaged, the eXtended FEM (XFEM) feature is used to simulate the delamination in the carbon/epoxy structure as well along with a hole in the MFC transducer. The characteristics of these induced damages are selected based on the experimental modelling in order to make the comparison between the experimental and modelling results possible. The original model with intact MFC and structure is modified by inducing damage in the MFC and/or the carbon/epoxy structure. Finally, 6 models are simulated and solved with various MFC/structure damage statuses. These models will be used to validate the results of the electromechanical impedance-based technique in Chapter 7.

CHAPTER 5 The Fatigue Performance of Degraded Piezo-Fibre-based Transducer

5.1. Introduction

In this chapter, the performance and properties of the Piezo-Fibre-bases transducer are investigated. As previously mentioned, the purpose of this research is to offer a reliable delineation technique which can be used to produce a self-diagnostic SHM system with the ability to detect not only the structural damage but also the damage related to the SHM system itself. Therefore, it is vital to have a comprehensive understanding of the performance and characteristics of the transducer and its electrical properties. There are two major categories which need to be explored in order to address this issue. Firstly, the electrical properties of the transducer and the impact of possible damage/degradation on each property should be clearly identified. Secondly, the sensitivity of these properties to structural damage should also be explored. In this chapter, an assessment is carried out to quantify the degradation in the electric characteristics of piezo-fibre-based transducers, under fatigue loading configuration. Changes in the electrical properties of these transducers such as capacitance and inductance have been measured and investigated, and details of this are provided in the following sections.

Structural Health Monitoring (SHM) has emerged as a feasible method with which to improve the safety and reliability of structures, thereby reducing their operational cost (Blackshire & Cooney, 2006). SHM technology is perceived as a revolutionary method of determining the integrity of structures and involves the use of multidisciplinary fields including sensors, materials, system integration and signal interpretation (Wilkie et al., 2000). However, as the application of SHM systems to monitor the status of the MFS becomes increasingly common, it has never been more important to determine the durability, reliability, and reparability of the SHM systems. In this context, the sensors or the sensor network must possess sufficient reliability so that they do not require replacement at intervals less than the economic lifetime of the components they are monitoring. The aim of this chapter is to investigate the behaviour of fibre-based piezoelectric sensors under fatigue loading by characterising their electrical properties over time.

5.2. Piezo-fibre-based Transducers

Piezoceramic fibre composite (PFC) actuators and sensors offer many advantages over conventional monolithic piezoceramic devices. PFC is composed of piezoelectric fibres, polymer and interdigitated electrodes (IDE) as shown in Figure 5-1. Among the structural components, piezoelectric fibres are active whilst the polymer is passive. The interdigitated electrodes are on both surfaces of the composite, which is a characteristic of the PFC. Developed by the NASA-Langley Research Centre, the Macro-Fibre Composite (MFC) actuators and sensors appear to be a more robust version of the PFC. The MFC patch has spawned great interest in the commercial and academic community as a tool in multiple engineering applications (Kessler et al., 2005). While the MFC's characteristics render it a singularly useful device, only limited characterisation and modelling research on the MFC can be located in the literature. There is a lack of understanding with regard to its long term durability and degradation under static and fatigue loading, as well as its electrical properties (Lloyd, 2004).

The MFC transducer consists of three primary components; active piezoceramic fibres aligned in a unidirectional manner, interdigitated electrodes (IDE), and an adhesive polymer matrix. Every MFC contains an orthotropic piezo-fibre/epoxy layer at its centre, which is then sandwiched between two layers of homogenous epoxy to add structural reinforcement. Laminated to the bottom and top of the epoxy/piezo-fibre layers are two more orthotropic layers of IDEs, running perpendicular to the piezoceramic fibres and encapsulated in Kapton. One distinct feature of the MFC, in contrast with conventional PFC, is that it employs rectangular fibres, which can affect the manufacturing process and the performance of the actuator. The rectangular fibre geometry of the MFC improves the contact between the interdigitated electrodes (IDE) and the piezoceramic fibres, thus reducing the attenuation of the IDE electric field due to the low dielectric constant of the epoxy matrix. Due to the in-situ poling scheme used in its manufacturing, the poling direction of the MFC's piezoceramic fibres align with the electric field produced by the MFC's interdigitated electrodes, thus enabling the high strain output of the MFC (Lloyd J.M., 2004). Recognising the superior qualities of MFCs for sensing and structural applications, researchers have adopted the MFC as the transducer of choice for the full spectrum of structural control, vibration suppression and structural monitoring projects. Due to its high conformability, high flexibility and low mass, the MFC does not introduce significant mass or stiffness coupling to host structures. MFC conformability also enables the mounting of the MFC to curved and flexible surfaces (Park et al., 2002). A comparison between the structure of PFC and MFC transducers is presented in Figure 5-1.

Interdigitated electrode pattern on polyimide film (top and bottom)

Permits in-plane poling and actuation of piezoceramic (d_{33} versus d_{31} advantage)

Structural epoxy

Inhibits crack propagation in ceramic. Bonds actuator components together.

Sheet of aligned rectangular piezoceramic fibers

Improved damage tolerance and flexibility relative to monolithic ceramic.

Interdigital electrodes

Piezoelectric ceramic fibers

Polymer matrix

(a) MFC   **(b) PFC**

Figure 5-1: Schematic View of MFC and PFC Transducers (courtesy: www.smart-material.com, 2010)

To investigate the performance of PFC and MFC under fatigue cycling, The MFC and PFC transducers are bonded to the surfaces of two identical carbon/epoxy structures using aerospace-grade adhesive as shown in Figure 5-2.
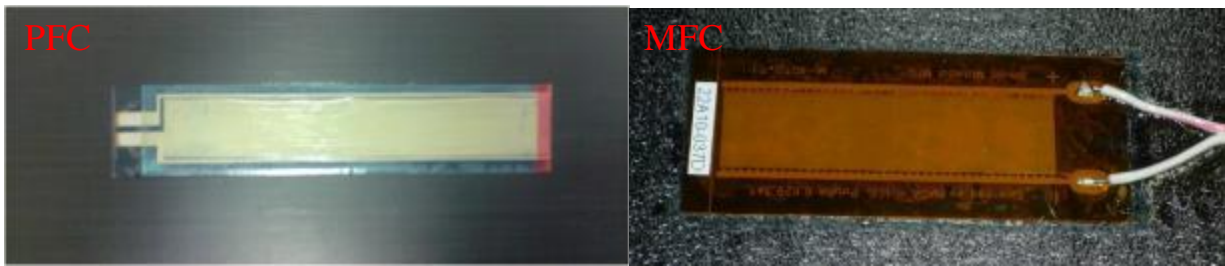
Figure 5-2: Piezo-fibre-based transducer mounted on the surface of carbon/epoxy plate

5.3. Experimental Investigations

The LCR meter is used in this section to measure the preliminary electrical properties of the transducer such as the capacitance, inductance, and resistance, and   the output voltage of the transducer due to mechanical excitation. The 3-point-bend test configuration is used to test the specimen under fatigue loading conditions. The first step to determining the advantages and characteristics of MFC is to evaluate the performance of the older generation, namely PFC. this is also beneficial, as the cost of PFC is much less than MFC and so more tests, including destructive evaluations, can be done. The changes in electrical properties of MFC and PFC transducers under fatigue loading configurations are analysed in this section. First, the electrical properties of the PFC are measured prior to and after the bonding to confirm that the bonding process has not affected the properties of the transducer. These electrical properties are also measured while the mounted transducer is under loading in order to investigate the degradation of the PFC.

5.3.1. LCR Meter Measurements

In order to evaluate the performance of the PFC sensor, the electrical properties of the sensor must be measured prior to the fatigue test. While there are various parameters which can be measured, some of the electrical properties are more sensitive to the degradation of the sensor such as Capacitance (C), Resistance (R), and Inductance (L) as they have direct relations to the integrity of the internal components of PFC. In order to measure these parameters, the PFC electrodes are connected to the oscilloscope and the Tenman 72-960 LCR meter. The following values are measured at a frequency of 1 kHz. These are taken to be the electrical properties of the intact PFC.

$$L = 4.01\ (H), \qquad C = 7.786\ (nF), \qquad R = 503.2 (\Omega)$$

5.3.2. Three-Point Bend Fatigue Test

The INSTRON® Machine (Figure 5-3) is used for the 3-point bend test under displacement control, at an increment of 0.5 mm per minute. The load is measured up to the breakage. The fatigue load range is then calculated according to the ASTM E399-90. The ultimate load is measured as 1795.5 N when the carbon/epoxy sample fails at 20 mm of displacement. The load range of 14 N and 140 N is selected based on the previous results and the initial frequency of f = 5 Hz is applied to the test. The test is under displacement control throughout in order to make sure that the possible delamination is under control. The displacement range is defined as -1.804 mm to -0.411 mm.
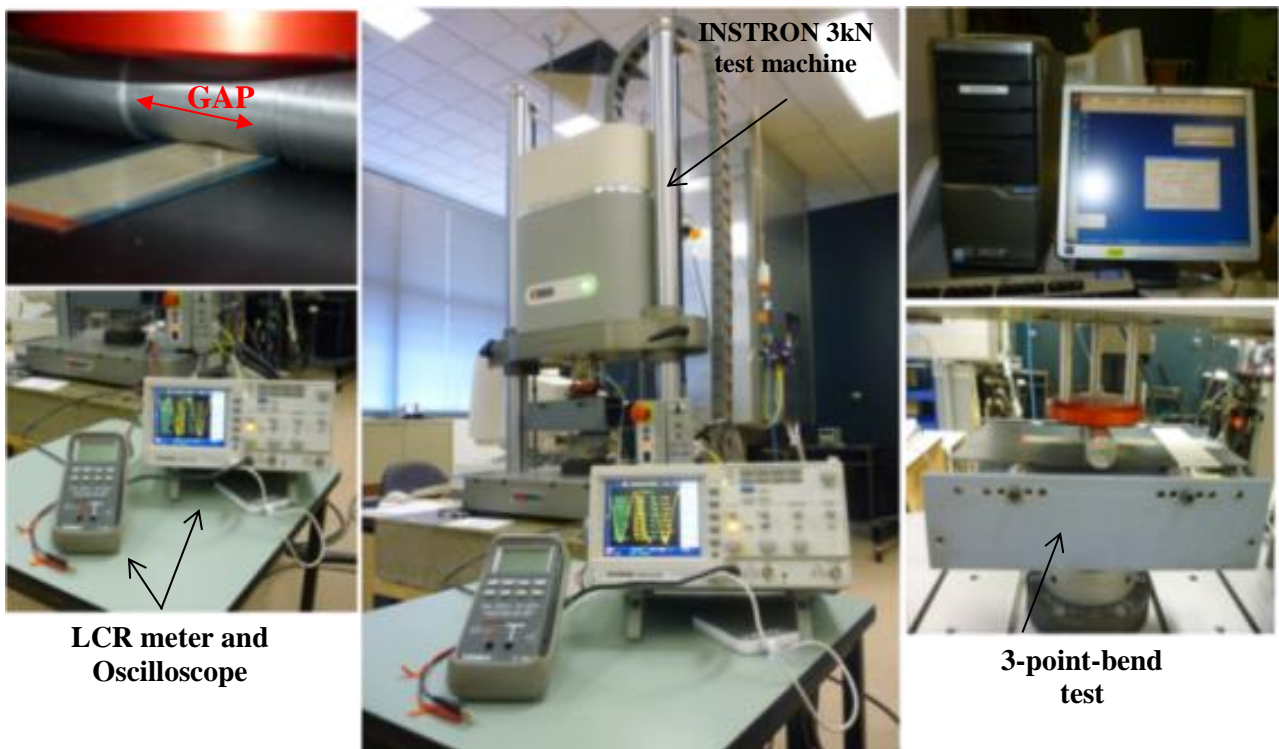
Figure 5-3: The experimental setup for fatigue test

As the purpose of this experiment is to determine the performance of the sensor under loading conditions and to continuously monitor the status of the structure as well as the sensor integrity, the electrical properties of the sensor are continuously measured and compared. Once a significant change is observed in any of the parameters, the test is paused and the sample is removed from the test rig in order for it to be inspected for any occurring damage/degradation. The C-Scan test is used to observe any physical damage in the composite whilst the optical microscope is used to inspect the sensor for any possible breakage in the PZT fibres or disconnection in the electrodes.

5.3.3. PFC Voltage Response

During the fatigue test, the output voltages of PFC are measured using the oscilloscope. The peak-to-peak voltage (V_{pp}) and maximum voltage (V_{max}) are plotted in Figure 5-4, which shows that a substantial drop in voltage occurs at around 40,000 cycles. This change could be due to either damage in the host structure or degradation of the sensor. It should be noted that the damage in the sensor might not be visibly detected at this point in the fatigue loading process. In order to delineate the mode of failure, it is essential to measure the additional electrical properties of the sensor. These parameters are discussed in the next sub-section.

5.3.4. PFC L/C/R Values

The electrical properties of a piezoelectric sensor include electrical resistance, inductance, and capacitance, and are measured using an LCR meter. The meter can characterise the amount of charge stored at a specific point which is known as electric potential. Typically measured in volts, this shows the exact static charge in the electric field of the object. The LCR meter employed in this investigation has the option of measuring these quantities at either 120 Hz or 1.0 kHz. In experiments to be discussed below, all of the parameters are measured at a frequency of 1.0 kHz. However, as the piezo-fibre based sensors such as MFC and PFC have a capacitive nature, it is expected that capacitance measurements will be more insightful.

As seen from Figure 5-5, there are two noticeable drops in the capacitance value. The first drop occurs after a similar number of cycles where the voltage is dropped. The C-Scan of the host structure finds no damage at these points of capacitance and voltage reductions, although some of PFC fibres are observed to sustain some breakage as shown in Figure 5-14. This result suggests that the cause of the drop in sensor output voltage is due to degradation of the sensors. The second considerable change in the capacitance measurements is observed after approximately 95000 cycles (Figure 5-5). The structures and PFC are again explored for any possible damage and this time

discernible damage is observed in the structure. The comparison between the C-scan results confirms the existence of a crack in the structure.
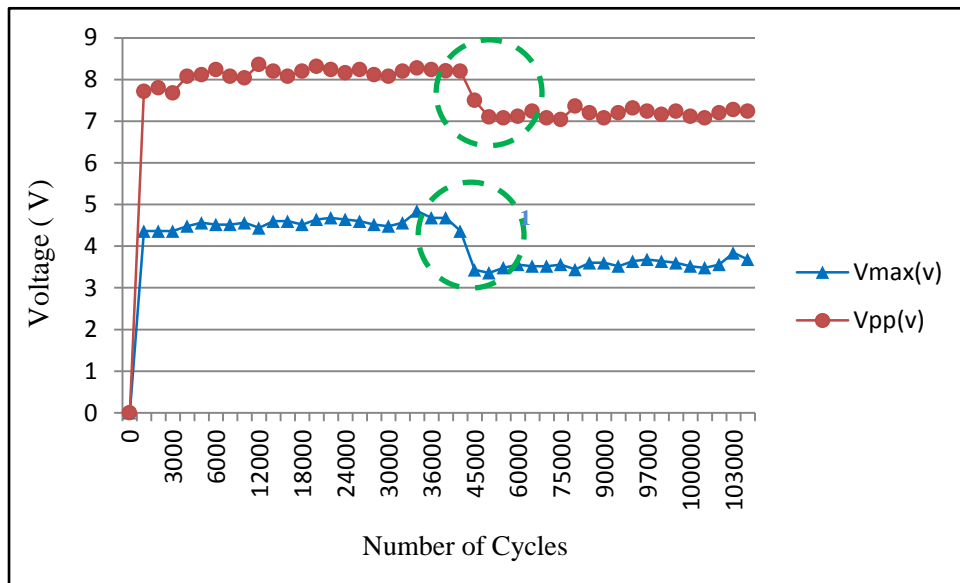
Figure 5-4: PFC Voltage measurements
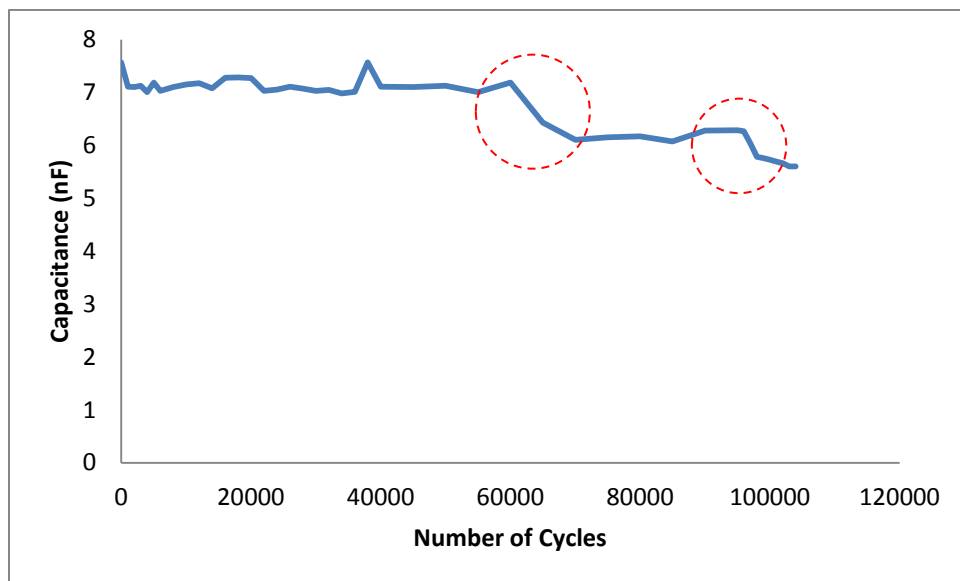
Figure 5-5: PFC Capacitance (C) Measurement

It can be seen from Figure 5-6 that the C-Scan shows a gap in the scanned picture of the structure. This gap represents the existence of an opening or crack, or, delamination in the carbon/epoxy structure. This is the reason for the second change in capacitance measurement.

These results show that after relatively low loads and a low number of fatigue cycles, sensors begin to deteriorate well before the structure does. This part of the experimental program, where the sensor is damaged, can be considered as one of the important gaps in SHM systems. As a result, the deployment of monitoring systems in the industry will need to be assessed for self-integrity before

structural integrity is monitored and ultimately managed. In this case, it is clear that a 'false positive' reading is obtained and this can be attributed directly to a malfunctioning sensor. The next challenge is to determine appropriate parameters which are sensitive to damage in the sensor and to discriminate between data from either the damaged sensors or the structure.
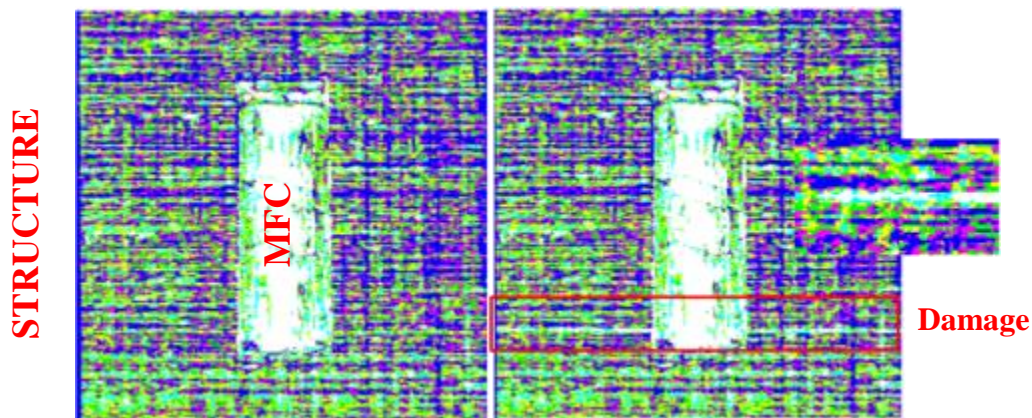
Figure 5-6: C-SCAN Test result

5.4. Post-damage investigations

In the previous section, the impacts of transducer damage and the structural damage on the electrical properties of the sensor are investigated. However, further investigation is required in order to determine the behaviour of the damaged sensor after damage occurs in its internal components, such as the piezo-fibres, IDEs, and epoxy. The effect of the damage within the sensor, particularly on its electrical properties needs to be identified by focussing on the damaged zones and measuring the parameters at these points. This evaluation can be achieved by detaching the damaged sensor from the structure in order to measure the electrical properties at intact and damaged zones of the sensor. The comparison of the measurements close to the damage zone and at intact zones of the sensor will provide us with the impact of sensor damage on its internal components and their relation to the sensor's electrical properties. In order to remove the sensor, the sample is heated up in the oven under 80ºC of temperature for 30 minutes and the sensor is carefully detached (Figure 5-7). Following this, the electrical properties of the sensor are measured so as to ensure that the detaching process does not affect the performance of the sensor. The values confirm that the sensor is properly removed from the structure without further damage.

In order to determine the effect of damage on the local properties of the sensor, the electrical properties are measured between each two parallel points of the electrodes (Figure 5-8). In the equivalent circuit of the PFC and MFC transducers, the piezo-fibres between each of the two electrode fingers (positive and negative) can be modelled with a capacitor. Therefore, the

capacitance measurement between each two neighbour electrode digits can provide us with the estimated local capacitance of that area. For Scanning Electron Microscopy (SEM) imaging, the sensor is cut into intact and damaged sections for further investigation, as described in the following sections.

Figure 5-7: The MFC sensor is detached from the structure.
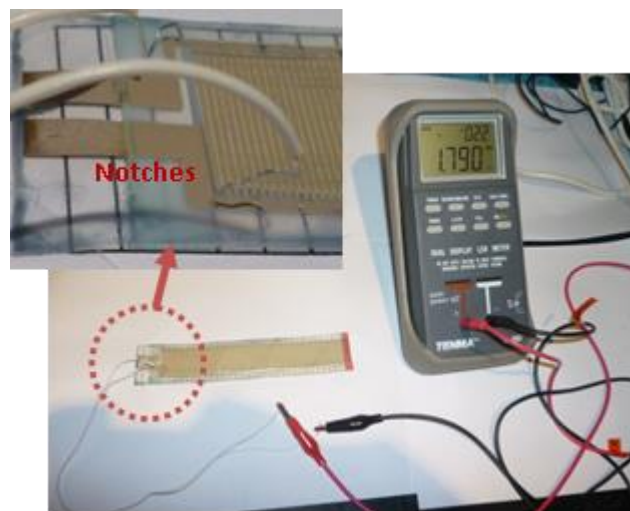
Figure 5-8: Local capacitance Measurements two parallel points

The aim here is to determine if the observed damage alters the properties between all the electrode points or whether the change is more significant at the damaged zones. The capacitance is measured by connecting the LCR meter to each set of two parallel points. As seen in Figure 5-9, the capacitance values are generally decreased when compared to the capacitance of the intact sensor which is 7.786 (nF) due to the damage. However, further reductions can be observed at the exact locations of the fibre breakage. Nevertheless, this reduction is not considerably different at the damaged areas compared to the intact parts of the sensor. These results show that the damage of the sensor does not considerably affect the local capacitance measurements. In other words, the capacitance is not significantly affected by the destruction of local components. This gives rise to the need for another parameter more local in nature which can be used to locally detect the damage

in the transducer. The next section describes the relation between capacitance and other electrical properties and provides a detailed overview of their dependency on the local damage.
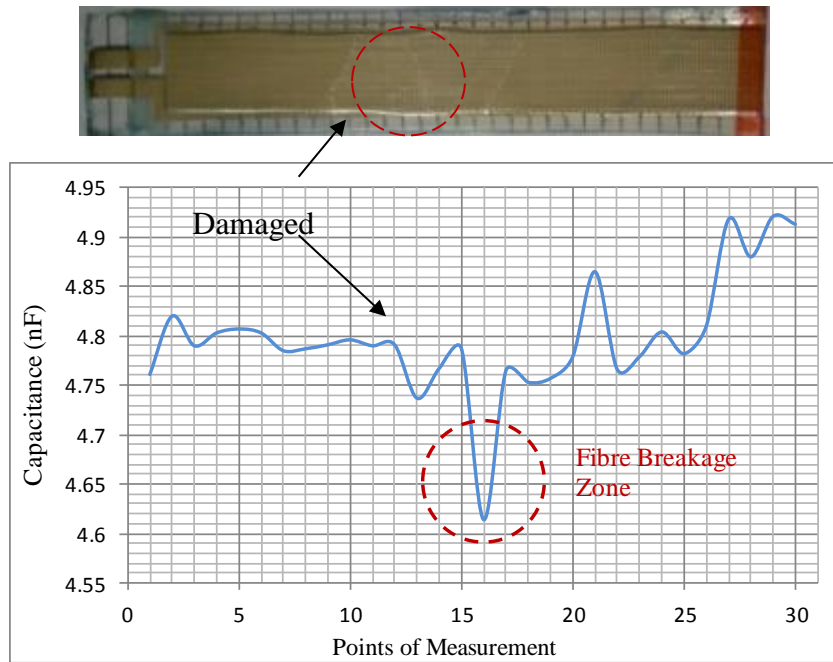
Figure 5-9: Capacitance measurements at damaged areas

5.4.1. Scanning Electron Microscopy (SEM)

The Philips XL30 SEM with Oxford Si (Li) X-ray detector is used to scan the damaged MFC and PFC sensors under the microscope. A guaranteed point resolution of 3.5 nm at 30 kV and 30 nm at 1 kV is achieved. The Energy Dispersive X-ray Spectrometer (EDXS) manufactured by Oxford Instruments, is fully integrated with the SEM XL30, and offers qualitative and quantitative elemental analysis of all elements down to boron (Z = 5). Images, spectra and X-ray maps from analysed micro-areas can also be acquired.
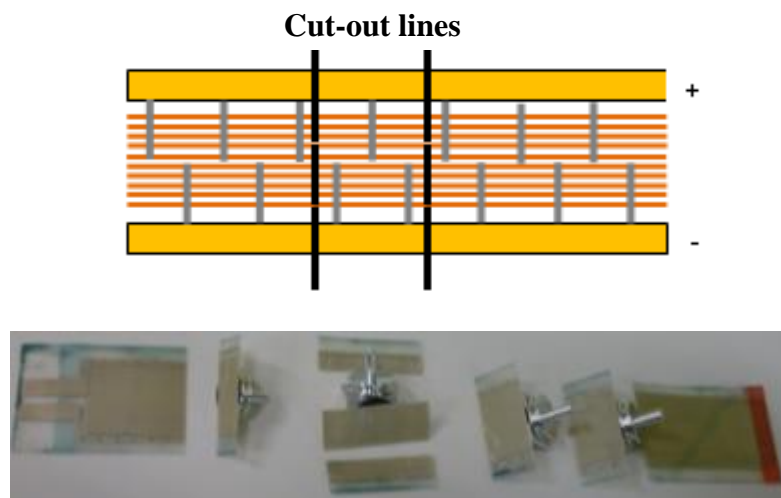
Figure 5-10: The sections of PFC with and without defect

143

The damaged areas are carefully cut out of the sensor (Figure 5-10) and placed on the pin. These samples are cut from the significant damaged zones for further investigation and to visually compare the damaged and undamaged zones of the sensor under microscope. However, as the outer surface of MFC and PFC transducers are non-conductive, they need to be gold coated prior to any SEM imaging. The sections of damaged MFC and PFC are mounted onto an aluminium SEM stub of appropriate size using carbon tape. These stubs are used to place the sections in the coating chamber. The SPI® Supplies Sputter Coater is used to gold-coat the samples (Figure 5-11). The coated samples are then carefully removed from the coating glass and placed in the stage of the Philips XL30 SEM (Figure 5-12).

More details on the sample preparation, gold-coating process and SEM test configuration are provided in Chapter 3 (Manufacturing and Experiments) above.

Figure 5-11: The SPI® supplies sputter coater and coated samples
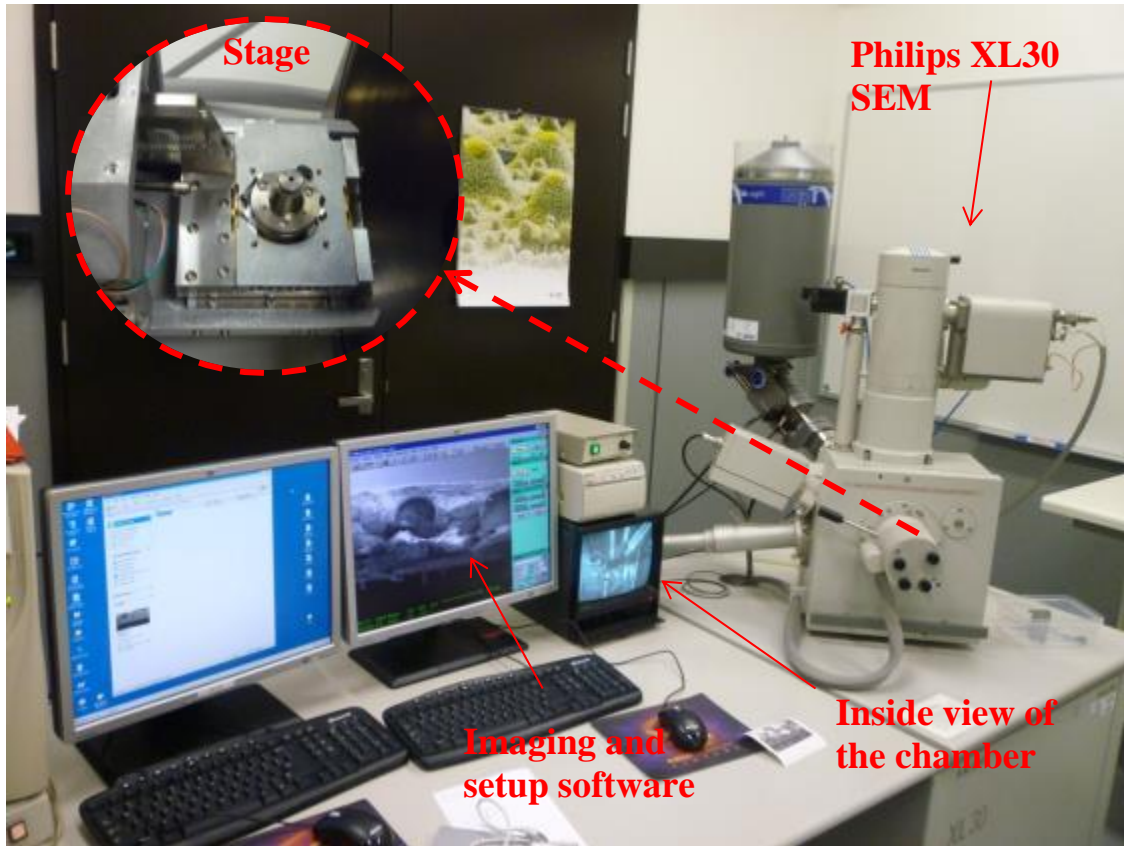
Figure 5-12: Philips XL30 SEM test setup

The final step of SEM is to scan the sample under a microscope and capture the required images with proper resolution and magnification. The damaged and intact sections of MFC and PFC transducers are individually placed in the stage of the XL30 SEM and scanned. For damaged sections, the aim is to find the damage type such as debonding, micro-breakage and micro-cracks within the layers of the transducer cross-section. Once the damage is located, the image is captured. For intact sections, the images of relevant locations are scanned and captured for comparison purposes. These comparisons are provided in Figure 5-13.
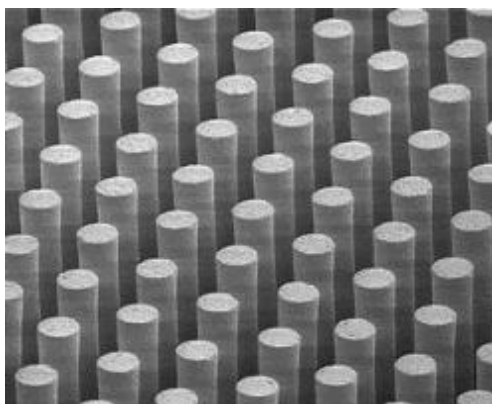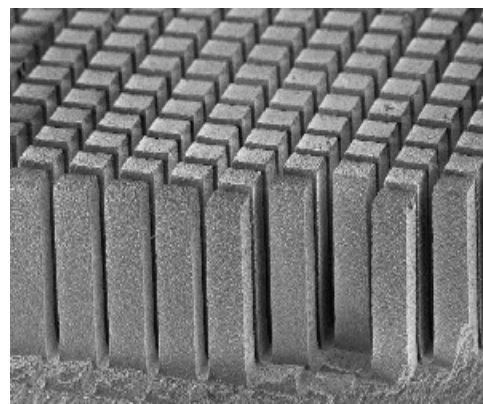
(PFC)   **(MFC)**

Figure 5-13: Shape of Fibres in MFC and PFC transducers (Gebhardt et al., 2013)

The first observation is shown in Figure 5-13 which is the comparison of the shape of fibres within the PFC and MFC transducers. As mentioned above, one of the improvements in MFC is to use the rectangular shaped fibres to improve the connectivity of interdigitated electrodes and the fibres. In Figure 5-14, the statuses of intact and damaged PFC fibres are compared. It is shown that there are significant changes in the shape of the fibres after the fatigue loading. This demonstrates that the transducer damage causes destruction in some of the fibres, which is one of the reasons for a reduction in capacitance value after the occurrence of damage. Furthermore, breakage within the fibres may interrupt the connection of the piezo fibres with the electrodes. This breakage will thus contribute to the drop in the transducer output voltage. As such, it is reasonable to deduce that additional piezo-fibre damage in the piezo-fibre layout will have a cumulative effect on overall voltage and the capacitance drop of the MFC and PFC sensors. The same comparison is provided for the MFC transducer which is shown in Figure 5-15.

(a)   (b)
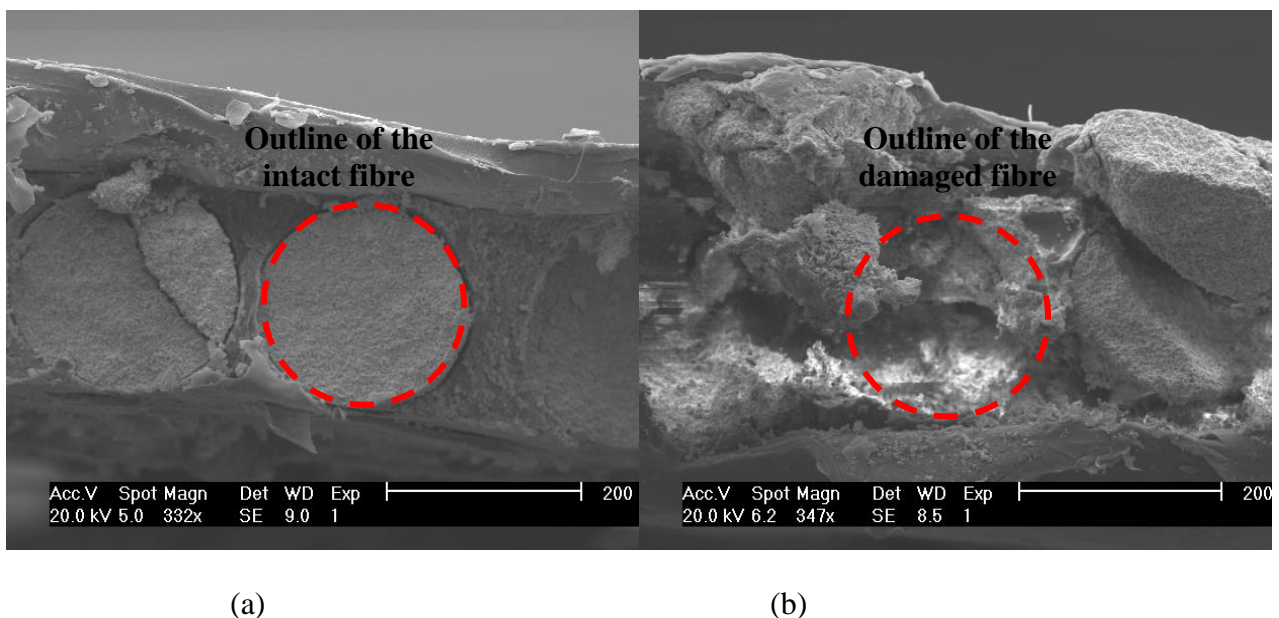
Figure 5-14: The SEM images of the sensor at (a) undamaged zone (b) damaged zone

Another observation from the SEM results is other types of damage rather than fibre breakage or damage. The MFC or PFC transducers are multifunctional and therefore consist of various internal components. When the damage occurs in the transducer, it can affect one or all of these components in the form of breakage, disconnection, cracking or debonding. As previously discussed, each damage type affects some of the electrical properties of the transducer. This is very important in understanding the behaviour of the damaged transducer and for identifying the source of damage in the transducer based on the changes in the relevant electrical properties. The breakage or crack in the fibres debilitates its ability to store the charge and leads to the reduction in the total capacitance of the transducer. Moreover, as the charge decreases, the generated current

would also decrease, thus potentially causing higher impedance (V/I). This issue will be investigated and discussed further in Chapter 7.
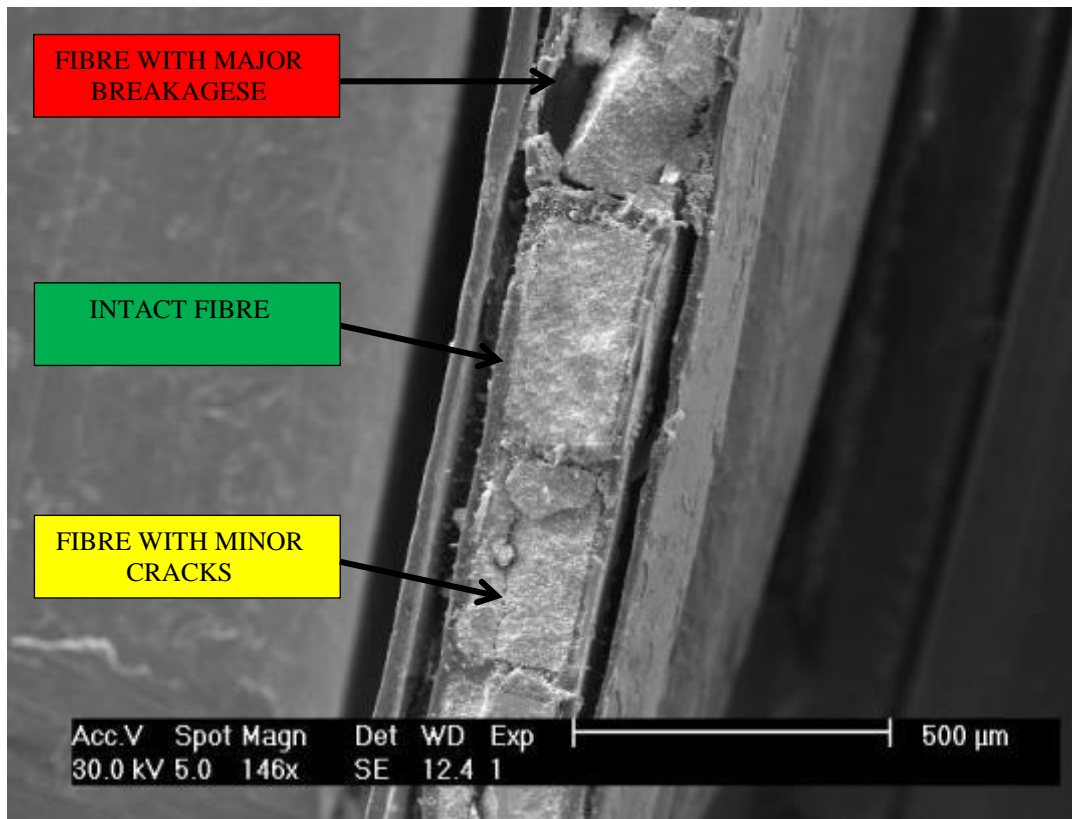
Figure 5-15: The SEM image of MFC transducer fibres
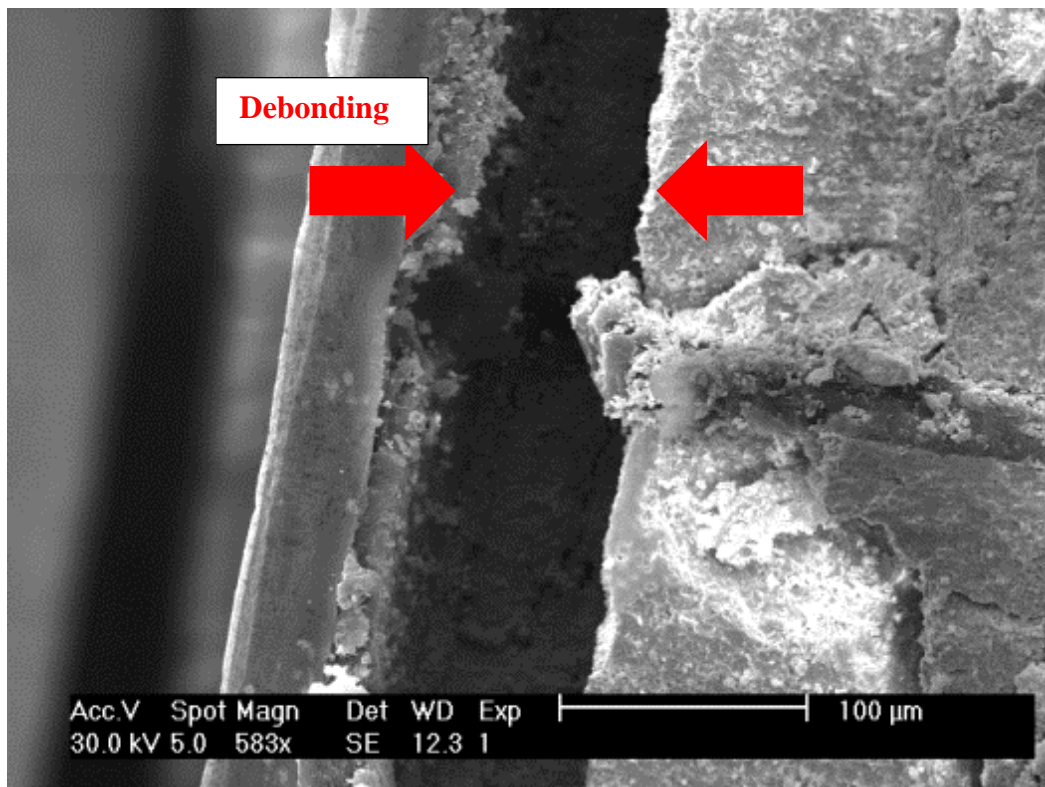
Figure 5-16: Debonding between Piezo-fibre and epoxy layer of MFC

The next observation is the debonding between the sub-components of MFC and PFC transducers. Generally speaking, the piezo-fibres are bonded to the epoxy layer between them and on the top and bottom. In this case, the disconnection occurs between the electrodes and de-bonded fibre(s) although the fibres are mostly intact and have a relatively similar capacitance value to before. However, the generated strain in the transducer due to the mechanical loading would change, thus affecting the output voltage of the transducer (direct piezoelectric effect). As such, it can be said that the debonding has more impact on the output voltage of the transducer compared to other electrical properties such as capacitance.

The debonding between the piezo-fibres and epoxy layer of MFC is shown in Figure 5-16. In this figure, the debonding is more significant compared to the damage in the piezo-fibre itself. In Figure 5-17, the debonding between the epoxy layer and Kapton layer is presented. The Kapton layer protects the fibres and electrodes on the top and bottom of the MFC transducer. Therefore, this debonding can significantly reduce the durability of the transducer. It can be seen that the fibres under this debonding are quite damaged. In Figure 5-18, debonding between a single fibre and surrounded epoxy is shown for the PFC transducer. It is observed that while the fibre still seems relatively healthy, the debonding occurs between the fibre and epoxy. The ceramic microstructure of the piezo-fibre is also clearly seen in this figure.
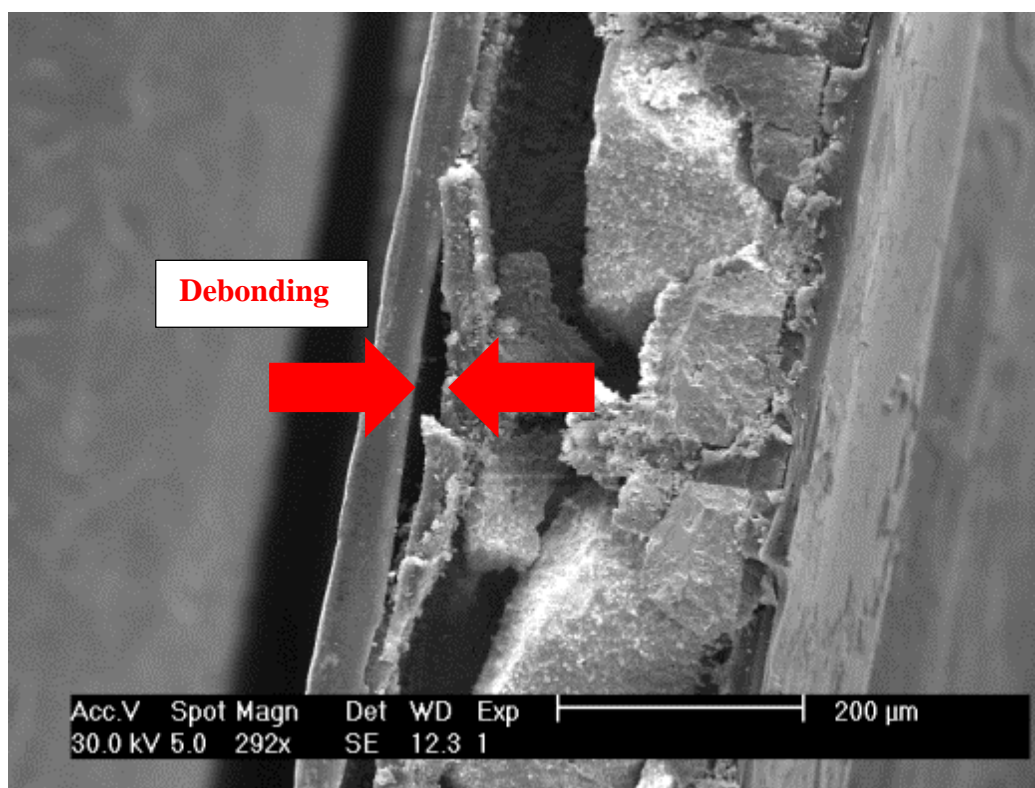
Figure 5-17: Debonding between epoxy layer and Kapton layer of MFC
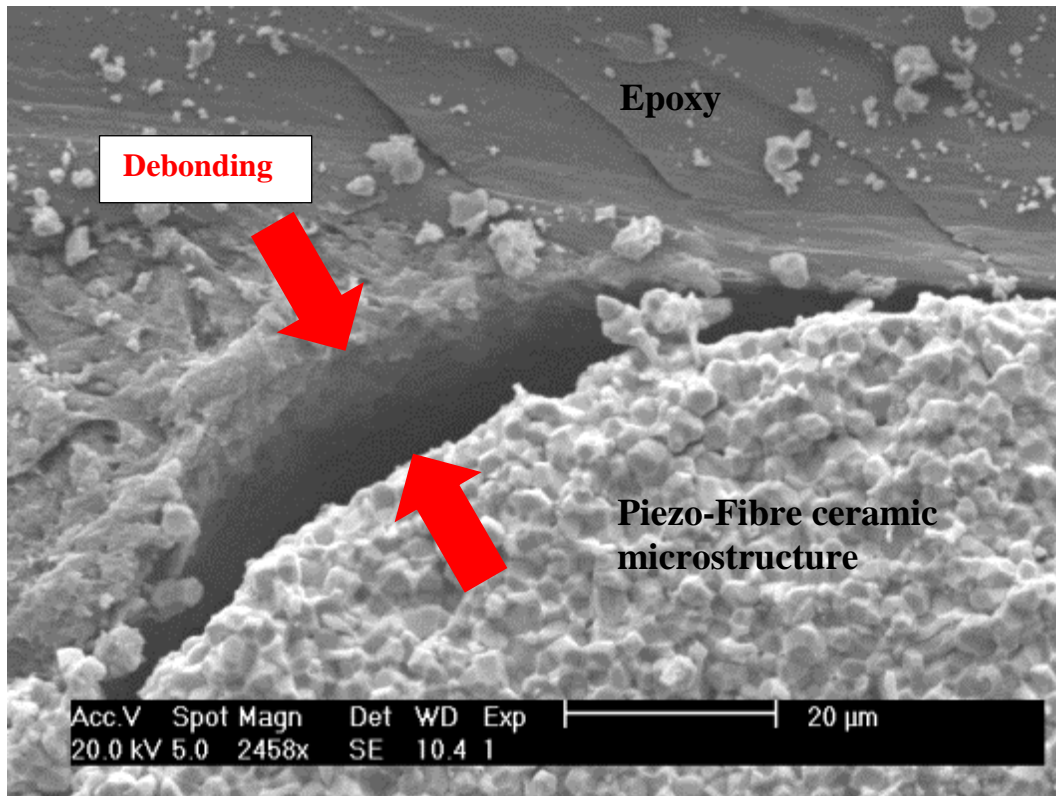
Figure 5-18: Debonding between Piezo-fibre and epoxy layer
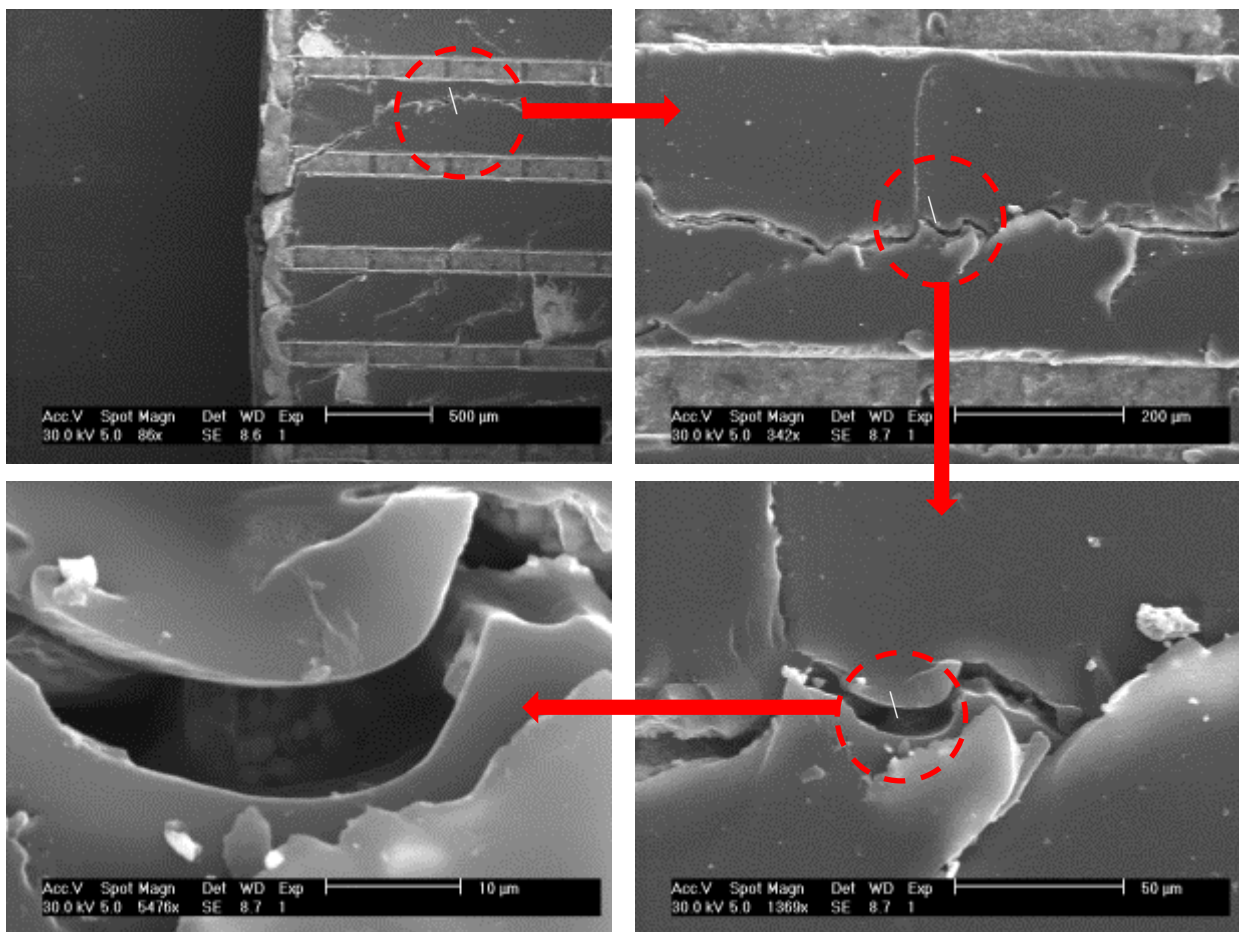
Figure 5-19: Epoxy damage in MFC transducer

Another damage type in the transducer is the breakage of the epoxy layer as shown in Figure 5-19. It can be seen from this figure that the epoxy layer is damaged due to fatigue loading. This damage type has two impacts on the performance of the transducer. Firstly, it reduces its mechanical strength as the epoxy layer is in charge of load bearing in the MFC and PFC transducers. Secondly, it modifies the relative permittivity (ε_r) of the transducer, which is based on the material between electrodes. The relative permittivity (also known as dielectric constant) is the ratio of the amount of electrical energy stored in a material by an applied voltage, relative to that stored in a vacuum. In other words, it is the ratio of the capacitance of a capacitor using that material as a dielectric, compared to a similar capacitor which has a vacuum as its dielectric (vacuum between the plates). Therefore, the change in the integrity of fibres between two interdigitated electrodes also affects the local relative permittivity which in return modifies the relative permittivity of the transducer. The relative permittivity, ε_r, can be measured for static electric fields using Equation 5-1 (Kuek et al., 2011):

Equation 5-1

$$\varepsilon_r = \frac{C_x}{C_0}$$

Where ε_r is the relative permittivity, C_0 is the capacitance of a test capacitor measured with vacuum between its plates and C_x is the capacitance with a dielectric between the plates.

5.5. Capacitance vs. Sensor Geometry

The capacitance can be calculated if the geometry of the conductors and the dielectric properties of the insulator between the conductors are known. The capacitance of a capacitor with two parallel plates both with the area of 'A' separated by a distance of "d" is approximately equal to the relationship shown in Equation 5-2 (Costa et al., 2011). Therefore, the capacitance between the electrodes of the MFC sensor is approximately represented by the following.

Equation 5-2

$$C = \varepsilon_r \varepsilon_0 \frac{A}{d}$$

Where A is the area of overlap between two electrodes, ε_r is the relative static permittivity of the material between the electrodes (for vacuum, $\varepsilon_r = 1$), ε_0 is the permittivity of vacuum and d is the separation between the electrodes.

The experimental results in this project show that the capacitance values decrease as the degradation escalates in the MFC sensor. It can be seen from Figure 5-1 that the capacitance is related to ε_r, ε_0, A and d. Therefore, the reduction in the capacitance value is caused by the misalignment of the electrodes, which increases the separation between them (d). In order to investigate this assumption, Scanning Electron Microscopy (SEM) testing is used to observe the alignments of the electrodes and the piezo-fibres, both before and after the capacitance reduction. Figure 5-14 shows that the breakage in the piezo-fibres causes misalignment in the interdigitated electrodes. This misalignment tends to increase the separation distance (d) between the electrodes which in turn lead to a reduction in the capacitance value. On the other hand, the local measurements of the capacitance (Figure 5-9) show that this reduction is almost constant throughout the whole sensor and further reduction at the damaged zones of the sensor is not significant. This point illustrates that the micro-cracking of the fibres is not the main cause for the reduction in the capacitance measurements and capacitance has more dependence on other parameters rather than "d". To investigate this issue, the relationship between the capacitance, strain coefficient (g_{33}) and voltage coefficients (d_{33}) of the sensor are explored as seen in Equation 5-3 (Overly T.G.S. et al., 2008):

Equation 5-3

$$C = \frac{d_{33}A}{g_{33}d}$$

Where C is the capacitance, d_{33} the strain coefficient, A is the electrode surface area, g_{33} is the voltage coefficient and d is the thickness separating the electrodes. This relationship implies that the drift in d_{33} and g_{33} values may also be responsible for the reduction in the capacitance measurements. In light of this, it can be argued that the d_{33} and g_{33} values are more sensitive to the degradation of the sensor when no visual sign is available. This would be a great advantage, particularly when the sensor system is not accessible to visually inspect. The sensitivity of the piezoelectric coefficient, d_{33}, to the sensor degradation is investigated in the next section.

5.5.1. Piezoelectric Coefficient vs. Capacitance of Piezo-fibres

As mentioned in the previous section, based on the local capacitance measurements, the effect of the piezoelectric coefficient (d_{33}) and voltage coefficient (g_{33}) on the capacitance is more significant than the misalignment of the subcomponents (d). To illustrate this point, the changes in the piezoelectric coefficient (d_{33}) of the sensor while the sensor is under fatigue loading are investigated. If the PZT fibres in the MFC sensors are considered as a parallel plate capacitor, then

151

the capacitance, C, depends on the area, A, and separation, d, of the plates as shown in Equation 5-4.

Equation 5-4

$$C = \varepsilon \frac{A}{d} = \varepsilon \frac{l_c b_c}{t_c}$$

Where l_c and b_c are the active length and width of the sensor and t_c is the thickness. For d_{33}-MFC, the strain is only along the 3 (poling) direction and averaged along this length of the sensor. Therefore, it is shown that the voltage relationship can be written as Equation 5-5:

Equation 5-5

$$V_c = \frac{d_{33} Y_c l_c b_c}{C_p} \varepsilon$$

where d_{33} and Y_c, are piezoelectric coefficient and Young`s modulus respectively and ε is the strain. The properties of the MFC sensor used for this experiment are shown in Table 5-1:

Table 5-1: Properties of MFC Type P1 M410

Model	M-410-P1
Overall Dimensions	54 mm × 22 mm
Active area dimensions (l_c , b_c)	40 mm × 10 mm
Max voltage	500 to 1500 V
Max tensile strain	< 4500 ppm
Thickness (t_c)	approx. 0.3 mm
Piezoelectric coefficient (d_{33})	4.40E2 PC/N
Young`s modulus (Y_c)	30.336 GPa

Therefore, the final relationship can be written as Equation 5-6 (Jeannette et al., 2006).

Equation 5-6

$$V_c = 12.1344 \frac{d_{33}}{C_p}$$

The post damage analysis of the sensor, which is presented in the previous sections, shows that the d_{33} and g_{33} values also change as a result of sensor damage. According to Equation 5-6, the output voltage of the sensor has a direct relation to d_{33} and an inverse relation to the capacitance. Furthermore, it has previously been shown that the sensor damage reduces the voltage response (Figure 5-20). As such, the reduction in the d_{33} should be more significant than the fall in capacitance which demonstrates that d_{33} is more sensitive to the changes in the integrity of the sensor. The relationship shown is used to estimate the d_{33} values from the voltage and capacitance measurements. It can be seen from Figure 5-21 that the percentage of d_{33} reduction is higher than that of the capacitance, thus proving that the d_{33} is also changed due to the sensor damage and can be used as a powerful tool to detect the damage in the sensor itself even without visual inspections.
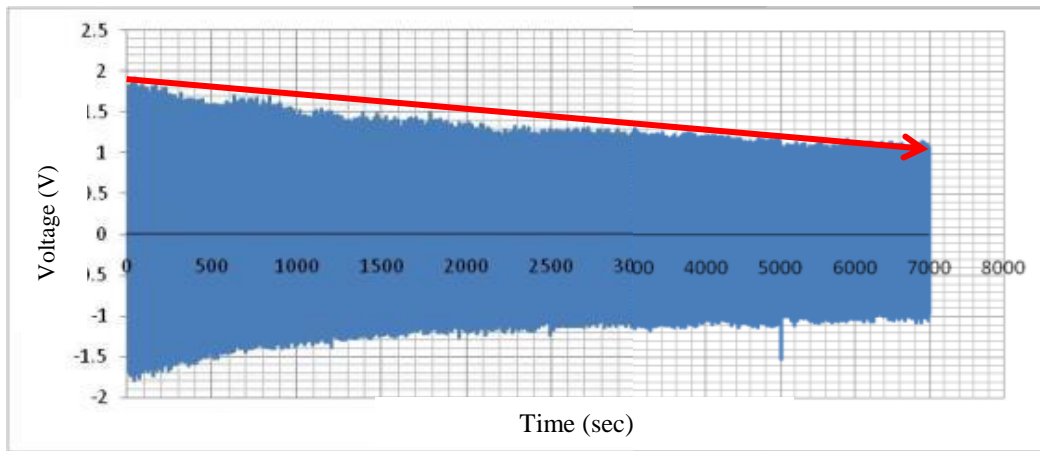
Figure 5-20: MFC output voltage
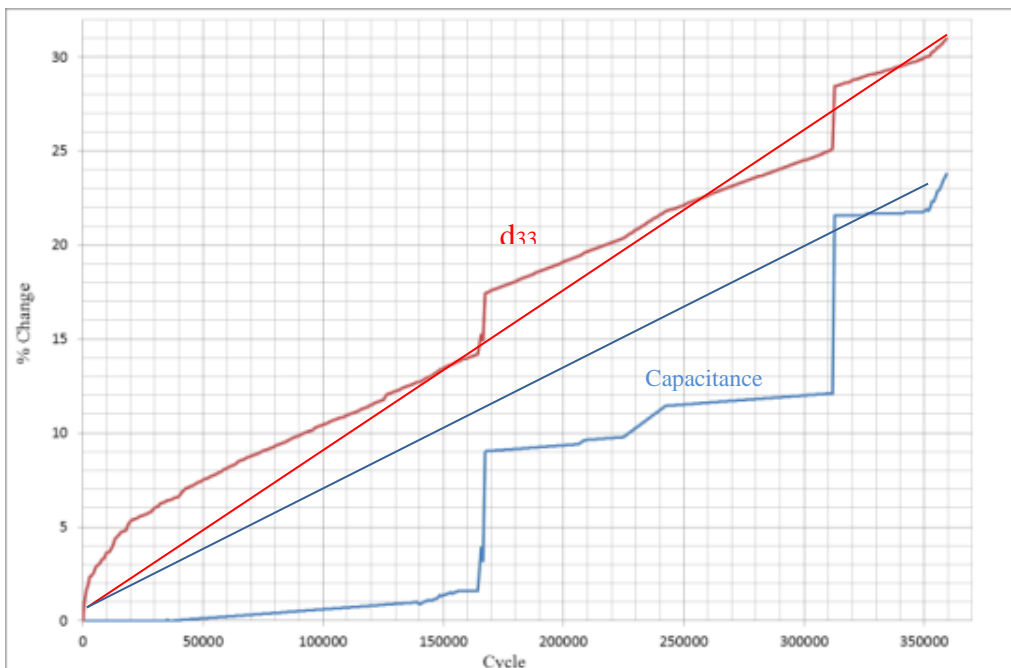
Figure 5-21: Percentage of fall in Capacitance and d33 measurements

153

5.6. The Comparison between PFC and MFC Performances

In previous sections, the properties of PFC and MFC sensors are investigated separately. However, the main transducer type used in this project is Macro Fibre Composite (MFC) which has significant advantages over other types of sensors such as strain energy density, controlled actuation in singular direction, flexibility, conformability, and durability. In this section, the properties of the PFC and MFC sensors are compared based on the theoretical information as well as conducted experiments. The properties of base piezoelectric material for MFC and PFC are shown in Table 5-2.

Table 5-2: MFC & PFC Properties

PROPERTIES	UNITS	PFC	MFC
d_{31} (Strain Constant)	M/V OR	-1.73E-10	-1.85E-10
d_{33} (Strain Constant)	M/V OR	3.80E-10	4.40E-10
g_{33} (Voltage Constant)	VM/N	2.50E-2	2.55E-02
K_{33} (Coupling Factor)		0.72	0.72
K_{31} (Coupling Factor)		0.36	0.33
K(Dielectric Constant)		1725	1850
Tan D_e (Dielectric Loss)	%	2	0.012
R (Density)	G/CM^3	7.5	7.7
T_c(Curie Temperature)	˚C	350	335
C_{11} (Compliance)	M^2/N	1.52E-11	1.85E-11
C_{33} (Compliance)	M^2/N	1.83E-11	2.07E-11

The visual status of the MFC and PFC sensors after 300000 cycles is shown in Figure 5-22. It can be seen that the PFC has visually detectable damage showing after 300000 cycles. These damage zones are also magnified using an optical microscope as shown in this figure. However, MFC does not have any visual damage after undertaking the same number of cycles, which shows its higher durability and reliability compared to the PFC sensor. The capacitance of the MFC and PFC sensors is plotted in Figure 5-23. It shows that the MFC has better performance in terms of

durability compared with PFC under fatigue loading condition. While the degradation in PFC starts after only 45000 cycles, the MFC shows significantly better robustness even after 350000 cycles. This comparison illustrates one desirable feature of the MFC sensor over the PFC sensor. Therefore, in this project, the degradation of the MFC as the more reliable sensor is further investigated.

(a)   (b)
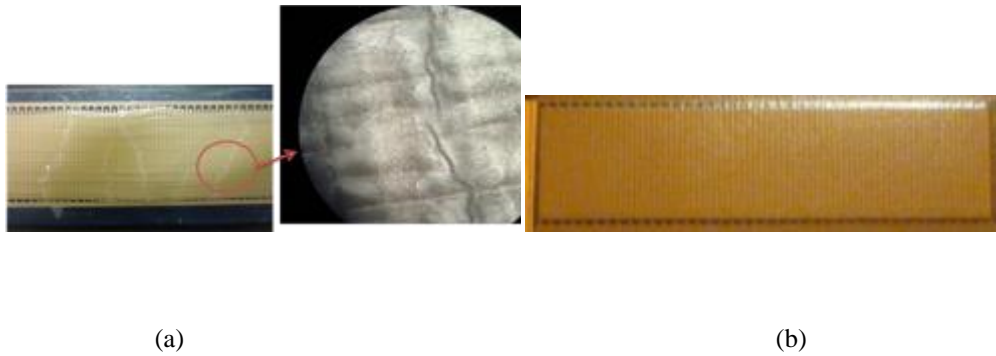
Figure 5-22: The status of the sensor after cyclic loading (a) PFC sensor has visual damages

(b) MFC is still intact after 300000 of cycles.
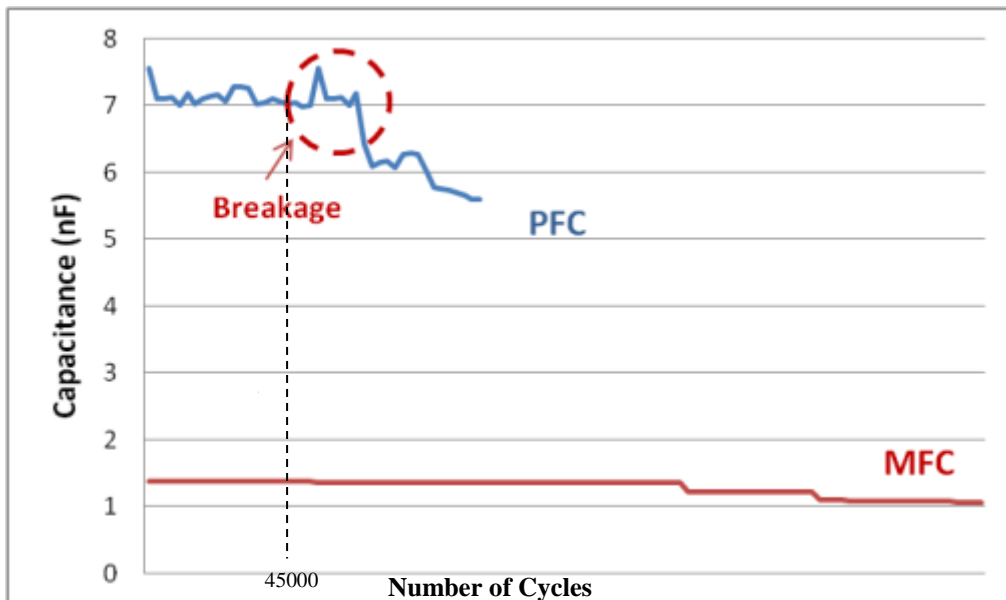
Figure 5-23: The comparison between PFC and MFC Capacitance

5.7.   Summary

This chapter addresses the characterisation of the MFC and PFC sensor responses and electrical properties in order to assess the status of the host structure and the sensors. A 3-point-bend test configuration is used to determine the fatigue performance of piezo-fibre based transducers (MFC & PFC) while they are bonded to a composite structure. The electrical properties of the PFC and MFC sensors such as capacitance and inductance are measured using an LCR meter. By comparing these measurements, it is observed that the proper bonding process will not have any

155

considerable effect on the integrity of the transducer and the structure. The 3-point-bend test configuration is used to apply the fatigue loading to the manufactured samples and the electrical properties of the sensor are continuously captured. It is noticed that the MFC has much better performance under fatigue loading when compared to PFC. PFC shows signs of degradation after approximately 45000 cycles while the MFC shows significantly better robustness even after about 300000 cycles. The monitoring of the key electrical properties of PFC and MFC sensors during the fatigue test emphasises that the capacitance has more sensitivity to the sensor degradation. Moreover, the change in the key electrical properties' measurements shows that degradation of the sensor starts prior to the structure, thus leading to 'false positive' readings from the sensors. The changes in the local measurements show that the capacitance is more sensitive to the properties of the sensor components such as piezoelectric coefficient and voltage coefficient rather than the micro-cracking misalignments.

As mentioned in the literature review, the impact of damage/degradation on the local properties of the PFC and MFC sensors is one of the areas which have not yet been properly investigated in other research. Therefore, this issue is investigated in the present chapter with The Scanning Electron Microscopy (SEM) technique used to investigate the impact of damage on the subcomponents of the sensor. The results show that the local misalignment of fibres and/or electrodes has less impact on capacitance reduction when compared to piezoelectric coefficients; a phenomenon which stems from fibre breakage and debonding between sub-layers of the sensor. The present approach yields an improved methodology with which to differentiate the degradation in the sensor from the structural degradation. This is vitally important as it can address one of the more important issues in the certification of the SHM systems.

CHAPTER 6 The Strain-based Delineation Technique

6.1. Introduction

This chapter investigates self-diagnostic techniques to distinguish transducer degradation from structural damage, using interdigital piezoelectric fibre transducers with a focus on the strain reading of the transducer. With the increasing application of structural health monitoring (SHM) systems to manage the on-going integrity of safety-critical structures, it is important to improve the reliability of SHM systems by reducing erroneous information from transducers. This requires a new capability to delineate failures associated with transducers and the transducer network from actual damage in the structure being monitored. This is especially important when the deleterious structural changes in the transducer occur without any discernible change in the structure being monitored. This chapter seeks to gain an insight into the transducer damage by comparing strain measurements experimentally determined from the transducer to those determined theoretically. The FEM simulation is also used to validate the experimentally measured strains. The results show that the delineation of structural damage from transducer degradation may be possible by making a continuous comparison of strain levels on the transducer with those on the structure.

Structural Health Monitoring (SHM) has provided engineers with the possibility of making the structures safer and more reliable in the harsh environment. These SHM methods determine the status of the structure as well as the embedded system itself by using various tools such as transducers, composite material, signal processing, and integrated systems (Beard et al., 2005). However, as the application of SHM systems to monitor the status of the MFS increases, it is extremely important to determine the durability, reliability, and reparability of the SHM system itself. In this context, the transducers or the transducer network must possess sufficient reliability so that they do not require replacement at intervals less than the economic lifetime of the components they are monitoring. For safety-critical structures, such as primary aircraft structures, it is imperative for SHM systems to demonstrate a probability of failure which is lower than that of the host structure. To achieve this very challenging goal, new technologies must be developed which are capable of distinguishing transducer failure from structural damage. There are two challenges

standing in the way of achieving this goal. The first challenge is to use the only available value which is the output of the MFC transducer and analyse it in such a way as to provide us with enough information on the integrity of the structure and the transducer. Secondly, we must have a practical technique in place which is capable of using the output of MFC and providing us with distinguished information on the status of the structure and transducer.

Two different approaches related to transducer performance during service can be discussed - MFC failure and MFC degradation (damage). The failure of the transducer can be easily detected as the transducer does not produce any measurable output. However, the degradation of the transducer is more complex and needs further investigation. The degraded transducer can still produce an output and can perform very well. This can lead to false negative or false positive signals about the status of the transducer/structure. For piezoelectric transducers, the transducer failures are inevitable after undertaking extreme loading and environmental conditions, since transducers are usually one of the more vulnerable components of the monitored structural system (Lynch et. al., 2012). Furthermore, the mechanical and electrical properties of MFC materials could also gradually degrade over time. The quality degradation of the transducer and bonding layer will become increasingly complex and confusing when a multiple number of transducers are employed over a long period of time which is a realistic scenario in the terms of the application of transducers in SHM. The key challenge is the continuous determination of the integrity of not only the structure but also the network of transducers. This is one of the main gaps in certifying the SHM systems which has not yet been addressed in the literature. These issues demonstrate the need for the characterisation of transducer response in order to identify whether the damage is caused within the transducer itself and/or is located within the host structure.

In this chapter, the ability of MFC to act as a strain transducer along with the strain transfer between MFC and the host structure is used to develop a diagnostic technique to discern between the state of the structure and that of the concomitant transducer. Three sets of strain are collected using the output voltage of MFC, strain gauge and theoretical calculations. It is shown in this chapter that the comparison of these 3 sets of values can be used as a practical delineation technique.

6.2. Experimental Process

The 3-point-bend test configuration is used for this part of the project. The details of the test setup are provided in previous chapters. The Carbon/Epoxy Sample with the MFC transducer is placed in the INSTRON test machine and the electrode leads are connected to the datalogger in order to measure the output voltage of the sensor. In addition, a strain gauge is bonded to the bottom surface of the carbon/epoxy plate at the same location as the MFC. The strain gauge is connected to the

strain indicator and recorder in order to continuously measure the strain level. The schematic view of the test rig is shown in Figure 6-1.
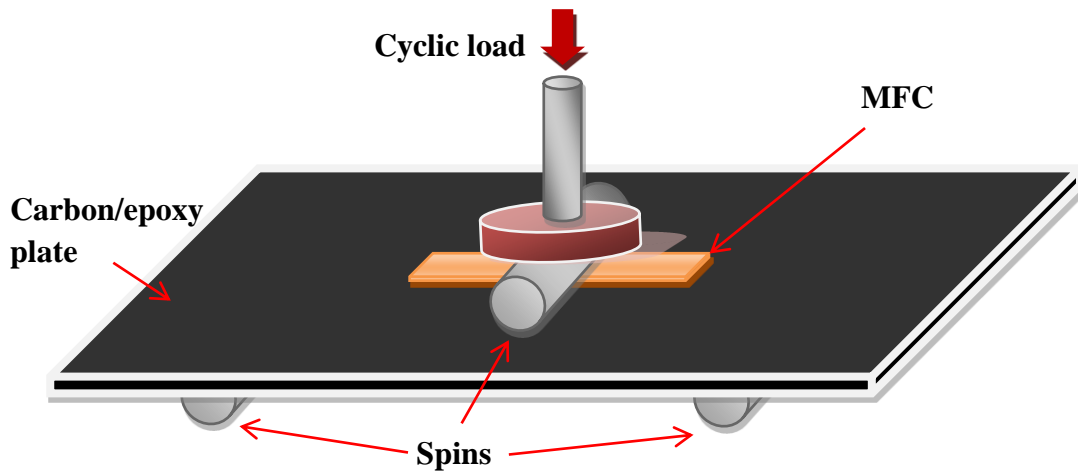
Figure 6-1: The schematic view of test rig

6.3. MFC Strain Measurement (ε_{MFC})

Macro Fibre Composite (MFC) is an advanced version of the piezoelectric transducer and consists of PZT materials. Therefore, we can still use the PZT strain theory formulation for the MFC strain. As discussed in the literature review for PZT materials, they generate electric charge (electric field) in response to mechanical excitation (strain) and vice versa. This is due to the coupling of mechanical and electrical properties of PZT materials. The strain, ε, in PZT materials is proportional to the applied electric field E. The relationship between the strain and electric field can be written as Equation 6-1 for the MFC sensor:

Equation 6-1

$$\varepsilon = dE$$

Where d is the piezoelectric strain coefficient. Generally speaking, the total strain, ε_T, in the MFC is caused by external loading as well as the applied electric field as shown in Equation 6-2:

Equation 6-2

$$\varepsilon_T = s\sigma + dE$$

Where s is the elastic compliance and σ is the stress. This equation presents the converse effect of piezoelectricity in the MFC transducer. In this chapter the MFC is under mechanical loading which generates an electric charge on the MFC. Therefore, the strain on the sensor would generate an

159

electric charge and the MFC can be used as a dynamic strain gauge. The electric displacement, D, is related to the electric field, E through Equation 6-3:

Equation 6-3

$$D = eE$$

In this Equation, e is the dielectric permittivity of MFC. According to the piezoelectric material formulations (refer to literature review for more detail), the electric displacement is also related to the stress. This is shown in Equation 6-4.

Equation 6-4

$$D = d\sigma$$

The summation of Equation 6-3 and Equation 6-4 is the total electric displacement, D_T, of the MFC transducer (Equation 6-5).

Equation 6-5

$$D_T = d\sigma + eE$$

In general, the electric charge is the electrical displacement of the conductor multiplied by the area and therefore, for MFC with interdigitated electrodes the electric charge can be written as below when the electric field applies to the electrode area of dA.

$$q = \int D dA$$

Moreover, the electric charge, q, and the output voltage of MFC are related by the capacitance of the MFC as seen in Equation 6-6:

Equation 6-6

$$V_{MFC} = \frac{q}{C_{MFC}}$$

Where V_{MFC} and C_{MFC} are the output voltage and capacitance of MFC respectively.

It should be noted that the above equations are in general form and that in order to use them for calculations and analysis, the directions of parameters such as the stress and strain vector and the electric field need to be specified. Furthermore, the piezo-fibres in the MFC sensor are parallel to

each other and can therefore be modelled as a parallel plate capacitor. As such, the capacitance, $C_{MFC,}$ depends on the area of A and the separation distance between two plates, d, as shown in Equation 6-7.

Equation 6-7

$$dC_{MFC} = \varepsilon \frac{A}{d} = \varepsilon \frac{l_{MFC} b_{MFC}}{t_{MFC}}$$

Where l_{MFC} is the active length of the MFC, b_{MFC} is the active width of MFC minus the summation of the width of epoxy layers between piezo-fibres and t_{MFC} is the thickness. The schematic structure of MFC is shown in Figure 6-2.
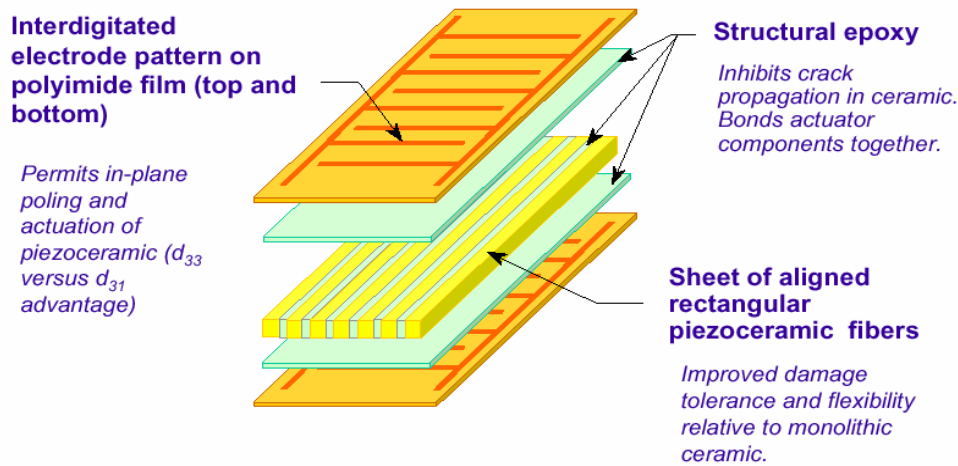
Figure 6-2: The structure of MFC (courtesy: www.smart-materiaol.com)

As we use the d_{33} MFC in this project, the strain only occurs along the 3 (poling) direction and is averaged along this length of the MFC. Therefore, using Equation 6-5, and Equation 6-6, it can be shown that the output voltage of the MFC sensor is calculated from Equation 6-8:

Equation 6-8

$$V_{MFC} = \frac{d_{33} Y_a l_{MFC} b_{MFC}}{C_{MFC}} \varepsilon$$

where d_{33} is piezoelectric coefficient, Y_c, is Young`s modulus and ε is the MFC strain. Therefore, the strain generated by the MFC is calculated from Equation 6-9.

Equation 6-9

$$\varepsilon = \frac{V_{MFC} C_{MFC}}{d_{33} Y_a l_{MFC} b_{MFC}}$$

161

In order to use the above equation to accurately determine the relationship between induced strain and generated voltage, the geometrical details of the type of MFC used in this research are shown in Table 6-1. However, the relationship presented in Equation 6-9 is not exactly the strain of MFC due to certain errors which must be corrected. The first set of errors is due to the shear lag effect (Sirohi et al. (2000)) which causes the strain on the MFC to differ from that on the host structure. This is due to the bonding layer which has a finite bonding layer thickness. According to Sirohi et al. (2000) and Bhalla et al. (2004) the correction factor for this error, K_s, is: (

Equation 6-10).

Table 6-1: Properties of MFC Type P1 M410

Model	M-410-P1
Overall Dimensions	54 mm $\times$ 22 mm
Active area dimensions (l_a, b_a)	40 mm $\times$ 10 mm
Max voltage	500 to 1500 V
Max tensile strain	< 4500 ppm
Thickness (t_c)	approx. 0.25 mm
Piezoelectric coefficient (d_{33})	3.74E-10 C/N
Young`s modulus (Y_c)	30.34 GPa

Equation 6-10

$$K_S = l_{eff}.b_{eff}$$

Where l_{eff} and b_{ff} are the effective length and width fractions of the MFC transducer respectively.

Furthermore, the assumption of having the strain in only 1-poling direction of the MFC is not completely accurate and requires some refinement. The experimental work conducted in this area also confirms the aforementioned statement and concludes that the correct assumption is to have strain in the 2-poling direction. Sirohi et al. (2000) have shown that the correction factor for Poisson`s effect, K_p, is as shown in Equation 6-11:

Equation 6-11

$$K_p = 1 - \nu$$

where ν is the Poisson`s ratio of the host structure. Using the above refinements, the final and correct relationship for the strain of the MFC sensor can be calculated from Equation 6-12 as shown below:

Equation 6-12

$$\varepsilon_{MFC} = \frac{V_{MFC}C_{MFC}}{K_s K_p d_{33} Y_a l_{MFC} b_{MFC}}$$

The strain value calculated using the above equation is considered as ε_{MFC} in future calculations.

6.4. Theoretical Strain Calculations (ε_T)

The next set of strain values is calculated based on the geometry of the 3-point-bend test and the equation of maximum deflection for the carbon/epoxy plate. In general, the MFC sensor generates electricity due to deformation or external loading. The MFC is bonded to the surface of the carbon/epoxy plate (thickness 1.6 mm) and placed in the experimental setup (refer to manufacturing section for further details). The applied vertical loading (3-point-bend test) causes deflection in the plate which can then be used to calculate the level of strain in the structure accordingly. As the MFC is bonded to the structure, by assuming the perfect bonding between MFC and the structure, then the strain level of the plate should be the same as the strain in the MFC sensor because the host structure is a thin plate. The aim of this section is to relate the vertical displacement of the plate's central point to the strain using the equation of deflection as well as the geometry of the 3-point-bend test configuration. The bending moment of the plate can be written as Equation 6-13:

Equation 6-13

$$M = \frac{-Fx}{2}$$

Where F is the applied load and x is measured from the left span. The bending moment by definition is described by Equation 6-14:

Equation 6-14

$$M = EI\frac{d^2y}{dx^2}$$

And the integration procedure leads to:

$$\int EI\frac{d^2y}{dx^2}dx = \int \frac{-Fx}{2}dx$$

$$EI\frac{dy}{dx} = \frac{-Fx^2}{4} + C_1$$

$$x = L/2, \frac{dy}{dx} = 0 \rightarrow C_1 = FL^2/16$$

$$\xrightarrow{\int} EIy = \frac{-Fx^3}{12} - \frac{-FL^2x}{16} + C_2$$

$$x = 0, y = 0 \rightarrow C_2 = 0$$

Therefore, the equation for the deflection of the beam is derived as Equation 6-15:

Equation 6-15

$$y = \frac{Fx}{48EI}(3L^2 - 4x^2)$$

As a result, the displacement of the central points (x=L) is calculated from Equation 6-16:

Equation 6-16

$$\delta = \frac{FL^3}{48EI}$$

where δ is the vertical displacement, b is the width of the plate, h is the height; L is the length of the support span and I is the second moment of area, which for the rectangular shapes can be written as $I=bh^3/12$.

Moreover, the basic governing equations in the 3-point-bend loading configuration according to the literature are shown in Equation 6-17:

Equation 6-17

$$\frac{M}{I} = \frac{E}{R} \quad , \quad \frac{M}{I} = \frac{\sigma}{y}$$

Where R is the radius of curvature of the plate and σ is the tensile/compressive stress on a plate with the distance of "y" from the neutral axis. By replacing the above equations in the 3-point-bend governing equations, the stress at the centre point of the surface can be written as Equation 6-18 (x=L/2, y=h/2):

Equation 6-18

$$\frac{FL/4}{bh^3/12} = \frac{\sigma_{max}}{h/2}$$

$$\Rightarrow \sigma_{max} = \frac{3FL}{2bh^2}$$

By combining Equation 6-16 and Equation 6-18, the relationship between the vertical displacement of the centre-point and its stress can be obtained from Equation 6-19.

Equation 6-19

$$\sigma = \frac{4Eb}{L^2}\delta$$

Finally, the strain-displacement relationship can be calculated from Equation 6-20:

Equation 6-20

$$\varepsilon = \frac{4b}{L^2}\delta$$

In this experiment, b=140 mm and L=250 mm and therefore the relationship between the vertical displacement and strain can be shown by Equation 6-21.

Equation 6-21

$$\varepsilon = 0.00896\delta$$

By measuring the displacement, strain in the fibre direction can be calculated by Equation 6-21.

6.5.   Finite Element Method (FEM)

The calculation of strain, based on the geometry of the test and equation of deflection, is applicable as long as the dynamics of the structure and loading configuration are predictable and the governing equations are available. However, the use of this calculation method can be hard and sometimes impossible for complex configurations and multiple numbers of transducers. The governing equations for structures with complex dynamic behaviour are not available and the derivation of these equations is relatively complex and inaccurate. This is even more unpredictable if the structure is in-service in the actual functioning environment, such as aircraft in-service in the harsh environment. As the purpose of this work is to present a practical technique which can not only be used on a laboratory scale but also in real-life conditions, FEM is used to calculate the theoretical strain of MFC as a replacement for the geometry-based theoretical strain calculation in the case of complex geometry of the structure or combined loading.
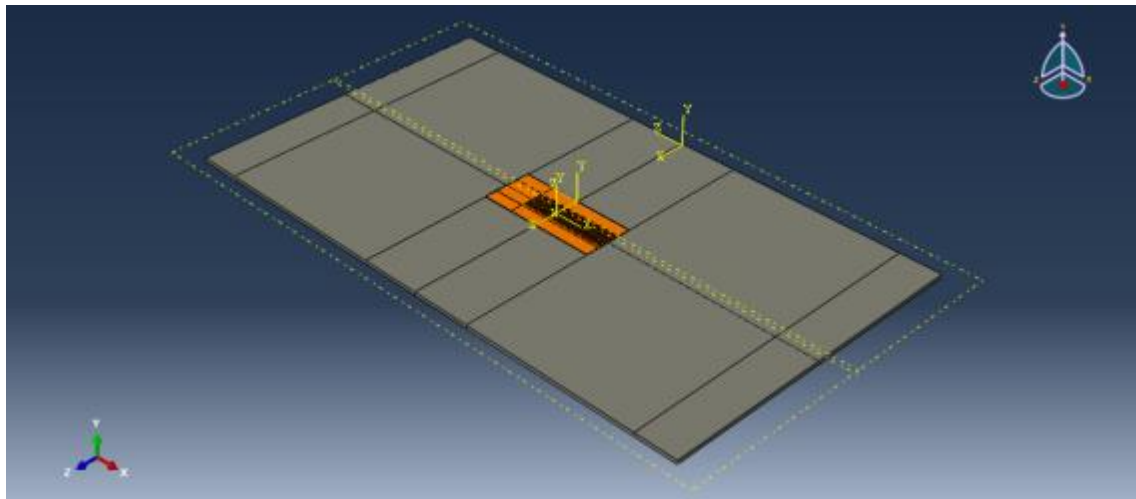
(a)
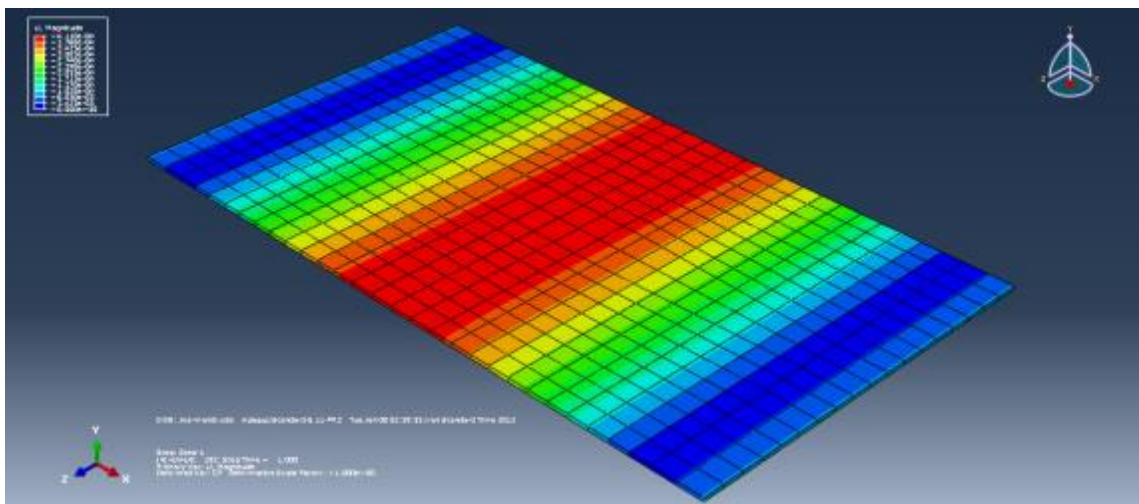
(b)

Figure 6-3: Simulation of MFC sensor bonded on Carbon/epoxy plate;
(a) Simulated model, (b) Vertical Deflection

For this purpose, an FEM model is developed using ABAQUS™ software to simulate the performance of MFC under the mentioned loading conditions. The strain level of the MFC can be calculated using ABAQUS software and this is used as the theoretical strain value in the strain-based technique. Figure 6-3 shows the FEM simulation of the carbon/epoxy plate with the MFC sensor. The details of the MFC modelling are provided in the FEM chapter. The visualisation of the simulated model at various strain levels is presented in Figure 6-4.
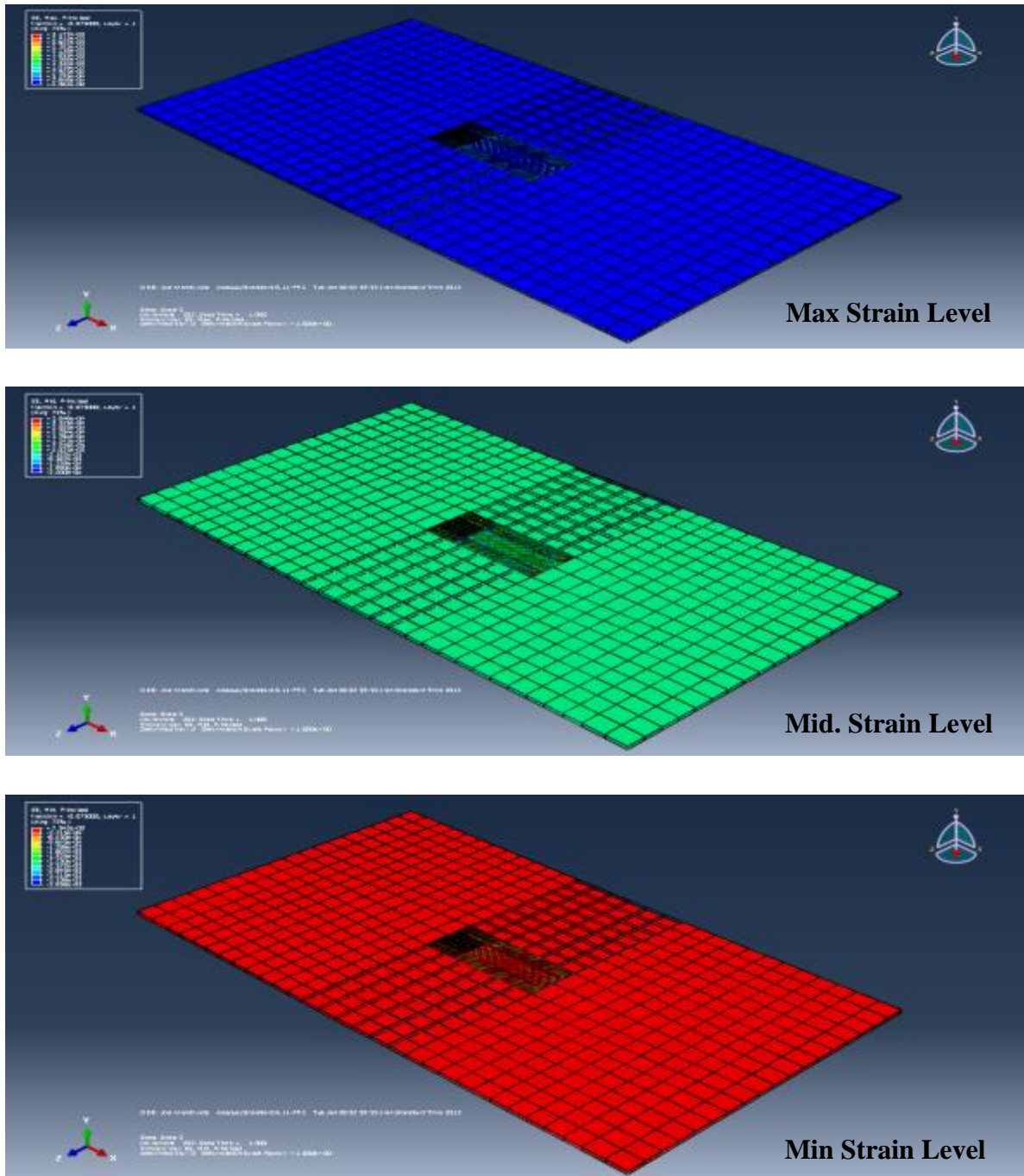
Figure 6-4: The strain distribution levels of simulated model (MFC bonded to the carbon/epoxy plate)

In order to validate the FEM simulation of MFC and the carbon/epoxy composite plate, the FEM results must be evaluated by using experimental measurements. However, it is also important to make sure that the bonding layer between the MFC and the composite structure is properly defined and that the two parts are accurately tied together in the FEM simulation. For an ideal interaction, the strain level at the bottom of the sensor and top of the structure (tied surfaces) should be similar. The "X-Y data" tool in ABAQUS is used to plot the stain level at nominated integration point at the bottom surface of the MFC and relevant integration point on the top of the carbon/epoxy plate. The comparison of the strain levels is presented in Figure 6-5.
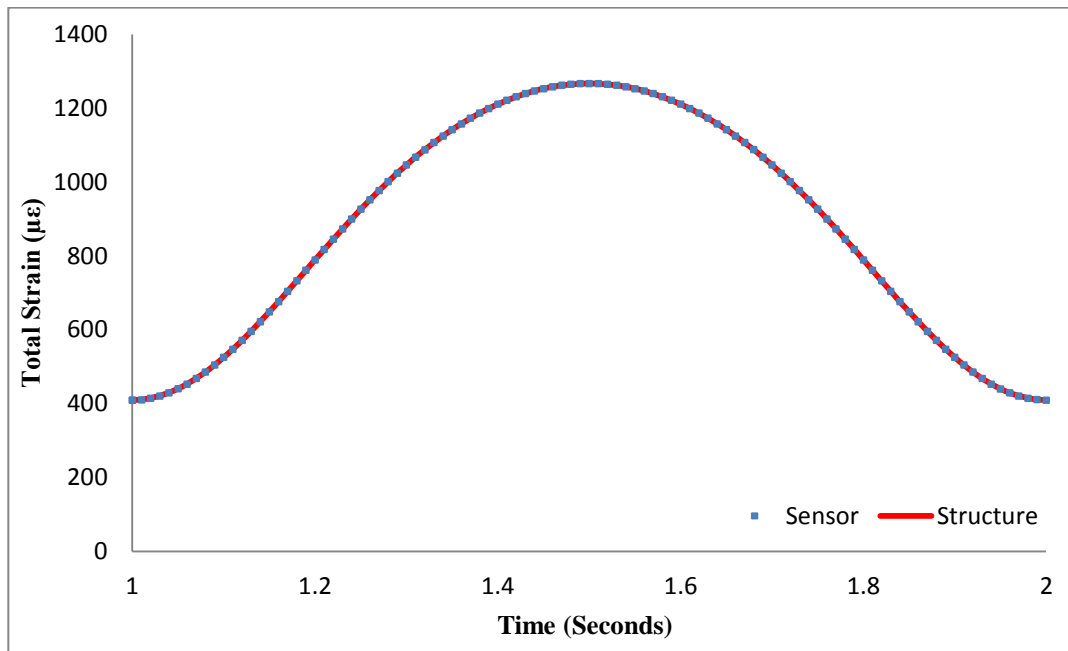
Figure 6-5: Comparison of strain levels at tied surfaces of the MFC and the structure

There are various strain fields which can be calculated through the ABAQUS simulation. The X-Y function of ABAQUS is used to tabulate the nominated output field and export it into EXCEL software using the Excel Utilities Plugin. In the visualisation module of the ABAQUS software, it is important to know which output is the required one. It is also necessary to understand the relationship of variables between the engineering and ABAQUS output in the Visualisation Module, as this will help users to obtain correct data analysis and carry out validation. The engineering strain (nominal strain) and engineering stress (nominal stress) can be expressed as Equation 6-22:

Equation 6-22

$$\varepsilon_{eng} = \frac{\Delta l}{l_0} \quad and \quad \sigma_{eng} = \frac{F}{A_0}$$

168

Where Δl is the extended length, the l_0 is the original length, F is the applied force and A_0 is the original cross-section.

In the ABAQUS simulation, the results are usually true strain (represent in ABAQUS as "LE") and true stress (Mises stress). Engineering stress and strain can be converted to true stress-log strain using Equation 6-23:

Equation 6-23

$$\varepsilon_{true} = \ln\left(1 + \varepsilon_{eng}\right) \quad and \quad \sigma_{true} = \sigma\_eng(1 + \varepsilon)$$

It is also possible to define the strain output as nominal strain (NE) which is the same as engineering strain. The total strain of the simulated model under defined loading and boundary conditions is plotted in Figure 6-6.
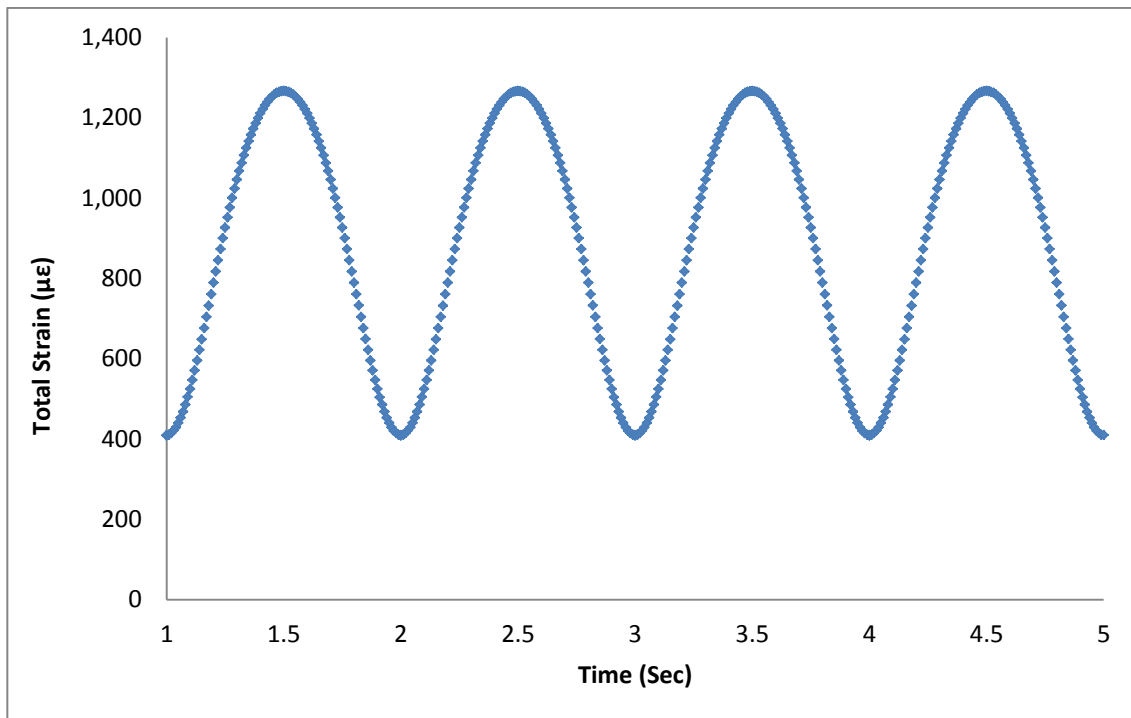
Figure 6-6: The total strain calculated by ABAQUS simulation

6.6.   Strain Gauge Measurement (ε_{SG})

The next set of strain values is measured using the strain gauge device. The strain gauge is the most commonly used device for the measurement of strain. The strain gauge is bonded to the structure by means of an adhesive at the same location as the MFC sensor but at the bottom of the plate, as shown in Figure 6-7. The strain gauge continuously measures the strain level of sample and records

the strain level of its local area. As the MFC sensor is bonded at the centre of the structure, the strain gauge is also bonded at the centre of the host structure to make the comparison possible. The test rig is shown in Figure 6-7. While the datataker is used to collect the voltage responses of the MFC, the strain indicator and recorder is also used to record the strain values measured by the bonded strain gauge. It should be noted that the gauge factor (GF) of the strain gauge should be considered when setting up the test rig.
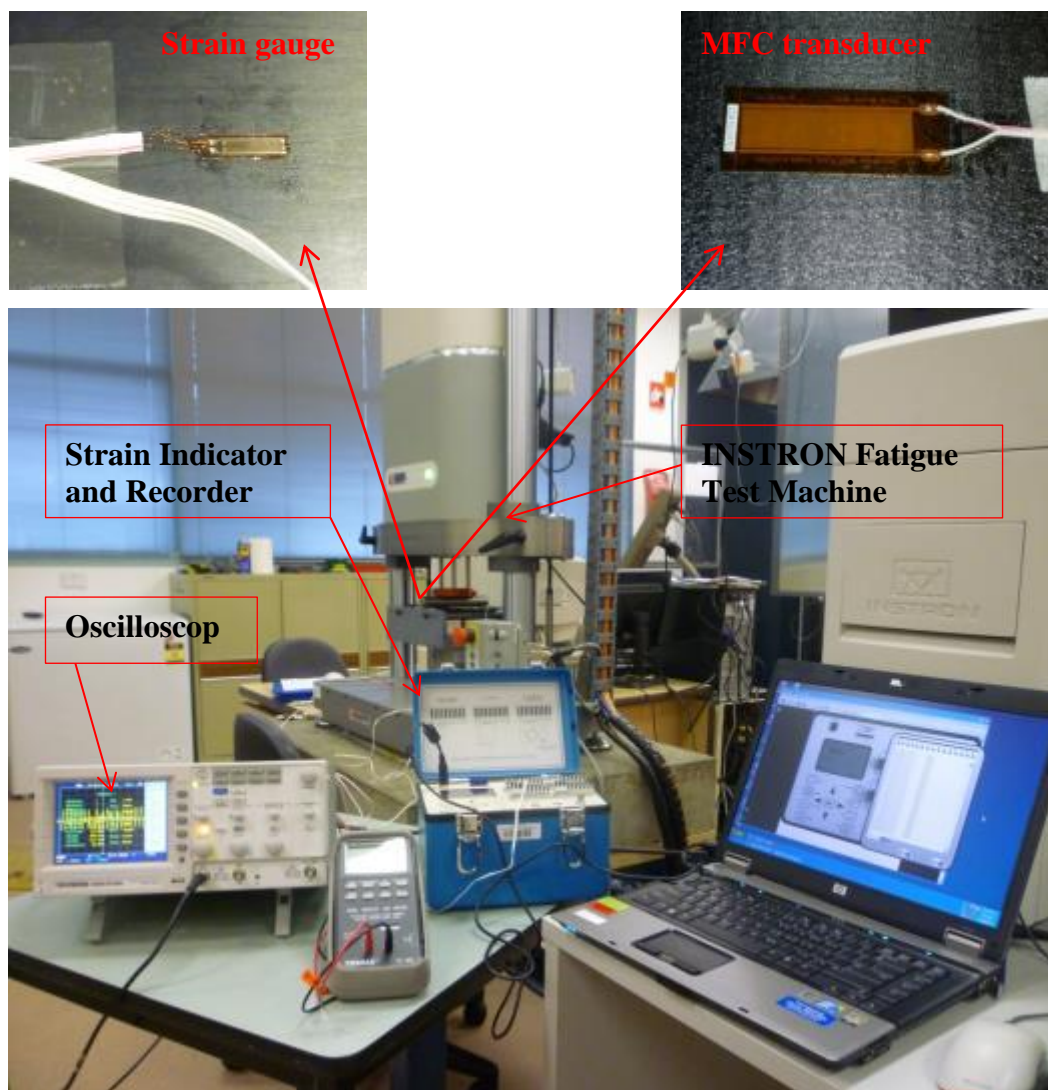
Figure 6-7: The strain measurement test rig

The strain gauge is connected to the Vishay P3 strain indicator and recorder which measures the strain level and transfers the values to the software on the computer through USB cables. By considering a perfect bonding between the strain gauge and structure, which is a valid assumption as the FEM results validate the experimental measurements, the strain level of the structure in the designated loading range is measured using the strain gauge. The strain gauge measurements are shown in Figure 6-8.

170
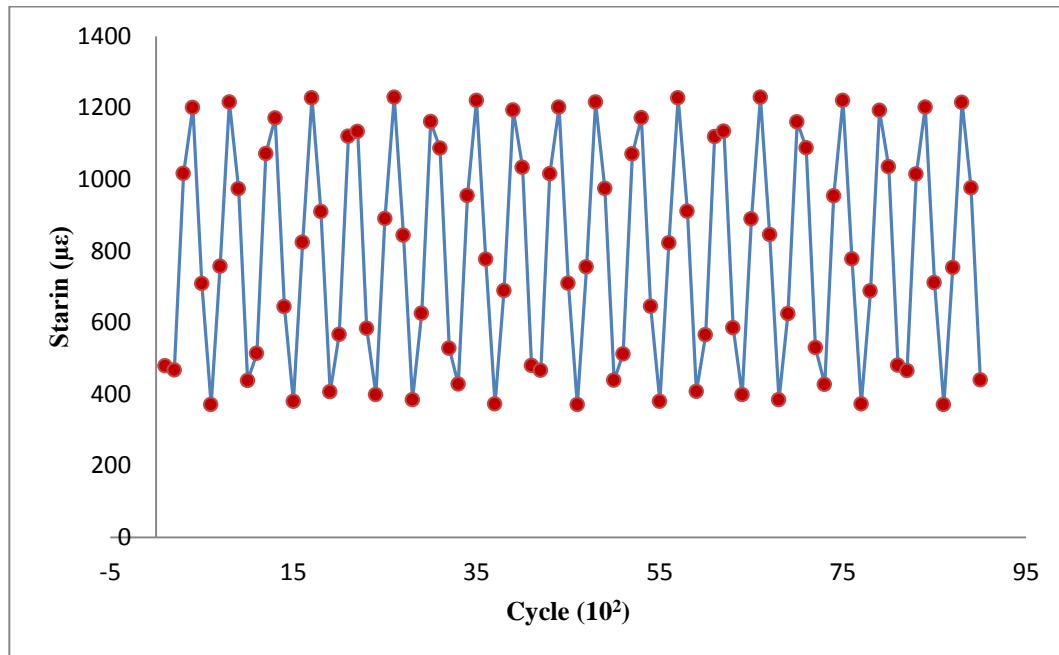
Figure 6-8: Strain gauge measurements

6.7.   Strain-based Delineation Technique

In the previous sections, three sets of strain values are experimentally measured and numerically simulated. The comparison of these strain values can be used to delineate the structural damage from sensor damage. From the work presented in this chapter, three scenarios can be considered in relation to the sensor/structure status. In the first scenario, the degradation of the sensor occurs prior to the structural damage. In the second scenario, the structural damage occurs when the sensor is still intact. This would be the most likely situation. In this scenario, the sensor is still intact and hence the changes in the sensor responses can be used to monitor any damage in the structure. However, the third scenario is more complex and has not yet been properly addressed. In this scenario, the degradation in the structure occurs when the sensor is already degraded. With this situation, the electrical properties of the sensor are already degraded at the time of the structural damage and therefore any further changes in the sensor response can be indicative of the progressive degradation in the sensor or the damage in the structure. These different scenarios are discussed in the following sections.

6.7.1. Healthy Transducer – Damaged Structure

In this scenario, the structural damage occurs when the sensor is still intact. This would be the most likely situation. Indeed, the sensor is still intact and therefore the changes in the sensor responses can be used to monitor any damage in the structure. The increase of the $\Delta_{structure}$ (defined below) in the strain-based technique demonstrates the degradation in the structure.

171

To address this issue, the strain measurements from strain gauges, ε_{sg}, are continuously captured and compared to the strain calculated from theoretical equation ε_T (FEM simulation). As long as the structure is intact, the difference between ε_T and ε_{sg} ($\Delta_{structure}$) is close to zero (Equation 6-24).

Equation 6-24

$$\Delta_{structure} = |\varepsilon_T - \varepsilon_{SG}|$$

However, once the degradation starts in the structure in the form of a crack, or delamination, $\Delta_{structure}$ begins to increase as the damage in the structure will result in a reduction of the strain gauge measurements. Figure 6-9 shows $\Delta_{structure}$ versus the number of cycles. Here, the difference between the theoretical strain and the strain gauge measurements is close to zero as expected up to 340000 cycles. However, there is a significant increase at around 340000 cycles, thereby demonstrating the change in the strain gauge measurements. This change can be indicative of structural damage. It should be noted that the strain gauge itself is considered to be intact as the failure of the strain gauge can account for the zero result in strain gauge measurements.
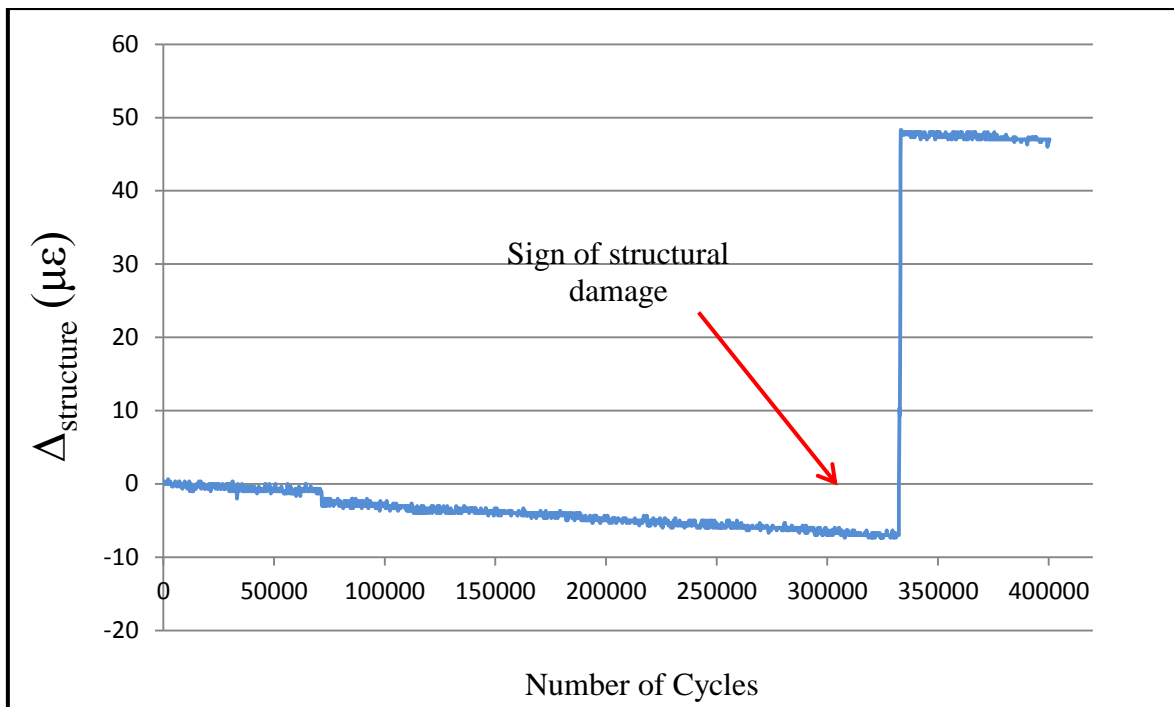
Figure 6-9: Difference between the calculated strain and strain gauge measurements of the host structure

6.7.2. Damaged Transducer – Healthy Structure

The MFC sensor generates electricity due to the deformation or external loading. As the MFC is bonded to the structure, by assuming the intact bonding between MFC and the structure, the strain

172

level of the plate should be the same as the strain in the MFC sensor. In order to detect degradation in the MFC, the strain values which are calculated from the MFC output voltage are consequently compared with the theoretical strain value. As long as the MFC is intact, the strain calculated from the theoretical relations (FEM simulation), ε_T, is the same as the strain derived from the MFC output voltage, ε_{MFC}. This is due to the fact that the fibres within the MFC bend in the same way as the host structure. However, once the degradation in the MFC sensor starts, these values will diverge due to the micro-cracks within the piezoceramic fibres caused by the fatigue. This difference can be used to monitor the degradation of the MFC sensor itself.

Equation 6-25

$$\Delta_{sensor} = |\varepsilon_T - \varepsilon_{MFC}|$$

Indeed, it can be concluded that the following rules are applied to the MFC sensor status.

$$if\ \Delta \cong 0\ \rightarrow \text{The MFC is intact}$$
$$if\ \Delta > 0\ \rightarrow\ \text{The MFC is damaged}$$

The Δ_{sensor} values are plotted in Figure 6-10. It can be seen that there is a gradual increase in the trend. This increase can be indicative of the degradation in the sensor due to fatigue. The degradation of the sensor causes a reduction in the ε_{MFC} and accordingly increases the Δ_{sensor}. The small fluctuations in the trend are due to the effect of the environmental noise and interference in the output voltage of the sensor. Furthermore, a considerable increase is observed from this graph after 150000 cycles which is indicative of the sensor damage. This is confirmed by visually inspecting the damaged transducer with an optical microscope.

6.7.3. Damaged Transducer – Damaged Structure

However, the third scenario is more complex and has not yet been properly addressed. In this scenario, the degradation in the structure occurs when the sensor is already degraded. In such a situation, the electrical properties of the sensor are already degraded at the time as structural damage and therefore any further changes in the sensor response can be indicative of the progressive degradation in the sensor or the damage in the structure. The presented strain-based technique can be used to differentiate the sensor degradation from structural damage in the third scenario. The continuous monitoring of the MFC sensor output voltage (strain) along with the reference values from theoretical calculations (FEM simulation) and strain gauge measurements can

173

be used to delineate the sensor damage from structural damage when both forms of damage are present in the structure. The above equations for the damaged structure and damaged sensor are still applicable in this scenario. The strain-based technique presented in this chapter is deemed capable of differentiating the sensor degradation from structural damage as it shows relatively good sensitivity to both damage scenarios.
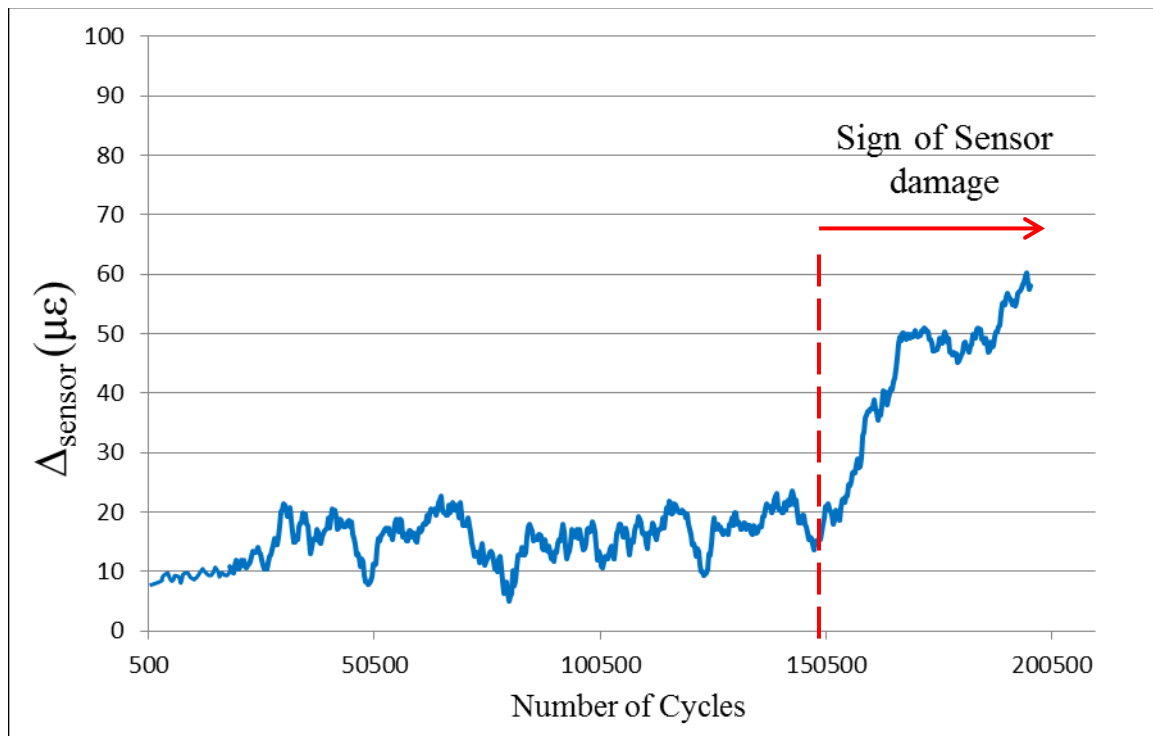
Figure 6-10: Difference between the calculated strain and MFC strain measurements

6.8. Summary

This chapter addresses the characterisation of the sensor response in order to assess the status of the host structure whilst the senor itself is also addressed. The strain-based technique is presented and its capability to differentiate between the sensor damage and the structural damage is discussed. This technique is based on the comparison of three sets of strain values, namely: strain gauge measurements, MFC strain measurements and theoretically calculated strain. The strain gauge, which is the most commonly used device for strain measurement, is bonded onto the bottom surface of the carbon/epoxy plate in order to provide the first set of strain values. The data is collected using a data-logger during the cyclic fatigue loading. The second set of strain data is calculated based on the output voltage responses of the MFC sensor which is bonded on the top surface of the carbon/epoxy plate as well. The constitutive equations of piezoelectric material are used as a basis to successfully derive a dedicated relationship for the type of MFC used in this project and to calculate the strain level of MFC using the generated voltage. The general form of this derived

relationship can also be used for other projects by defining the appropriate properties of the sensor into the relationship. This relationship is employed, along with the output voltage of MFC due to cyclic loading, to calculate the strain for the type of MFC used in this project. The comparison of the MFC strain calculations with the strain gauge readings has validated the accuracy of this analytical technique. Finally, the third set of strain data is calculated based on the theoretical relationship between the geometry of the 3-point-bend test and sample, applied loading and strain level on the sample. A relationship is derived which can be used to calculate the strain based on the displacement of the centre of the sample. However, it is observed that the capability of this method is limited and is only valid for simple configurations and geometries. Therefore, the FEM-based software package known as ABAQUS is used to simulate the designated sample in order to provide us with the theoretical value of strain for complex situations. The strain distribution of the simulated model under identical loading conditions to the experiments is numerically calculated using ABAQUS/Solver. Furthermore, the FEM results are also used to validate the experimental measurements.

This novel strain-based technique is successfully tested and observations reveal that the difference between theoretically calculated strain and the strain gauge measurements should be close to zero as long as the structure is intact and any increase in this difference can be indicative of structural degradation. Moreover, the comparison between MFC strain measurements and the calculated strains from theoretical equations can be used to monitor the status of the sensor itself. As long as the difference between these two values is close to zero, the sensor can be assumed to be structurally sound. This technique is also experimentally tested for samples with various structure-sensor damage statuses. The results show that the present approach is capable of differentiating the degradation in the sensor from the structural degradation which yields an improved methodology to address one of the main concerns in regards to the functionality of the transducers in SHM systems.

CHAPTER 7 Electromechanical Impedance-based Technique

7.1. Introduction

The main principle in Electromechanical Impedance (EMI)-based Structural Health Monitoring (EISHM) is that the electrical impedance of the piezoelectric transducer, which is bonded to the structure, is coupled with the mechanical impedance of the host structure and therefore any change in the structural integrity will affect the electrical impedance of the transducer. The Lead Zirconate Titanate (PZT) transducers and their new generation of fibre-based transducers such as Macro Fibre Composite (MFC) have been widely used in the EMI/SHM field. A variety of electromechanical impedance-based techniques have been investigated recently by researchers mostly in terms of how to identify single damage in the host structure (Park G. et al., 2006). However, the actual scenario in terms of transducer-structure interaction is different as the structure can be affected by multiple damage conditions. Furthermore, the transducer itself is also subject to possible damage and degradation which must also be considered. This is important as it may lead to false positive or false negative situations. These situations can considerably affect the reliability of all the efforts which have been made to use the electromechanical impedance signatures of the transducer to monitor the status of the host structure (Giurgiutiu, V. et al, 1998 and Park G.H.et al., 2004). In fact, these efforts have led to a number of novel electromechanical impedance–based systems; the effectiveness of which has already been proven. Nevertheless, most of these techniques are focussed on detecting the damage in the structure using the bonded piezoelectric transducer and are not capable of monitoring the propagation of the initial damage in the structure and the status of the transducer itself. In other words, the capability of using the electromechanical impedance of the system to delineate the structural damage from the transducer damage needs to be investigated as this could solve one of the main issues in the body of knowledge related to existing SHM techniques.

In this chapter, the Macro Fibre Composite (MFC) transducer bonded to the structure is used to monitor the status of the structure and also to determine the effect of damage/degradation within the MFC itself on electromechanical impedance measurements. These goals are achieved through a series of experiments on the specimens with the artificial damage in various locations of the

structure and the MFC transducer. The electromechanical components, including real impedance (resistance) and imaginary impedance (reactance), are measured for each damaged specimen and compared to the healthy specimen, in order to obtain valid and practical parameters which are capable of delineating various damage scenarios such as structural damage or transducer damage etc. This task can be achieved through the continuous measurement of specific component(s) of the electromechanical impedance, with more sensitivity to the damage in the structure or the transducer. Finally, these experimental measurements are compared to Finite Element Method (FEM) calculations in order to validate experimental results.

Structural Health Monitoring (SHM) techniques have been the subject of many studies, developments, and applications over recent years. The main objective of all these efforts is to make the civilian and military infrastructures safer, more reliable and durable. Among all these studies, the piezoelectric active sensing approach in general, and the electromechanical impedance method in particular, have received the most attention due to their many advantages such as compactness, light-weight, low-power consumption (Park et al., 2003), ease of integration into critical structural areas, ease of activation through electrical signals, higher operating frequencies, and low cost (Overly et al., 2008). The basic principle of the electromechanical impedance method is to use high frequency vibrations to monitor the local area of a structure for changes in structural impedance which would indicate damage or imminent damage (Overly, T.G.S. et al., 2008). However, the main focus of this chapter is on the sensor self-diagnostics application of the impedance method. The AD5933 network analyser kit, which is the Analog Device Inc. low-cost solution for real world and low cost impedance measurements (Overly, et al., 2008), is used in this research as a miniaturised solution to present an impedance-based structural health monitoring system. The goal of this chapter is to develop a technique with which to delineate the damage in the structure from the degradation/damage in the transducer through an extensive analysis of the transducer's electromechanical impedance components. The development of a device which meets these requirements is critical in transitioning from the current practice of SHM to field deployment.

In order to evaluate the functionality of this technique, 6 samples are made with induced damage at the various locations of the transducer and the structure. The aim of this process is to identify the impact of transducer damage/degradation and structural damage on the electromechanical impedance measurements of the transducer.

7.2. Electromechanical Impedance-based Technique

7.2.1. Background of the Impedance Technique

As previously mentioned, the impedance-based technique has become one of the main focusses of research in the field of structural health monitoring (SHM). This is mainly due to the clear advantages of the technique over other methods. The impedance technique was first presented by Liang, Sun & Rogers (1994) and the application of piezoelectric material in this technique was investigated by Sun (1995) through a series of frequency-dependant experiments. The possibility of employing the impedance technique for SHM technology was widely investigated by Chaudhry (1995). He conducted a series of experiments to determine the effect of the distance between structural damage which is both close and far from the piezoelectric sensor (Mascarenas et al., 2006). Bois (2004) was one of the first researchers to use PZT sensors for the detection of delamination damage in the composite structure.

The detection of abrasive wear and tooth bending fatigue in precision gears using the impedance method was carried out by Lalande (1996). In addition to this, one of the initial extensive works was conducted by Wang (1998) and this sought to monitor the molding transfer process for composite manufacturing setting. The importance of this work lay in the fact that it was possible to correlate electromechanical response characteristics with both the area of a PZT wafer which was wetted with resin and with the extent to which the resin had cured. The applications of the impedance method in built-in-bridge structures were evaluated by both Ayres (1998) and Park et al. (2000), where the impedance method showed its ability to detect damage even in extreme conditions. Pohl (2001) studied the ability of the impedance method to detect low velocity impact damage in FRP plates. Lin et al. (2010) investigated the possibility of using the impedance method for metallic structures. These are only a few examples of work which has been done on the initiation and improvement of the impedance-based SHM technique over the last few years. This information would help to identify the gaps which need to be filled in order for this method to be completely practical and useful in real life. These gaps and challenges are presented in the next section.

7.2.2. Current Gaps and Challenges

The impedance-based method has become one of the major tools used in Structural Health Monitoring due to its many advantages such as using small size transducers, low power requirement, being model-independent and using high frequency excitations for damage detection which eliminates environmental noise and vibrations (Wang et al., 2012). However, there are a

few disadvantages which must be addressed in order to improve the quality of the impedance-based technique. One of the issues with this method is the impedance analyser, which is used to collect electromechanical impedance measurements. The common impedance analysers such as Agilent 4294A are heavy-weighted and are not suitable for online damage detection outside the laboratory. They are also fairly expensive which increases the cost of the SHM system considerably. This calls for a low-weight, portable and low-cost impedance analyser with similar accuracy to that of the bulky impedance analysers.

Another challenge in the impedance-based method is to find the parameters with significant sensitivity to the possible damage in the host structure and/or the transducer. The continuous monitoring of these parameters will provide us with the possibility of detecting damage/degradation once the change is observed in the measurements. This has not yet been properly investigated in the current research and requires further work. In other words, the changes in the impedance measurements should be analysed in order to assess whether they represent the degradation/damage in the host structure, the transducer itself, or both in the most complex situation. This calls for comprehensive and more detailed investigation in order to determine appropriate parameters with the ability to delineate the degradation/damage in the structure from that in the transducer itself. Another important issue in any damage detection method is that it is repeatable. This is extremely important because the measurements should be identical and repeatable so that the changes observed in the measurements are only due to the damage/degradation rather than measurement error. In order for this method to be repeatable, the measurement technique should be consistent and accurate whilst the transducer must have enough sensitivity to possible changes in the integrity of the structure and in the transducer itself.

The purpose of this chapter is to address the issues associated with the current impedance-based methods and propose a practical technique which can be used on not only a laboratory scale but also in a real environment. This goal is targeted in this research project by suggesting a low-cost, miniaturised and accurate setup which is capable of activating the transducer, collecting its responses and characterising the responses to detect and diagnose the generation or propagation of damage/degradation in the transducer and the structure.

7.2.3. Electromechanical Impedance Theory

The transducers used for impedance-based SHM are based on the direct effect of piezoelectric material where a piezoelectric material generates an electrical charge when mechanically strained. In general, measurement of the structure's dynamic characteristics using a piezoelectric transducer in order to determine the status of the structure is called Impedance-based SHM. This is due to the

coupling between the electrical impedance of the transducer with the mechanical impedance of the host structure. The mechanical impedance can be defined as Equation 7-1 (Qiu, 2010):

Equation 7-1

$$Z_{mechanical} = \frac{Force}{Velocity}$$

An overview of the impedance method used in this project is summarised as follows, (see Figure 7-1):
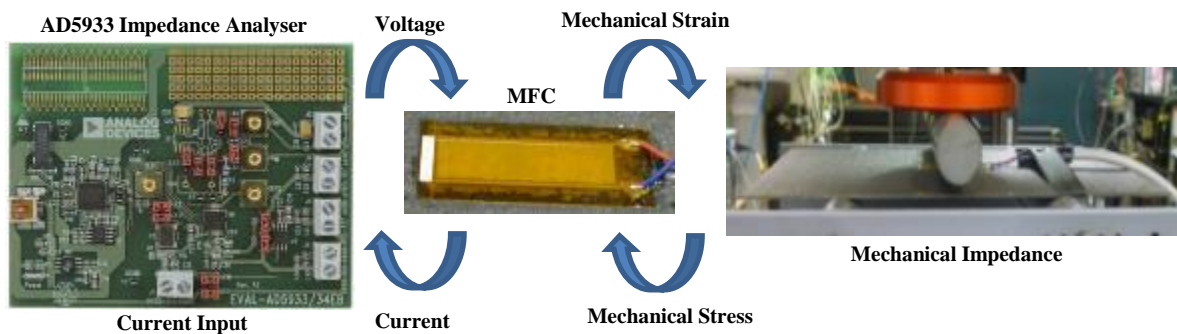
Figure 7-1: Block diagram of the Impedance method

The impedance analyser excites the piezoelectric transducer bonded to a structure with a sinusoidal signal. This electrical excitation generates the mechanical excitation in the transducer due to its converse effect. The bonding layer transfers the mechanical excitation to the structure which affects its structural dynamics through mechanical impedance relations. As the transducer is bonded to the structure, any change in the dynamics of the structure also affects the transducer. Therefore, the change in the mechanical impedance of the structure causes a strain on the transducer. The direct effect of the transducer converts this mechanical strain to a current output in the piezoelectric transducer. The ratio between the initial voltage induced to the transducer and the final output current applied to the transducer is generally called electromechanical impedance, and this is measured by the impedance analyser connected to the transducer electrodes. The measured electromechanical impedance is normally presented versus a designated frequency range. The impedance analyser determines the FRF (Frequency Response Function) of the structure and measures it over the designated bandwidth. As the structure becomes damaged, the mechanical properties of the structure such as damping, stiffness and mass will change. Each damage type normally affects one of the mechanical properties more than the rest. Therefore, any change in these properties also affects the mechanical impedance of the structure, which in turn changes the

frequency response function of the structure measured by the impedance analyser. Moreover, the status of the transducer's subcomponents such as electrodes, piezo-fibres, and protective area, would also affect the electromechanical impedance components. Therefore, the continuous measurement of the impedance can provide us with the ability to detect possible damage or degradation in either the structure or the transducer after observing the change in the measurements.

As shown by Waltengus et al. (2010), the relationship between mechanical impedance ($Z_s(\omega)$) and electrical impedance ($Z_{MFC}(\omega)$) can be written as Equation 7-2.

Equation 7-2

$$Y(\omega) = \frac{I}{V} = ia\omega \left(\varepsilon_{3x}^T - \frac{Z_s(\omega)}{Z_s(\omega) - Z_a(\omega)} d_{3x}^2 Y_{xx}^E \right)$$

where "V" is the excitation voltage, "I" is the current output from the PZT, "a" is a geometric constant, d_{3x}^2 is the piezoelectric coupling constant, Y_{xx}^E is the Young's modulus, and ε_{3x}^T is the dielectric constant of the PZT at the zero stress condition. This equation shows that the electrical impedance of the transducer is directly coupled with the mechanical impedance of the structure.

However, most of the recent work in impedance-based SHM mainly focussed on monitoring the status of the structure rather than the transducer. Therefore, it is common for these researchers to only consider the real portion of the impedance measurement for SHM applications and simply assume that the changes in the imaginary portion of the impedance measurement result solely from the temperature changes. However, this statement is only valid as long as the transducers and the bonding layer are intact and the structural damage is simple. It is observed in this research that even complex structural damage would affect the imaginary portion of impedance. However, once the transducer itself is degraded, the changes in the responses could be a false positive indication as the structure is still intact but the transducer is degraded. This is the area of SHM which has not been properly investigated by researchers, and it remains one of the main gaps in the body of knowledge surrounding Structural Health Monitoring.

Another issue with the impedance-based technique is to determine the optimum wavelength for excitation signal. This is a challenging issue as it needs to be sensitive enough to detect small damages and also global enough to estimate the size of the larger damage. According to Park et al. (2007), the wavelength of any excitation should be smaller than the characteristic wavelength of the damage to be detected. It is observed in this project that at very low frequencies (less than 10

KHz), the MFC transducer excitation is not enough to couple the electrical properties of the transducer with the mechanical properties of the structure and the measured electrical impedance is only valid to detect possible damage or degradation in the transducer itself. At very low frequency, the electromechanical coupling between the structure and the transducer is fairly weak as the excitation signal is not strong enough to actuate the structure. Therefore, the impedance measurements at extremely low frequencies (less than 300Hz) are subject to various noises and should be avoided. Furthermore, the appropriate signal wavelength is dependent on the nature of the test and the amount of noise in the environment. Generally speaking, the recommended frequency range for electromechanical impedance-based SHM testing is 10-400 kHz. However, this frequency range can be modified based on the nature of the test. Of course, the measurement of the electromechanical impedance over the whole range will significantly decrease the sensitivity of the readings and as such only a portion of this bandwidth is used for any application. While there is no standard to determine the appropriate frequency range for an SHM application, it was suggested by Figueiredo et al. (2012) and Park et al. (2006) that choosing the high frequency range makes the transducer more sensitive to small and local damage and also eliminates the impact of the bonding layer and environmental noises and vibrations.

In this research, the frequency bandwidth of 0.1-100 kHz is used based on the size of the structure and the MFC transducer and the size of induced damage. The selection of this frequency range is also designed to investigate the quality of electro-mechanical coupling between the transducer and the structure at low and high frequencies.

7.3. Application of MFC transducers in Electromechanical Impedance

One of the main areas of the electromechanical impedance-based technique is the piezoelectric transducer. As such, it is extremely important to properly determine the performance and application of the piezoelectric transducers. In general, two different approaches can be considered towards their application; static and dynamic (impedance). The static approach simplifies the behaviour of the piezoelectric transducer by assuming that the actuator force is frequency independent (Bhala et al., 2004). The actuator force is calculated by assuming the existence of static equilibrium between the strains, the transducer, and the structure.

In order to determine the performance of MFC in the static approach, the model shown in Figure 7-2 is used. In this model, the MFC is considered to be a thin bar in balance with the host structure. The top surface of the MFC, which is not bonded to the structure, is modelled as clamped while the other surface is bonded to the structure which is represented by its static stiffness. Therefore, the axial force caused by the plane stress can be written as Equation 7-3:

Equation 7-3

$$F_P = wh\sigma_3 = wh(\epsilon_3 - d_{33}E_3)Y^E$$

Where w is the width, h is the thickness, σ_3 is the stress in 3-direction, and ϵ_3 is the strain in 3-direction of the MFC.
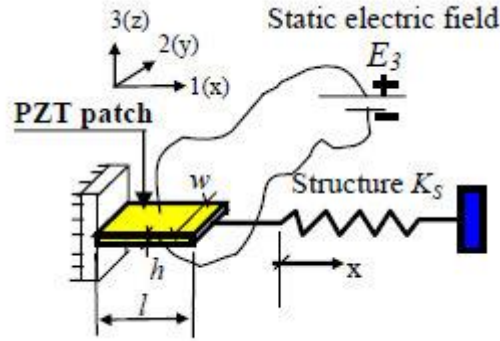
Figure 7-2: Modelling of MFC-Structure interaction by static approach (Bhala et al., 2004)

The axial force can be written as:

$$F_S = -K_s x = -K_s l\epsilon_3$$

Where x is the displacement at the top of MFC (end of MFC in the model) and l is the length of MFC.

The equilibrium of the force means that F_p and F_s should be equal and therefore the strain (ϵ_3) is calculated from Equation 7-4:

Equation 7-4

$$\epsilon_3 = \frac{d_{33}E_3}{(1 + \frac{K_s l}{Y^E wh})}$$

The assumption that MFC is in a static equilibrium with structure, neglects the damping in the calculations. These simplifications in the static approach only provide us with a rough estimation of the system status at low and extremely low frequencies, thus meaning that the level of error is significantly large. This is even more obvious for the frequencies close to the resonant frequency of the MFC or the structure.

In order to avoid these errors a more common and reliable approach, which is based on the dynamic behaviour of the MFC as well as the structure, is widely used. This is called the dynamic, or in more common terms the "electro-mechanical impedance", approach. In this approach, the

constitutive equations are derived with the assumption of dynamic equilibrium between the structure and the MFC transducer. In this model, the mechanical impedance, Z, represents the structure, and a vibrating thin layer represents the MFC, as shown in Figure 7 3. As is shown in Figure 7 3 b, the mechanical impedance is used instead of static stiffness in the dynamic approach.

(a)   (b)
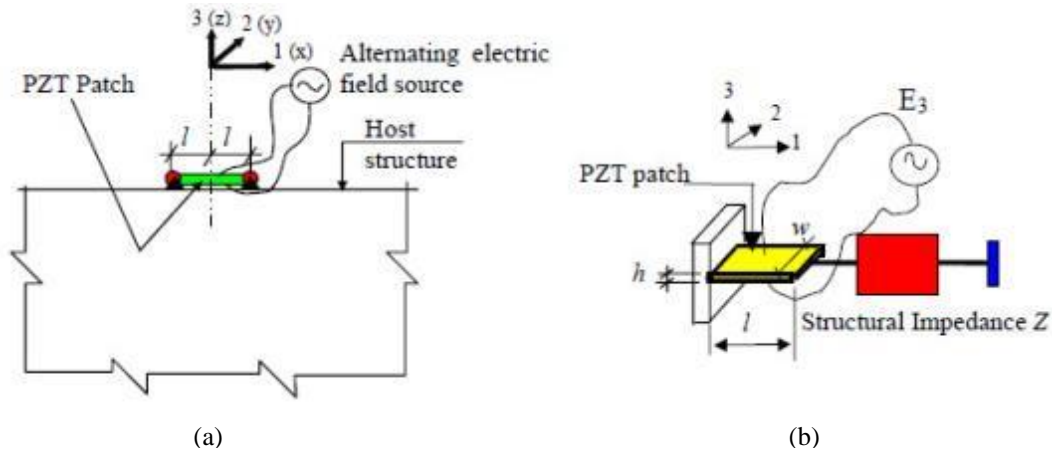
Figure 7-3: Modelling MFC-structure interaction by impedance (dynamic) approach. (a) MFC bonded to structure under electric excitation, (b) Model of right half of MFC and host structure (Bhala et al., 2004)

Based on the dynamic equilibrium of the MFC and structure, the governing differential equation can be driven by Equation 7-5.

Equation 7-5

$$\bar{Y}^E \frac{\partial^2 w}{\partial x^2} = \rho \frac{\partial^2 w}{\partial t^2}$$

Where w is the displacement at any part of MFC in direction 3, at any constant of time. By definition, the mechanical impedance of the structure is related to the normal force in MFC, as seen below (Overly et al., 2007):

$$F(x = l) = w\hbar\sigma_3(x = l) = -Z\dot{w}(x = l)$$

Where Z is the mechanical impedance and σ_3 is the stress in direction 3. As previously mentioned, the stiffness in the static approach should be replaced with the impedance (Z_{MFC}) in the dynamic approach, which is defined as Equation 7-6 (Bhala et al., 2004):

Equation 7-6

$$Z_{MFC}(\omega) = \frac{w_{MFC}\hbar_{MFC}Y^E}{j\omega l_{MFC}} \frac{kl_{MFC}}{\tan(kl_{MFC})}$$

184

Where w_{MFC} is the width, h_{MFC} is the height and l_{MFC} is the length of the active part of the MFC.

On the other hand, the mechanical impedance of the structure can be calculated from Equation 7-7.

Equation 7-7

$$Z_S = \frac{-m_s\omega^2 + j\omega C_s + K_S}{j\omega}$$

Where m is mass, C is the damping coefficient, ω is the excitation frequency, and K_S is the stiffness.

Therefore, the total impedance of a MFC transducer-structure system which is determined by the coupling between the electrical impedance of the MFC and the mechanical impedance of the structure can be written by using Equation 7-6 and Equation 7-7. This relationship is shown in Equation 7-8.

Equation 7-8

$$Z_{total} = \frac{V}{I} = \left[j\omega C \left(1 - k_{33}^2 \frac{Z_s(\omega)}{Z_{MFC}(\omega) + Z_s(\omega)} \right) \right]^{-1}$$

This electromechanical coupling can also be represented by the electrical admittance which is the transverse of electrical impedance (Equation 7-9).

Equation 7-9

$$Y(\omega) = \frac{1}{Z} = \frac{I}{V} = i\omega a \left(\bar{\epsilon}_{33}^T - \frac{Z_s(\omega)}{Z_{MFC}(\omega) + Z_s(\omega)} d_{33}^2 Y_{33}^E \right)$$

where d_{33} is the MFC coupling constant, $\bar{\epsilon}_{33}^T$ is the dielectric constant, a is the MFC material`s geometric constant, and $Y_{33}^E$ is the host structure`s complex young`s modulus with the zero electric field.

In Equation 7-8 and Equation 7-9, the geometrical details of the MFC and the coupling constant and dielectric constant of the MFC transducer are known. Therefore, using the above system of equations, the theoretical value of the electromechanical impedance can be calculated to verify the experimental and computational results.

7.3.1. Equivalent Circuit of MFC/Structure E/M Coupling

In electrical engineering, an equivalent circuit is normally used to simplify the calculation and analyse a more complex circuit in order to aid analysis. In this section, the equivalent circuit is used to identify the coupling between the electrical properties of the MFC transducer and the mechanical properties of the structure. Figure 7-4 presents the commonly applied electric circuit which is used for the electromechanical measurements (Roseik et al., 2010). This equivalent circuit consists of the following elements connected in a series: power supplier − electromotive force V_{IN}, piezoelectric transducer and referential resistor R. Therefore, the electromechanical impedance, Z_E, is calculated from Equation 7-10.

Equation 7-10

$$Z_E = \frac{V}{I} = \frac{V_{IN} - V_{OUT}}{V_{OUT}/R} = R \left(\frac{V_{IN}}{V_{OUT}} - 1 \right)$$
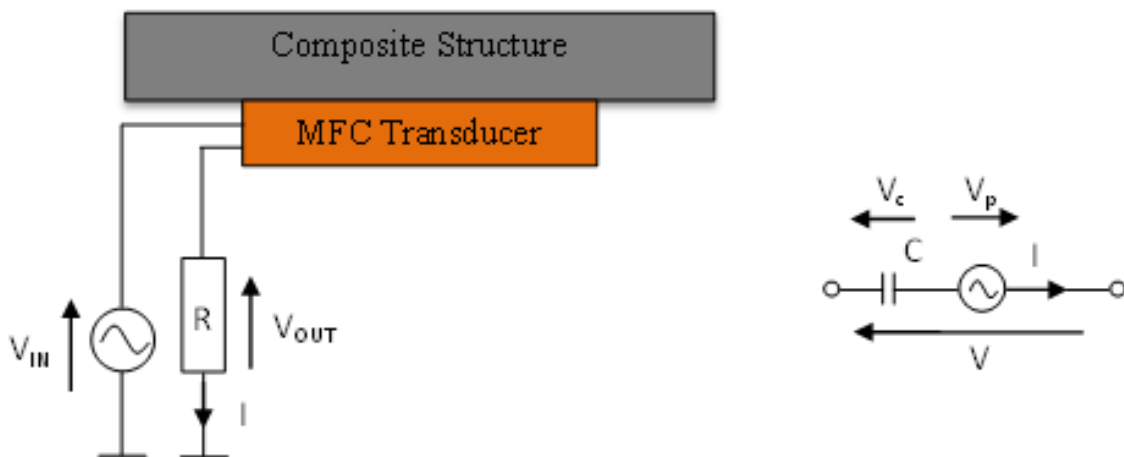
Figure 7-4: (a) Scheme of electric circuit used for measurement of electromechanical impedance,

(b) Resultant model of piezoelectric transducer (Roseik et al., 2010)

In the above figure, the referential resistor, R, is used to measure the current I. Moreover, the Voltage, V, which is the transducer voltage, can be calculated with known voltages V_{IN} and V_{OUT}. The piezoelectric transducer can be substituted with the series connection of capacitor C and electromotive force V_P as shown in Figure 7-4. Indirectly measured voltage V depends on the value of V_P generated in the piezoelectric transducer according to the direct piezoelectric effect. As a result, any change of mechanical properties caused by damage finally influences Z_E (Equation 7-10). This is also the case for the transducer because the damage in the transducer,

affects the V_P and/or C, based on the nature of damage, and therefore the output current would change, which is an indication of transducer damage/degradation.

7.4. Analytical Approach

The general form of constitutive equation for linear piezoelectric materials based on ANSI/IEEE 176-1987, describes a tensorial relationship between mechanical and electrical variables, as shown in Equation 7-11 (Rosiek et al., 2010):

Equation 7-11

$$\epsilon_{ij} = S^E{}_{ijkl}\sigma_{kl} + d_{kij}E_k$$

$$D_j = d_{jkl}\sigma_{kl} + \varepsilon_{jk}^T E_k$$

Where ϵ_{ij} is the mechanical strain, σ_{kl} is the mechanical stress, E_k is the electric field and D_j is the electrical displacement. Moreover, S^E is the mechanical compliance of the material at zero electro field (E=0),$\epsilon^T{}_{jk}$ is the dielectric permittivity at zero mechanical stress (σ=0), and d_{jkl} is the piezoelectric coupling between the electrical and mechanical variables. These constitutive equations can also be written using matrices (Equation 7-12):

Equation 7-12

$$\{\epsilon\} = S^E.\{\sigma\} + dt.\{E\}$$

$$\{D\} = d.\{\sigma\} + \varepsilon^T.\{E\}$$

Where D is the electric displacement in C/m^2, ϵ is the strain vector in V/m, σ is the stress in N/m^2, ε^T is the dielectric matrix, d is the induced strain, and S^E is the compliance matrix. As previously mentioned, the superscript T shows that the measurements are under a constant stress condition, while the superscript E represents a constant or zero electric field. The subscript is introduced to the transposed matrix. Furthermore, the constitutive equation in stiffness form, mechanical stress as a function of strain, and the electric field, can be written as Equation 7-13:

Equation 7-13

$$\{\sigma\} = C^E.\{\epsilon\} - e_t.\{E\}$$

$$\{D\} = d.\{\epsilon\} + \varepsilon^S.\{E\}$$

Where ϵ^S is the dielectric matrix, c^E is the stiffness matrix, e is the induced stress matrix and e^t is its transposed matrix. Comparing the above Equations, we can conclude Equation 7-14:

Equation 7-14

$$\{\sigma\} = (S^E)^{-1}.\{\varepsilon\} - (S^E)^{-1}.dt.\{E\}$$

$$\{D\} = d(S^E)^{-1}.\{\sigma\} + \varepsilon^T - d.(S^E)^{(-1)}.dt.\{E\}$$

Above Equations demonstrate the following relationship between property matrices:

$$\begin{cases} (S^E)^{-1} = C^E \\ e = d.(S^E)^{-1} = d.C^E \\ \varepsilon^S = \varepsilon^T - d.(S^E)^{-1}.dt \end{cases}$$

The matrices of piezoelectric coefficients d_{ij} and e_{ij} are defined as:

$$d_{ij} = \left(\frac{\partial D_i}{\partial \sigma_j}\right)^E = \left(\frac{\partial \epsilon_i}{\partial E_j}\right)^\sigma$$

$$e_{ij} = \left(\frac{\partial D_i}{\partial \epsilon_j}\right)^E = -\left(\frac{\partial \sigma_j}{\partial E_i}\right)^\epsilon$$

These are related to each other by a material constant matrix through Equation 7-15:

Equation 7-15

$$d = e\delta^E$$

It should be noted that "d" and "e" are determined not only at the constant electric field and strain or stress respectively, but also at a constant temperature. The effect of temprature on the piezoelectric coefficient values is negligible. So the expansion form is written as Equation 7-16:

Equation 7-16

$$\begin{Bmatrix} \epsilon_1 \\ \epsilon_2 \\ \epsilon_3 \\ \epsilon_4 \\ \epsilon_5 \\ \epsilon_6 \\ D_1 \\ D_2 \\ D_3 \end{Bmatrix} = \begin{bmatrix} S^E_{11} & S^E_{12} & S^E_{13} & S^E_{14} & S^E_{15} & S^E_{16} & d_{11} & d_{21} & d_{31} \\ S^E_{21} & S^E_{22} & S^E_{23} & S^E_{24} & S^E_{25} & S^E_{26} & d_{11} & d_{22} & d_{23} \\ S^E_{31} & S^E_{32} & S^E_{33} & S^E_{34} & S^E_{35} & S^E_{36} & d_{13} & d_{23} & d_{33} \\ S^E_{41} & S^E_{42} & S^E_{43} & S^E_{44} & S^E_{45} & S^E_{46} & d_{14} & d_{24} & d_{34} \\ S^E_{51} & S^E_{52} & S^E_{53} & S^E_{54} & S^E_{55} & S^E_{56} & d_{15} & d_{25} & d_{35} \\ S^E_{61} & S^E_{62} & S^E_{63} & S^E_{64} & S^E_{65} & S^E_{66} & d_{16} & d_{26} & d_{36} \\ d_{11} & d_{12} & d_{13} & d_{14} & d_{15} & d_{16} & \varepsilon^T_{11} & \varepsilon^T_{21} & \varepsilon^T_{31} \\ d_{21} & d_{22} & d_{23} & d_{24} & d_{25} & d_{26} & \varepsilon^T_{21} & \varepsilon^T_{22} & \varepsilon^T_{23} \\ d_{31} & d_{32} & d_{33} & d_{34} & d_{35} & d_{36} & \varepsilon^T_{31} & \varepsilon^T_{32} & \varepsilon^T_{33} \end{bmatrix} \begin{bmatrix} \sigma_1 \\ \sigma_2 \\ \sigma_3 \\ \sigma_4 \\ \sigma_5 \\ \sigma_6 \\ E_1 \\ E_2 \\ E_3 \end{bmatrix}$$

The parameters on the main diagonal are the strictly mechanical and electrical effects which are coupled through d_{ij} parameters located outside of the main diagonal. The above system of

equations is significantly simplified for materials exhibiting 4mm crystalline class (e.g. PZT, MFC etc.). This is related to the symmetry of elastic and electromechanical properties. According to ANSI IEEE 170 standards, if the device is poled along axis 3 and the piezoelectric material is a transversely isotropic around the 1-2 plane, Equation 7-16 can be simplified as shown in Equation 7-17:

Equation 7-17

$$
\begin{Bmatrix} \epsilon_1 \\ \epsilon_2 \\ \epsilon \\ \epsilon_4 \\ \epsilon_5 \\ \epsilon_6 \\ D_1 \\ D_2 \\ D_3 \end{Bmatrix} =
\begin{bmatrix}
S^E_{11} & S^E_{12} & S^E_{13} & 0 & 0 & 0 & 0 & 0 & d_{31} \\
S^E_{21} & S^E_{22} & S^E_{23} & 0 & 0 & 0 & 0 & 0 & d_{32} \\
S^E_{31} & S^E_{32} & S^E_{33} & 0 & 0 & 0 & 0 & 0 & d_{33} \\
0 & 0 & 0 & S^E_{44} & 0 & 0 & 0 & d_{24} & 0 \\
0 & 0 & 0 & 0 & S^E_{55} & 0 & d_{15} & 0 & 0 \\
0 & 0 & 0 & 0 & 0 & S^E_{66} & 0 & 0 & 0 \\
0 & 0 & 0 & 0 & d_{15} & 0 & \varepsilon^T_{11} & 0 & 0 \\
0 & 0 & 0 & d_{24} & 0 & 0 & 0 & \varepsilon^T_{22} & 0 \\
d_{31} & d_{32} & d_{33} & 0 & 0 & 0 & 0 & 0 & \varepsilon^T_{33}
\end{bmatrix}
\begin{bmatrix} \sigma_1 \\ \sigma_2 \\ \sigma_3 \\ \sigma_4 \\ \sigma_5 \\ \sigma_6 \\ E_1 \\ E_2 \\ E_3 \end{bmatrix}
$$

Using the relationships described previously, we can also write the above equation in this form (Equation 7-18):

Equation 7-18

$$
\begin{Bmatrix} \sigma_1 \\ \sigma_2 \\ \sigma_3 \\ \sigma_4 \\ \sigma_5 \\ \sigma_6 \\ D_1 \\ D_2 \\ D_3 \end{Bmatrix} =
\begin{bmatrix}
C^E_{11} & C^E_{12} & C^E_{13} & 0 & 0 & 0 & 0 & 0 & d_{31} \\
C^E_{21} & C^E_{22} & C^E_{23} & 0 & 0 & 0 & 0 & 0 & d_{32} \\
C^E_{31} & C^E_{32} & C^E_{33} & 0 & 0 & 0 & 0 & 0 & d_{33} \\
0 & 0 & 0 & C^E_{44} & 0 & 0 & 0 & -d_{24} & 0 \\
0 & 0 & 0 & 0 & C^E_{55} & 0 & -d_{15} & 0 & 0 \\
0 & 0 & 0 & 0 & 0 & C^E_{66} & 0 & 0 & 0 \\
0 & 0 & 0 & 0 & d_{15} & 0 & \varepsilon^S_{11} & 0 & 0 \\
0 & 0 & 0 & d_{24} & 0 & 0 & 0 & \varepsilon^S_{22} & 0 \\
d_{31} & d_{32} & d_{33} & 0 & 0 & 0 & 0 & 0 & \varepsilon^S_{33}
\end{bmatrix}
\begin{bmatrix} \epsilon_1 \\ \epsilon_2 \\ \epsilon \\ \epsilon_4 \\ \epsilon_5 \\ \epsilon_6 \\ E_1 \\ E_2 \\ E_3 \end{bmatrix}
$$

Most of the commercially available piezoelectric transducers are subject to a d_{33} or d_{31} effect. The d_{33} effect corresponds to the deformation of a specimen in the direction of the driving electric field (also poling direction), while the d_{31} effect implies the deformation of the plane perpendicular to the electric field vector (Figure 7-5). In this research, the d_{33} MFC is used due to its higher piezoelectric properties. This effect is described below:

7.4.1. Constitutive Equation for d₃₃ Macro Fibre Composite (MFC)

The electric field in the d_{33} MFC is not purely in one direction unlike the d_{31}. However, the strength of the electric field along the direction of the fibres is significantly more powerful, and therefore we consider the electric field in the d_{33} MFC to be in the same direction as the fibres. The plane stress theory assumes that the $T_1=0$. Therefore, the constitutive equation in this condition can be simplified as Equation 7-19.
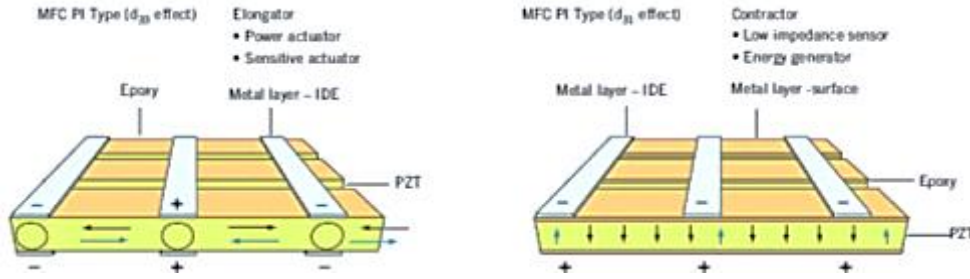
Figure 7-5: Macro Fibre Composite in elongator (d₃₃) and contractor (d₃₁) modes (Allan, 2011)

Equation 7-19

$$
\begin{Bmatrix} \epsilon_2 \\ \epsilon_3 \\ \epsilon_4 \\ \epsilon_5 \\ \epsilon_6 \\ D_3 \end{Bmatrix} = \begin{bmatrix} S_{22}^E & S_{23}^E & 0 & 0 & 0 & d_{32} \\ S_{23}^E & S_{33}^E & 0 & 0 & 0 & d_{33} \\ 0 & 0 & S_{44}^E & 0 & 0 & 0 \\ 0 & 0 & 0 & S_{55}^E & 0 & 0 \\ 0 & 0 & 0 & 0 & S_{66}^E & 0 \\ d_{32} & d_{33} & 0 & 0 & 0 & \varepsilon_{33}^T \end{bmatrix} \begin{Bmatrix} \sigma_2 \\ \sigma_3 \\ \sigma_4 \\ \sigma_5 \\ \sigma_6 \\ E_3 \end{Bmatrix}
$$

Where E_i and D_i are the components of the electric field vector and electric displacement vector, and σ_i and ϵ_i are the components of the stress and strain vector. The definitions of these components according to the 1-2-3 axis are:

$$
\begin{Bmatrix} \epsilon_1 \\ \epsilon_2 \\ \epsilon_3 \\ \epsilon_4 \\ \epsilon_5 \\ \epsilon_6 \end{Bmatrix} = \begin{Bmatrix} \epsilon_{11} \\ \epsilon_{22} \\ \epsilon_{33} \\ 2\epsilon_{23} \\ 2\epsilon_{13} \\ 2\epsilon_{12} \end{Bmatrix} \qquad \begin{Bmatrix} \sigma_1 \\ \sigma_2 \\ \sigma_3 \\ \sigma_4 \\ \sigma_5 \\ \sigma_6 \end{Bmatrix} = \begin{Bmatrix} \sigma_{11} \\ \sigma_{22} \\ \sigma_{33} \\ \sigma_{23} \\ \sigma_{13} \\ \sigma_{12} \end{Bmatrix}
$$

The d_{33} Macro Fibre Composite by itself is under the Elastic field, E_3, along direction 3, and the stress is along the same direction. The constitutive equation relationship for the d_{33} MFC can then be written as Equation 7-20:

Equation 7-20

$$D_3 = d_{32}\sigma_2 + d_{33}\sigma_3 + \epsilon_{33}^T E_3$$

$$\epsilon_3 = S_{32}^E \sigma_2 + S_{33}^E \sigma_3 + d_{33} E_3$$

7.5. Experimental Procedure

A series of experiments have been conducted in order to evaluate the functionality of the proposed technique. A number of structures with bonded transducers with various conditions in terms of the health of the structure and the transducer are tested with the proposed impedance-based technique using an AD5933 impedance analyser. The goal is to delineate the damage/degradation in the transducer from the structure by gathering the information from the AD5933 board only. This raw data will be analysed, and the sensitive impedance component to the transducer and the structure will be determined. The continuous monitoring of these components can provide us with enough information to distinguish these two from each other.

It should be noted that the impedance values have some error due to the internal resistance and capacitance of the board itself. However, this error is not significant and the values are sufficiently reliable. Furthermore, the shapes of the impedance measurement are completely accurate and without error. Generally speaking the algorithms used for the impedance method are only concerned with impedance measurement shape changes. For SHM purposes, the relative values of the measurements are adequate when it comes to determining the integrity of the structure and the transducer.

The impedance-based technique used in this research has three steps; data collection using AD5933, analysing the data to determine the status of the structure and transducer, and finally releasing the outcome. The main concern in this research is on the first and the second step as the main issues in real time SHM fall within these two steps. In actual in-situ SHM, we only have access to the data measured by the transducer via the measuring instrument (AD5933), and no analysis software or post-processing tool is available to analyse the raw data. This calls for an in-depth understanding of the parameters which are capable of detecting and diagnosing the possible damage/degradation in the transducer or the structure.

The AD5933 evaluation board is used to measure the electrical impedance components of the MFC transducer. The variations of these components are observed in the frequency range of 0.3-100 KHz for all 6 samples (refer to manufacturing chapter for more details on the preparation process of 6 samples). The Real and Imaginary components of the impedance (admittance) and the

impedance magnitude are measured while the structure is constantly excited with an external voltage. There are various components which can be measured and calculated such as Real and Imaginary Impedance, Impedance Magnitude, RMSD of the Real Impedance, and Real and Imaginary Admittance, etc. Furthermore, 5 possible damage/degradation scenarios can occur; transducer damage, degradation of the electrical properties of the sensor, generation of the damage in the structure, propagation of existing damage or a mixture of all four situations. In order to delineate these possible disorders from each other, appropriate components should be identified which are particularly sensitive to each of the above disorders. This can help us to identify the source of the disorder by monitoring the relevant component.

During experiments, the electromechanical impedance components are measured and compared for all 6 samples with induced damage in various locations of the structure and transducer. The measurement technique is identical for all 6 samples as described in the manufacturing chapter. This is to ensure that all of the observed changes are purely due to the structural and/or transducer damage and also to confirm the repeatability of the technique. Five electromechanical components are measured and plotted for each sample; Real impedance (Resistance), Imaginary impedance (Reactance), impedance magnitude, real admittance (Susceptance) and imaginary admittance (conductance). These plots are then compared between each of the two relevant situations in order to identify the effect of various damage scenarios on these components.

7.6. Validation of Experimental Result with FEM

In order to validate the experimental results, the bonded MFC transducer on carbon/epoxy plate is simulated using the FEM software package ABAQUS. Unlike the simulation in the strain-based technique, which modelled the passive behaviour of the MFC transducer, the converse effect of MFC is taken into account in this chapter. Six samples are simulated with the similar specifications as experiments.

In the previous section, we used an analytical approach to explain the electromechanical behaviour of the MFC transducer and to relate the mechanical impedance of the structure to the electrical impedance of the transducer through analytical equations. However, arriving at an analytical solution to equations describing more complex systems can become fairly complicated. Furthermore, it is often difficult to define all of the characteristics of an experiment such as the status of the samples and loading condition in the analytical model, thereby making the results incomparable with the experimental results. The finite element method (FEM) software package called ABAQUS is used in this project to validate the experimental measurements. This is due to

the ability of FEM to perform the numerical analysis of complicated structures using small-element discretisation.

In this section, the MFC bonded onto the Carbon/Epoxy plate is modelled and the FEM coupled-field approach is used to predict the electromechanical impedance spectrum of the MFC following which the results are compared with the experimental measurements. The loading and boundary conditions are defined for the structure and voltage constraints are applied to the MFC electrodes. A time harmonic analysis is conducted on the simulated FEM model and the concentrated electrical nodal charge (CECHG) values are calculated with respect to the frequency. From the electrical charge, the electric current is calculated, following which the Electromechanical impedance of the system is calculated in the defined frequency range from the ration V/I where V is the voltage constraint applied to the MFC and I is the electric current calculated from electric charge on the interdigitated aspect of the MFC transducer using Equation 7-21.

Equation 7-21

$$I = j\omega \sum Q$$

Where ω is the operating frequency, j is $\sqrt{-1}$, and $\sum Q$ is the total nodal charge.

In order to perform the electro-mechanical analysis, the elements should be able to deal with both electrical and mechanical fields through the electromechanical coupling coefficient, so that a change in one field will induce a change in the other field. A C3D8E element type is used for this purpose. The excitation voltage is applied to the negative and positive leads of the MFC in the form of electric potential and in the same frequency range as the experiments. The excitation signal causes the corresponding current to flow through the electrodes of the MFC, which can be calculated as previously described. This is similar to the way in which the AD5933 impedance analyser excites the transducer and measures the impedance.

As it was mentioned before, for the excited MFC transducer, the resonance occurs when the MFC responses are very large. These resonances can be either mechanical or electromechanical. The mechanical resonances are associated with the structure while the electromechanical resonances are due to the coupling between the MFC and the structure. The electromechanical resonances happen due to the electrical excitation of MFC which generates electromechanical response such as mechanical vibration and a change in the electric admittance and impedance. In a situation where the electrical excitation is harmonic and constant (constant voltage) at given frequency, the electrical resonance is associated with the situation whereby a device is drawing very large

currents. As the admittance becomes very large, the current drawn under constant-voltage excitation also becomes very large because I=YV where Y is admittance. In the mechanical response, the electrical resonances also become very large. This happens because the electromechanical coupling of the piezoelectric materials transfers energy from electrical input into the mechanical response.

To verify the electromechanical impedance measurements using the AD5933 impedance analyser, the electromechanical impedance is calculated using ABAQUS software and plotted in Figure 7-6 to Figure 7-11. It can be seen from these plots that the simulation results compare very well with the experimental measurements. The variations between the experimental and simulation results may be due to the impact of soldering, connecting wires to the MFC leads, manufacturing imperfection and internal components of the AD5933 impedance analyser. The overall conclusion is that a very good agreement can be seen between the FEM simulation and the experimental data of the electromechanical impedance of the MFC transducer bonded onto the Carbon/Epoxy plate.
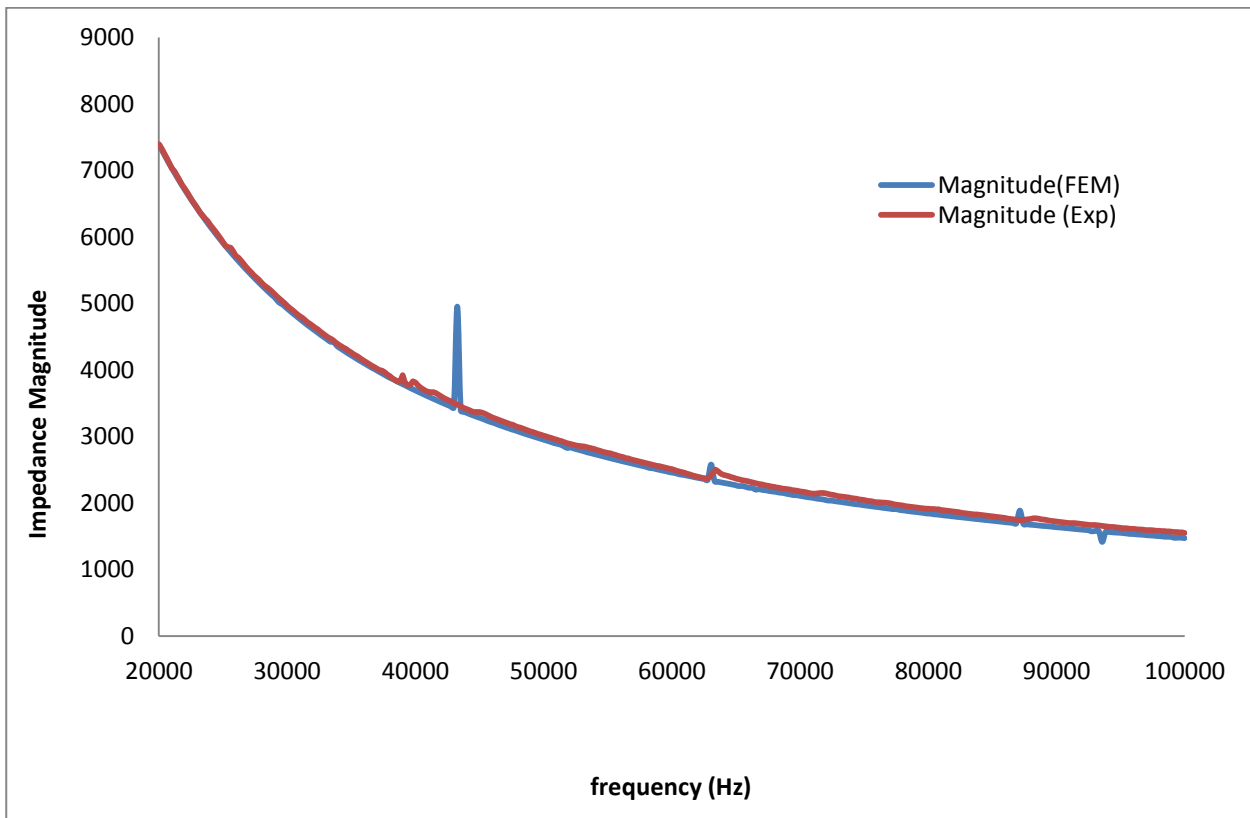
Figure 7-6: HSEN_HST
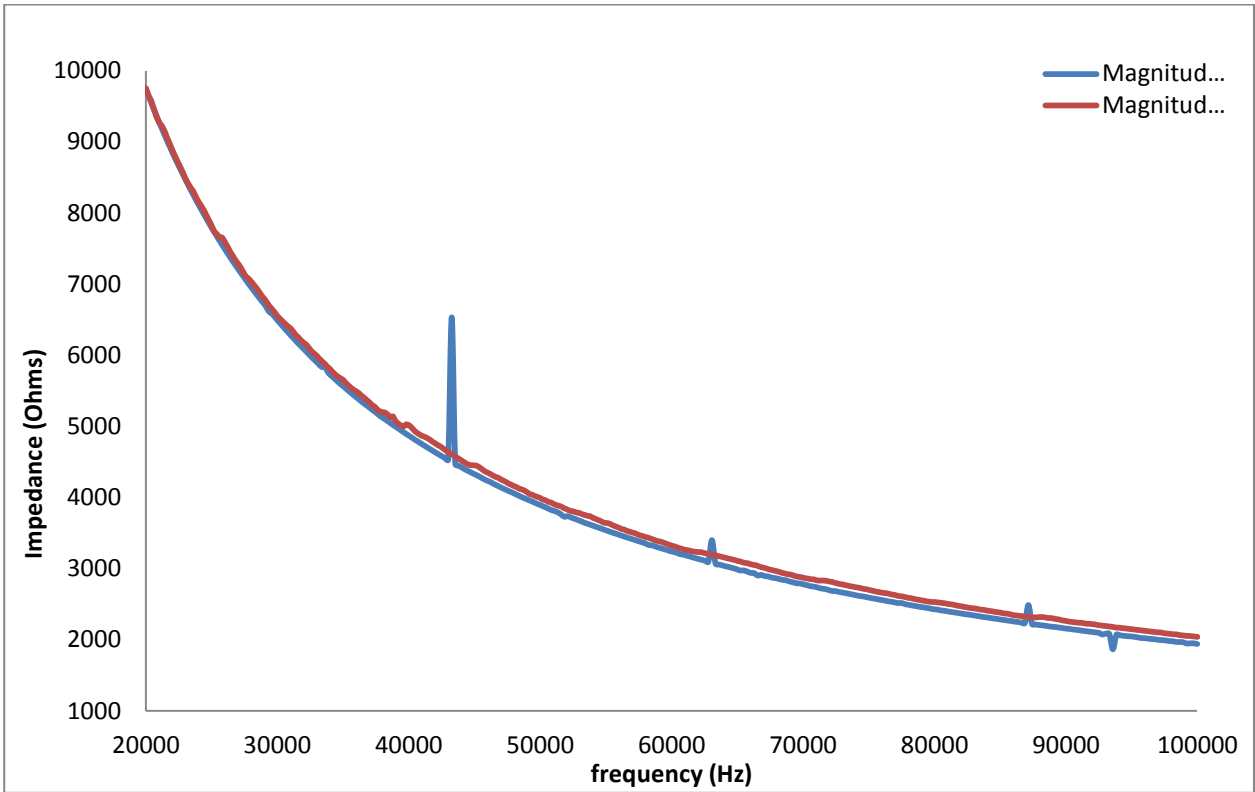
Figure 7-7: DSEN_HST
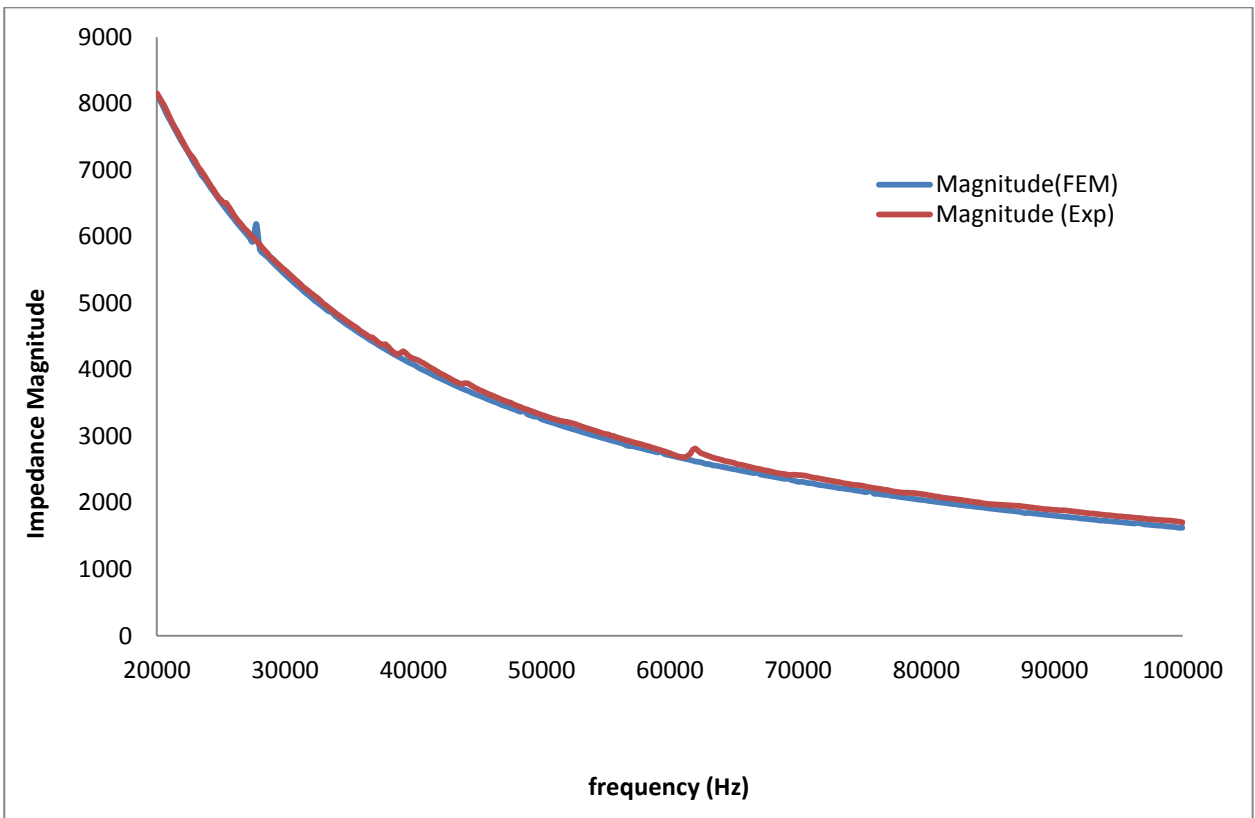
Figure 7-8: HSEN_DST_MIDDLE

195
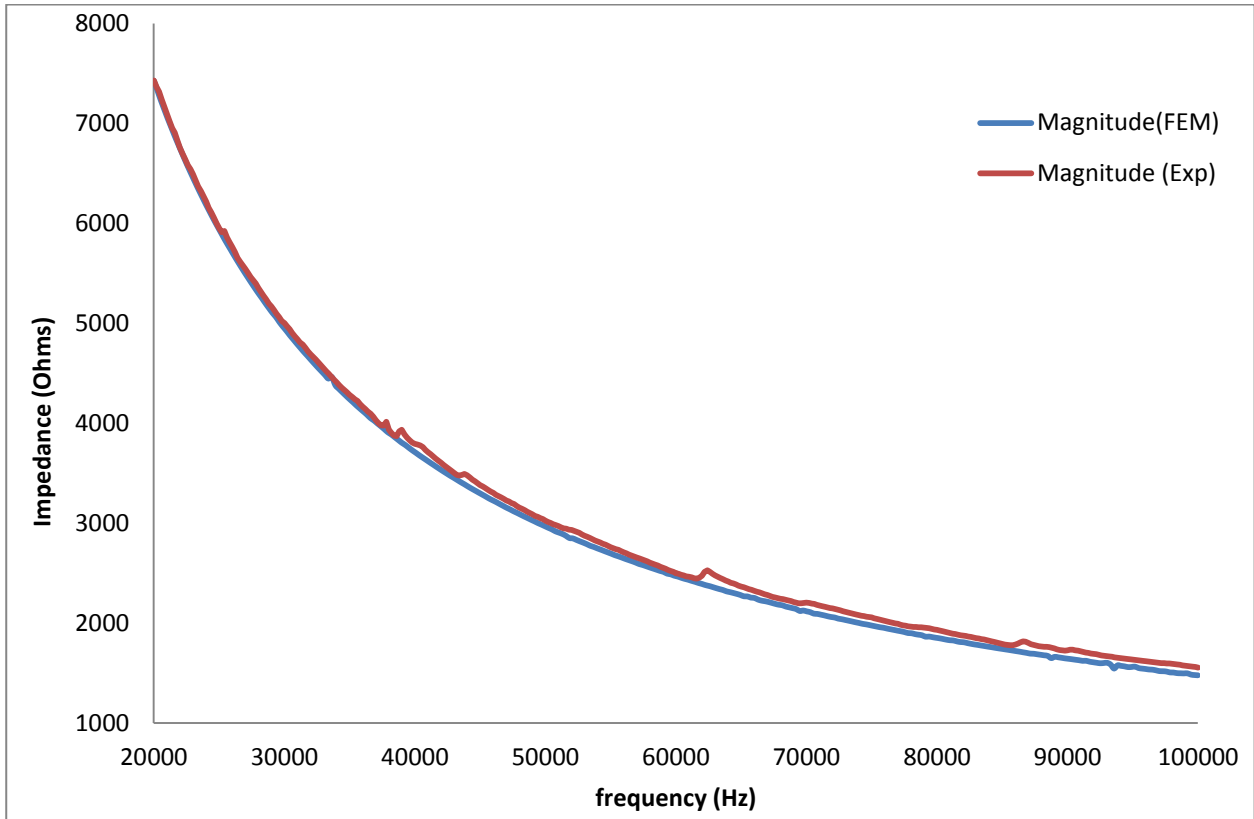
Figure 7-9: HSEN_DST_SIDE
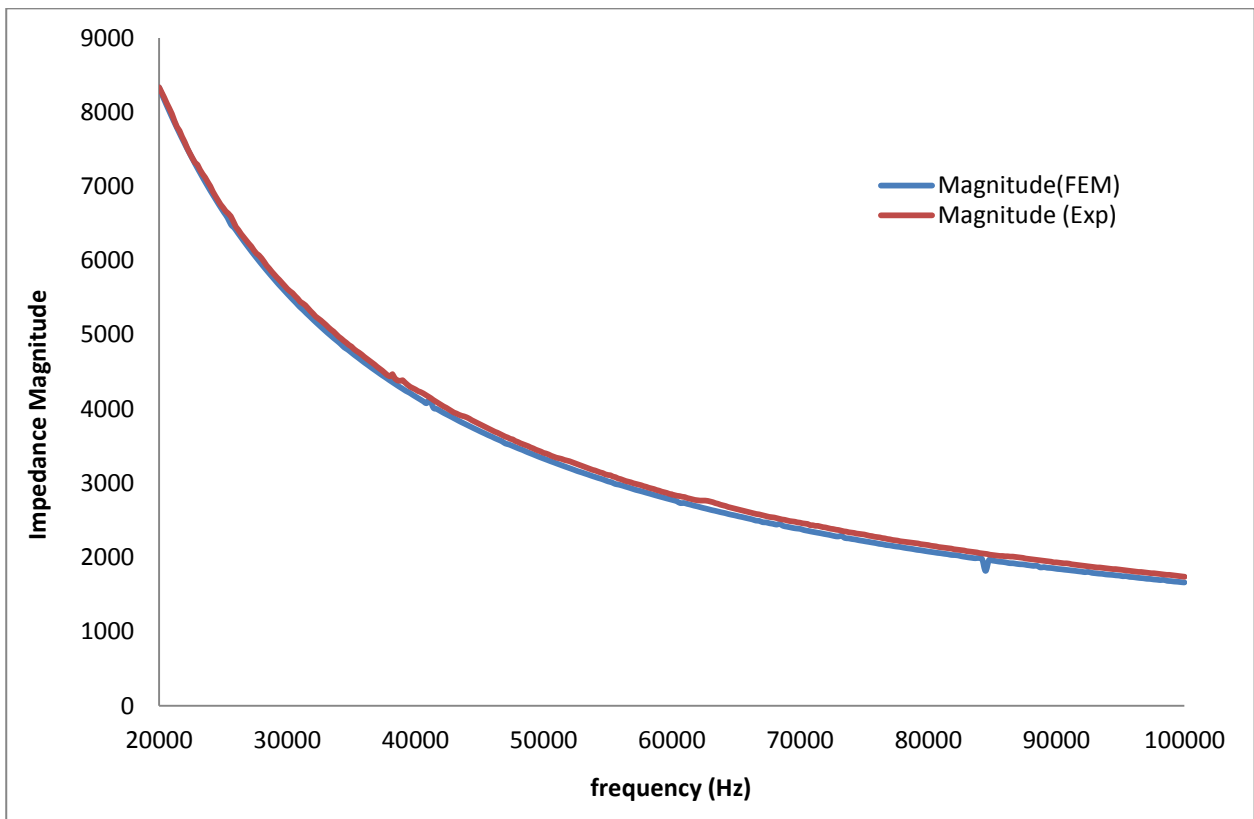
Figure 7-10:DSEN_DST_MIDDLE

196
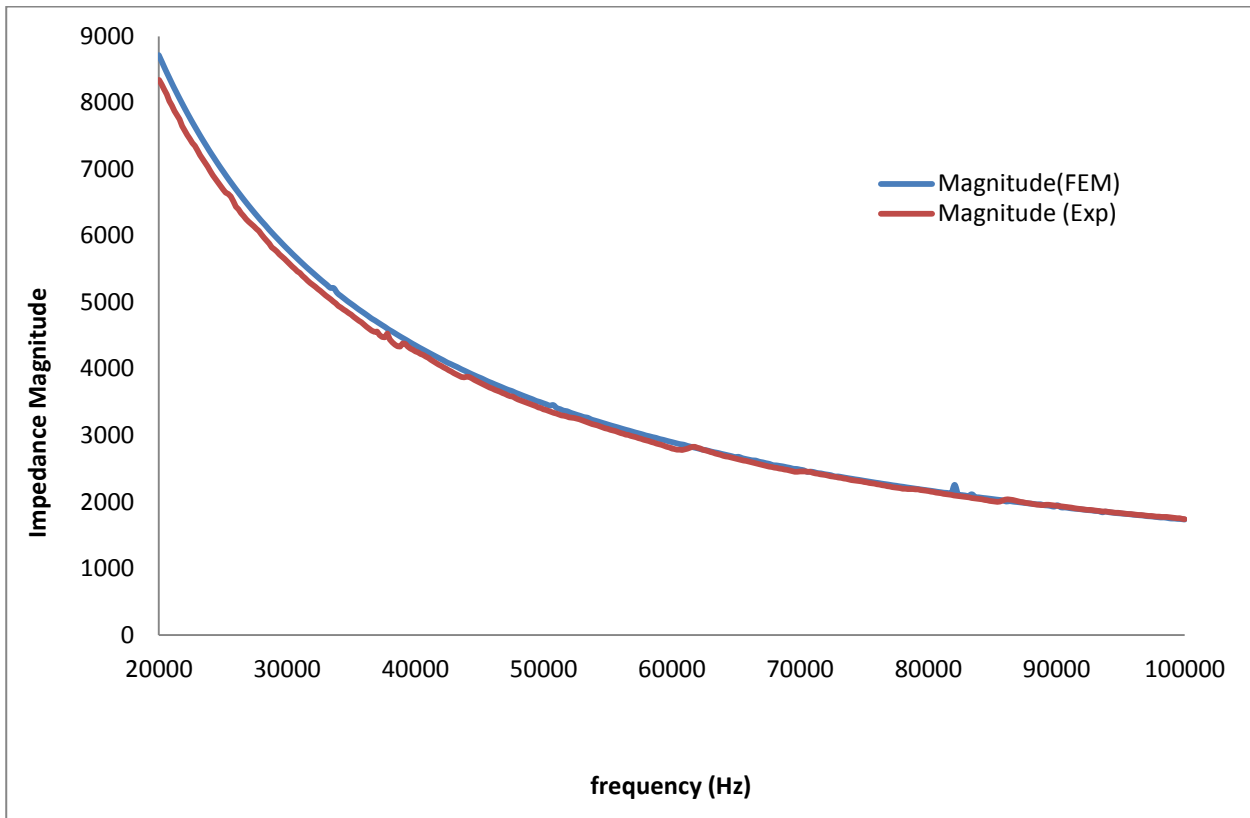
Figure 7-11:DSEN_DST_SIDE

7.7. Experimental results

The Real and imaginary impedance, impedance magnitude, and conductance and susceptance (real and imaginary admittance) are plotted and compared in this section. These comparisons are based on the effect of various damage scenarios, including the host of the damage (structure or transducer), and the location of the damage (close or far from the transducer), on the impedance and admittance components. As can be seen from Figure 7-12 - Figure 7-53, each damage scenario has certain effects on all or some of these components, as identified below. In general, the measurements follow a similar pattern, thus confirming the repeatability of the measuring technique and also the validity of the measurements.

The impedance magnitudes for all 6 samples are presented in Figure 7-12 below. Due to the nature of the impedance magnitude, which is the summary of the impedance of all components in the electromechanical the impedance measuring system, it can be argued that the overall accuracy of the system can be estimated by the continuous monitoring of impedance magnitude. In Figure 7-12, the trend of the impedance magnitude for all 6 samples follows the same pattern, thus confirming the reliability and functionality of the measuring rig. These values are also validated for all 6 samples through the FEM analysis, as previously described. The comparison between the

measurement and analytical calculation for the healthy sample in Figure 7-13 also shows a perfect match which confirms the reliability of the proposed technique. As mentioned in the FEM section, the analytical calculation of the damaged samples is not accurate, possibly as the realistic definition of these parameters in the electromechanical impedance is often too complex due to the nonlinear dynamic behaviour of the damage. Following abbreviations are used in the rest of this chapter to show the type of sample, in terms of structure/transducer damage statuses, being tested.

- **HSEN_HST:** Healthy Sensor is bonded on healthy structure
- **HSEN_DST_MIDDLE:** Healthy sensor is bonded on damaged structure where damage is at the middle of the plate (close to sensor)
- **HSEN_DST_SIDE:** Healthy sensor is bonded on damaged structure where damage is at the side of the plate (far from sensor)
- **DSEN_HST:** Damaged sensor is bonded on healthy structure
- **DSEN_DST_MIDDLE:** Damaged sensor is bonded on damaged structure where damage is at the middle of the plate (close to sensor)
- **DSEN_DST_SIDE:** Damaged sensor is bonded on damaged structure where damage is at the side of the plate (far from sensor)
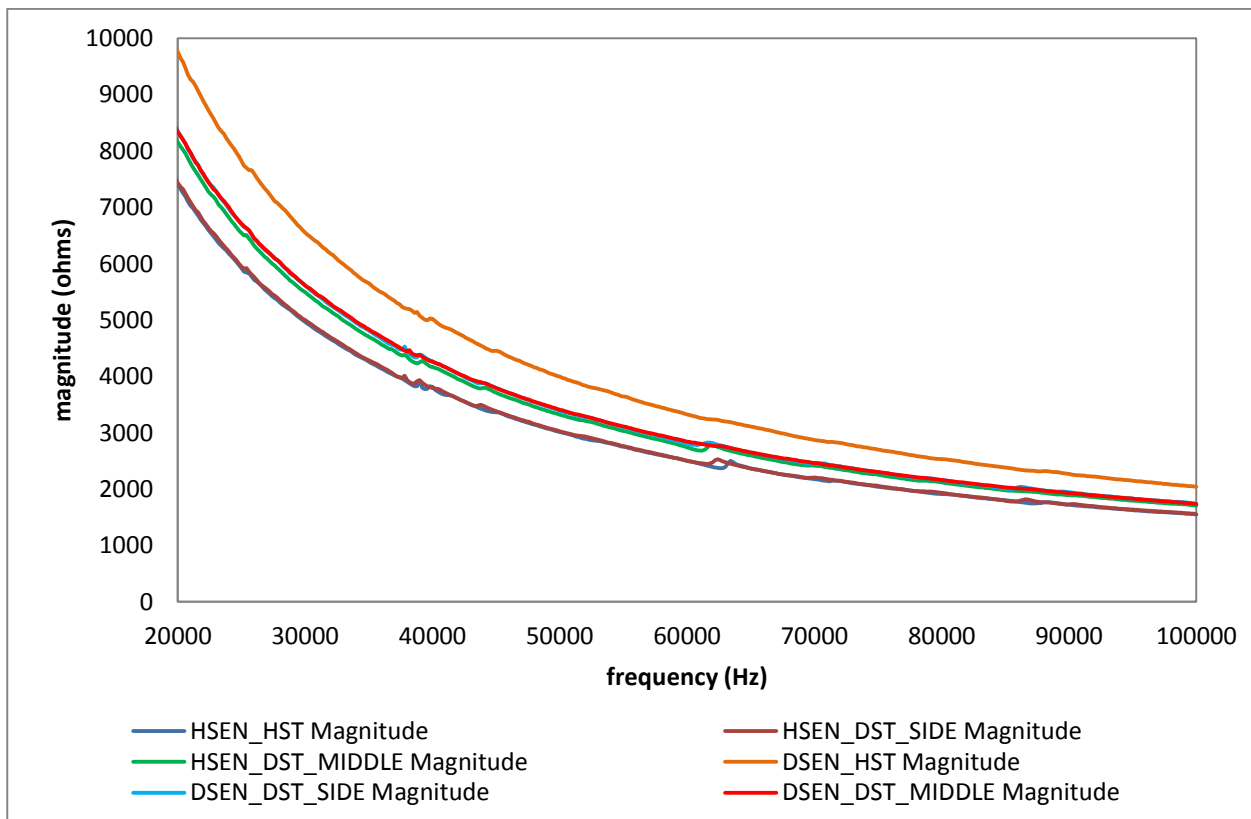
Figure 7-12: Electromechanical Impedance magnitude for all six samples

198

7.7.1. Real Impedance (R)

The Real Impedance measurements are plotted from Figure 7-14 to Figure 7-22. As was discussed previously, the structure is modelled as a Resistance in the equivalent circuit of the electromechanical impedance, and therefore the changes in the structure are more significant on the Real part of impedance. However, the following plots show that the structural damage also affects the imaginary measurements due to the bonding between the structure and the MFC transducer. The comparison between the real impedance of the healthy sample and samples with structural damage at the middle and side of the structure is presented in Figure 7-14. In this plot, the locations of the resonance peaks are similar while the magnitudes of the peaks are different. As previously mentioned, the real part of the impedance is relevant to the R (structure) and V_p (voltage generated in MFC) in the equivalent circuit of the bonded MFC on the structure. The comparison of the Real impedance measurements between all 6 samples is provided in the following plots. The damage reveals itself as a frequency shift in the dominant resonances present in the impedance plots, as peaks splitting, and as the appearance of new harmonics which are not present in the healthy sample spectrum.
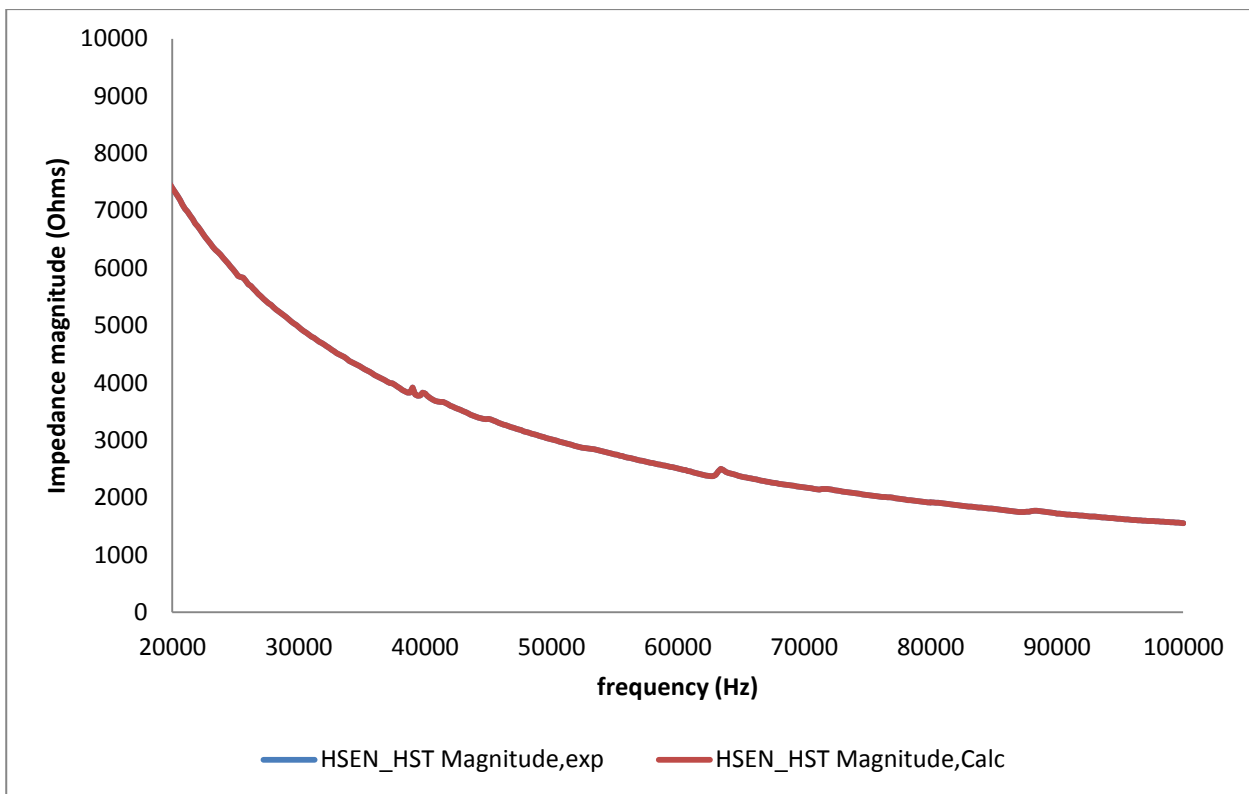
Figure 7-13: Comparison of analytical calculations and experimental measurements of impedance magnitude for HSEN_HST

Figure 7-14 plots the comparison between the healthy sample (HSEN_HST) and the HSEN_DST_MIDDLE sample. It is observed from this figure that the damage in the structure close to the transducer shifts most of the peaks towards lower frequencies. This can be explained through the electromechanical coupling between the structure and the transducer. The generation of damage (Teflon) increases the compliance of the structure and causes the frequency shift of resonance frequencies towards lower values. Generally speaking, when the MFC becomes excited with induced voltage it generates mechanical excitation due to the converse effect of the piezoelectric material. This mechanical excitation transfers into the structure via the bonding layer and affects the dynamic of the structure through mechanical impedance relations. This would generate a strain in the structure, which transfers back to the MFC transducer through the bonding layer and generates a current on the MFC due to a direct piezoelectric effect. The ratio of the induced voltage (V) over the generated current (I) is used to calculate the electromechanical impedance components. The resonance peaks occur when the sum of structural and transducer impedances reach a Maximum. Furthermore, any change in the integrity of the structure would change its characteristics, including damping and stiffness, which modify the mechanical impedance of the structure. In addition, it has previously been demonstrated that mechanical impedance is also dependent on frequency. Therefore, any change in the structural characteristics due to damage modifies the resonance frequencies in which the summation of the mechanical and electrical impedances reach Maximum and, this in turn, affects the impedance spectrum in the form of a frequency shift.

Figure 7-14 shows the variation of electromechanical impedance due to structural damage at the middle of the structure. As it was mentioned previously, the structural damage increases the compliance of the structure. Furthermore, the structural damage reduces the mechanical impedance of the structure, and considering the fact that electromechanical impedance has an inverse relation with frequency, it causes the summation of electrical and mechanical impedances to become maximum at lower frequencies, as can be observed in this figure. The previous statement is also valid for samples with damage at their side, as shown in

Figure 7-15. The frequency shift can be observed in the HSEN_DST_SIDE towards lower values. However, the magnitudes of resonance peaks are slightly reduced, and the slope of real impedance for the damaged sample is also shifted towards lower values. This is because the increase in the compliance of the structure which has the damage at the side is less than the one which has the excitation at the middle. This generates less electromechanical impedance at resonance frequencies and through the slope of the plot.
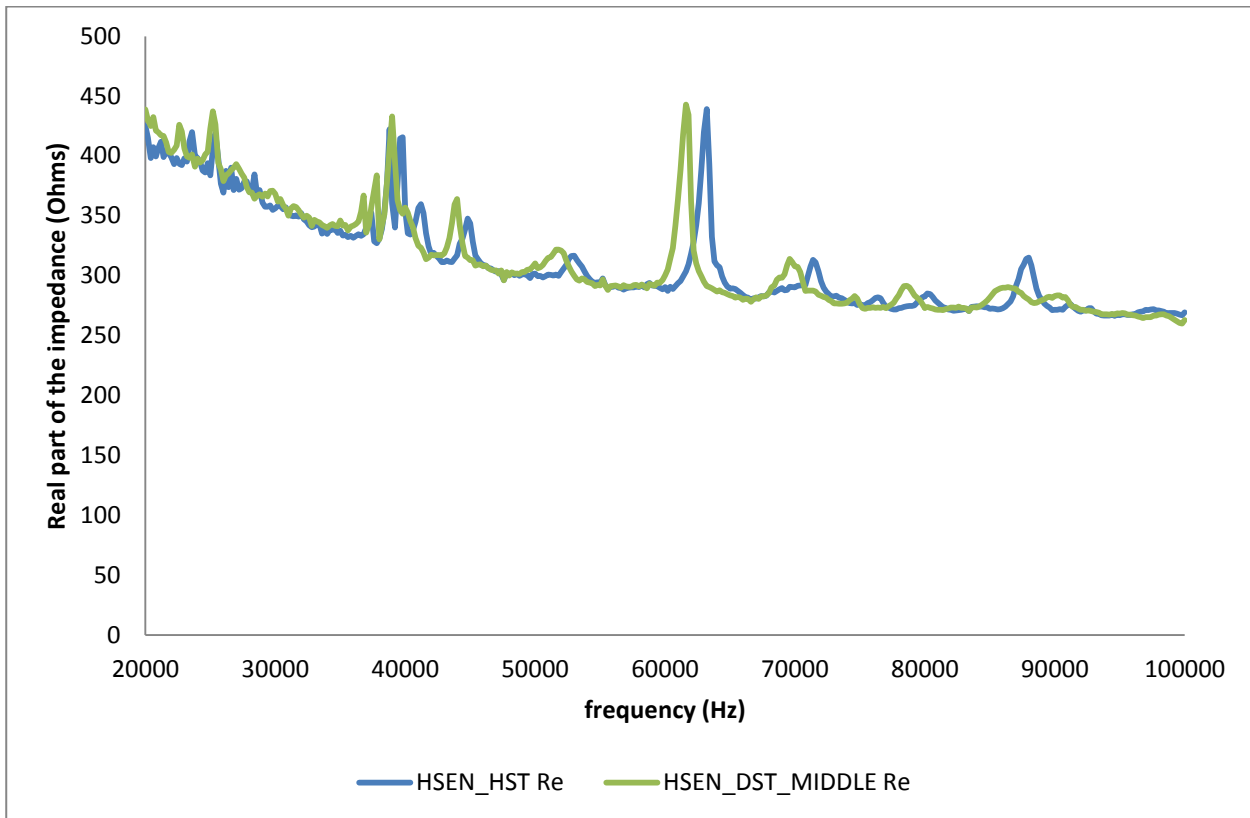
Figure 7-14: Real impedance comparison (HSEN_HST and HSEN_DST_MID)

It can be argued that the presence of damage in close proximity to the transducer (Middle) shifts the resonance frequency peaks of real impedance towards lower values, while the presence of damage on the far field (Side) reduces the magnitude of resonance peaks and shifts the resonance frequencies and the slope of real impedance towards lower values. The comparison of HSEN_DST_MIDDLE and HSEN_DST_SIDE is provided in Figure 7-16.

The detection of damage in the sample with the healthy transducer has the least complexity when compared to other damage scenarios. Any changes in the electromechanical impedance components can be considered as a sign of structural damage, and the only challenge is to relate the variation of the responses to the damage status in terms of location and severity. However, the situation where the transducer is degraded has more complexities, as the delineation between the structural damage and the damage in the transducer itself is essential. The changes in the electromechanical impedance signatures should be analysed in order to determine the main cause of any of these changes. The real impedance measurement for samples with damaged transducers (DSEN_HST) against the healthy samples is plotted in Figure 7-17 and discussed here.
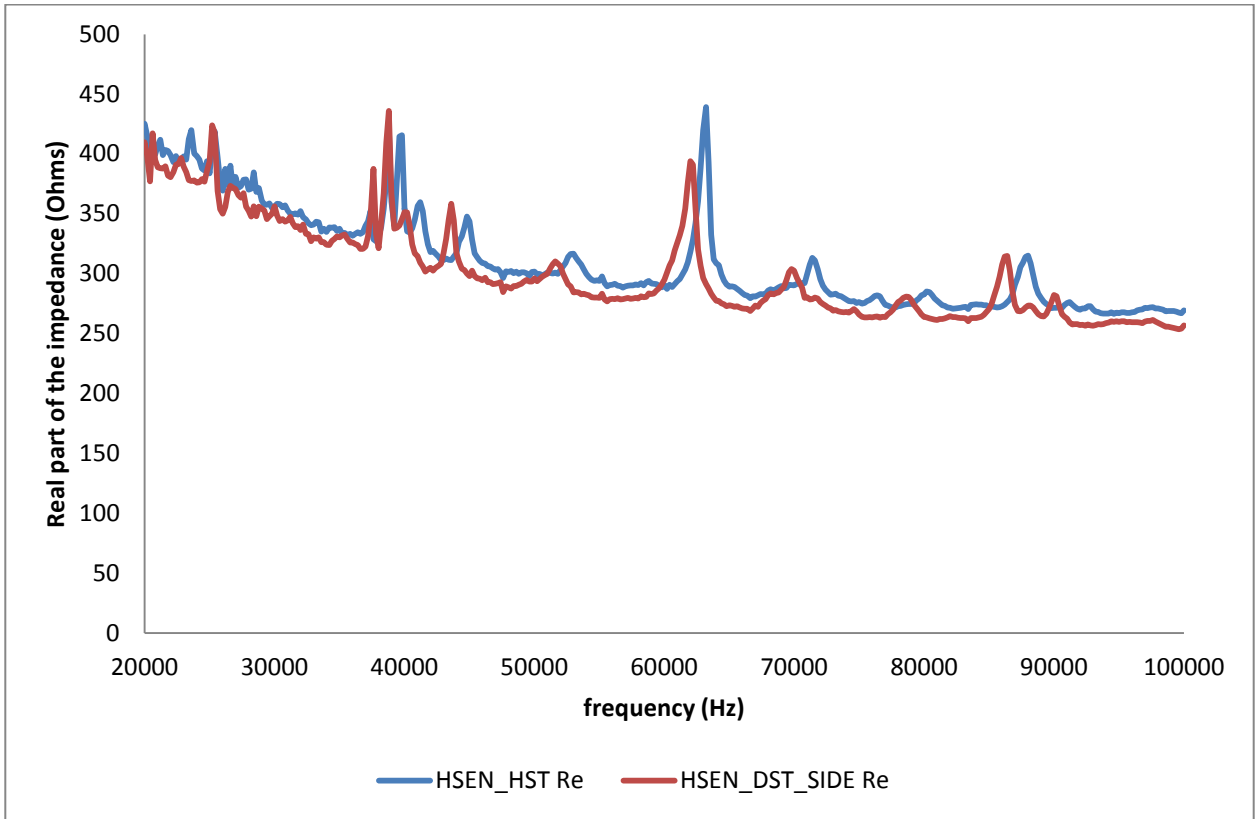
Figure 7-15: Real impedance comparison (HSEN_HST and HSEN_DST_SIDE)
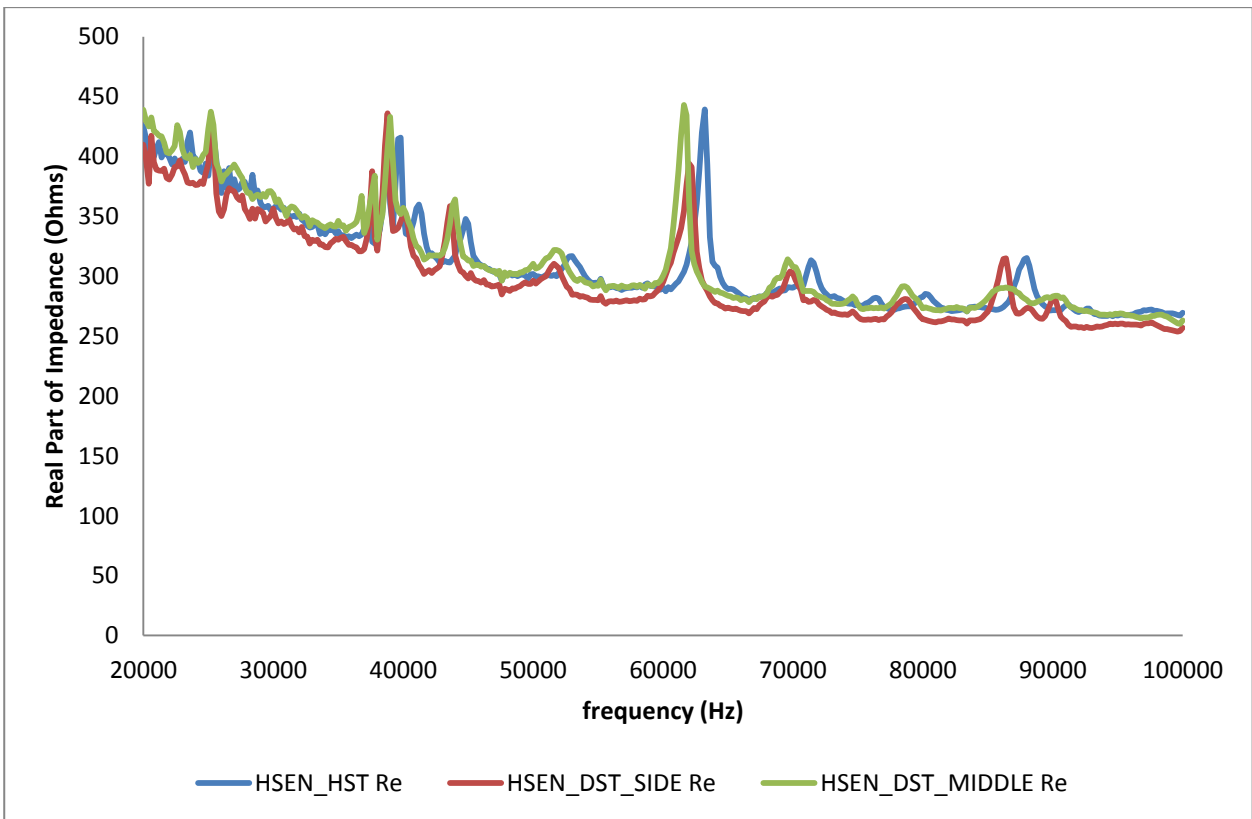
Figure 7-16: Real impedance comparison (HSEN_HST, HSEN_DST_MIDDLE and HSEN_DST_SIDE)

The separation between two plots in this figure is significant, thereby showing that the transducer damage would also affect the real impedance. The general trends of the two plots are similar, which confirms the reliability of measurements. Moreover, the locations of the peaks are also similar, as highlighted in Figure 7-17. However, the magnitudes of the peaks are dropped and there is a shift in the slope of DSEN_HST towards lower values. It was observed during initial tests that the sensitivity of the MFC transducer and its electrical properties are affected by the generation of damage or degradation in the transducer, which in turn modifies its electrical impedance. Furthermore, the electromechanical coupling behaviour of the bonded MFC transducer on the carbon/epoxy plate was described through an equivalent circuit in the previous section. Therefore, the changes in the impedance plot due to the damage in the transducer can be described through this equivalent circuit as shown in Figure 7-4 and explained in Equation 7-10 .

The initial experiments showed that the capacitance value of MFC drops when damage occurs in the transducer. This is related to the capacitive part of the circuit. The electrodes which are collecting the charge from the piezo-fibres and the connections between fibres and electrodes are also subject to damage/degradation. This is related to the resistive part of the equivalent circuit. In Figure 7-17, the upward shift of the DSEN_HST real impedance plot is caused by the reduction in the V_{OUT} due to the impact of induced damage in the resistive part of the transducer, as the capacitive part is more traceable in imaginary impedance.
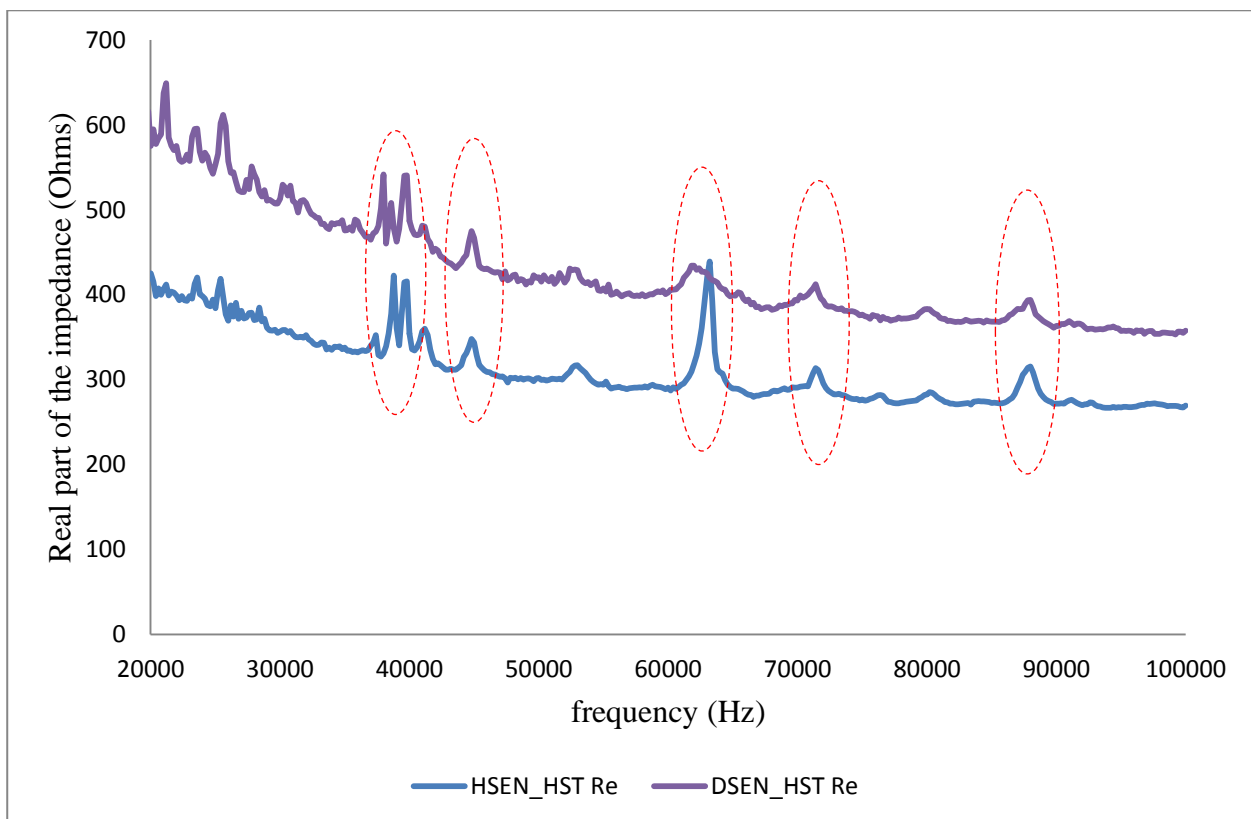
Figure 7-17: Real impedance comparison (HSEN_HST, DSEN_HST)

203

The similar location of resonance frequencies of the healthy sample and DSEN_HST illustrates that the pure transducer degradation will not shift the resonance frequencies. In other words, the frequency shift in resonance peaks in the real impedance spectrum is a sign of structural damage. The reduction in the magnitude of resonance peaks is more significant at the resonance frequency of a free MFC transducer (about 60 KHz), which is due to the degradation of the transducer's electrical properties and can be considered as a sign of transducer damage.

The more complex scenario is when both the transducer and structure are damaged. The comparison between the healthy sample and DSEN_DST_MIDDLE is plotted in Figure 7-18. As shown in Figure 7-14 and Figure 7-17, the transducer damage reduces the magnitude of resonance peaks and also shifts the slope of real impedance towards lower values while the damage at the middle of the structure shifts the resonance frequencies towards lower frequency values. The frequency shifts and the reduction in resonance peaks magnitude can still be observed in this figure but the upward shift is eliminated. This is due to the behaviour of the damaged transducer in detecting structural damage as this change was also observed for the situation where the sample had transducer damage only. For the sample with the damaged transducer, it is shown that the piezoelectric coefficient degrades. As such, for the same amount of excitation voltage, less mechanical excitation would be generated. This mechanical excitation, which is less than that from the healthy transducer, transfers to the structure and affects the dynamics of the structure through mechanical impedance relations. However, the excitation wave is not as strong as the healthy transducer and therefore cannot capture all of the changes of the mechanical impedance. In other words, the similar magnitude of the slope of the real impedance between the healthy sample and the DSEN_DST_MIDDLE is a false negative sign and does not mean that the transducer is still intact.

For the purposes of additional investigation, in Equation 7-22 the transducer is not connected on the substrate structure, the $Z=1/i\omega C$, which is due to the capacitive nature of the MFC transducer. However, the impedance of the bonded transducer also depends on the stiffness of the structure and the electromechanical coupling between the transducer and the structure. The growth of the induced damage in the structure reduces its stiffness (k_{str}), which in turn increases the value of the bracketed part of the equation. The inverse of the bracket values is then decreased. Therefore, the total value of impedance in the case of structural damage will be decreased. On the other hand, the damage in the transducer has two impacts in this equation. First, as previously shown, the damage in the piezoelectric fibres reduces the total capacitance of the transducer (C) so the "$1/i\omega C$" part of the impedance will be increased in the case of transducer damage. Secondly, the impact of transducer damage is the reduction of the stiffness of the MFC due to the damage to the structure

of the MFC itself. This would reduce the stiffness of the MFC (k_{MFC}). This also reduces the value of the relationship in brackets and increases its inverse.
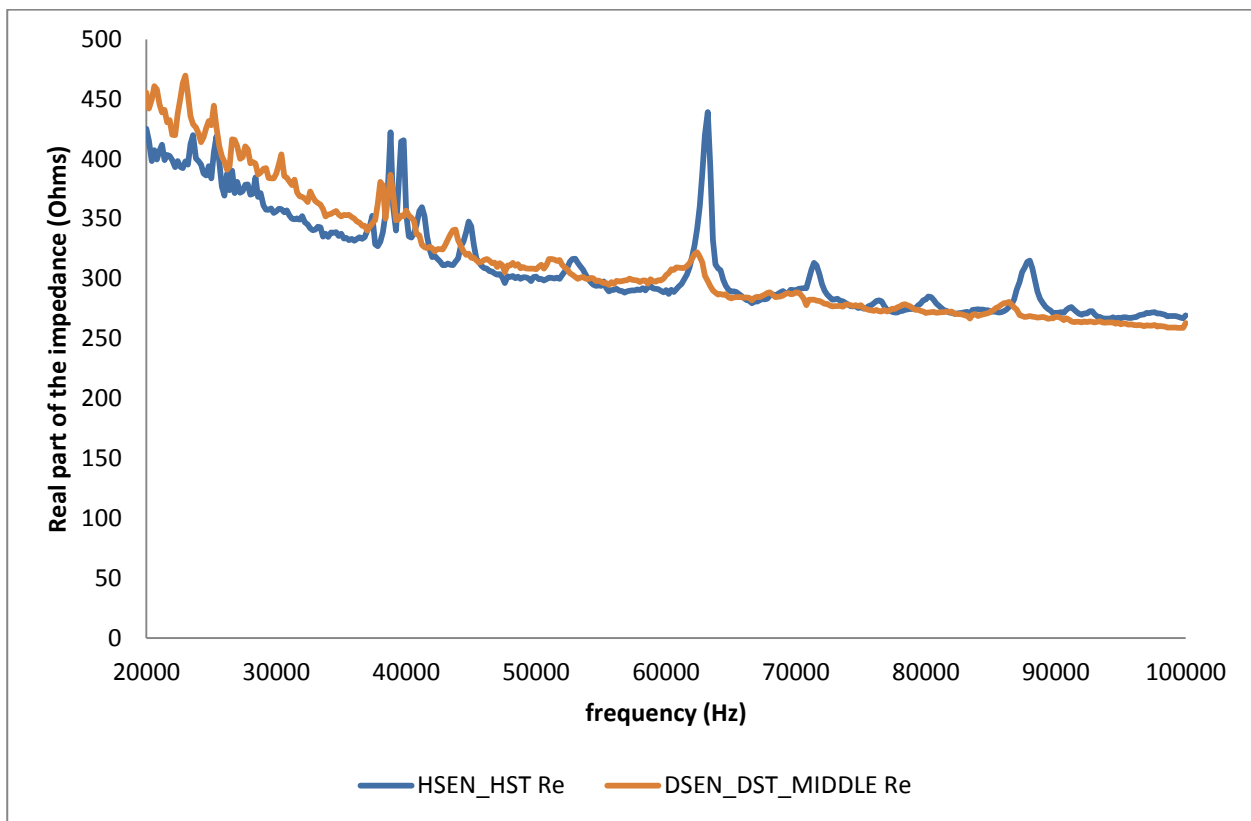
Figure 7-18: Real impedance comparison (HSEN_HST, DSEN_DST_MIDDLE)

As a result, the total impedance will increase due to the damage in the structure of the MFC transducer, and therefore, while the structural damage reduces the impedance, the transducer damage increases the value of electromechanical impedance. However, due to the nature of electromechanical impedance it is not possible to completely delineate the real and imaginary parts of it and predict the behaviour of the damaged transducer in terms of damage detection in the structure.

This called for another parameter with the ability to show the real and imaginary components of the electromechanical impedance separately. This parameter is known as electromechanical admittance ($Y_{(\omega)}$), which is the inverse of electromechanical impedance as shown in Equation 7-23. As can be seen from this equation, the real and imaginary parts can be distinguished from each other in order to explain the changes in the real and impedance admittance

Equation 7-22

$$Z = \frac{1}{i\omega C}\left(1 - k_{33}^2 \frac{k_{str}}{k_{MFC} + k_{str}}\right)^{-1}$$

205

Here, $Z(w)$ is the electro-mechanical impedance as seen at the MFC transducer terminals, C is the zero-load capacitance of the MFC transducer, k_{33} is the electro-mechanical cross coupling coefficient of the MFC transducer, $k_{str}(w)$ is the dynamic stiffness of the structure, and k_{MFC} is the stiffness of the MFC transducer. In addition, the relationship between these parameters and the electro-mechanical admittance, $Y(\omega)$, can be written as Equation 7-23.

Equation 7-23

$$Y = \frac{1}{Z} = i\omega C \left(1 - k_{33}^2 \frac{k_{str}}{k_{MFC} + k_{str}}\right)$$

The similar types of changes seen in Figure 7-18 are observed in Figure 7-19, which is the comparison between the real impedances of HSEN_HST and DSEN_DST_SIDE. Indeed, the same discussion as above can also be used to explain these changes. The comparison between DSEN_HST, DSEN_DST_MIDDLE and DSEN_DST_SIDE is provided in Figure 7-20. A downward shift can be seen in the slope of DSEN_DST_MIDDLE and DSEN_DST_SIDE compared to the DSEN_HST plot.

This is caused by the behaviour of the damaged transducer in detecting structural damages. It emphasises that the structural damage in the existence of transducer damage shifts the real impedance towards lower impedance values. The damage in the transducer has already increased the E/M impedance but the generation of structural damage causes an increase in the V_{OUT} (Equation 7-10) and therefore reduces the impedance which is the reason for the downward shift. This reduction is lower when the structural damage is far from the transducer as the damaged transducer couldn`t capture all the characteristics of the damage at the side due to the degradation of transducer properties. Therefore, the magnitude of the resonance peaks is larger for the real impedance spectrum of DSEN_DST_SIDE in respect to the DSEN_DST_MIDDLE.

The performance of the damaged and healthy transducer in terms of detecting structural damages in the transducer's close and far field is presented in Figure 7-21 and Figure 7-22. It is observed that the difference between the responses of the healthy and damaged transducer is more significant when the structural damage is within the close field of the transducer.
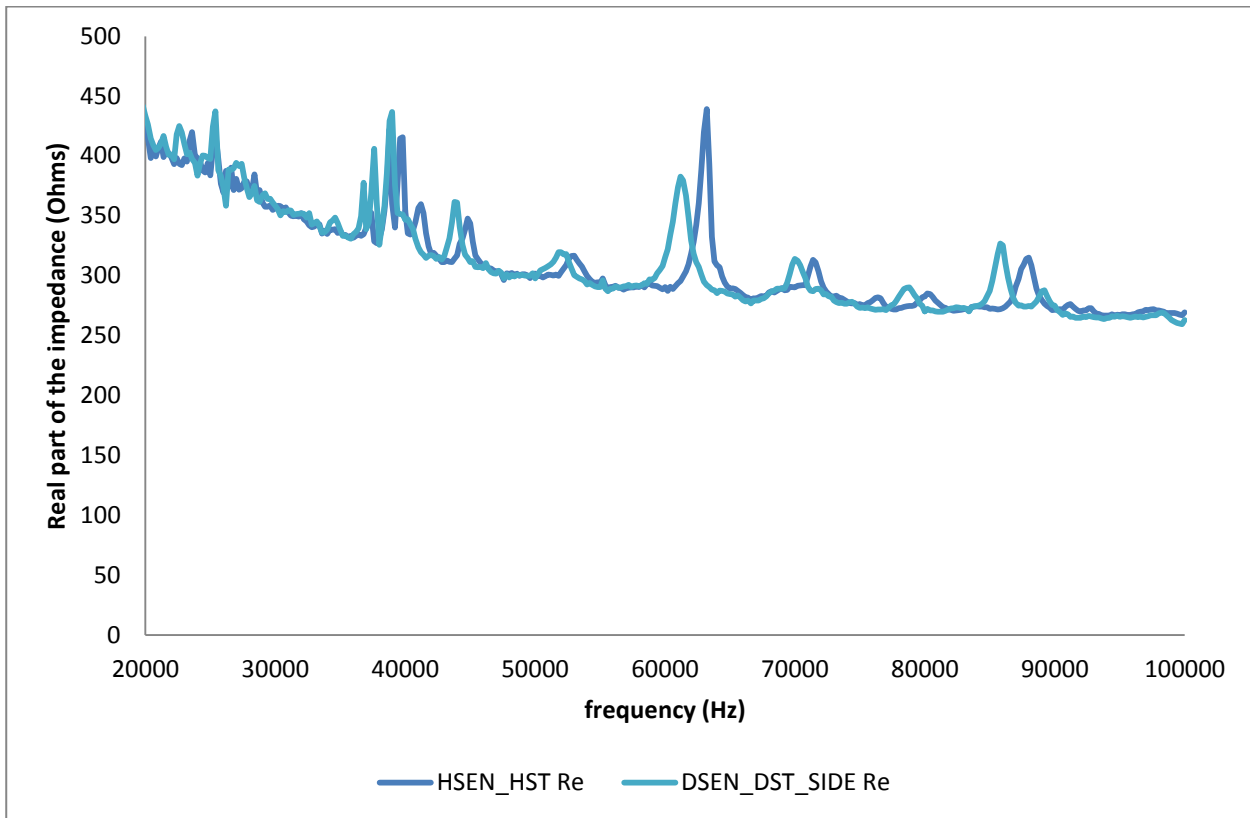
Figure 7-19: Real impedance comparison (HSEN_HST, DSEN_DST_SIDE

As the status of the structure is similar in both the HSEN_DST_MIDDLE and the DSEN_DST_MIDDLE samples, this difference is due to the ability of the damaged transducer to detect structural damages. Whilst the same excitation voltage comes into the healthy and damaged transducer, the damaged transducer generates less mechanical excitation (strain) as the d_{33} is reduced in the damaged transducer.

As such, less mechanical excitation would transfer to the structure and affect the dynamics of the structure through mechanical impedance relations. This excitation wave moves through the structure and captures the changes in the structural integrity. Therefore, damage close to the transducer location has greater impact on the excitation waves compared to far field damage. This is even more significant for the damaged transducer, as its performance in terms of exciting the structure is already degraded. Therefore, the damage in the middle of the structure can still be captured, although the excitation wave is not strong enough to detect damage at the side, thus illustrating that the higher resonance peaks in DSEN_DAT_SIDE are false positive signs and not indicative of more serious damage.
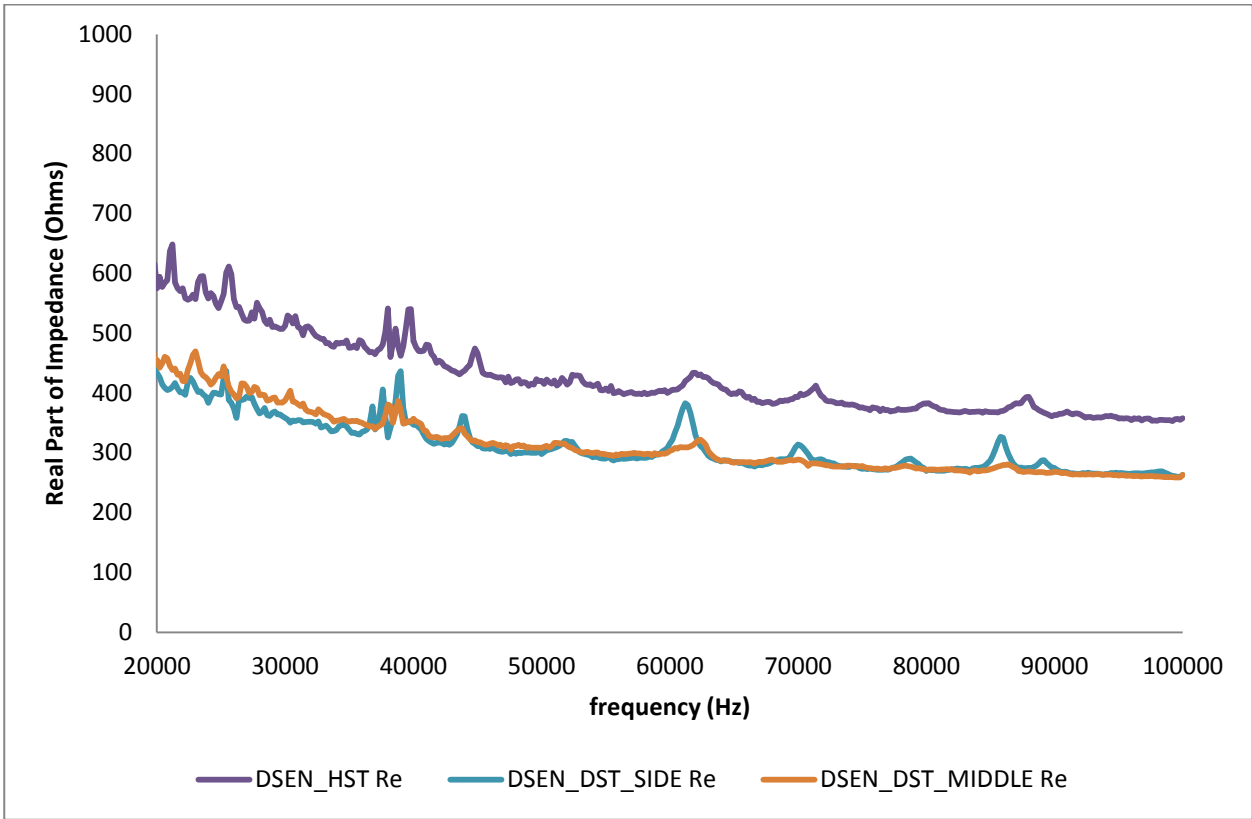
Figure 7-20: Real impedance comparison (DSEN_HST, DSEN_DST_MID and DSEN_DST_SIDE)
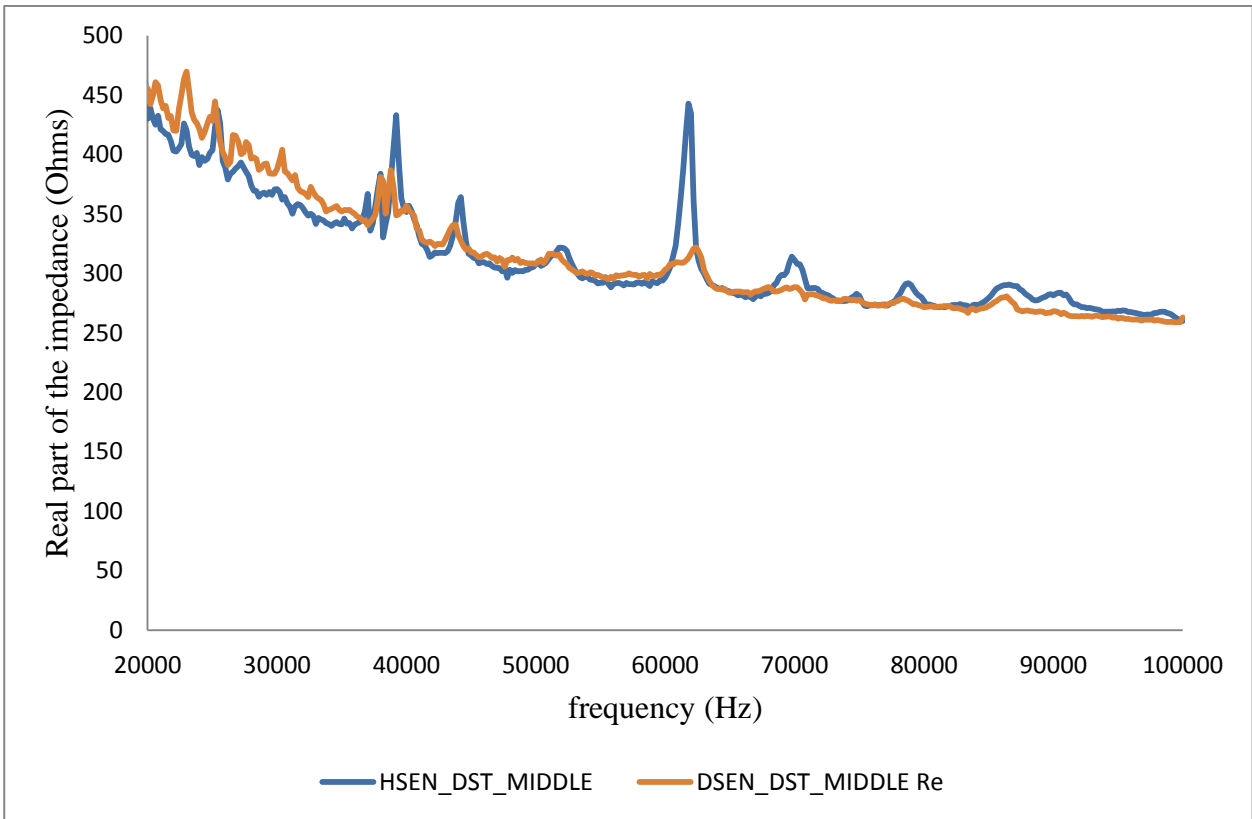
Figure 7-21: Real impedance comparison (HSEN_DST_MID, DSEN_DST_MID)
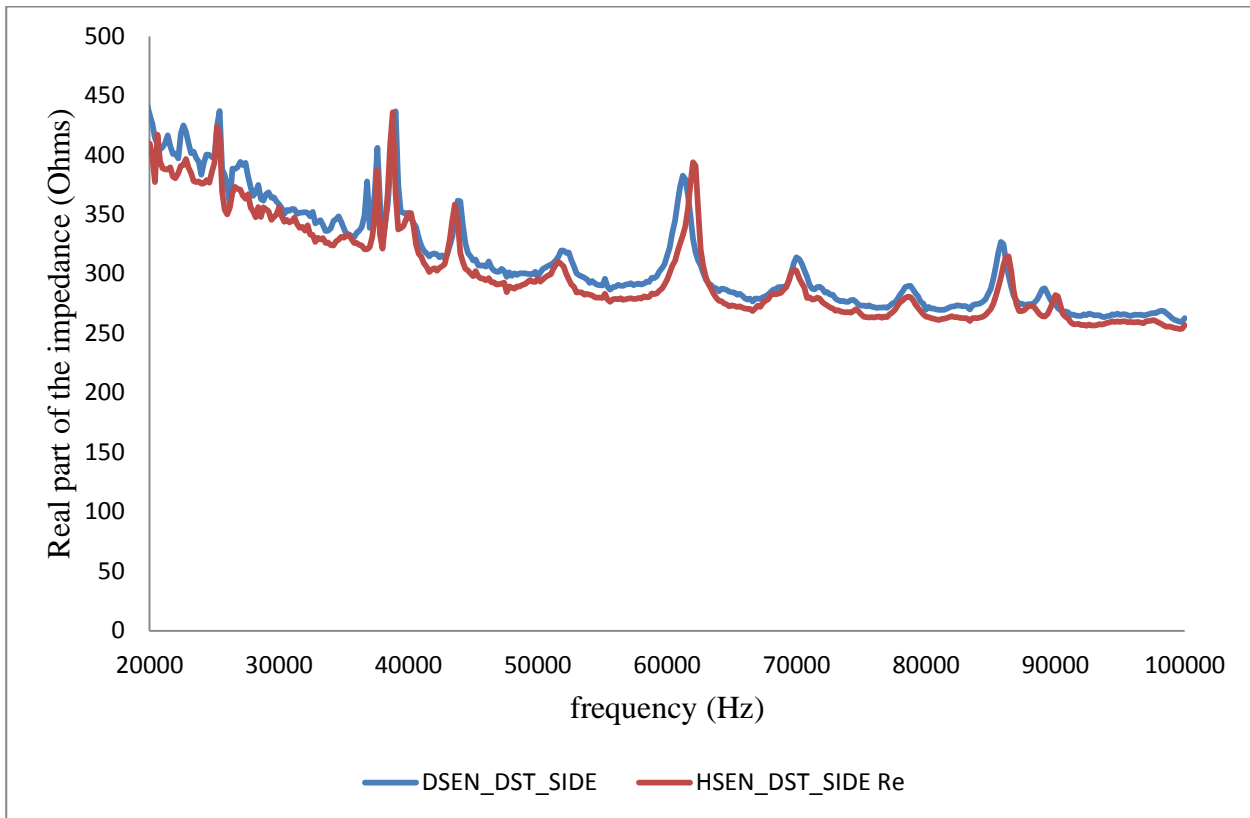
Figure 7-22: Real impedance comparison (HSEN_DST_SIDE, DSEN_DST_SIDE)

7.7.2. Imaginary Impedance (X)

Considering the capacitive nature of MFC electrical impedances, the imaginary part of the impedance should be more sensitive to the possible damage/degradation in the MFC transducer itself. Indeed, it has previously been shown that the equivalent circuit of the MFC consists of a capacitor and V_p generated in the transducer. Without V_p, the electrical impedance of the capacitor is equal to $1/ j\omega C$ (C is capacitance) which is purely imaginary. Furthermore, it was identified in previous chapters that the breakage or destruction of the piezoceramic fibres causes a subsequent reduction in the MFC transducer's capacitance. The damage in the electrodes reduces their ability to generate voltage and therefore change the V_p of the transducer which is a function of structural mass, stiffness or damping as confirmed by numerous studies. This is in accordance with the real part of impedance. Therefore the damage in the transducer affects both the real and imaginary portion of impedance, while it has a more significant impact on the imaginary part due to the type of induced damage, which is the breakage of fibres. The comparisons between the imaginary impedance of all six samples are discussed and plotted from Figure 7-23to Figure 7-31.

For the free MFC transducer, the impedance would be purely capacitive and the 1/jwC relation can be used to calculate the impedance. However, the bonded active MFC shows a different impedance

spectrum, as the mechanical impedance of the host structure is also coupled with the electrical impedance of the transducer. As a result, this electromechanical coupling must be considered when explaining the electromechanical impedance components variations. The generation of the crack in the structure increases the damping, which in turn increases the impedance of the structure (Equation 7-7).

As mentioned earlier, voltage induced into the MFC (V) generates the mechanical excitation due to its converse effect. The bonding layer transfers the mechanical excitation to the structure, thus affecting its structural dynamics through mechanical impedance relations. Therefore, the change in the mechanical impedance of the structure causes a strain on the transducer. The direct effect of the transducer converts this mechanical strain to a current output (I) in the piezoelectric transducer. The ratio of V/I is measured with an impedance analyser and plotted against the designated frequency range. This V/I magnitude ($|Z|$), along with the phase (θ) difference between induced voltage and generated current are used to estimate the real and imaginary part of impedance, as shown in Equation 7-24.

Equation 7-24

$$Z = \frac{V}{I} \quad , \quad |Z| = \sqrt{R^2 + X^2}, \quad \theta = arcttan\left(\frac{X}{R}\right)$$

$$R = |Z|cos\theta \quad X = |Z|sin\theta$$

As shown in Figure 7-23, the structural damage increases the damping, which in turn increases the impedance of the structure (Equation 7-7). In this case, the strain generated in the structure would be less, thereby reducing the current output of the transducer, meaning that the ratio of Z=V/I would increase when the damage occurs in the structure. As such, the trend of the HSEN_DST_MIDDLE in this figure is shifted towards higher negative values when compared to the HSEN_HST sample.

The comparison between the healthy sample and the HSEN_DST_SIDE, which has artificial structural damage far from the transducer, is presented in Figure 7-24. The same argument as HSEN_DST_MIDDLE is applied for this sample. However, the difference between the two plots is not significant, which could be due to the distance between the transducer and the structural damage. For imaginary impedance, the MFC and structure are obscured by the impedance variations due to the frequency dependency. So the changes by structural damage are not significant in the spectrum of imaginary impedance. The impact of structural damage on imaginary impedance is even less noticeable for damages far from the transducer. As a result, even though identical

damage is induced at the middle and side of the structure, the difference between the healthy sample and HSEN_DST_SIDE is not as much as its difference with HSEN_DST_MIDDLE.

Figure 7-23: Imaginary impedance comparison (HSEN_HST, HSEN_DST_MID)
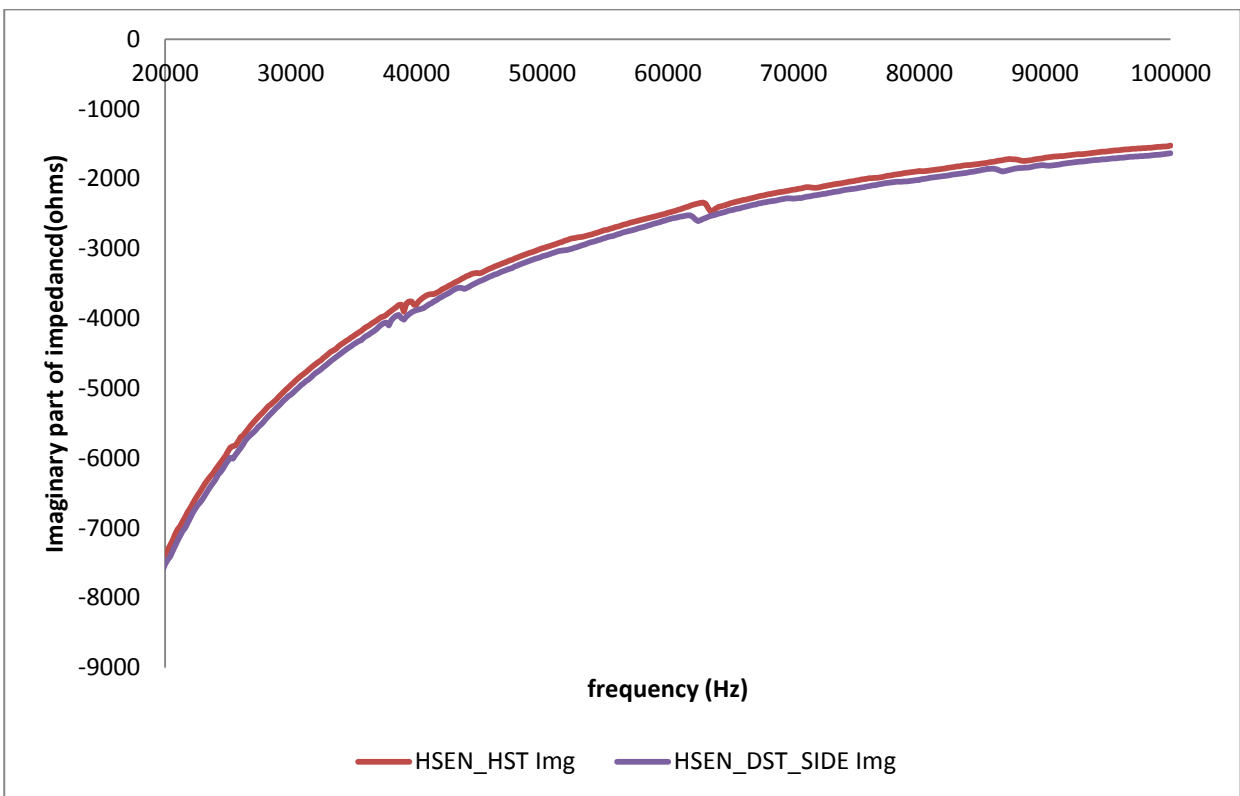
Figure 7-24: Imaginary impedance comparison (HSEN_HST, HSEN_DST_SIDE)

The ability of the MFC transducer to detect the structural damages close (HSEN_DST_MIDDLE) and far (HSEN_DST_SIDE) from its locations is provided in Figure 7-25.
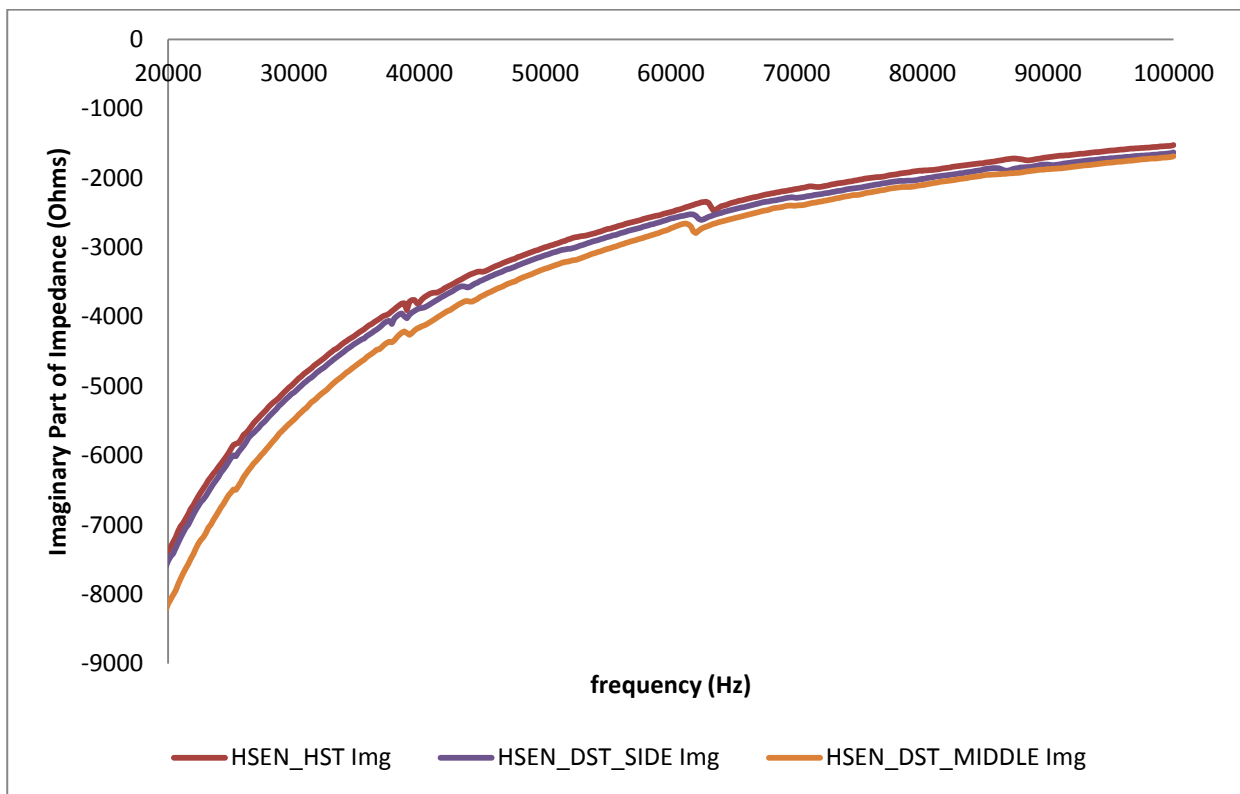
Figure 7-25: Imaginary impedance comparison (HSEN_HST, HSEN_DST_MID and HSEN_DST_SIDE)

It is shown that the generation of damage in the structure shifts the imaginary impedance slope towards values which are higher in magnitude. Moreover, the imaginary impedance slope of the sample with damage close to the transducer has increased further compared to the sample with structural damage at the side. This means that the amount of shift is relevant to the distance of the structural damage to the transducer. Another comparison is provided in Figure 7-26, thereby allowing us to observe the effect of sensor damage on imaginary impedance. It can be seen that the transducer damage results in further changes in the imaginary impedance plot when compared to structural damage, thus confirming that the imaginary impedance is more sensitive to damage in the transducer. The damage in the transducer reduces its capacitance, as shown previously which in turn increases the electrical impedance due to the inverse relationship between the capacitance and electrical impedance. Therefore, the slope of DSEN_HST in this figure has higher values compared to the healthy sample.

The difference between the imaginary impedance of the healthy sample and the sample with the damaged transducer can also be explained through the electromechanical impedance relationship. The same amount of voltage is introduced into both the healthy and damaged transducers bonded on healthy structures (HSEN_HST and DSEN_HST), but the damaged transducer generates less

212

strain as shown in previous chapters, with the piezoelectric coefficient (d_{33}) reducing when the damage occurs in the transducer. As a result, the mechanical excitation which transfers to the structure would be less for the damaged transducer. This leads to a lower strain coming back from the structure to the transducer, which in turn generates a lower output current. Therefore, for the same amount of excitation voltage, the output current would be less for the damaged transducer, thus making its V/I (electromechanical impedance) ratio higher compared to healthy transducers.

The most complex situation in the electromechanical impedance-based technique is where both the transducer and the structure are damaged. These situations are investigated through the comparison of healthy samples with DSEN_DST_SIDE and DSEN_DST_MIDDLE as plotted in Figure 7-27 and Figure 7-28. It was shown in previous plots that both structural and transducer damage increase the imaginary portion of impedance while this increase is more significant for transducer damage. Therefore, the trends of these two figures also show an increase in the imaginary impedance, as expected. Moreover, the comparison of these two damage scenarios is plotted in Figure 7-29. In this figure, the trends of these two damage scenarios are very similar in both shape and magnitude. It can be argued that the damage in the transducer reduces its sensitivity, thus meaning it is not able to distinguish the damage location in the structure.

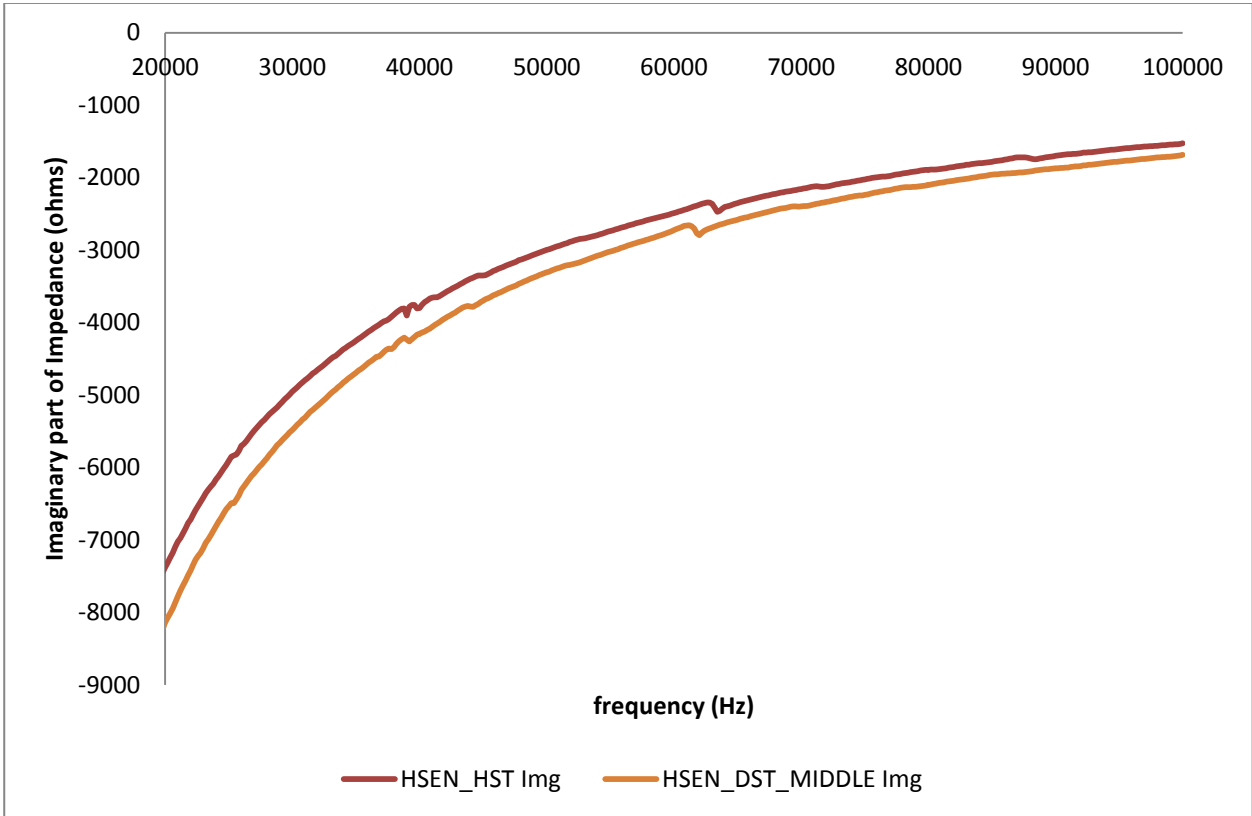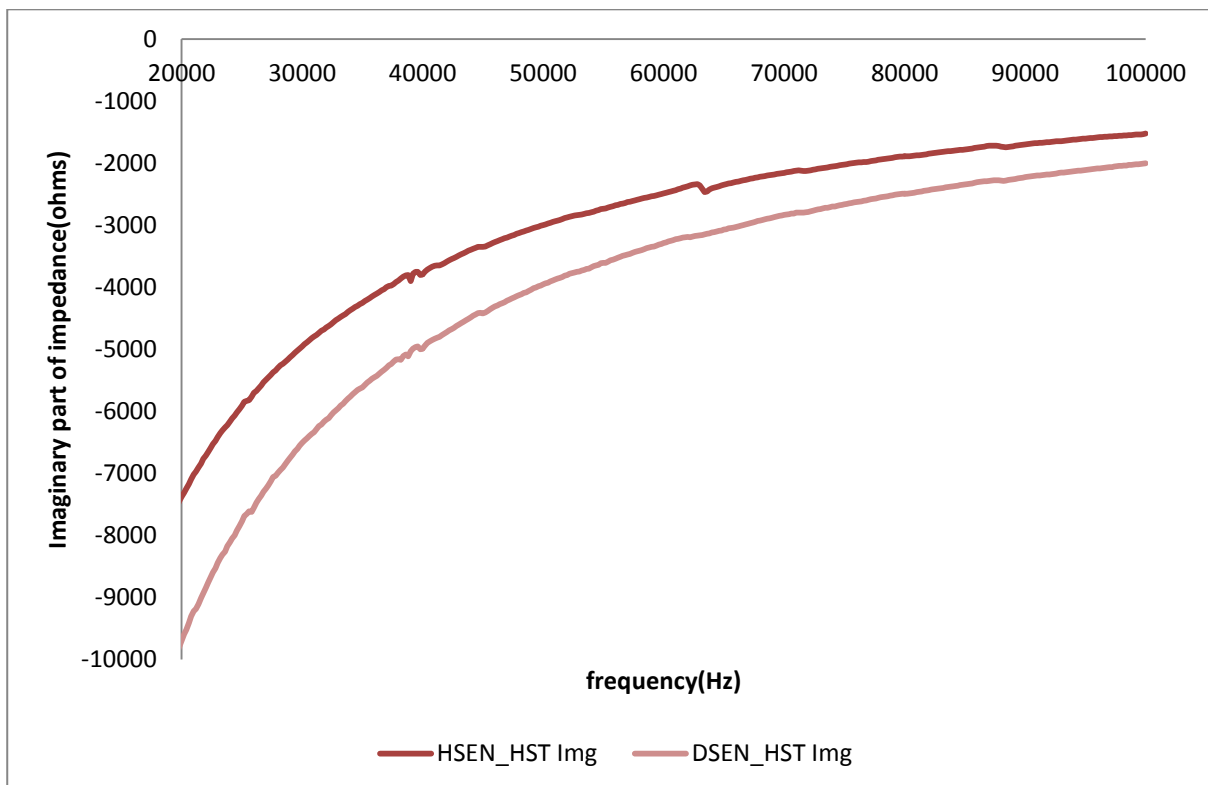**Figure 7-26: Imaginary impedance comparison (HSEN_HST, DSEN_HST)**

213
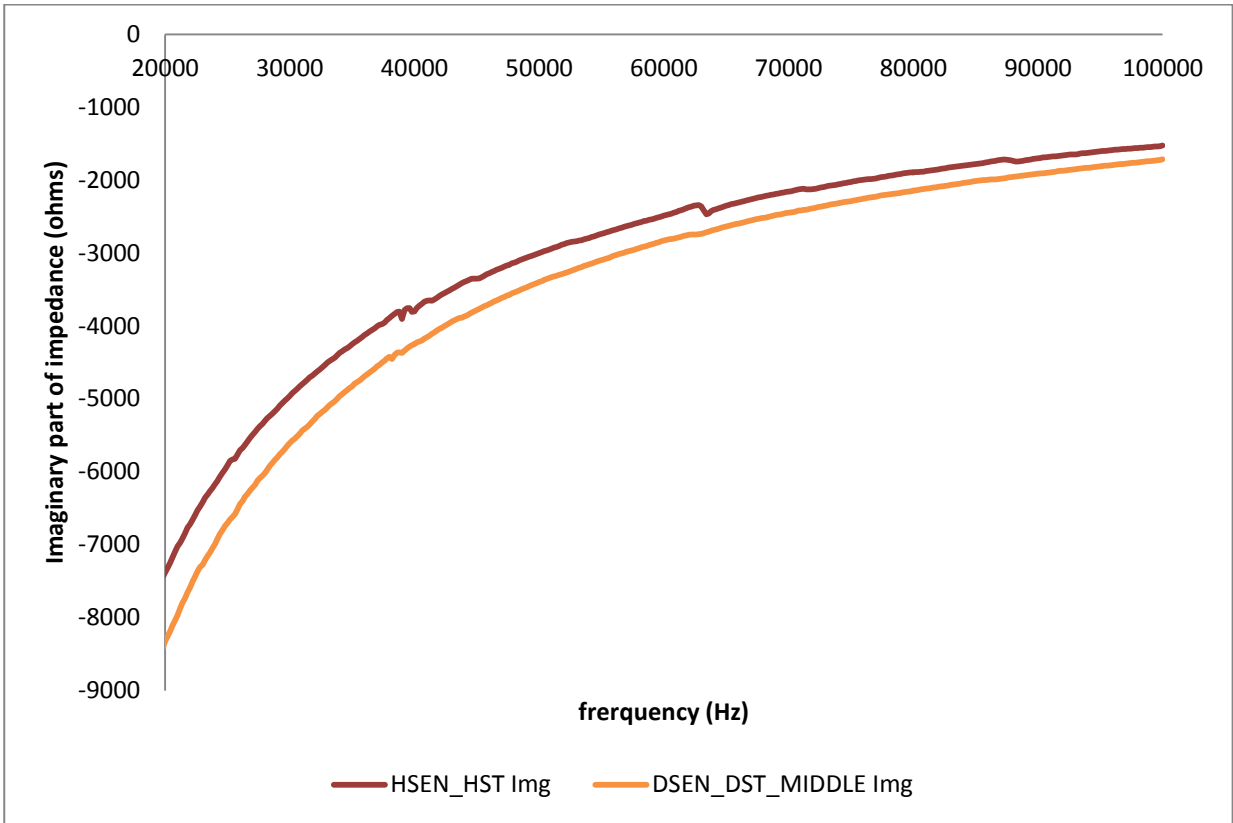
Figure 7-27: Imaginary impedance comparison (HSEN_HST, DSEN_DST_MID)
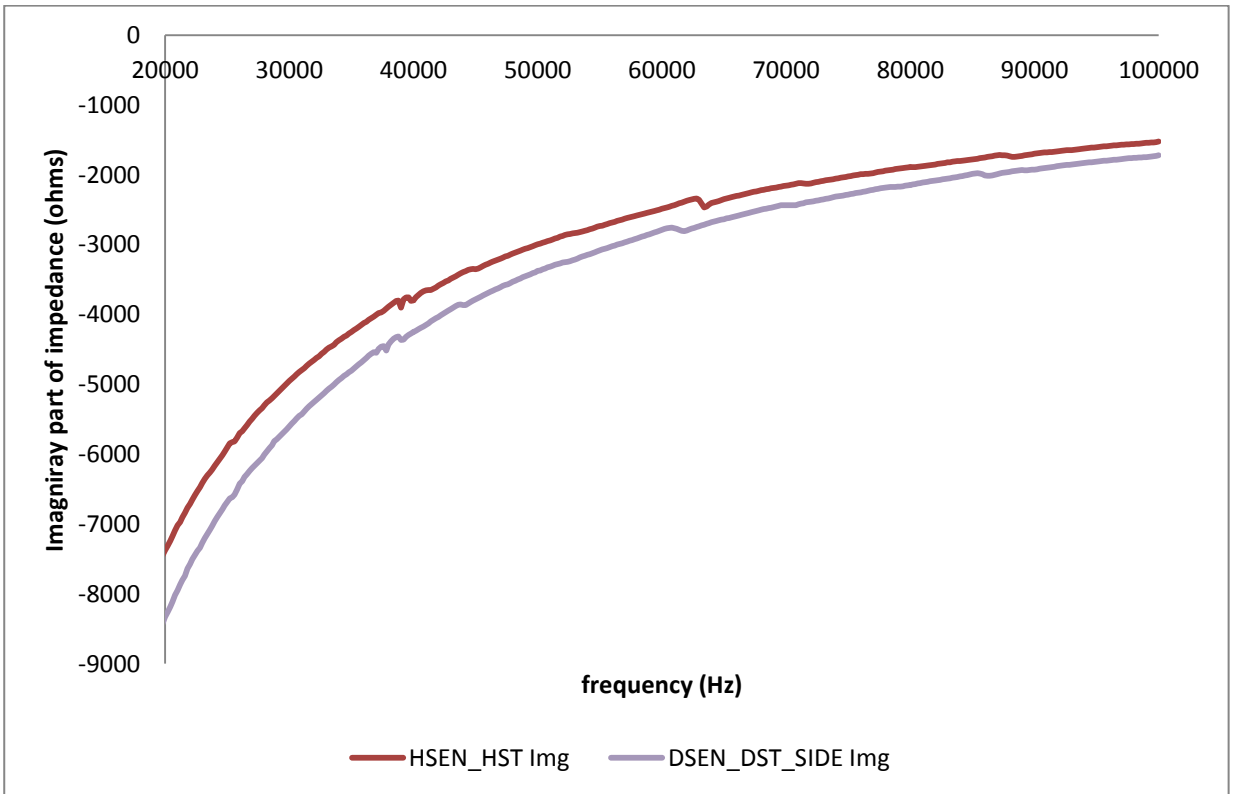
Figure 7-28: Imaginary impedance comparison (HSEN_HST, DSEN_DST_SIDE)
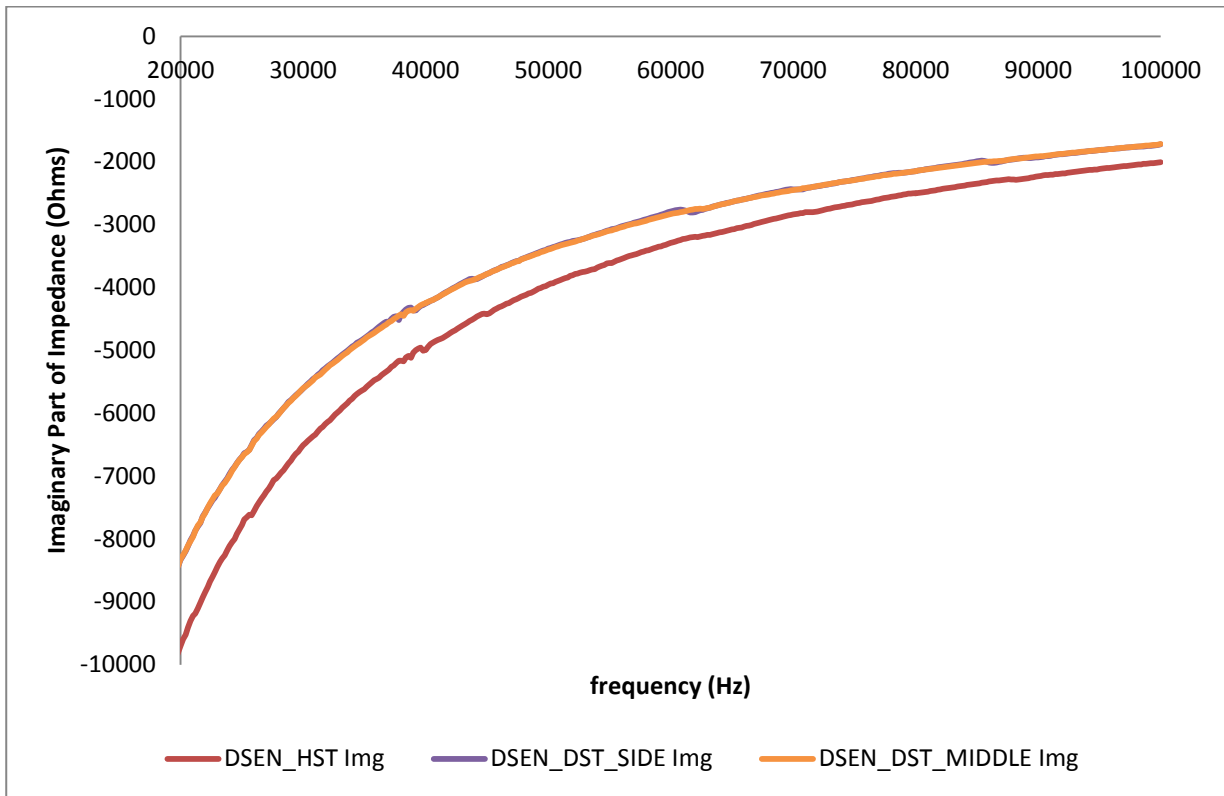
Figure 7-29: Imaginary impedance comparison (DSEN_HST, DSEN_DST_MID, and DSEN_DST_SIDE)

It can be argued that for the structural damage detection when the transducer is also damaged, the reduction of the stiffness of the structure due to damage is more detectable for the transducer. This reduction also reduces the mechanical impedance of the structure, which in return increases the mechanical excitation which transfers back to the transducer. This also generates more current on the transducer due to the direct piezoelectric effect which reduces the V/I ratio. Therefore, even though both structural and transducer damage increase the absolute imaginary value (downward shift), this shift is lower for the situation where both the structure and transducer are damaged, as some of the increases in the imaginary magnitude would be compensated by the reduction stemming from the stiffness reduction due to structural damage.

In order to evaluate the sensitivity issue of the damaged transducer to detect structural damage, the comparisons of the imaginary impedances for the healthy and damaged transducer bonded onto the structures with identical damage are plotted in Figure 7-30 and Figure 7-31. In Figure 7-30, the HSEN_DST_MIDDLE is plotted against DSEN_DST_MIDDLE, thus showing the ability of the damaged transducer to detect the structural damage close to the location of the transducer compared to the healthy transducer. Unlike the previous figure, the imaginary impedance of the damaged and healthy transducer when the damage is far from the transducer location differs in Figure 7-31. In the HSEN_DST_SIDE sample, the transducer is still intact and can detect the structural damage far from its location. However, the transducer in DSEN_DST_SIDE is damaged,

215

and its sensitivity is degraded. In light of this, it could not completely capture all of the mechanical impedance changes due to the structural damage, which makes its plot different from the healthy transducer. The damage in the transducer caused a phase between the induced voltage and output current, thus explaining the higher values of the HSEN_DST_SIDE compared to the HSEN_HST. Moreover, the imaginary impedance measurements of DSEN_DST_SIDE are higher than HSEN_HST, which confirms that the transducer is still capable detecting structural damage. It can be concluded that the structural damage shifts the slope of imaginary impedance towards higher values (absolute values) and that the more serious the damage, the larger the shift becomes. However, the fact that the imaginary impedance values for HSEN_DST_SIDE are higher than for DSEN_DST_SIDE can be categorised as a false positive sign of structural damage. In other words, the statuses of the structures are identical in these two samples, and the reason for the further shift in the HSEN_DST_SIDE is the degradation of the transducer sensitivity in DSEN_DST_SIDE. This calls for an investigation of other electromechanical components which are capable of delineating such a complex situation.
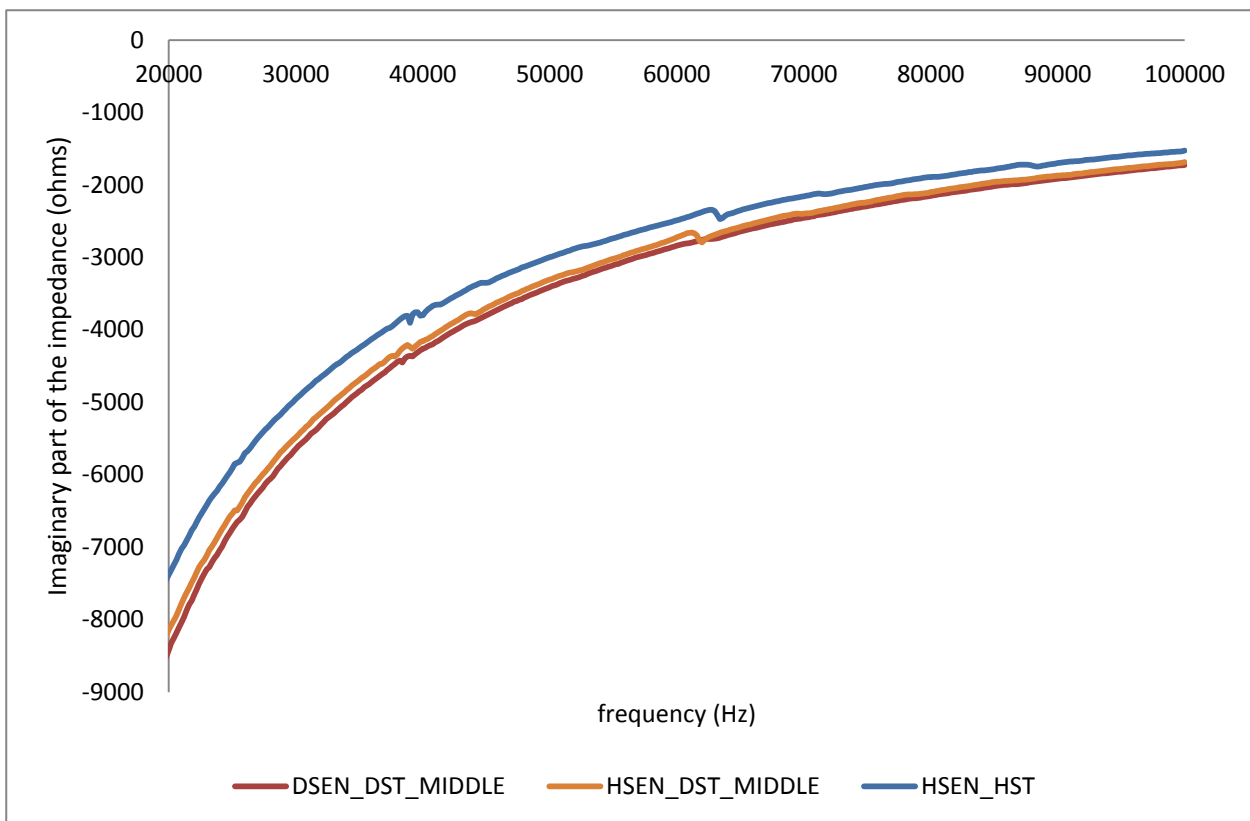
Figure 7-30: Imaginary impedance comparison (HSEN_HST, HSEN_DST_MID, and DSEN_DST_MID)
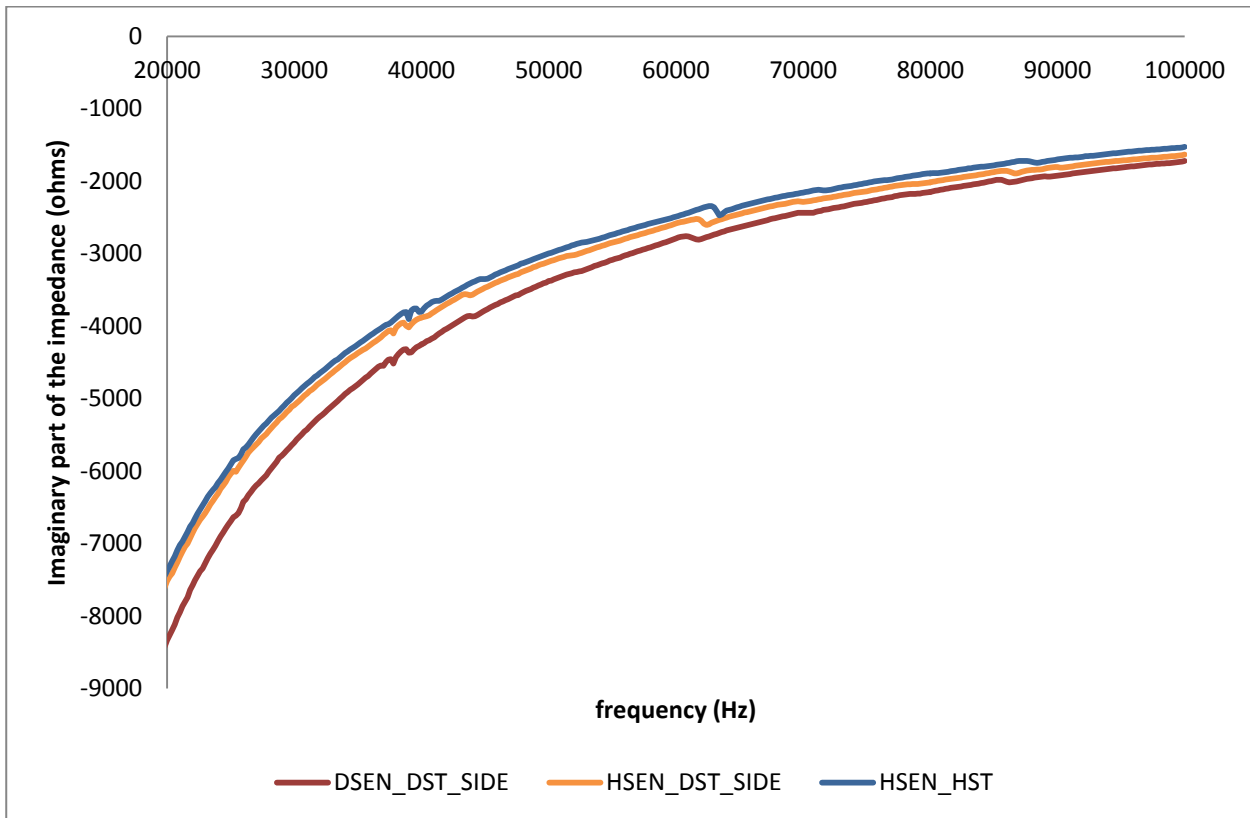
Figure 7-31: Imaginary impedance comparison (HSEN_HST, HSEN_DST_SIDE, and DSEN_DST_SIDE)

7.7.3. Real Admittance (Conductance G)

It has been observed that the real and imaginary impedance parameters are not suitable to explain the behaviour of the transducer and the structure in the case of both being damaged. With this in mind, another parameter must be used in order to delineate the impacts of transducer damage and structural damage on the measurements. For this purpose, electromechanical admittance (Y), which is the inverse of electromechanical impedance, is used in this research. The real and imaginary components of admittance are called conductance (G) and susceptance (B), and are defined as Equation 7-25:

Equation 7-25

$$Y = G + iB$$

Where

$$G = \frac{R}{R^2 + X^2} \ (siemens) \qquad B = -\frac{X}{R^2 + X^2} (siemens)$$

Therefore, the magnitude and phase of the admittance are given by:

217

Equation 7-26

$$|Y| = \sqrt{G^2 + B^2} = \frac{1}{\sqrt{R^2 + X^2}} \qquad \varphi = \arctan\left(\frac{B}{G}\right) = \arctan\left(-\frac{X}{R}\right)$$

It can be seen from the above equations that the admittance components are calculated from impedance components. Therefore, Equation 7-25 and Equation 7-26 are used to calculate the conductance and susceptance of all six samples using the measured impedance values. The comparison of the admittance values are plotted and discussed in the following graphs. The fact that the real and imaginary admittances are relevant to both real and imaginary impedances, make them reliable parameters for the mixing damage situations. The effects of damage at the middle and side of the structure (close and far field of transducer) on real admittance (conductance) are presented in Figure 7-32 and Figure 7-33. In both cases, a downwards shift of the conductance slope towards lower conductance values is observed. This is due to the reduction in the stiffness of the structure with damage, which in turn reduces the real part of admittance (Equation 7-23). Moreover, the damage in the structure reduces the magnitude of resonance peaks, which is due to the fact that the summation of mechanical and electrical admittance of the damaged structure has reduced when the real impedance increases because of structural damage. Furthermore, the resonance peaks are shifted towards lower frequency values.
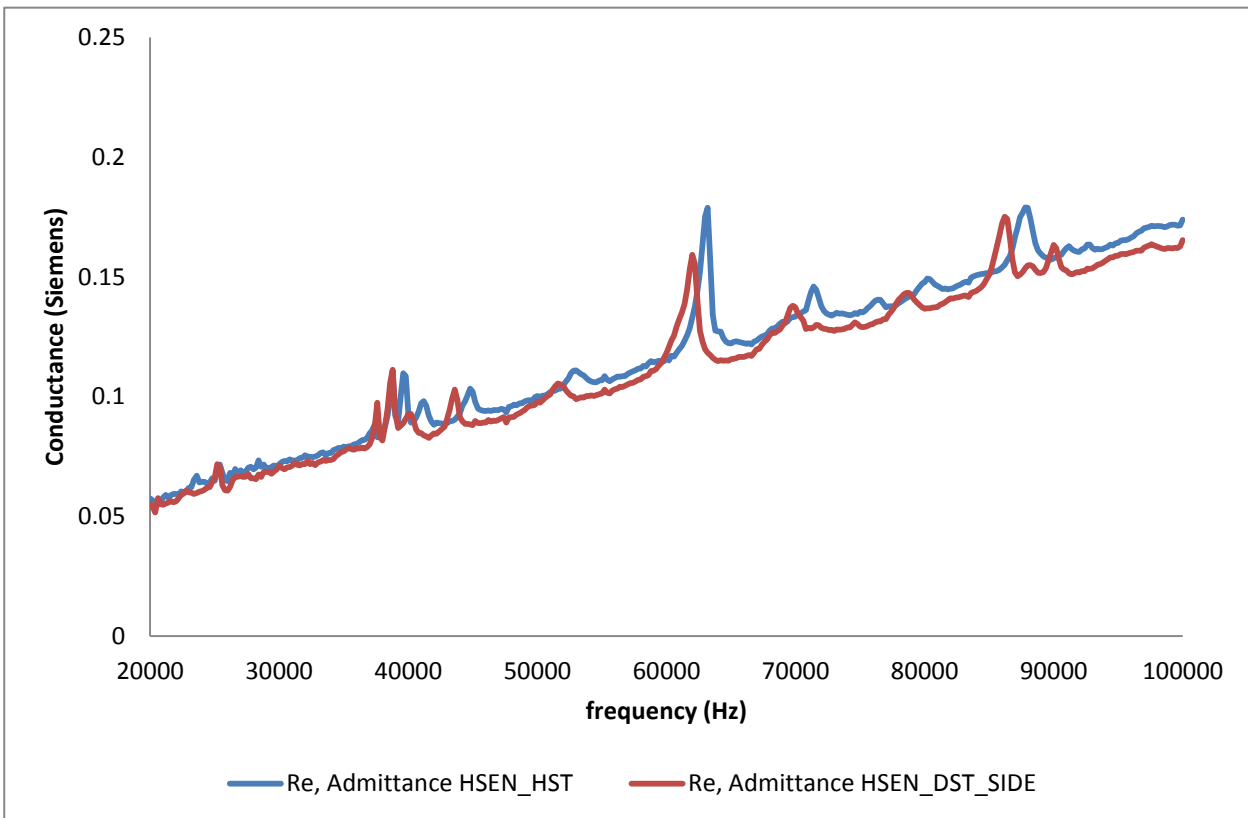
Figure 7-32: Conductance comparison (HSEN_HST, HSEN_DST_SIDE)
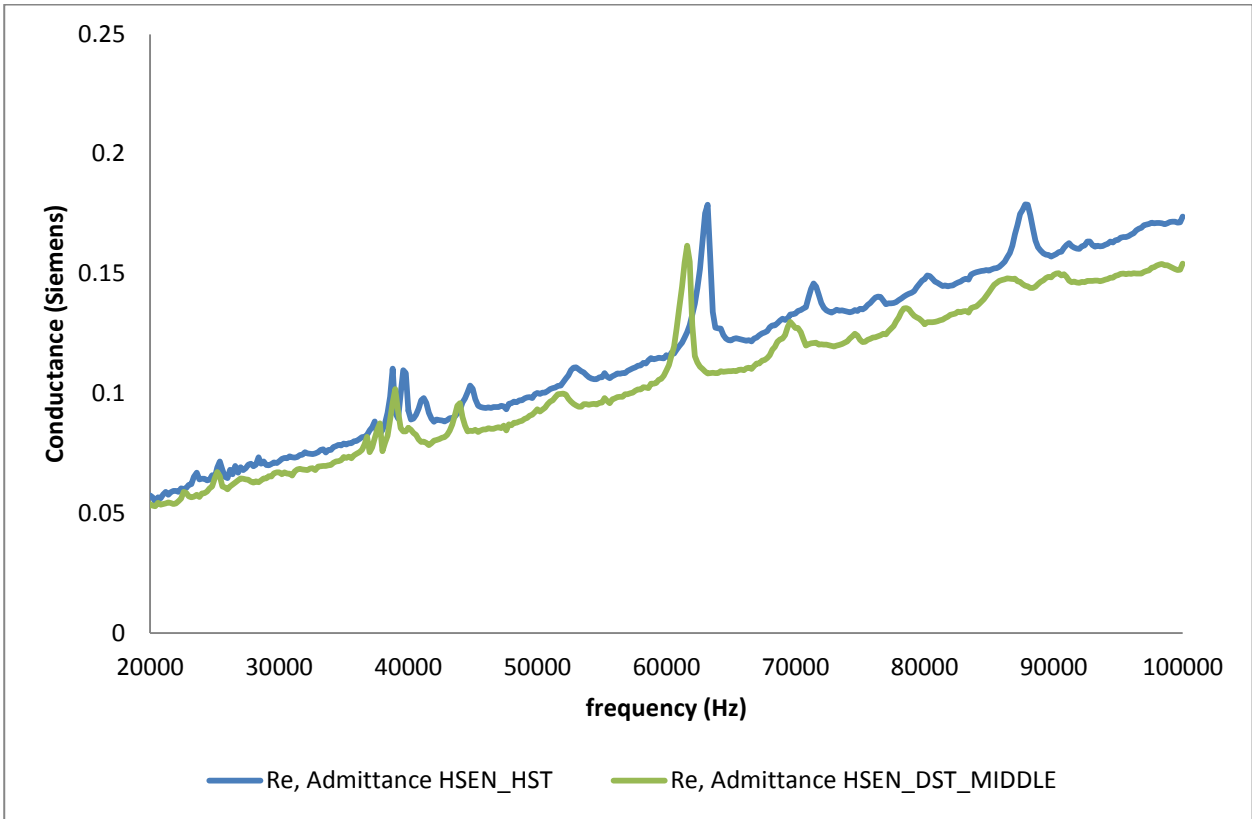
Figure 7-33: Conductance comparison (HSEN_HST, HSEN_DST_MID)
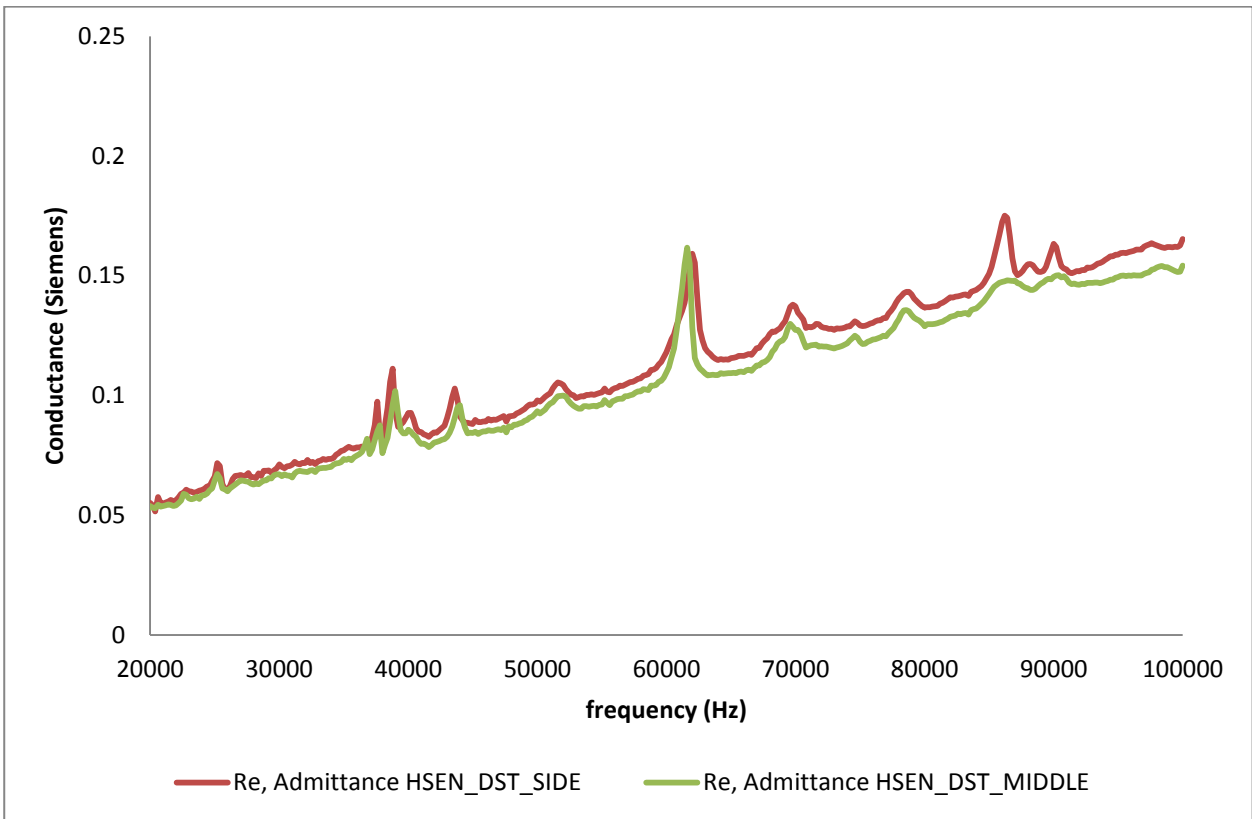
Figure 7-34: Conductance comparison (HSEN_DST_MID, HSEN_DST_SIDE)

The reason for the further downward shift of the conductance for HSEN_DST_MIDDLE compared to HSEN_DST_SIDE (Figure 7-34) is the fact that the transducer is more sensitive to the structural damage in the close field, which causes a further reduction in the conductance of the structure with damage at the middle.

The effect of transducer damage on the conductance values is presented in Figure 7-35. The trends of the healthy sample and DSEN_HST are similar, thus illustrating that the degraded transducer is still performing. However, the magnitude of the peaks, especially at the resonance frequency of the transducer (about 60 KHz), is drops significantly, which is due to the weakness of the damaged transducer in exciting the structure with enough mechanical excitation to capture all its characteristics and generate resonance peaks. In addition, a minor shift in the slope of the plot towards higher values can be observed, and this is due to the increase in the real admittance caused by the transducer damage (Equation 7-23). It can be argued that the damage in the structure shifts the slope of conductance towards lower values, while the damage in the transducer shifts it towards higher values.
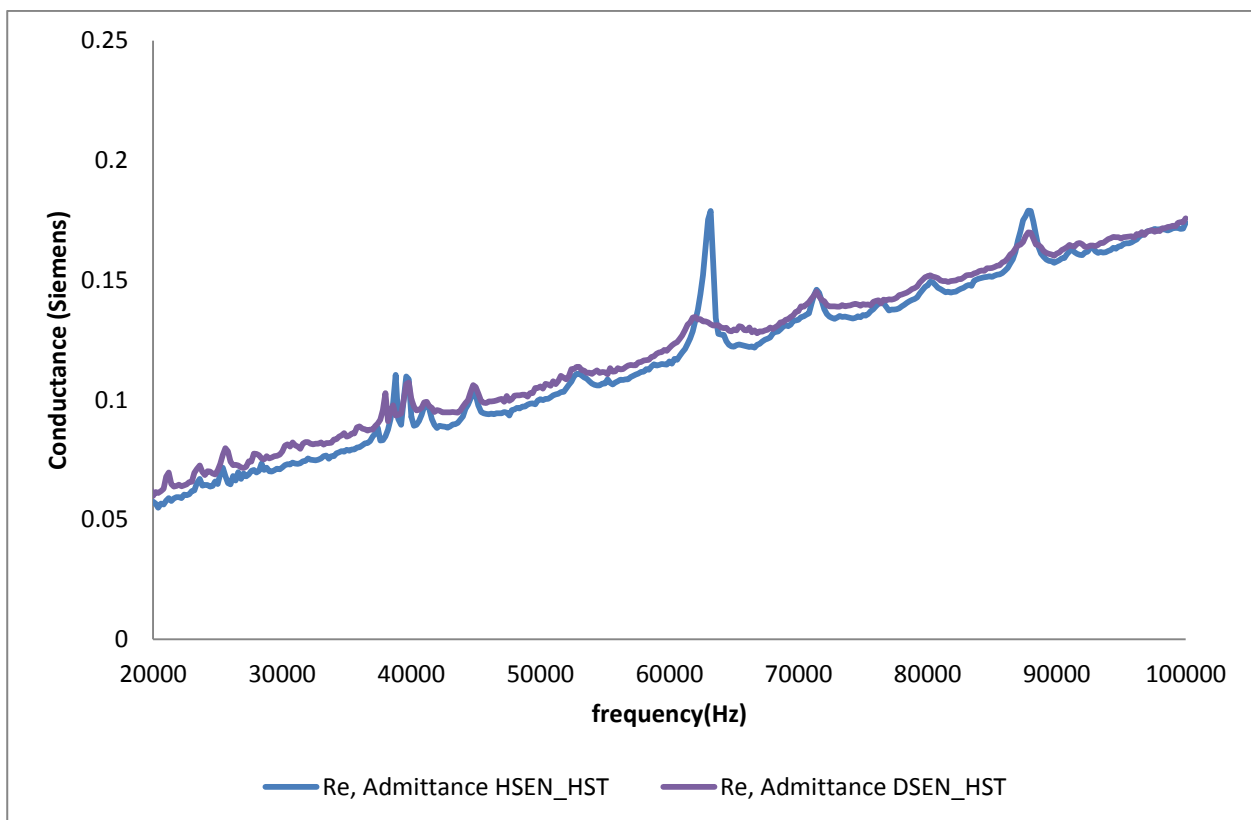
Figure 7-35: Conductance comparison (HSEN_HST, DSEN_HST)

The most complex scenario is where both the transducer and the structure are damaged (DSEN_DST_SIDE and DSEN_DST_MIDDLE). This scenario could not be investigated properly

through the impedance relationships in previous sections, thus raising the need for another parameter to delineate the behaviour of the transducer and the structure when both are damaged. The comparison of these samples with the healthy ones is provided in Figure 7-36 and Figure 7-37. It is observed from these two figures that the separations of plots of healthy and damaged samples are increased as the frequency gets higher. The lower frequencies are more sensitive to the far field of the transducer while the higher frequencies are more sensitive to the transducer's local area. Therefore, further reductions are observed in higher frequencies in Figure 7-36 compared to Figure 7-37. This is due to the fact that for the DSEN_DST_MIDDLE sample, both structural and transducer damage is in the local area of the transducer. According to Equation 7-25, the conductance depends on the structural status and the transducer status. Therefore, the total values of conductance, according to its relationship with R and X, are reduced, as seen in these two figures.

Furthermore, the magnitude of resonance peaks is significantly reduced in DSEN_DST_MIDDLE (Figure 7-36) while for DSEN_DST_SIDE, this reduction is considerably less. Moreover, the resonance peaks are shifted towards lower frequency values for both cases as seen in Figure 7-38.
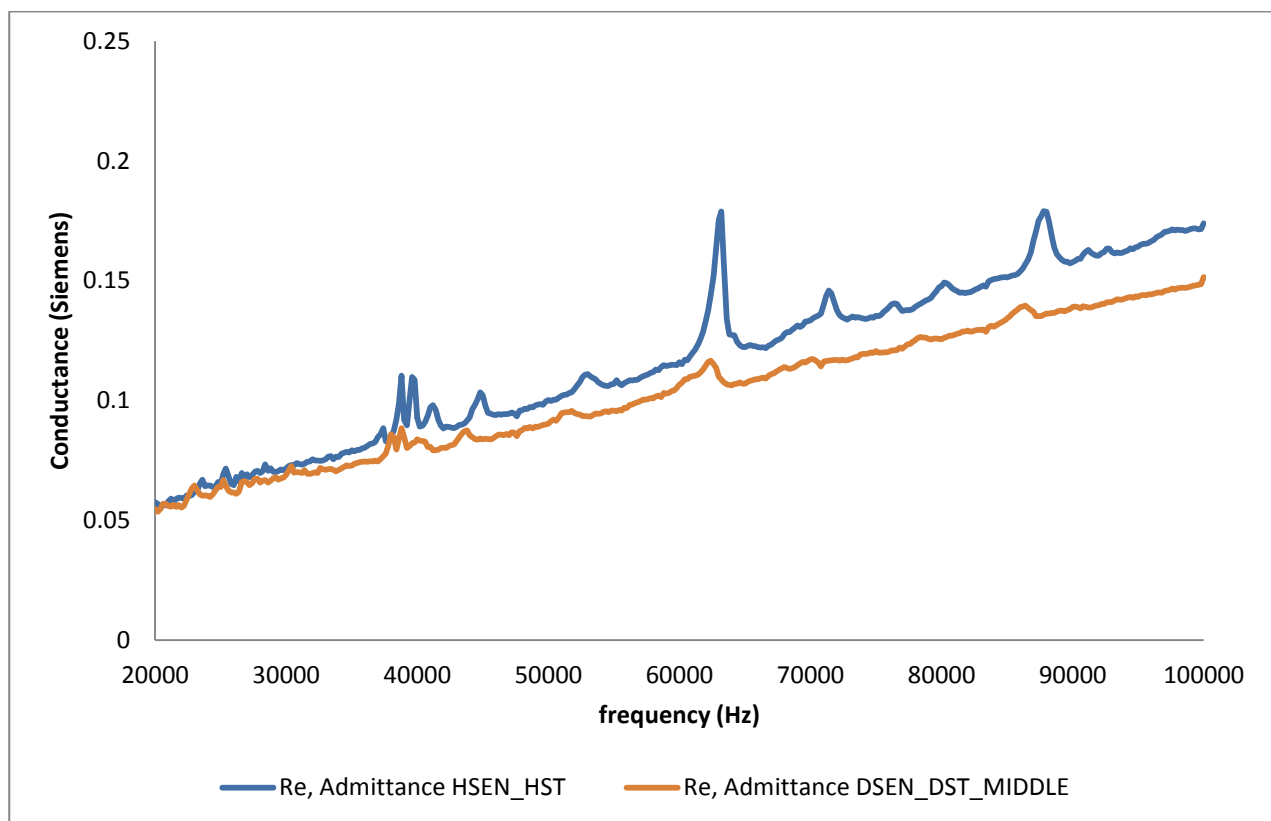
Figure 7-36: Conductance comparison (HSEN_HST, DSEN_DST_MID)

Figure 7-37: Conductance comparison (HSEN_HST, DSEN_DST_SIDE)
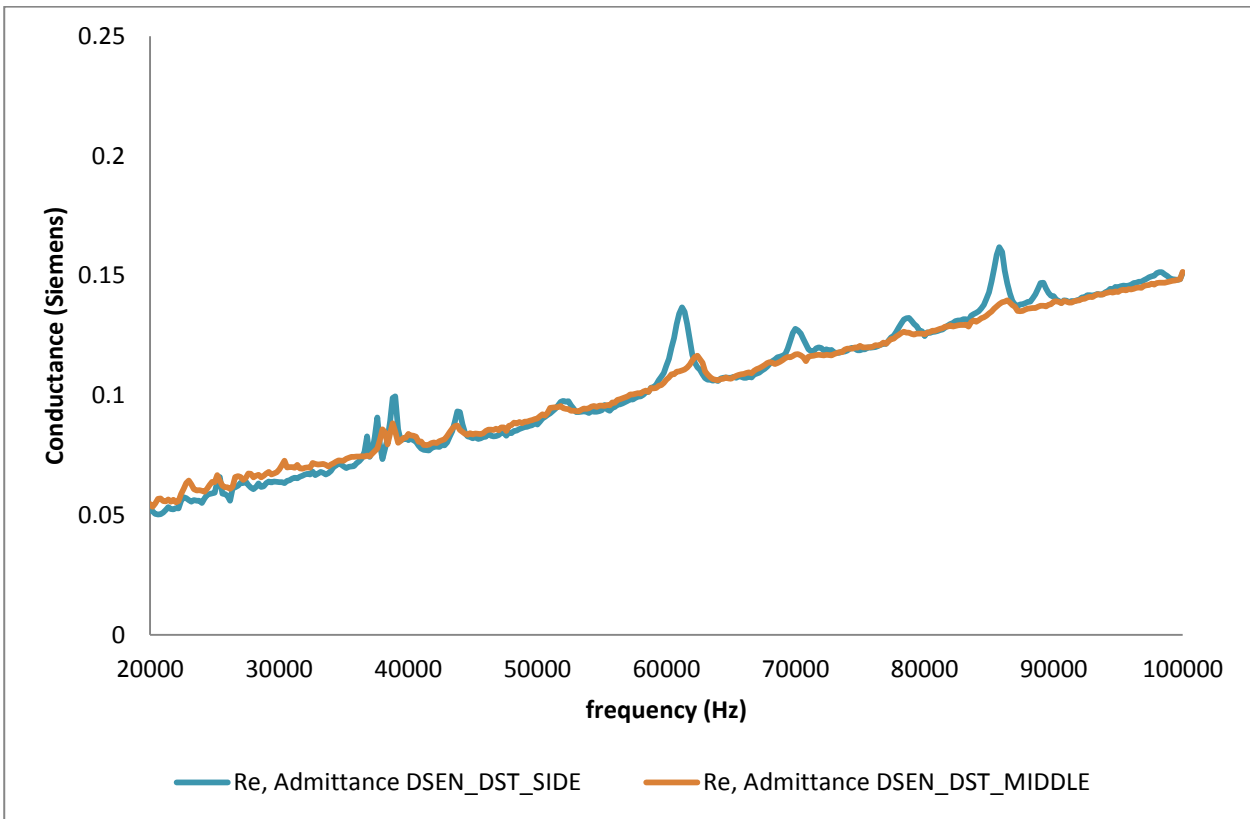
Figure 7-38: Conductance comparison (DSEN_DST_MID, DSEN_DST_SIDE)

The performance of the healthy and damaged transducer in detecting structural damage in the transducer's close (Middle) and far (Side) fields is provided in Figure 7-39 and Figure 7-40. From Figure 7-39, it can be seen that the magnitude of the resonance peak of the MFC (about 60000Hz) is slightly reduced while the magnitude of other peaks remains constant. This shows that the damaged transducer has weak performance in detecting structural damage in the far field. On the other hand, the responses of the damaged transducer when the structural damage is close to its field (Figure 7-40) are considerably different. Both the transducer and structural resonance peaks are significantly reduced, in magnitude, thus confirming the sensitivity of the damaged transducer to local structural damage. It is observed from these figures that the behaviour of the damaged transducer in terms of detecting structural damage for DSEN_DST_SIDE and HSEN_DST_SIDE is due to the excitation signal of the damaged transducer not being strong enough to capture the far field structural damage which is the case of a false negative indication.

Figure 7-39: Conductance comparison (HSEN_DST_SIDE, DSEN_DST_SIDE)

Figure 7-40: Conductance comparison (HSEN_DST_MID, DSEN_DST_MID)
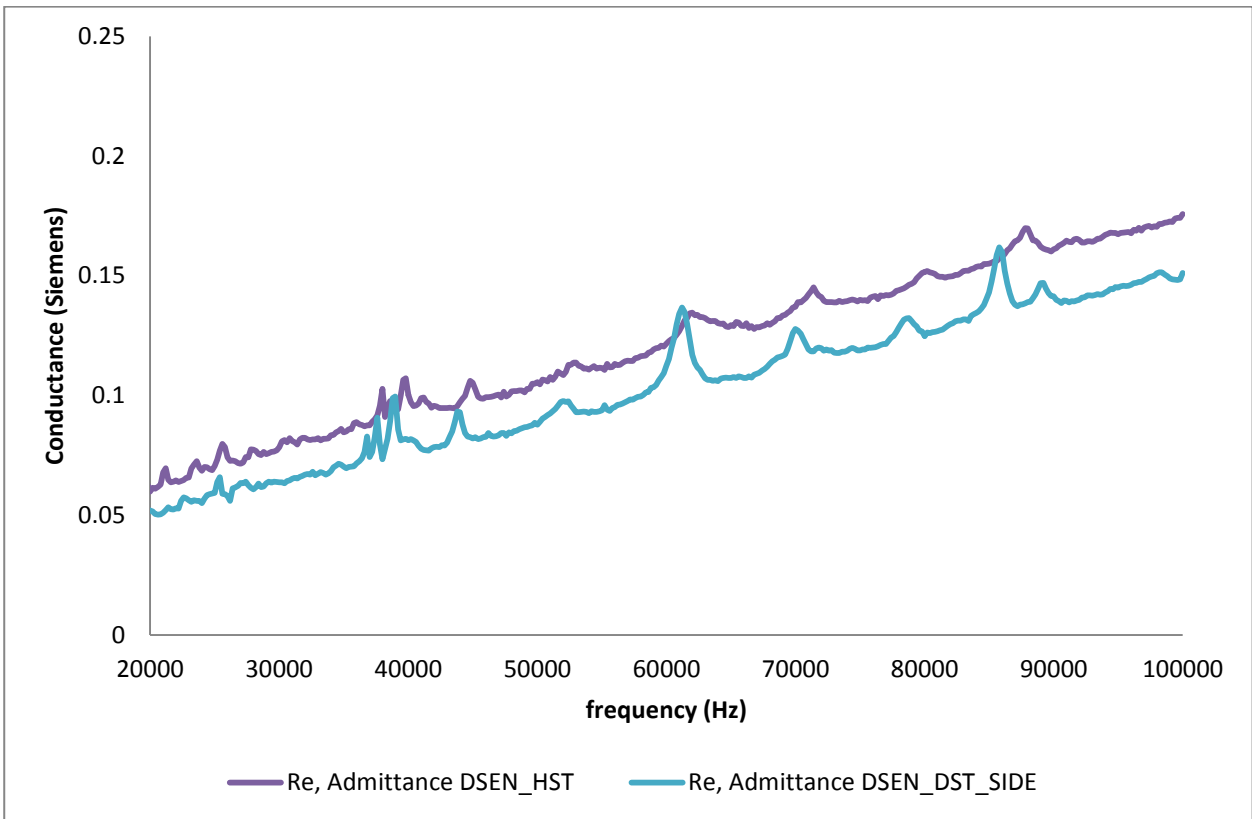
Figure 7-41: Conductance comparison (DSEN_HST, DSEN_DST_SIDE)
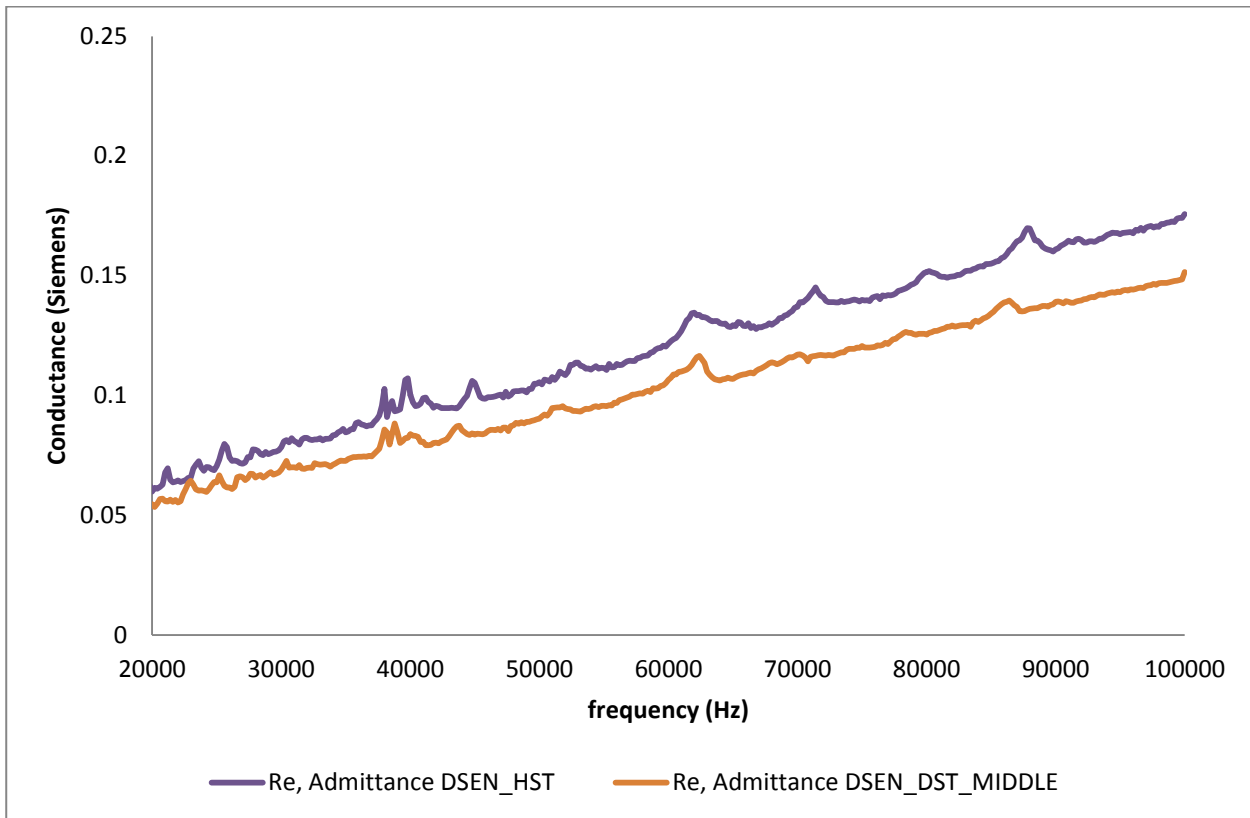
Figure 7-42: Conductance comparison (DSEN_HST, DSEN_DST_MID)

Figure 7-41and Figure 7-42 are comparing the conductance of the sample with the damaged transducer when the structure is either intact or damaged (middle or side). These plots can be used to explain how useful the responses of the damaged transducer are when it comes to detecting structural damage. It is observed that in both cases, the damage in the structure shifts the slope of conductance values towards lower values. When looking at conductance plots, it can be argued that this parameter can perform well in terms of detecting transducer damage and structural damage. Moreover, it may include false negative indications when both the transducer and the structure are damaged, especially for structural damage in the transducer's far field.

7.7.4. Imaginary Admittance (Susceptance B)

The next parameter which is used to delineate transducer damage from structural damage is the imaginary admittance, known as susceptance (B). The relations for this parameter have been previously provided in Equation 7-25 and Equation 7-26. The susceptance values are calculated based on real and imaginary impedance and presented in Figure 7-43 to Figure 7-53 as below. All 6 samples with various damage situations are plotted and compared using susceptance. The comparison of the healthy sample and the sample with damaged structure close and far from the transducer is provided in Figure 7-43and Figure 7-44. It is observed that in both cases, the structural damage shifts the slope of susceptance towards higher values. Furthermore, the

225

magnitudes of the resonance peaks are reduced and peaks are shifted towards lower frequency values. This is due to the increasing compliance of the structure when the damage is introduced into the structure.

As previously mentioned, the lower frequencies are more indicative of the overall condition of the system while the higher frequencies are more sensitive to local damage. In these two samples, HSEN_DST_SIDE and HSEN_DST_MIDDLE, the transducer is intact and damages are induced in both structures with similar dimensions and different locations. Therefore, the slopes of susceptance for both samples are relatively similar at low frequencies while their differences become significant at higher frequencies as the HSEN_DST_MIDDLE has the structural damage at the local area of the transducer. The comparison of these two samples is provided in Figure 7-45. The ability of susceptance to detect damage in the transducer is investigated in Figure 7-46. It is observed that the susceptance of the sample with damaged transducer is shifted towards lower values. This is due to the reduction in the capacitance value of the damaged transducer which affects the susceptance relation. Moreover, the magnitudes of resonance peaks are dropped, especially at the resonance frequency of the transducer (about 60000Hz) which occurs due to the degradation of transducer performance stemming from damage which is more significant at the resonance frequency of free MFC. It can be argued that the susceptance shows more sensitivity to the transducer status when compared to the structural status.
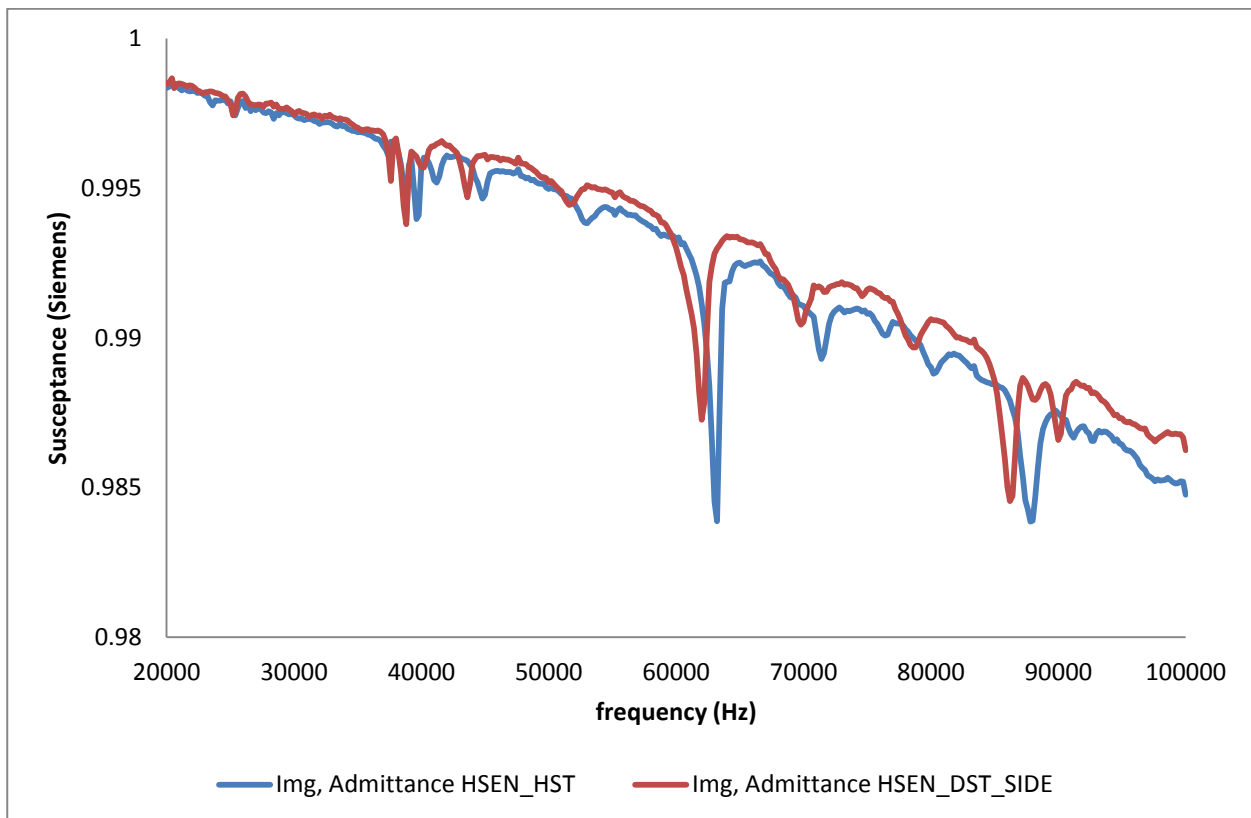
Figure 7-43: Susceptance comparison (HSEN_HST, HSEN_DST_SIDE)
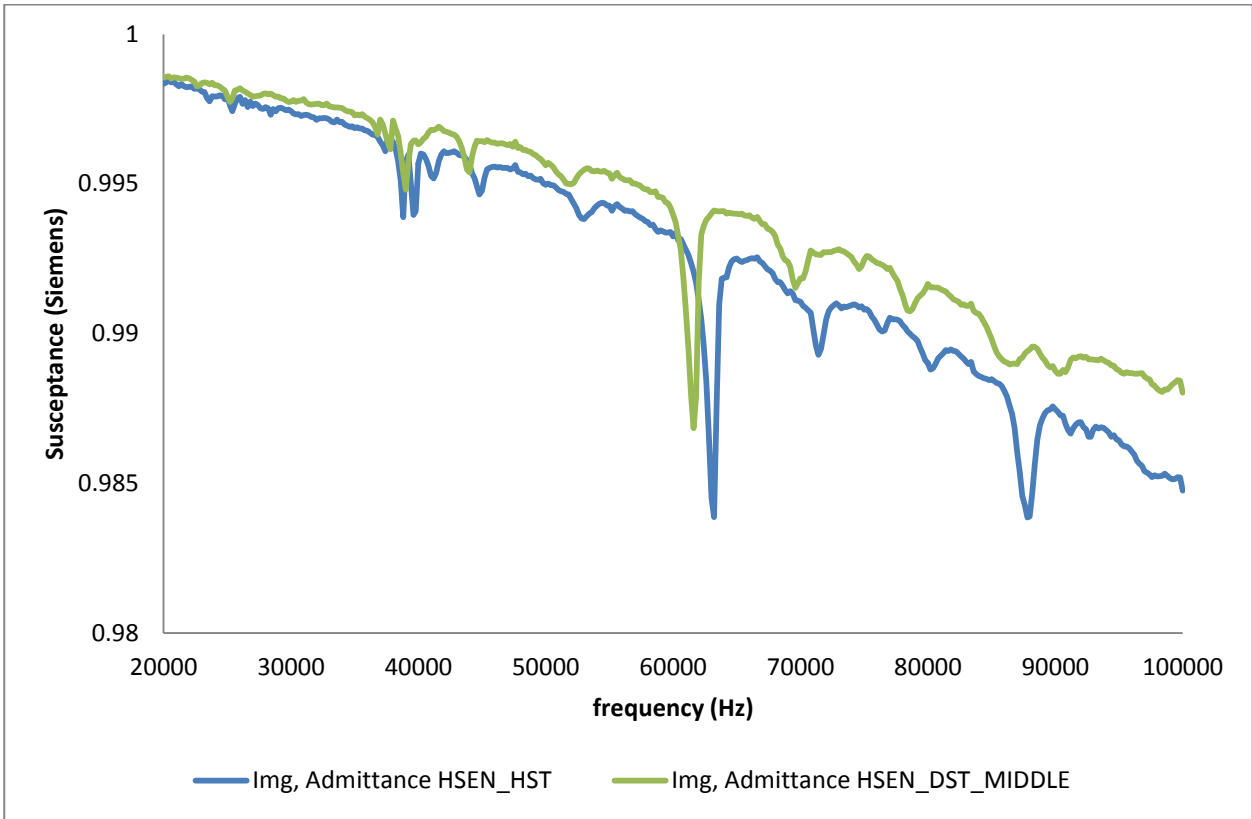
Figure 7-44: Susceptance comparison (HSEN_HST, HSEN_DST_MID)
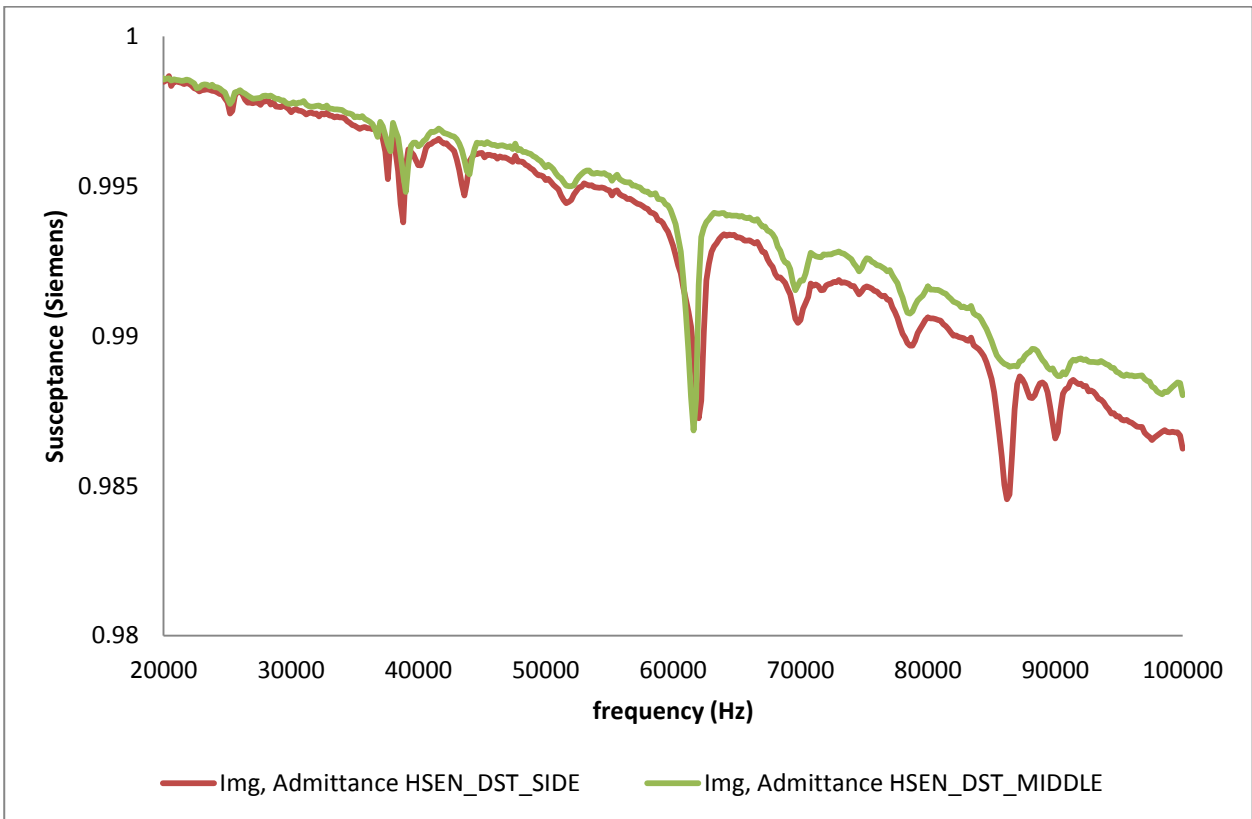
Figure 7-45: Susceptance comparison (HSEN_DST_MID, HSEN_DST_SIDE)

As previously mentioned, neither the impedance parameters nor conductance are capable of accurately distinguishing the structural damage from the transducer damage when the sample is subject to both damage scenarios. Figure 7-47 and Figure 7-48 investigate the usefulness of susceptance in delineating these two situations. In Figure 7-47, the slope of imaginary admittance is shifted towards higher values and the resonance peaks are mostly reduced in magnitude (especially at resonance peak of the transducer) and shifted towards lower frequencies. The same observations are applied for Figure 7-48. However, the reductions in resonance peaks are more significant for DSEN_DST_MIDDLE when compared to DSEN_DST_SIDE (Figure 7-49).
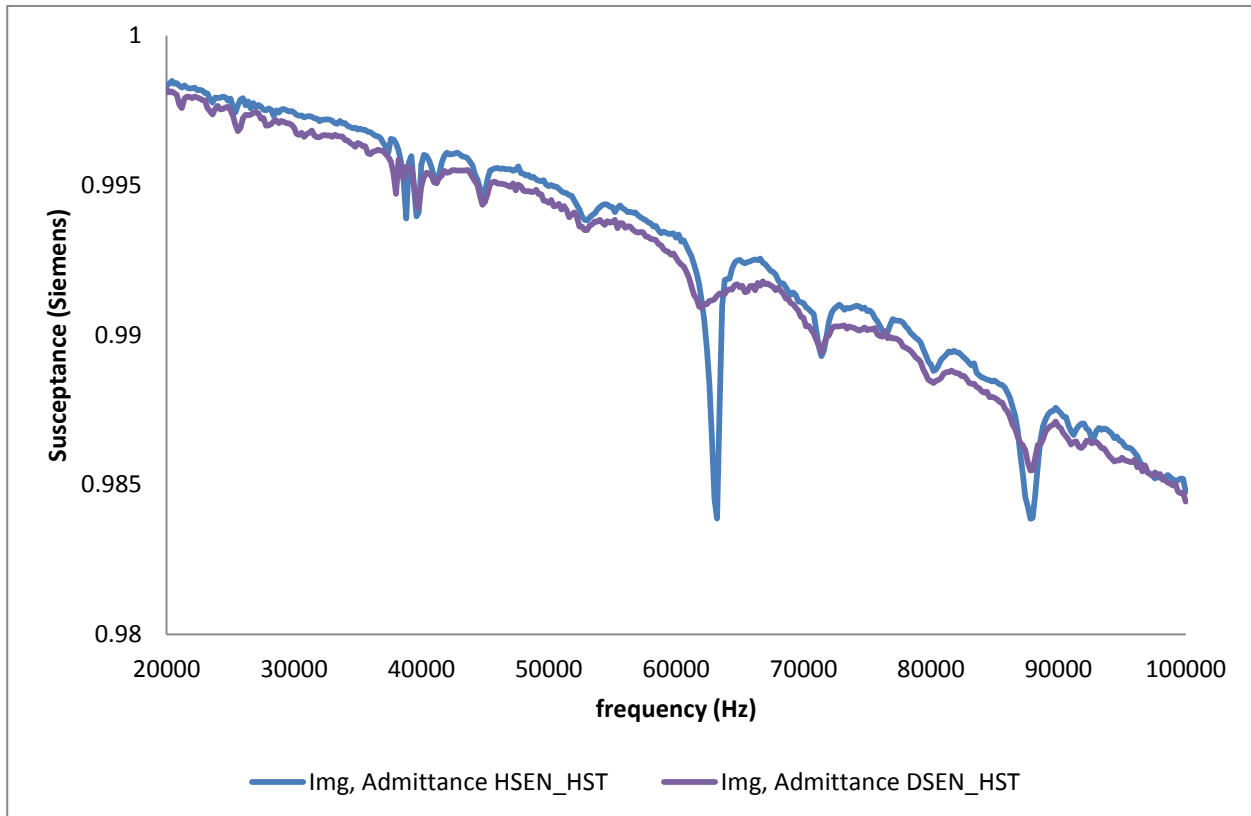
Figure 7-46: Susceptance comparison (HSEN_HST, DSEN_HST)

Unlike other parameters, the variations of the susceptance values for samples with both structural and transducer damages can be described through its variation for each damage scenario separately. In other words, the changes in the susceptance plot due to transducer damage and due to structural damage are superimposed in the transducer + structural damage scenario. It is shown that the structural damage shifts the slope of susceptance toward higher values and slightly shifts the resonance peaks towards lower frequencies while damage in the transducer reduces the magnitude of resonance peaks and shifts them towards lower frequency values. These variations can still be separately detected in DSEN_DST_SIDE and DSEN_DST_MIDDLE plots. Therefore, it can be argued that susceptance is the most appropriate parameter to be used for detecting structural damage from the measurements by a degraded transducer.

228
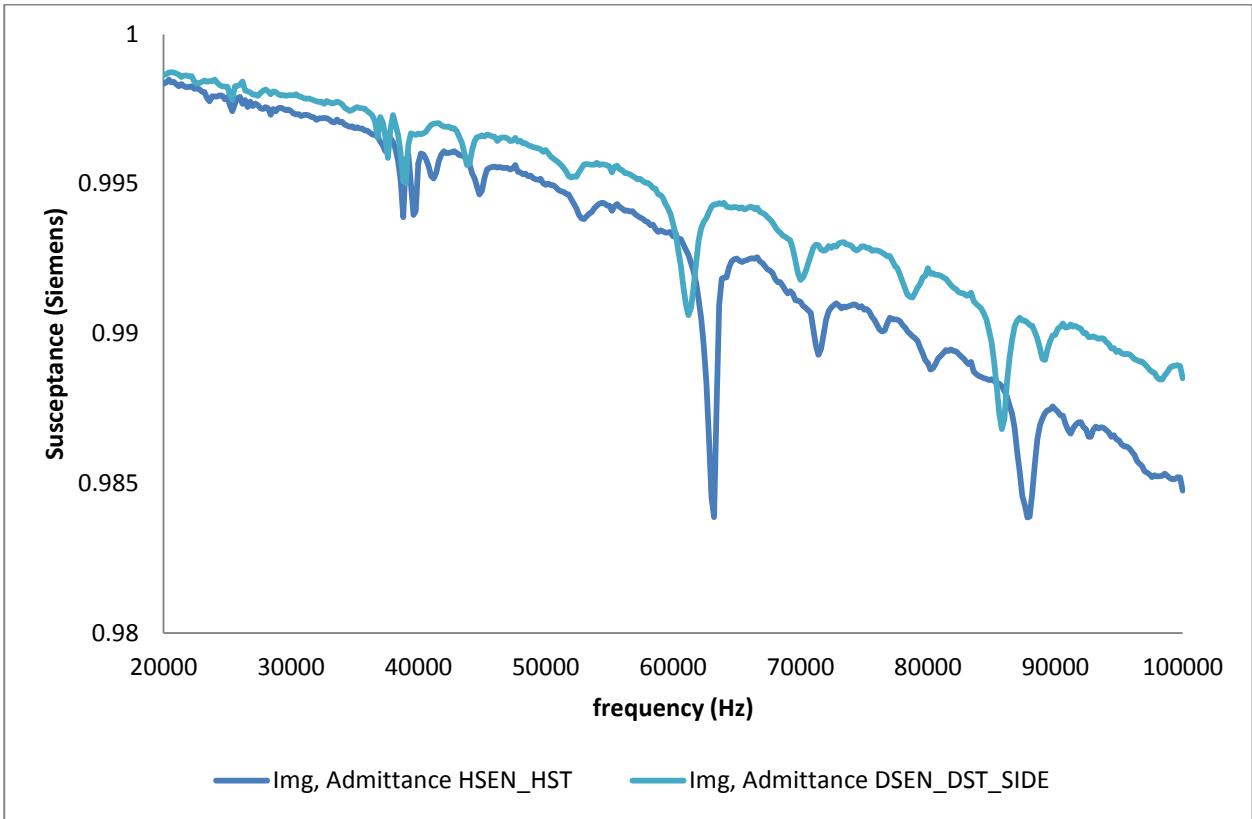
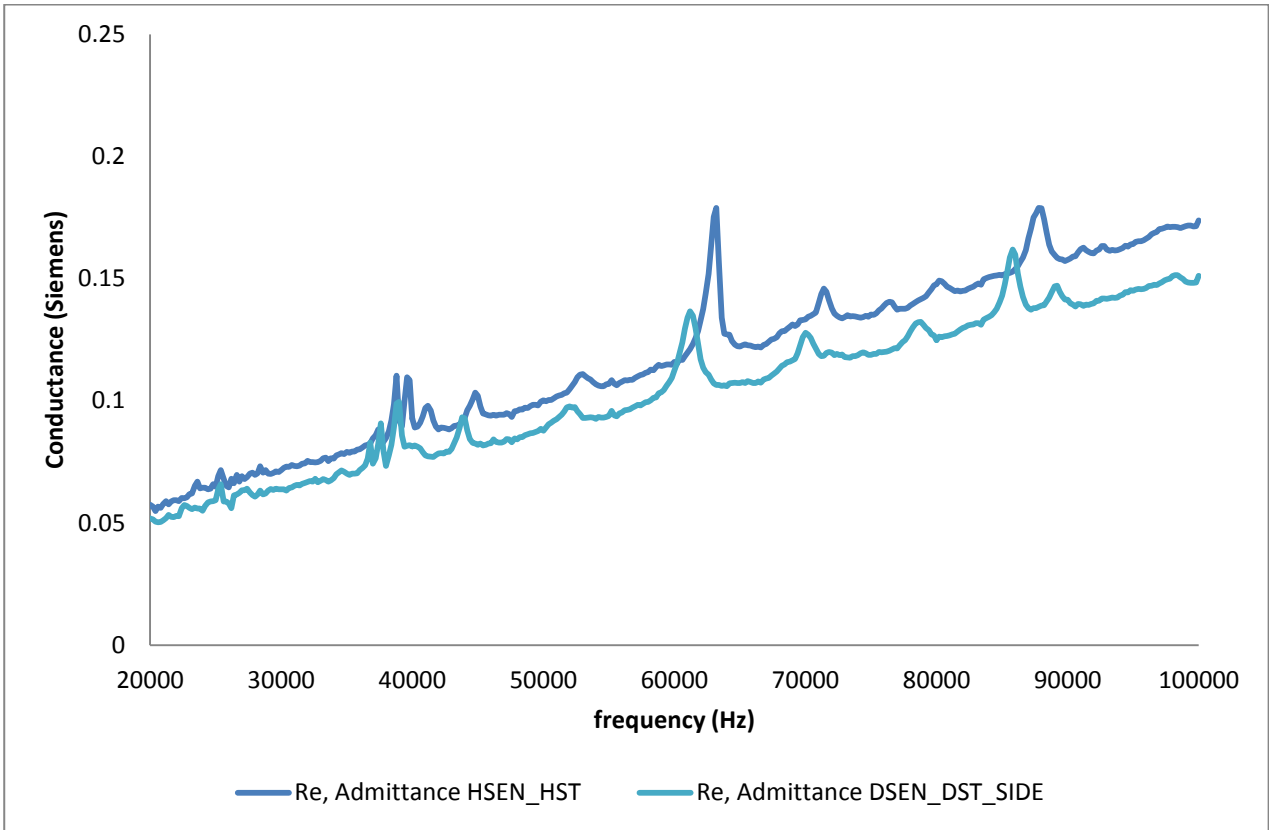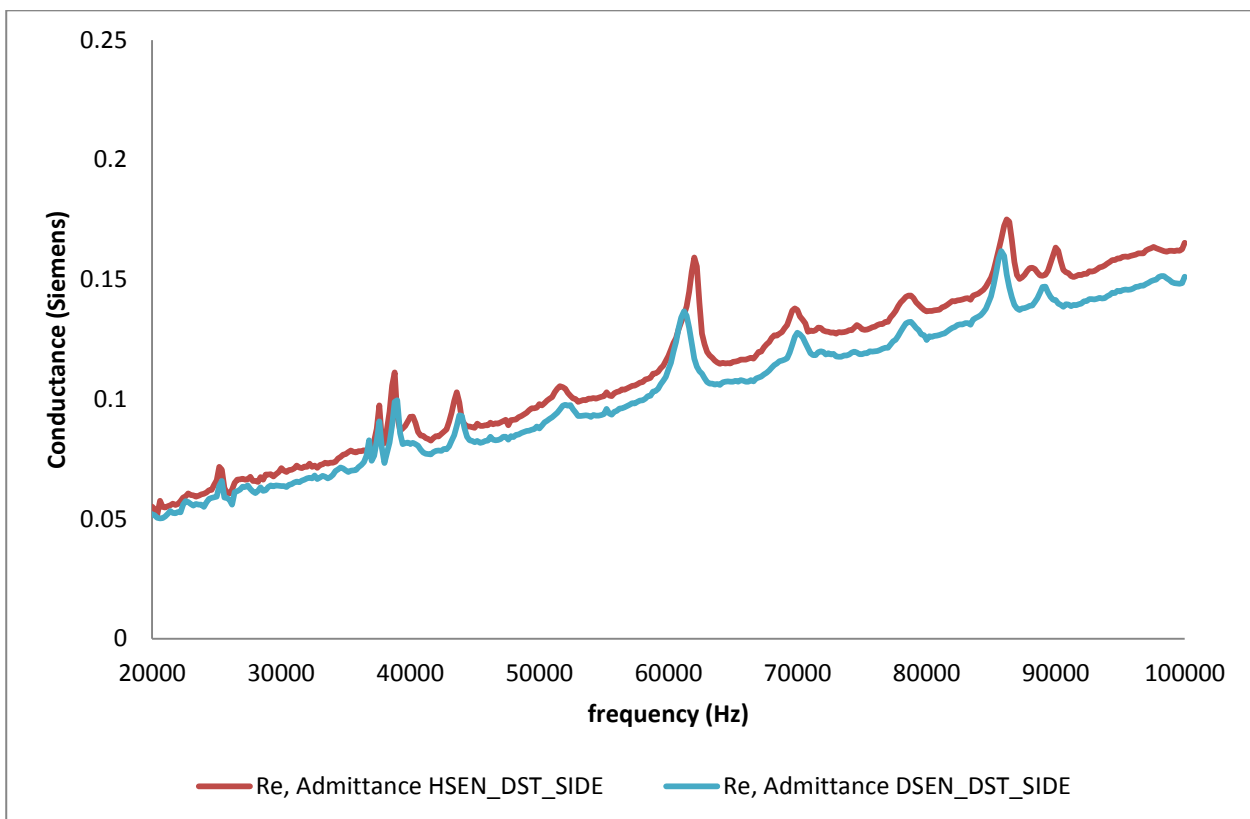**Figure 7-47: Susceptance comparison (HSEN_HST, DSEN_DST_SIDE)**
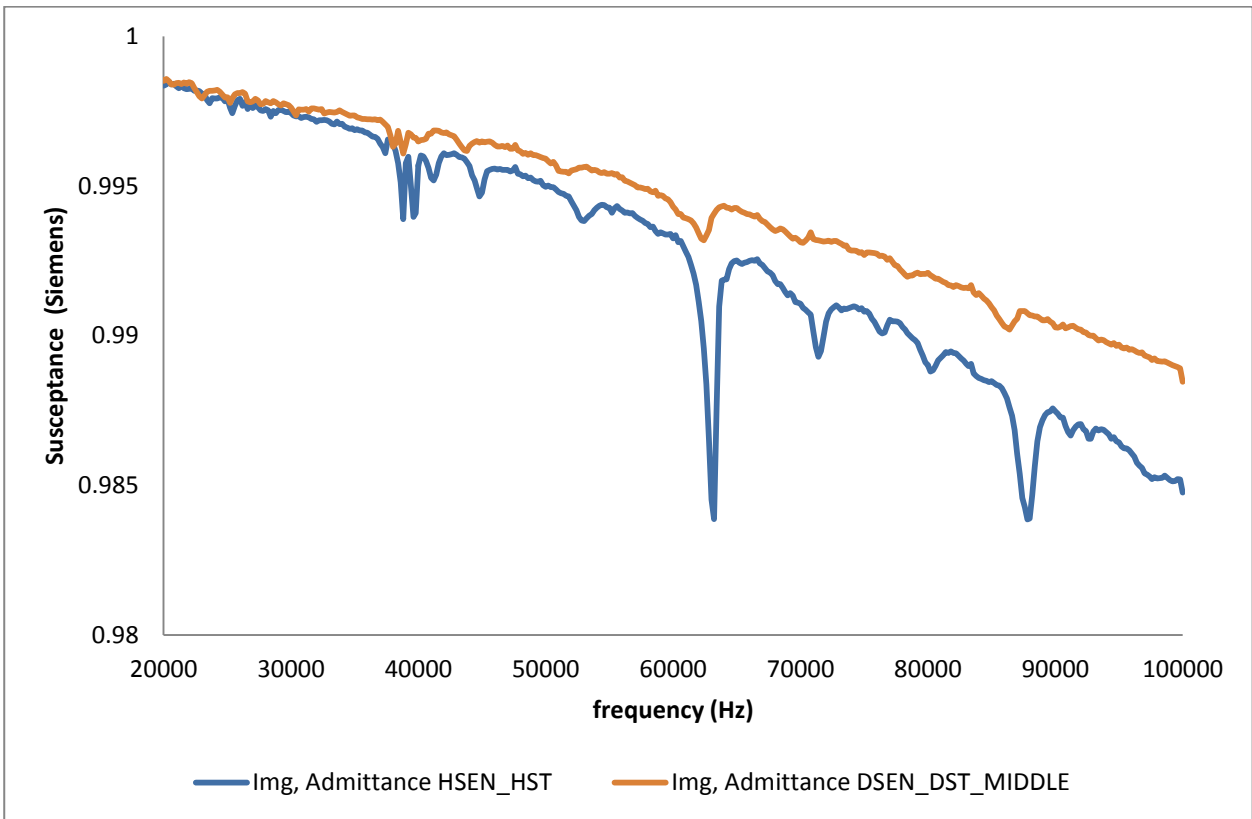
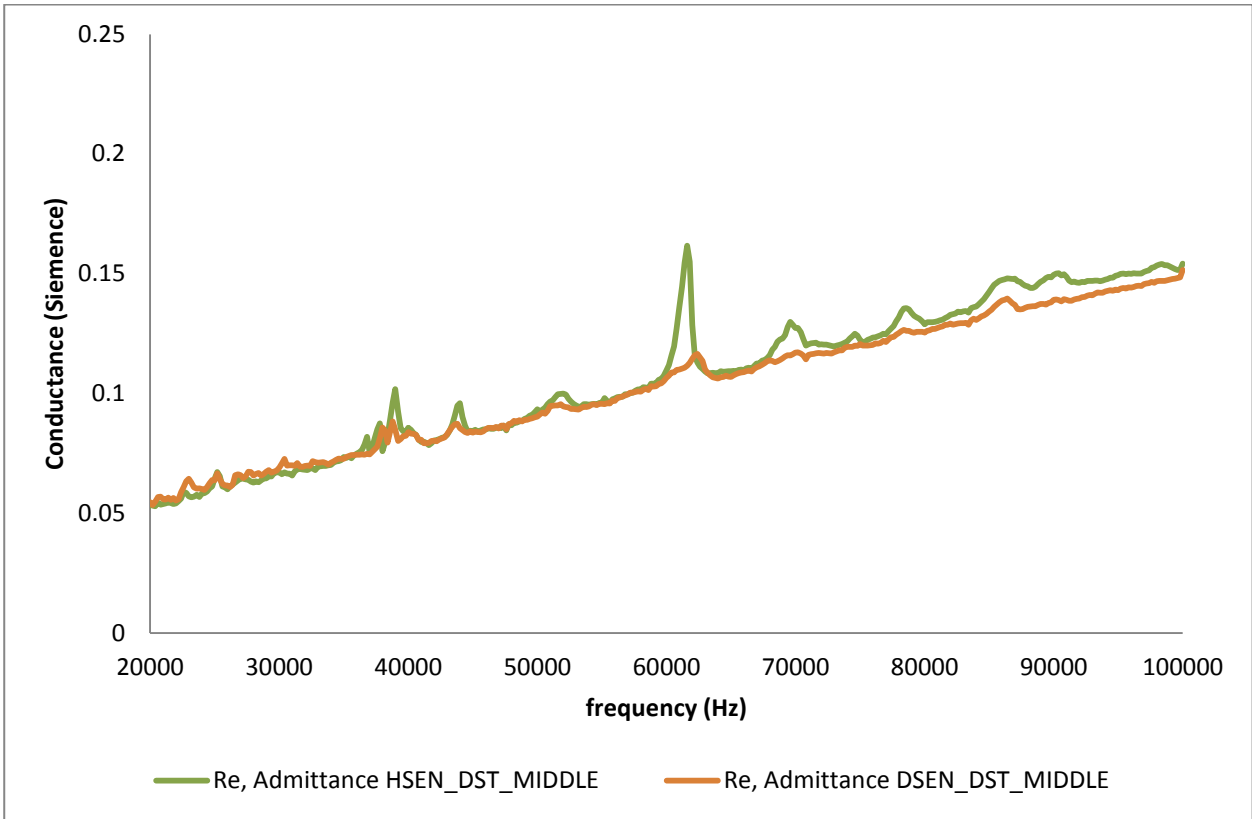**Figure 7-48: Susceptance comparison (HSEN_HST, DSEN_DST_MID)**
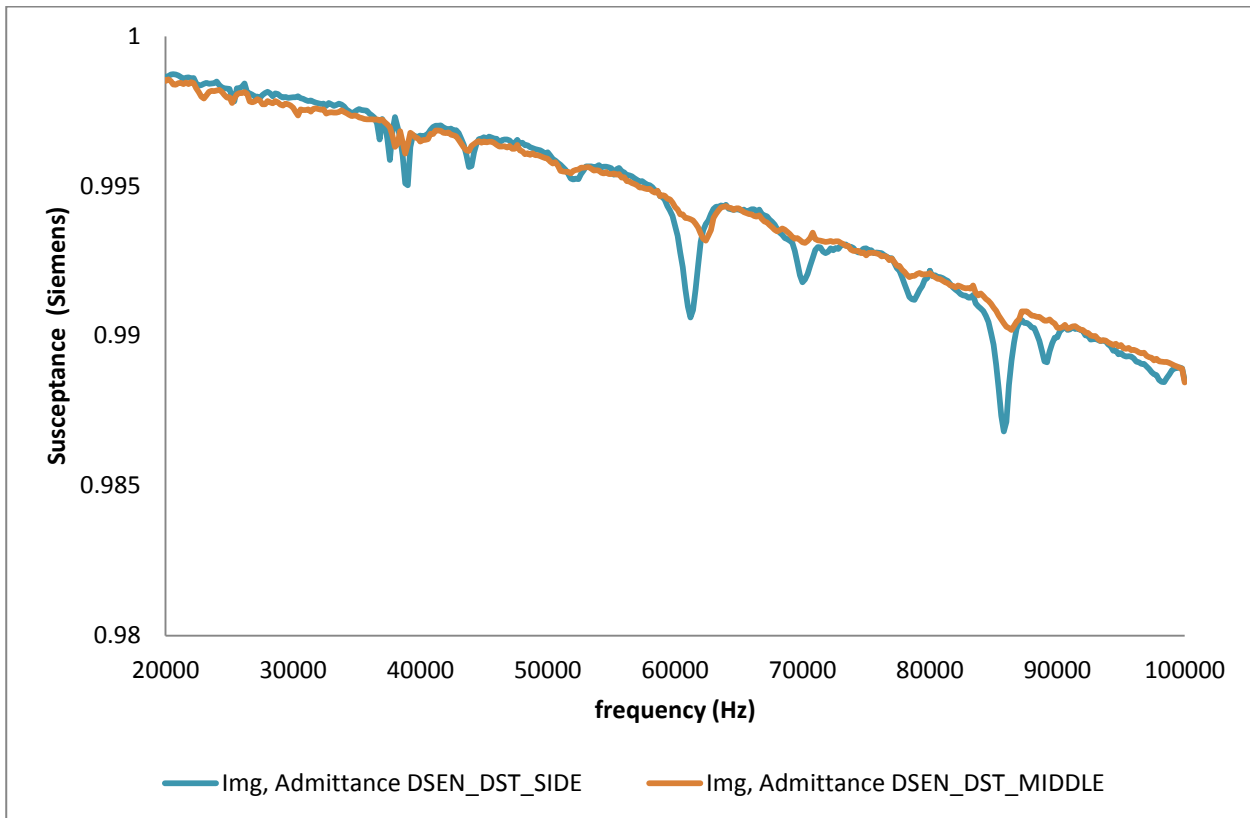
Figure 7-49: Susceptance comparison (DSEN_DST_SIDE, DSEN_DST_MID)

The performance of the healthy and damaged transducer in terms of detecting an identical structural damage is compared and plotted in Figure 7-50 and Figure 7-51. In Figure 7-50, the susceptance of damaged and healthy transducers bonded onto the identical structures with damage far from the transducer is plotted. It is observed that the slope of DSEN_DST_SIDE is shifted towards higher values. Indeed, as shown in Figure 7-43, the damage in the structure shifts the slope of susceptance towards higher values as well. Therefore, it is illustrated that the damaged transducer generates further upward shift in the slope of susceptance when compared to the healthy transducer, which is due to the reduction in the stiffness of the damaged transducer (k_{ef}) thus in return increasing the admittance.

Furthermore, the resonance peaks are reduced in magnitude and also shifted towards lower frequency values for the sample with damaged transducer. By looking at Figure 7-43, we can see that the observations from the comparison of HSEN_DST_SIDE and DSEN_DST_SIDE are also observed in the comparison of the healthy sample and HSEN_DST_SIDE. However, these changes are not completely recognisable in the comparison of DSEN_HST and DSEN_DST_SIDE (Figure 7-51). Hence, the damaged transducer causes similar but further changes in the susceptance spectrum, such as further reduction in resonance peaks and further frequency shift towards lower values in the susceptance plot. This observation illustrates that the level of change in the susceptance i.e. Frequency shift, magnitude reduction etc. is related to the severity of the

damage in the sample when the structural damage is in the far field of the transducer. In other words, while the scale of changes is more extreme for the sample with further damage, the type of changes are similar and can be compared.
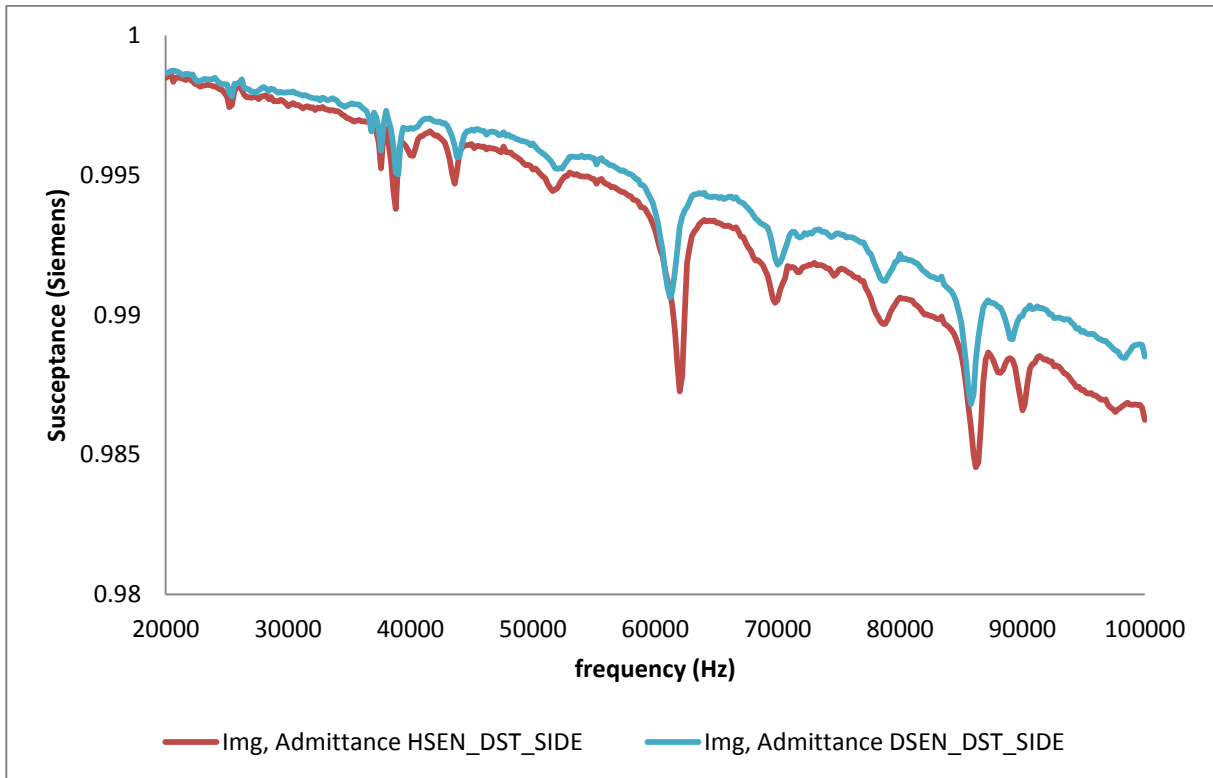

Figure 7-50: Susceptance comparison (HSEN_DST_SIDE, DSEN_DST_SIDE)
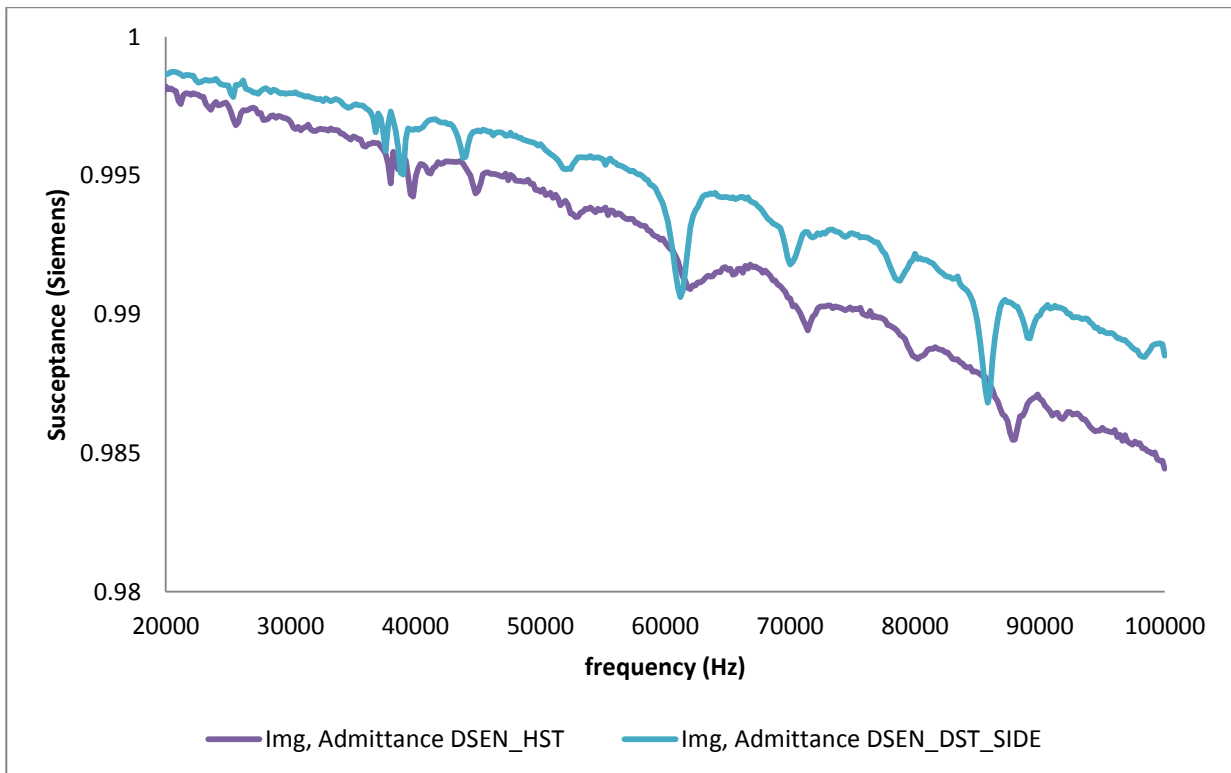
Figure 7-51: Susceptance comparison (DSEN_HST, DSEN_DST_SIDE)

Therefore, it can be discussed that the similar type of changes in the spectrum of susceptance are expected to be observed for following order of damage occurrence in transducer and the structure. In other words, using susceptance as the preferred parameter, it can be possible to not only detect structural damage far from the healthy transducer, but also accurately detect transducer damage as it doesn`t generate new type of changes in the spectrum and only extend the severity of existing changes.

<p style="text-align:center">HSEN_HST→HSEN_DST_SIDE→DSEN_DST_SIDE</p>

In contrast, as it was shown in Figure 7-52, the comparison of HSEN_DST_MIDDLE and DSEN_DST_MIDDLE illustrated that the changes of susceptance when the structural damage is close to the transducer cannot be properly explained through the discussion for Figure 7-50 and doesn`t follow the above order.
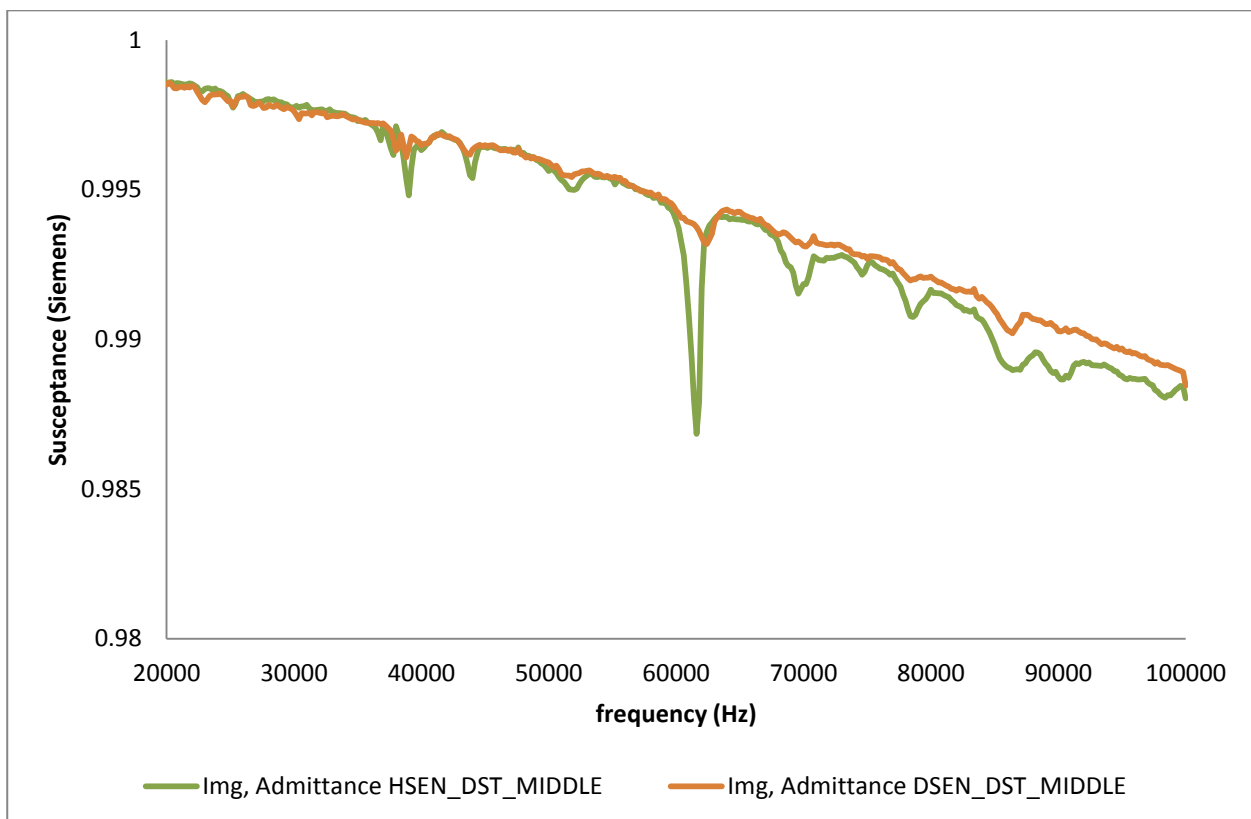
Figure 7-52: Susceptance comparison (HSEN_DST_MID, DSEN_DST_MID)

However, by comparing the changes of susceptance for DSEN_HST to the healthy sample (Figure 7-46) and then comparing the changes in DSEN_DST_MIDDLE in Figure 7-52, it is determined that the susceptance is also a proper parameter to detect transducer damage and also structural damages close to the damaged transducer. In Figure 7-52, similar but further changes are

observed in DSEN_DST_MIDDLE as compared to DSEN_HST (Figure 7-53). The slope of susceptance is similar to the HSEN_DST_MIDDLE and shifts slightly upward compared to HSEN_HST which is not significant and is due to the structural damage. Therefore, the similar changes in the spectrum of susceptance are expected to occur for following order of structural/transducer damages. In other words, the susceptance provided us with the ability to not only detect transducer damages when the structure is still intact, but also accurately detect structural damages close to the location of damaged transducer.

HSEN_HST→DSEN_HST→DSEN_DST_MIDDLE
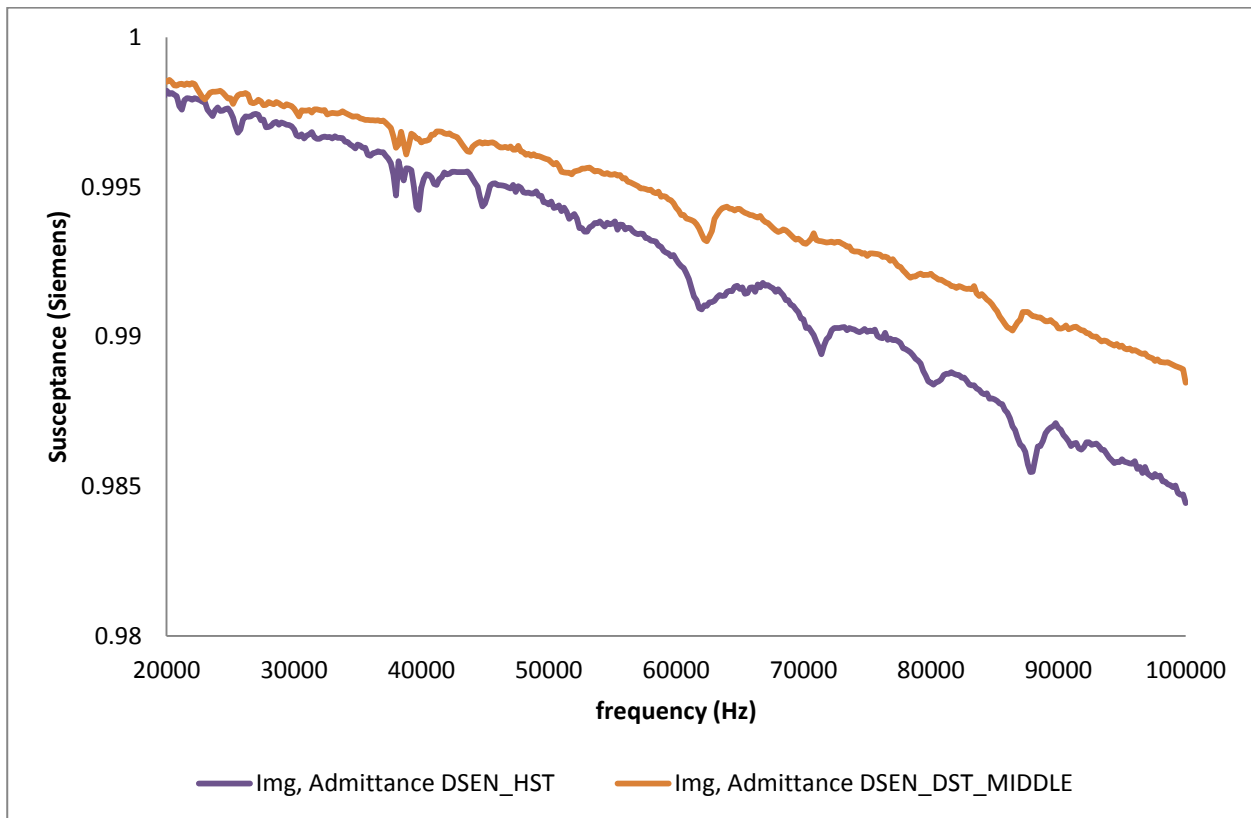
Figure 7-53: Susceptance comparison (DSEN_HST, DSEN_DST_MID)

In addition, the comparison between HSEN_DST_MIDDLE, HSEN_DST_SIDE and HSEN_HST illustrates that there is a peak at around f = 43810 (Hz) in the samples with damaged structure in various locations and the healthy sensor which does not exist in the healthy sample.

7.8. Discussions and Results

A summary of discussions on the capability of the aforementioned electromechanical parameters for delineating various damage scenarios is presented in Table 7-1. This table shows the variations of each electromechanical parameter to different damage scenarios. In general, there are four main

situations in terms of transducer/structure damage status. The generation of damage in the structure when the transducer is still intact, the generation of damage in the transducer when the structure is still intact, the generation of damage in the structure while the transducer is already damaged and the generation of damage in the transducer when the structure is already damaged. These four situations along with the effect of damage location in the structure are tabulated in Table 7-1 and further discussion is also provided for each electromechanical parameter as seen below.

Table 7-1: The summary of E/M delineation technique

E/M Delineation Summary				Real Impedance (Re)	Imaginary Impedance (X)	Real Admittance (B)	Imaginary Admittance (G)
Healthy Transducer/Healthy Structure	Healthy Transducer	Damaged Structure	Close Field of Transducer	←	⇓	↓ ↘ ←	⇑ ↘ ←
			Far Field of Transducer	← ↘ ↓	↓	⇓ ↘ ←	↑ ↘ ←
	Damaged Transducer	Healthy Structure		↓ ↘ ⌒	⇊⇊	↘ ↑ ⌒	↓ ↘ ⌒
		Damaged Structure	Close Field of Transducer	↓ ↘↘	⇑	↓ ↘↘	↑ ← ↘
			Far Field of Transducer	↓ ↘	⇑	↓ ↘	↑ ← ↘
	Damaged Structure	Close Field of Transducer	Damaged Transducer	↘↘	↑	↓ ↘ ⌒	↑ ← ↘
		Far Field of Transducer	Damaged Transducer	↑ ←	↑	⇓ ↘↘ ⌒	↑ ⇇ ↘↘

234

The definitions of signs used in above table are shown below:

- ←   Lower Frequency Shift of Resonance Peaks
- →   Higher Frequency Shift of Resonance Peaks
- ↗   Magnitude Reduction of Resonance Peaks
- ↙   Magnitude Increase of Resonance Peaks
- ↓   Downward Shift of the spectrum
- ↑   Upward Shift of thr Spectrum
- ⌒   Considerable Magnitude Reduction of MFC Resonance Peak
- ⌣   Considerable Magnitude Increase of MFC Resonance Peak
- ⇇   Further Lower Frequency Shift
- ⇉   Further Higher Frequency Shift
- ↗↗   Further Magnitude Reduction
- ↙↙   Further Magnitude Increase
- ⇊   Further Downward Shift
- ⇈   Further Upward Shift

7.8.1. Real impedance Summary

1. The presence of damage in close proximity to the transducer (Middle) shifts the resonance frequency peaks of real impedance towards lower values while the presence of damage on the far field (Side) reduces the magnitude of resonance peaks and shifts the resonance frequencies as well as the slope of real impedance towards lower values.

2. Damage in the transducer reduces the magnitudes of the resonance peaks and shifts the slope real impedance towards lower values, although the location of peaks remains constant.

3. The frequency shift in resonance peaks in the real impedance spectrum is a sign of structural damage. The reduction in the magnitude of resonance peaks (especially at the resonance frequency of a free transducer) is a sign of transducer damage.

4. The real impedance of the damaged transducer when the structural damage is in its close field shifts the resonances towards lower frequencies and reduces their magnitudes

5. A downward shift in the slope of the damaged transducer's real impedance is a sign of structural damage and the magnitude of resonance peaks has a direct relation to the distance between the transducer and structural damage.

6. For the damaged structure, a significant reduction in the magnitude of resonance peaks is a sign of transducer damage if the structural damage is in close proximity to the transducer. However, the plot remains unchanged if the structural damage is in the far field of the transducer, which is a false negative sign.

7.8.2. Imaginary impedance Summary

1. The downward shift in the slope of imaginary impedance is a sign of structural damage. The amount of shift has an inverse relation to the distance between the transducer and structural damage. It also has a direct relation to the severity of the structural damage.

2. The transducer damage induces further changes in the imaginary impedance plot when compared to structural damage, thus confirming that the imaginary impedance is more sensitive to damage in the transducer.

3. The generation of transducer damage when the structure is already damaged causes an upward shift in the slope of imaginary impedance while the generation of structural damage when the transducer is already damaged causes a further upward shift of the slope of imaginary impedance.

4. The similarity between the damaged transducer imaginary impedance plots when the structural damage is in close and far proximity to the transducer shows that the imaginary impedance is not sensitive to the damage location in the structure.

5. While both structural and transducer damage cause a downward shift in the imaginary impedance spectrum, this shift is less for the situation where both structure and transducer are damaged compared either the transducer or structure being an individual damage source.

6. The imaginary impedance spectrum of the healthy and damaged transducer are similar when the structural damage is in close field of the transducers, thus illustrating that the damaged transducer is still capable of properly detecting the structural damaged close to its field.

7.8.3. Real Admittance (Conductance) Summary

1. The structural damage causes a downward shift of the conductance slope towards lower values, thus reducing the magnitude of resonance peaks and shifting them towards lower frequency values.

2. The amount of downward shift has a direct relation to the severity of the structural damage as well as its distance to the transducer location.

3. The transducer damage reduces the magnitude of the resonance peaks, especially at the resonance frequency of the transducer and slightly shifts the slope of the conductance plot towards higher values.

4. It can be argued that the damage in the structure shifts the slope of conductance towards lower values while the damage in the transducer shifts the slope towards higher values.

5. When both the structure and the transducer are damaged, the separations of plots of healthy and damaged samples are increased as the frequency becomes higher. The lower frequencies

are more sensitive to the far field of the transducer while the higher frequencies are more sensitive to the local area of the transducer. Therefore, further reductions are observed in higher frequencies when the structural damage is in close proximity to the transducer.

6. For the damaged transducer, the reductions in the magnitude of resonance peaks have a direct relation to the distance between the transducer and damage in the structure. The closer the damage is, the higher the reduction magnitudes of the resonance peaks.

7. For the damaged structure, the generation of transducer damage reduces the magnitude of resonance peaks and shifts the slope of conductance towards lower values, especially at the resonance frequency of the transducer. However, the reductions in the magnitude of peaks are relevant to the distance between the transducer and structural damage. Moreover, the downward shift of the slope of conductance has a direct relation to the distance between the structural damage and transducer location.

8. For the damaged transducer, the generation of structural damage causes a downward shift in the conductance spectrum. The magnitude of the resonance peaks has a direct relation to the distance of structural damage to the transducer.

7.8.4. Imaginary Admittance (Susceptance) Summary

1. The structural damage shifts the slope of susceptance towards higher values, thus reducing the magnitudes of resonance peaks and shifting them towards lower frequency values.

2. The amount of shift at high frequencies (higher than transducer frequency) is in an inverse relation to the location of the damage.

3. The transducer damage causes a downward shift in the slope of the susceptance plot. Moreover, the magnitude of the resonance peaks is dropped, especially at the resonance frequency of the transducer.

4. By analysing the impact of structural damage and transducer damage on the susceptance values, it is observed that the susceptance shows more sensitivity to the transducer damage compared to structural damage.

5. Unlike other impedance and admittance parameters, the variations of the susceptance values for samples with both structural and transducer damage can be described through their variation for each damage scenario separately.

6. The changes in the susceptance spectrum of samples with both transducer and structural damage are the superimpositions of changes caused by each damage type individually. Some of the changes are the upward shift of the susceptance spectrum, a frequency shift of resonance peaks towards lower values and reduction of the magnitude of resonance peaks.

7. The magnitude of resonance peaks, when both structure and transducer are damaged, has a direct relation to the distance between structural damage and the transducer.

8. For the damaged structure, the generation of transducer damage shifts the slope of conductance towards higher values, thus shifting the resonance peaks towards lower frequencies and reducing their magnitude. The greater the distance between the structural damage and the transducer, the more pronounced these changes become.

9. For the damaged transducer, the generation of structural damage shifts the slope of conductance towards higher values, thus shifting the resonance peaks towards lower frequencies. However, the structural damage in close proximity to the transducer reduces the magnitude of resonance peaks while those in the far field of the transducer increase the magnitude of resonance peaks. This specification of susceptance can be used to not only delineate the transducer damage from structural damage but also to estimate the location of structural damage.

10. It is observed that when the structural damage is in the far field of the damaged transducer, the impact of structural damage is more dominant and the changes can be explained through those which result when the sample has structural damage only. Therefore, same logic can be used to explain the changes of susceptance for the following sequence.

$$HSEN\_HST \rightarrow HSEN\_DST\_SIDE \rightarrow DSEN\_DST\_SIDE$$

11. In contrast, it is observed that when the structural damage is in close proximity to the damaged transducer, the impact of transducer damage is more dominant and the behaviour of the transducer can be explained through those which are identified for the sample with transducer damage only. Therefore, the following sequence can be used to explain the changes of susceptance plot.

$$HSEN\_HST \rightarrow DSEN\_HST \rightarrow DSEN\_DST\_MIDDLE$$

7.9. Summary

This chapter has investigated the delineation of structural damage from MFC transducer damage/degradation of electrical properties. The general background of the E/M impedance technique has also been discussed and the existing gaps identified. The proposed technique has been explained theoretically as well as through the equivalent circuit of bonded MFC on the structure. It has shown that the MFC can be modelled with a capacitor, with similar capacitance to that of the MFC, and V_{IN} while the structure can be modelled with a resistor. The analytical approach towards the electromechanical coupling between bonded MFC transducer and host

structure has also been derived and effective factors on each part have been identified. Furthermore, the experimental measurements of electromechanical impedance have been validated with the FEM numerical results from Chapter 6. The outcome shows a very good matching between the numerical and experimental results.

Five electromechanical parameters have been selected based on the analytical and theoretical investigations to delineate various damage scenarios. These parameters are real impedance (Resistance), imaginary impedance (Reactance), real admittance (Conductance), imaginary admittance (Susceptance) and Imaginary magnitude. The Analog device AD5933 Impedance Analyser has been used to electrically excite the MFC by sending a voltage and measuring the electromechanical impedance components in the designated frequency range. The theoretical relation was then used to calculate the admittance components.

The aim of this chapter is to imply the electromechanical parameters to distinguish the structural damage from MFC transducer damage in various damage scenarios. A total of 6 samples with various structure/transducer damage scenarios have been manufactured and the aforementioned E/M parameters have been collected for all of them. Finally, the plot of each parameter against the frequency range of 30-100 KHz has been calculated and the changes of each parameter for all 6 samples have been analysed in order to determine the most effective parameter to detect each damage scenario.

CHAPTER 8 Electromagnetic Interference Investigations

8.1. Introduction

The aim of this research project is to identify and address the concerns regards the reliability and functionality of SHM systems in multifunctional composites. This task can be achieved by developing a proper understanding of the issues and gaps in the certification of sensor systems whilst also utilising a practical SHM technique with the ability to diagnose occurring damage in different parts of the multifunctional composites such as the transducer or host structure. As mentioned in previous chapters, the Macro-Fibre Composite (MFC) transducer, as one of the most sophisticated piezo-fibre-based piezoelectric transducers, is used in this project. While the MFC's characteristics render it a singularly useful device, there is limited research pertaining to the characterisation and modelling research on the MFC. Furthermore, it is poorly understood, particularly in terms of its underlying operating principles, its dependence on design parameters and its electrical properties (Lloyd, 2004).

In other words, the fact that the MFC technology is based on an empirical design process means that further investigation is needed when it comes to the specification and explanation of the mechanical, electronic and electromagnetic properties as well as actuation and sensing capabilities of the MFC (Kessler et al., 2002). The experimental results in this research show that the piezo-fibre sensors` responses could be affected by electromagnetic interference. This issue gives rise to two concerns regarding the performance of the sensor. Firstly, the effect of electromagnetic interference on the sensor responses and the reliability of the sensor should be investigated. Secondly, the possibility of using a piezo-fibre sensor as an RF device in wireless structural health monitoring could be considered.

In terms of the first concern, a series of filtering and isolation is applied to the experimental setup and the sensor responses are compared before and after the isolation. In order to investigate the second issue, the sensor should be excited with different radio frequencies to find the frequency bandwidth which the sensor resonates and generates voltage. The aim of this chapter is to investigate the effect of these electromagnetic interferences on the MFC transducer while it is bonded onto the surface of the structure.

8.2. Background

Electromagnetic interference (EMI) refers to a situation where an electric circuit is affected by the interference from an electromagnetic induction or radiation coming from an external source (Sue et al., 2011). This interference may interrupt or degrade the performance of the circuit and cause false negative or false positive situations. The EMI can come from a variety of sources such as objects with rapidly changing electrical currents, electromagnetic motors etc. However, this effect can also be used intentionally in some cases such as radio jamming, as in some forms of electronic warfare (Born et al., 1999).

Furthermore, there are two prominent types of EMI; conducted EMI and radiated EMI. Conducted electromagnetic interference is caused by the physical contact of the conductors as opposed to radiated EMI which is caused by induction (without physical contact of the conductors) (Yeates et al., 2012). Electromagnetic disturbances in the EM field of a conductor will no longer be confined to the surface of the conductor and will radiate away from it. This persists in all conductors and mutual inductance between two radiated electromagnetic fields will result in EMI. Radiated EMI or RFI is also categorised into two types; narrowband and broadband. Narrowband interference usually comes from intentional transmissions such as radio and TV stations, pager transmitters, cell phones, etc. Broadband interference usually comes from incidental radio frequency emitters such as electric power transmission lines, electric motors etc.

In this chapter, the source of electromagnetic interference comes from the electric motor in the test machine. Anywhere electrical power is being turned off and on or where the direction is changed rapidly, is a potential source. Computers, digital equipment and televisions are some of the examples in this category. The rich harmonic content of these devices means that they can interfere over a very broad spectrum. A characteristic of broadband RFI is its inability to filter it effectively once it has entered the receiver chain. Therefore, an in-depth investigation must be carried out in order to eliminate the interference effect on the affected circuit. This challenge will be discussed and experimented in the following sections.

8.2.1. Reducing the EMI in integrated circuits

One of the main sources of EMI is Integrated circuits. However, the integrated circuit by itself does not generate a significant amount of interference and therefore in most cases, it must couple with larger objects such as circuit boards and cables to radiate significantly. The common solutions to reduce the EMI in integrated circuits are: using decoupling capacitors, using series resistors for high speed signals and V_{CC} filtering (Mohamed, 2010). Shielding is also a common solution for EMI

reduction. However, it adds to the expense of shielding through things such as shielding gaskets which need to be considered. At lower frequencies, (scale of 100MHz), most of the RMI comes from the I/O cables and transfers to the circuit through ground pins and V_{CC}. At higher frequencies (above 500 MHz), traces become electrically longer and higher above the plane. In this case, techniques such as wave shaping and embedding traces between planes can be used. However, a more reliable solution would be to perform EMI shielding through the use of RF gaskets and copper or aluminium tapes. In the next section, the theory of electromagnetic interference shielding will be discussed.

8.3. Theoretical Background

8.3.1. Electromagnetic interference (EMI) shielding

As previously mentioned, EMI refers to a situation where the performance of an electrical circuit is degraded or affected by an undesirable interference caused by electromagnetic conduction or radiation from an external source like electric engines. The most common solution to EMI is to protect the affected circuit with an EMI shielding material or structure. In order to evaluate the effectiveness of EMI shielding, the "shielding effectiveness" (SE) parameter is defined in decibels (dB) as shown in Equation 8-1 (Gibson, 2010).

Equation 8-1

$$SE = 20 \log \frac{E_i}{E_t} = 20 \log \frac{H_i}{H_t}$$

Where E_t is the transmitted electric field, E_i is the incidental electric field, H_t is the transmitted magnetic field and H_i is the incidental magnetic field. The SE can also be simply described as Equation 8-2:

Equation 8-2

$$SE = 20 \log \frac{E \ field \ received \ from \ source \ with \ no \ sheild}{E \ field \ received \ from \ sheilded \ source}$$

The SE for electrically conducting metallic materials is excellent. However, due to the weight and other properties, non-metallic materials such as polymers and polymer composites are increasingly used to replace metals. SE is particularly important for multifunctional materials and structures which are typically based on polymer composites, and where both electrical and mechanical functions are typically involved. In order to achieve acceptable SE, the polymer must be either an

intrinsically conducting polymer (ICP) or be filled with a conducting material such as carbon fibres or Nano-tubes or be properly shielded with high conductive material such as aluminium.

8.4. Description of the Problem

The source of electromagnetic interference in this experiment is the electrical engine of the INSTRON test machine. A considerable amount of noise is observed in the measured output voltage of MFC transducer which was not expected in the initial estimations. Furthermore, the amount of observed noise is higher than typical vibration or acoustic noises seen in dynamic tests. In order to investigate the exact source of this interference, various investigations are carried out, including measuring the output voltage of MFC while turning the test machine ON and OFF and using other testing machines with hydraulic engines. During these investigations, it is observed that while the reduction in vibration of the environment does not significantly reduce the noise level, turning off the electromagnetic engine as well as using the test machine with hydraulic engine significantly reduces the noise level. The initial investigations confirm that the MFC is subject to electromagnetic interference, which is also the source of extra noise in the voltage responses. This observation calls for further investigation into this phenomenon as described in the following sections.

8.5. Experimental Investigations

Two approaches are explored with regard to the electromagnetic interference on the MFC and its voltage responses. With the first approach, the aim is to identify the main recipient of the interference in the MF transducer such as piezo-fibres or electrodes, and eliminate this interference through proper shielding and insulation methods. With the second approach, the possibility of using the sensitivity of the MFC transducer to electromagnetic field as a diagnostic tool to delineate healthy and damaged transducers is investigated. These two approaches are presented below.

8.5.1. Shielding and Insulation against EMI

As previously mentioned, the effect of electromagnetic interference on the MFC voltage responses is incidentally observed. Therefore, the first aim is to point out the source and recipient of this interference. The next step is to clarify the main recipient of the electromagnetic interference which causes the noise in voltage readings. Generally speaking, there are three parts in the test rig which could be affected by the EMF; wires, MFC and carbon fibres of the carbon/epoxy plate. The

effect of electromagnetic field on each part is described and appropriate solutions for shielding and insulation are investigated in this section.

8.5.1.1. Replacing the metallic spin with plastic spin

The spin of the 3-point-bend-test, which applies the cyclic loading on the samples, is made of metallic material by default. In order to eliminate the possible transmission of electromagnetic interference thorough the spin to the MFC transducer, a new spin with similar dimensions to the original one is made out of rigid plastic and replaced in the test rig as shown in Figure 8-1. The noise in the MFC output voltage is then measured for both plastic and metallic spin conditions as presented in Figure 8-2. It can be seen from this figure that while noise level is generally decreased for plastic spin, it does not significantly reduce the noise level, thus illustrating the need for further insulations and shielding.
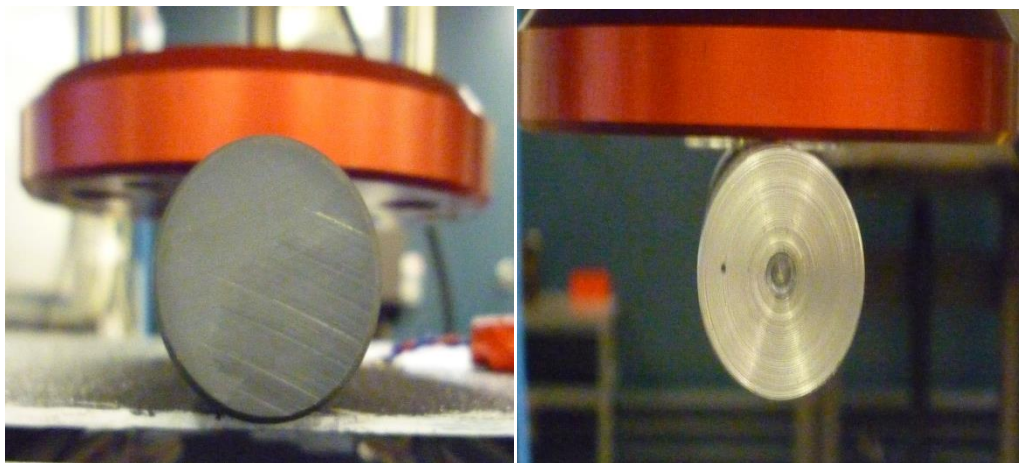
Figure 8-1: Replacing the metal spin with rigid plastic spin in the test rig

8.5.1.2. Shielding the Cables

Any current-carrying conductor, including a cable, radiates an electromagnetic field. Likewise, any conductor or cable will pick up energy from any existing electromagnetic field around it. These effects are often undesirable, in the first case amounting to unwanted transmission of energy which may adversely affect nearby equipment or other parts of the same piece of equipment; and in the second case, unwanted pickup of noise which may mask the desired signal being carried by the cable. In addition, the cable may be carrying power supply or control voltages, potentially polluting them to such an extent as to cause equipment malfunction. In this experiment, the cables which connect the MFC electrode leads to the datataker can be one of the sources of electromagnetic interference. In general, one of the easiest ways of eliminating this effect is to use

the shielded cables. The wires within these cables are complexly decoupled from any external electromagnetic field. The normal and shielded cables used in this project are shown in Figure 8-3.
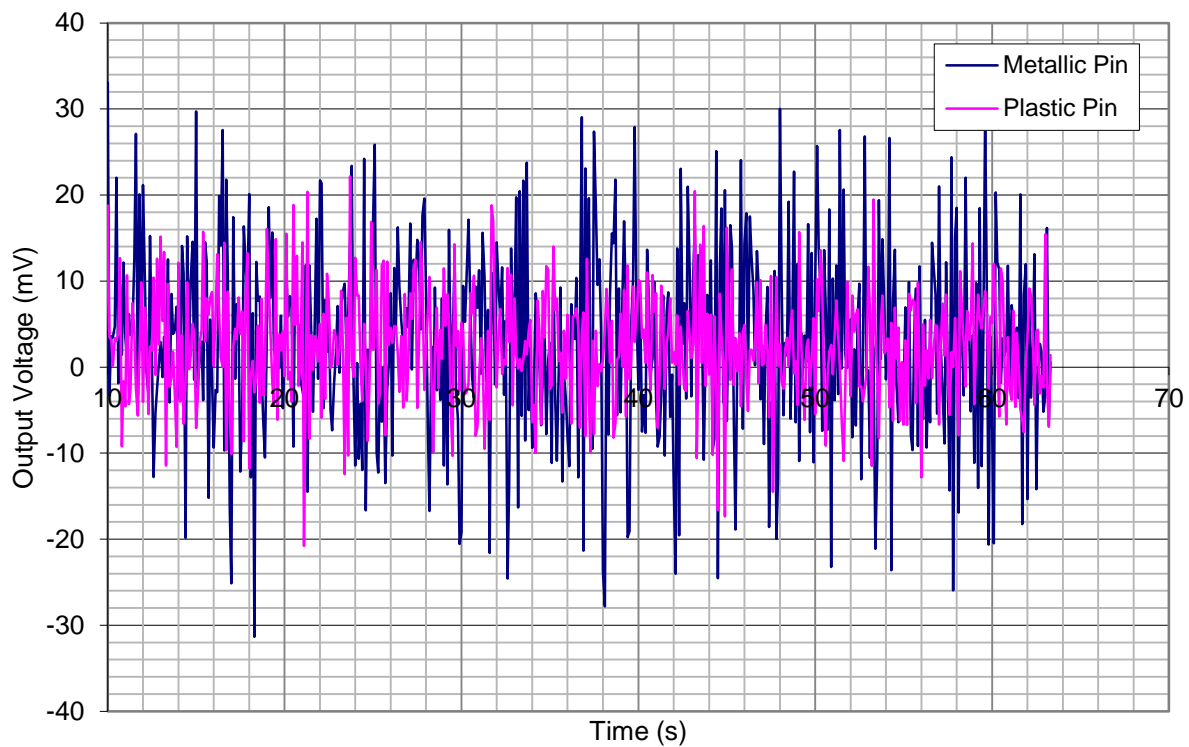
Figure 8-2: Comparison of the noise level when the central spin is plastic and metallic

The effect of cable shielding on the noise level in MFC voltage responses is provided in Figure 8-4. From this figure, it is shown that the cable shielding does not have a significant impact on the electromagnetic interference reduction. In other words, while using shielded cables can reduce the interference with electromagnetic fields in general, the main receiver of the electromagnetic interference in this experiment which causes the observed noise in the voltage responses is not the cables. Therefore, it can be discussed that the recipient of this interference would be either the MFC sensor or the carbon fibre structure. In order to investigate this hypothesis, a series of experiments are conducted and the results are compared simultaneously to identify the main receiver of electromagnetic noise as described below.

8.5.1.3. High-Conductive Material Shielding

In order to identify whether or not the transducer is subject to electromagnetic interference or the carbon/epoxy structure (carbon fibres), the MFC transducer is shielded with aluminium tape (thin layer) as is the aluminium plate (thick layer). This is to isolate the transducer and connected cables from the electromagnetic field. In addition, the remaining noise can be counted for the carbon/epoxy structure. It should be noted that adding the aluminium tape and particularly the

aluminium plate might change the voltage response level. The aluminium shielding process and shield transducer under loading are shown in Figure 8-5and Figure 8-6 respectively.

Shielded
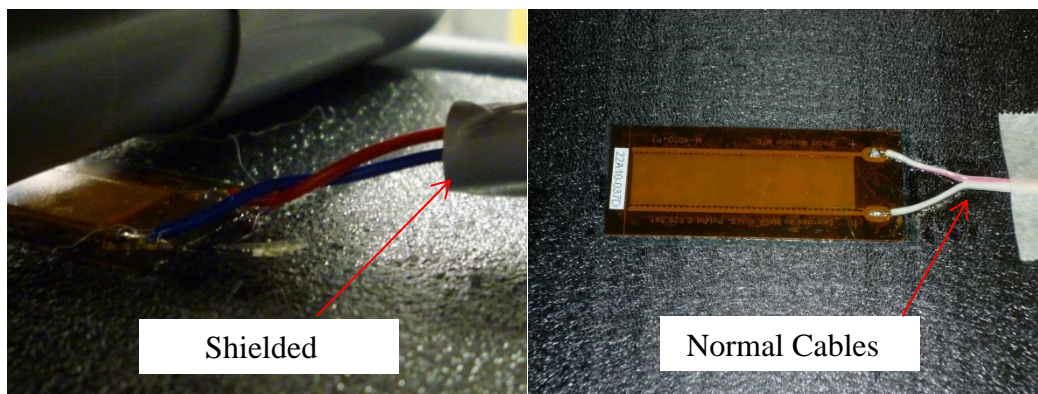
Normal Cables

Figure 8-3: Replace the normal cables with shielded cables
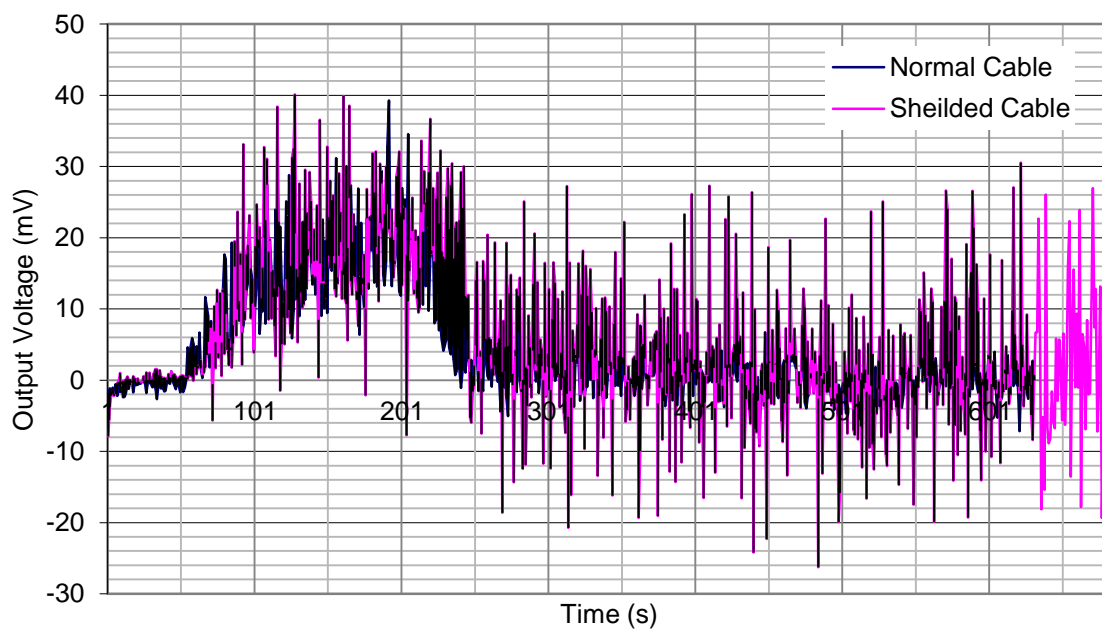
Figure 8-4: Comparison between the voltage responses after using shielded cables

Aluminium Block
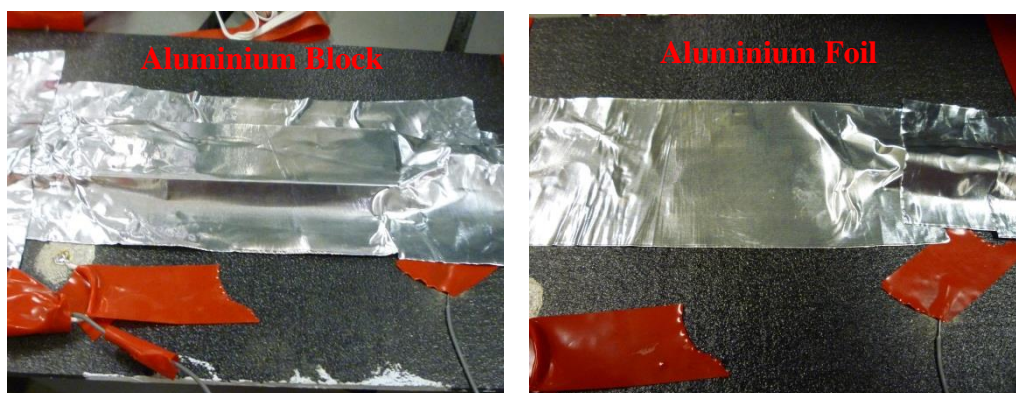
Aluminium Foil

Figure 8-5: Shielding the transducer with aluminium
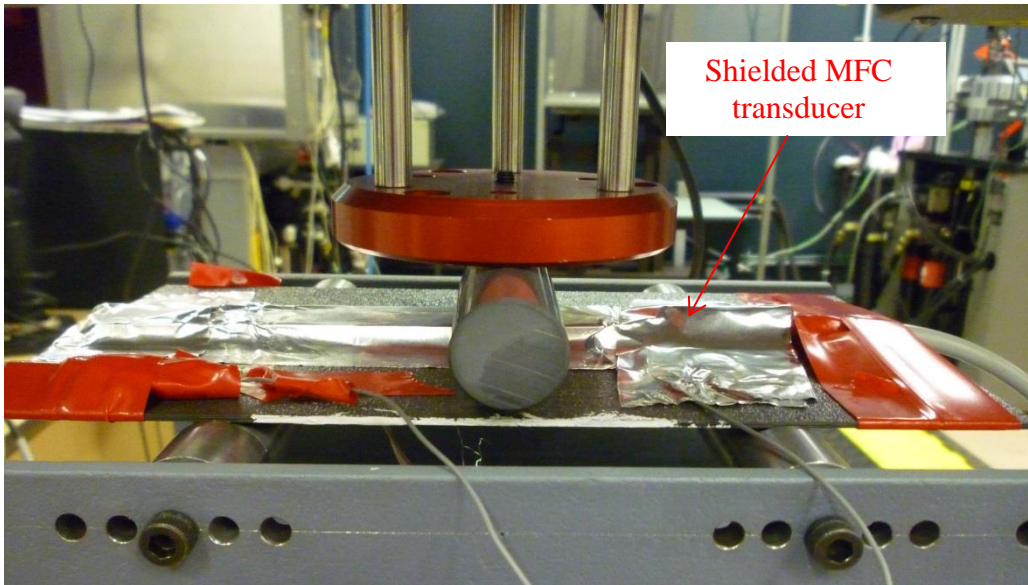
Figure 8-6: Shielded MFC transducer in the test rig

In general, the amount of reduction depends on the shielding material, its thickness, size of shielded surface and the frequency of the EM field. However, the effect of EMI shielding does not necessarily improve for the thicker shielding or at higher frequency conditions. In order to investigate this effect, the noise levels are plotted and compared before and after shielding for both the thick and thin aluminium layers in Figure 8-7 and Figure 8-8. It can be seen from both figures that the reduction in the noise level is significant and the noise amplitude after transducer shielding is reduced to only about 1 mV. It can also be argued that the transducer itself is the main recipient of the EM interference based on these results. It should be noted that the results for aluminium shielding are compared against the sample with shielded cables. To compare the effectiveness of the thin and thick aluminium shielding, these results are also compared in Figure 8-9.
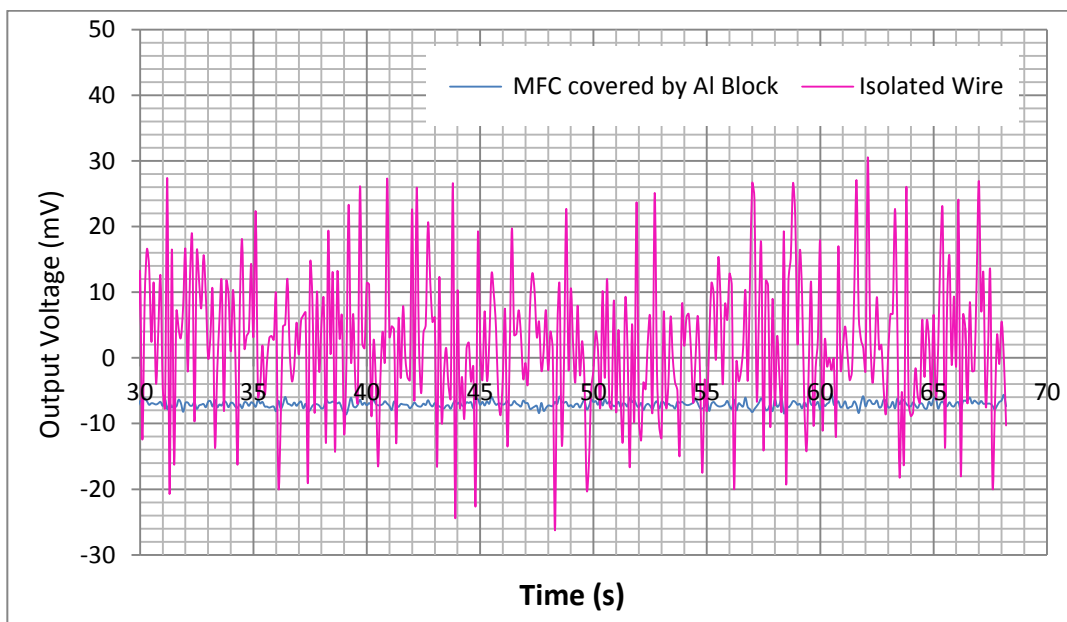
Figure 8-7: Effect of Shielding the MFC with Aluminium plate (Thick layer)
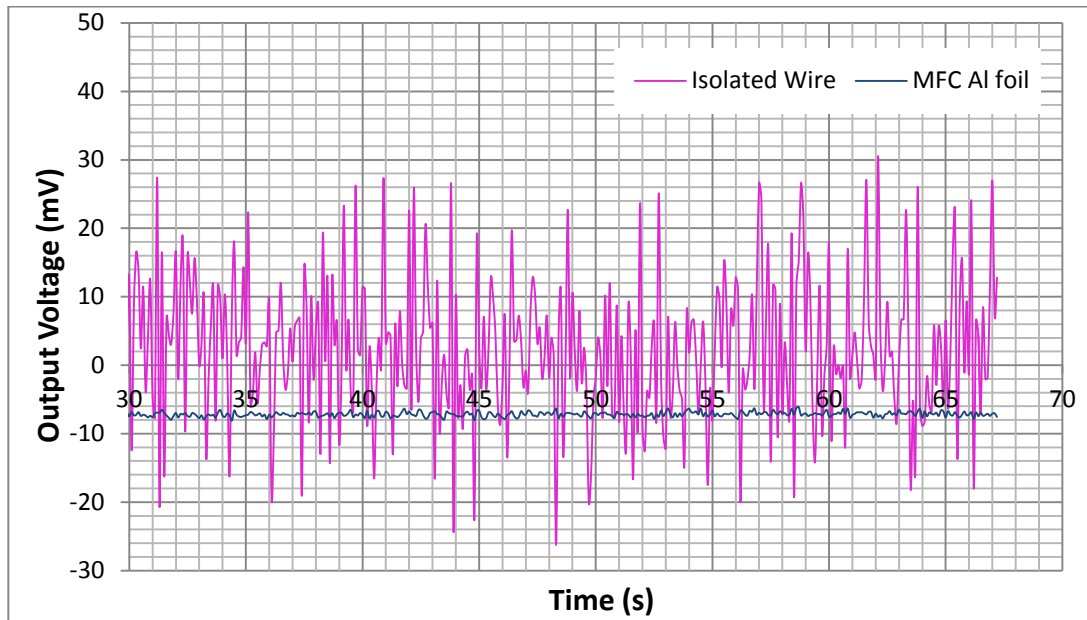
Figure 8-8: Effect of Shielding the MFC with Aluminium Foil (Thin layer)
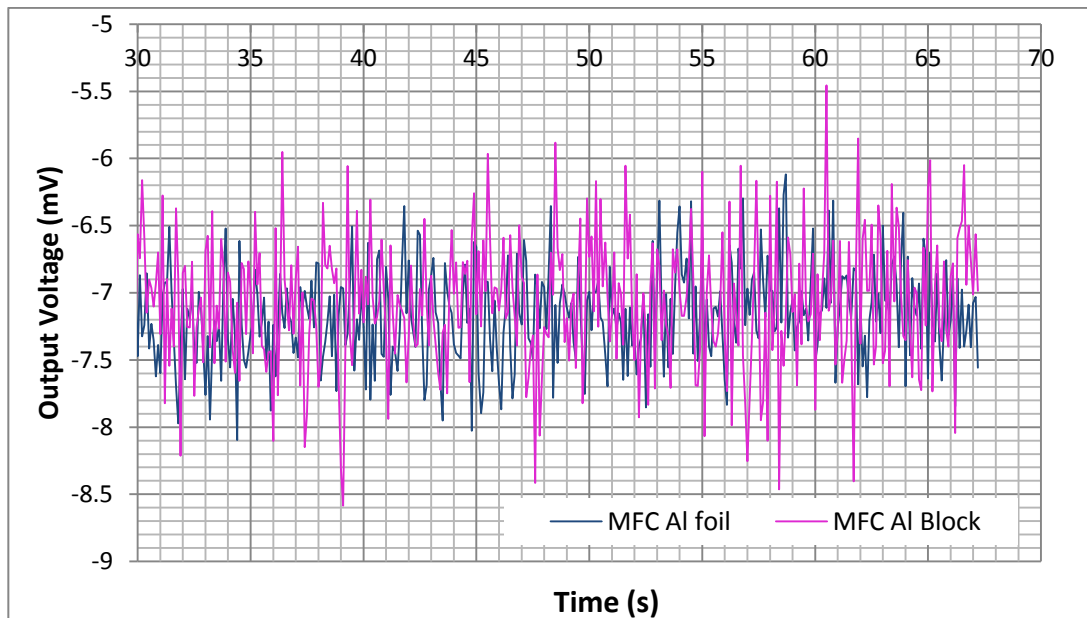
Figure 8-9: Effectiveness of the think and thick layer aluminium shielding

The comparison of the effectiveness of the aluminium shielding based on its thickness illustrates that the interference amplitude is relatively similar for both cases.

8.5.1.4.   MFC and PZT Comparison

The results from the previous section show that the main recipient of the electromagnetic interference is the MFC transducer. Therefore, it is essential to evaluate the effect of EMI on the MFC transducer compared to traditional PZT. In fact, the comparison of PZT and MFC helps us to establish whether or not the piezoceramic material is the main source of interference or the special

structure of the MFC makes it sensitive to EM interference. To make this comparison possible, a PZT with the same specifications is also bonded to the surface of the carbon/epoxy plate (Figure 8-10). The aim is to find out whether or not the piezoceramic materials are subject to electromagnetic interference. The PZT is bonded to the structure using conductive epoxy whilst the cable is soldered to the surface of PZT (electrode lead). The noise level of PZT and MFC voltage responses are then measured using a datataker. 2 channels were used to measure the voltage outputs simultaneously. This comparison is plotted in Figure 8-11.
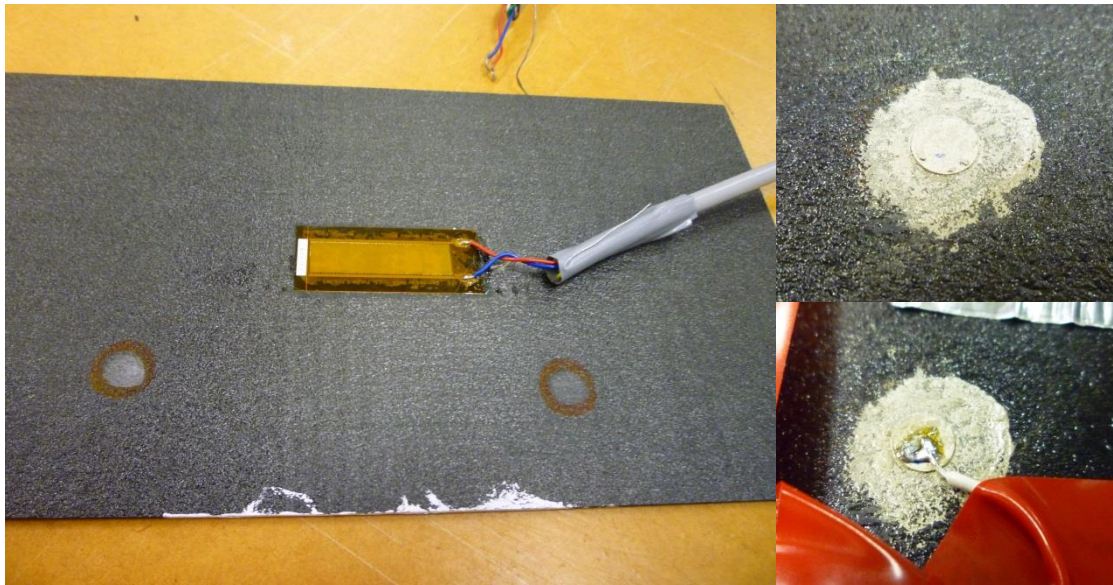
Figure 8-10: The bonding process for PZT transducer on the carbon/epoxy structure
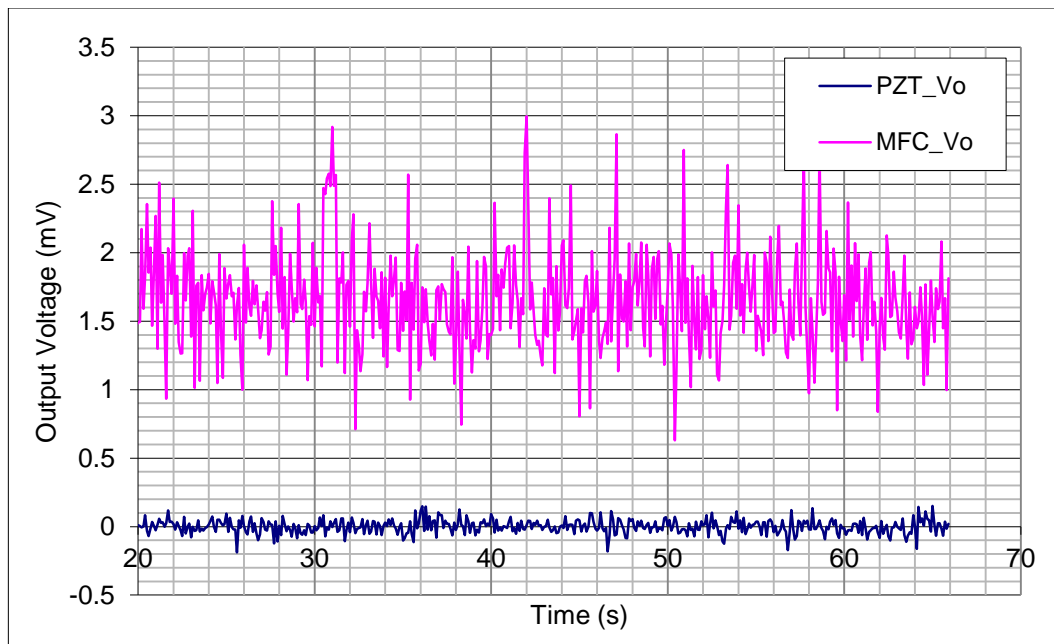
Figure 8-11: Comparison between PZT and MFC voltage responses due to electromagnetic field

The comparison between PZT and MFC voltage responses in the existence of the electromagnetic field illustrates that the traditional PZT is not affected by the EMI while the MFC shows much higher noise level. In other words, this effect is specific to the piezo-fibre based transducers such as MFC rather than the piezoelectric transducers in general. As the purpose of this comparison is to determine the sensitivity of PZT and MFC transducers to electromagnetic fields, the measurements are taken while the test machine is ON (electromagnetic field) although no mechanical loading is applied to either of the transducers. In other words, while the voltage response for PZT is close to zero, which is expected when no external mechanical or electrical loading is applied, the MFC still generates voltage response without any mechanical/electrical loading.

In fact, it is found during these investigations that the piezo-fibre-based transducers like MFC are sensitive to electromagnetic fields and generate electrical responses accordingly. Considering the usual applications of piezoelectric transducers and specifically the new generation of piezo-fibre-based transducers, which is mostly subject the high-frequency electromagnetic fields, this effect is very important and can have advantages and disadvantages for the certification of this type of transducer. On the one hand, it can lead to false positive readings due to the extra voltage generation caused by electromagnetic interference, whilst on the other hand, this sensitivity may be used as a self-diagnosis tool for piezo-fibre-based transducers. The later argument is discussed in the following sections.

8.5.2. Self-diagnosis Technique based on Electromagnetic Interference

In previous sections, various shielding and insulations techniques have been used to eliminate the EM interference on the voltage responses of the MFC transducer. It is found that proper shielding of the MFC transducer using material with high-conductivity such as aluminium can significantly reduce the interference. However, one of the goals of this research is to find a parameter which can be used to detect and diagnose possible damages in the transducer itself. Therefore, the possibility of using the sensitivity of the MFC transducer to the electromagnetic field as an effective parameter to detect transducer damage is explored through a series of conducted experiments.

In these experiments, the scattering parameter of healthy and damaged transducers is compared while the horn antenna, which is the standard antenna for antenna measurements, is used to generate an electromagnetic field around the sample. The horn antenna used for this research is the broadband horn antenna model DRH-118™ from Sunol Sciences™ (1-18 GHz, Transmit/Receive). Furthermore, the network analyser is used to send a signal to the horns and the transducer itself

and collect the relevant S-parameters such as S_{11}, S_{12} etc. in a specific frequency range. The details of the network analyser are provided in the following section. The aim of this investigation is to determine whether or not the S-parameters of the MFC transducer differ for healthy and damaged status.

8.5.2.1. Network Analyser

For antenna measurements, the most useful and important piece of equipment is the network analyser (NA), which is essentially a combination of a transmitter and a receiver. Normally it has two ports and the signal can be generated or received from either port. The VNA is frequency-domain equipment (it can obtain the signal in the time domain using Fourier transforms) (Huang & Boyle, 2008). There are two types of network analyser (Huang & Boyle, 2008):

- Scalar network analyser (SNA) which measures the amplitude of the parameters of a network.
- Vector network analyser (VNA) which measures both the amplitude and phase of the parameters of a network.

The VNA is much more powerful than the SNA; in addition to the parameters which can be measured by the SNA, it can also measure some very important parameters such as the complex impedance, which is essential for antenna measurements (Huang & Boyle, 2008). The VNA used for experimental tests of this project is shown in Figure 8-12. The architecture of a typical VNA is illustrated in Figure 8-13. The source signal can be transmitted from either Port, 1 or 2, to the antenna, which is controlled by a switch. Part of the signal from the source is provided directly to the reference R, which will be compared with the received signal by the central processing unit (CPU).
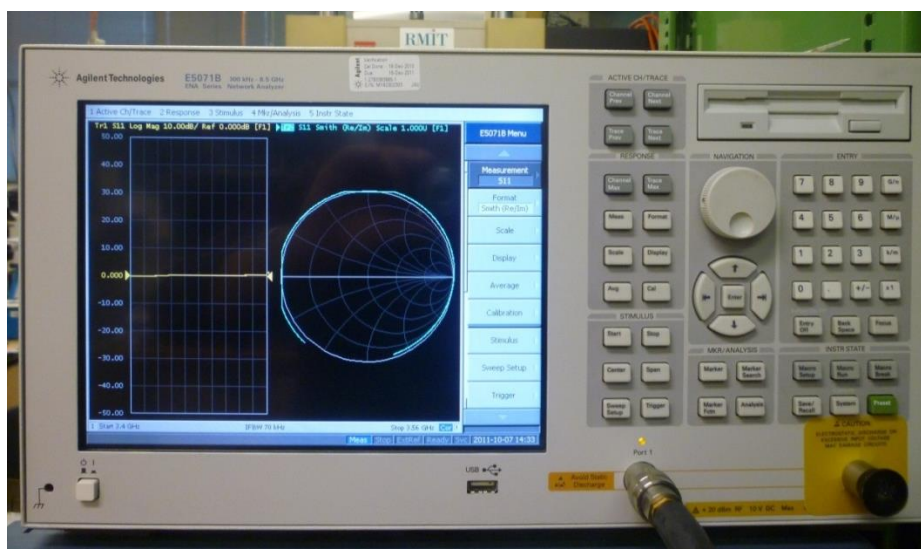
Figure 8-12: The VNA used for experimental tests
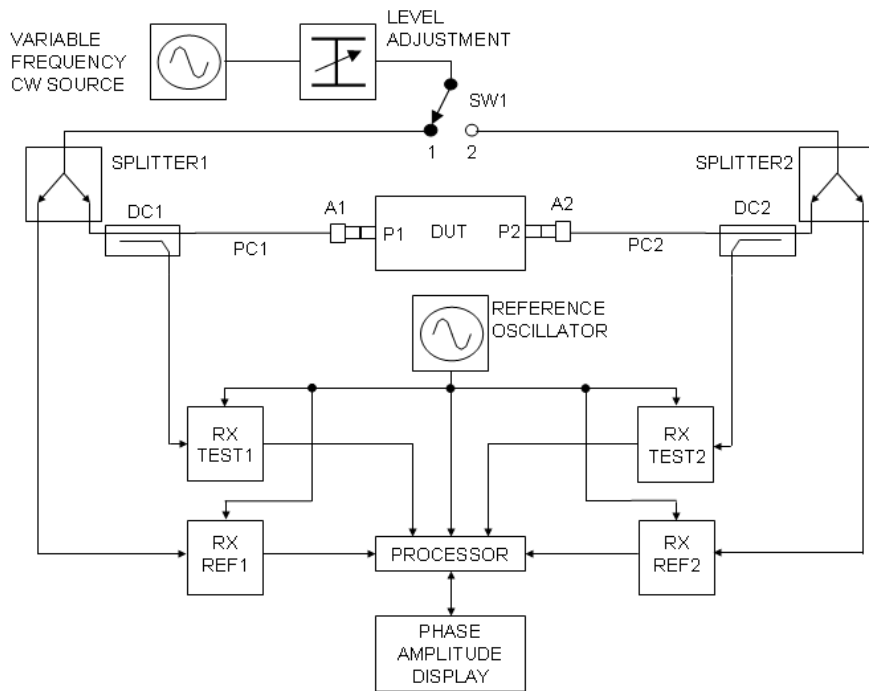
Figure 8-13: Architecture of a typical VNA (Daliri, 2010)

For antenna measurements, the typical parameters which can be measured by a VNA include (Balanis, 2009):

Transmission measurements:

Gain

- Insertion loss
- Insertion phase
- Transmission coefficients
- Electrical length
- Electrical delay
- Deviation from linear phase
- Group delay

Reflection measurements:

- Return loss
- Reflection coefficients
- Reflection coefficients vs. distance
- Impedance
- VSWR

In order to remove the effects of the cable and connectors (attenuation and phase shift), they must be calibrated (Huang & Boyle, 2008). The standard calibration needs three terminations for one-port calibration (short, open and load/matched) (Huang & Boyle, 2008). After connecting each terminator to the cable, one frequency sweep in the frequency range of the measurement must be performed. The calibration kit used in this research is shown in Figure 8-14. The calibration process is also shown in Figure 8-15.

Figure 8-14: Calibration kit used for antenna measurement.
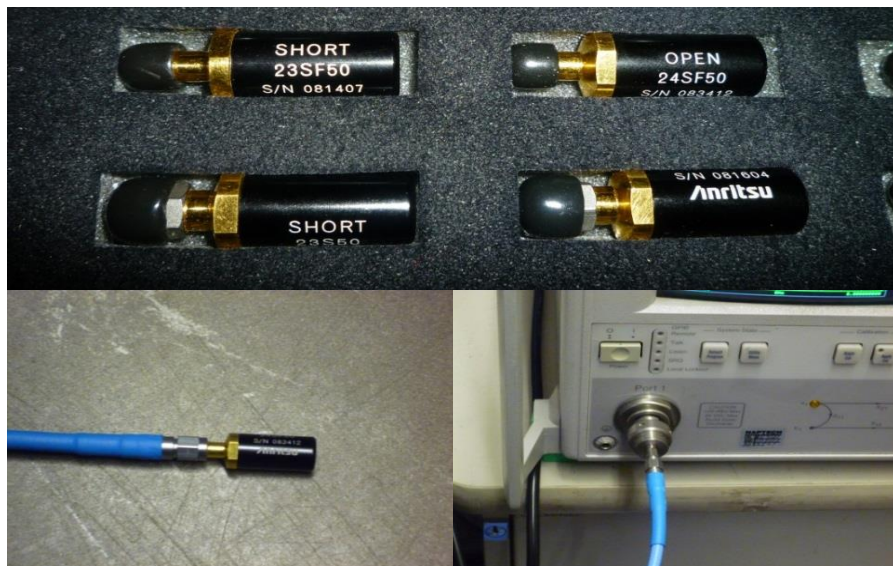
Figure 8-15: The calibration of the network analyser

Various errors which may be introduced into the measurement include (Huang & Boyle, 2008):

- System errors (can be removed by calibration)
- Random errors
- Drift errors

8.5.2.2.   Sample Preparation

In order to connect the MFC transducer to the network analyser, the electrode leads should be connected to the coaxial cable port which is compatible with coaxial cables connecting the MFC and Horn to the network analyser. The initial cabling configuration is shown in Figure 8-16.
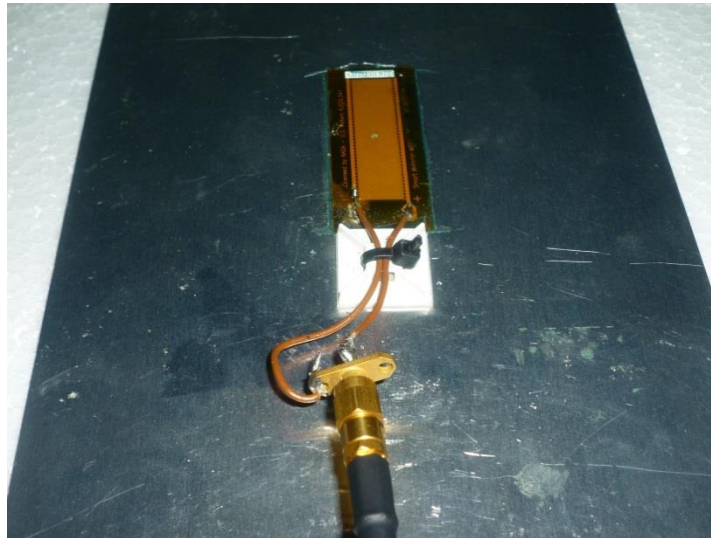
Figure 8-16: Initial coaxial cable port connection setup

However, it is observed during the initial tests that this configuration is not stable and may change the integrity of the measured values. Therefore, the setup shown in Figure 8-17 is used to connect the MFC to the coaxial cable. The attached setup may also affect the s-parameter measurements, although measuring baseline data and comparing other measurements with this baseline would eliminate this effect as the location of the setup is stable and does not move during the test.
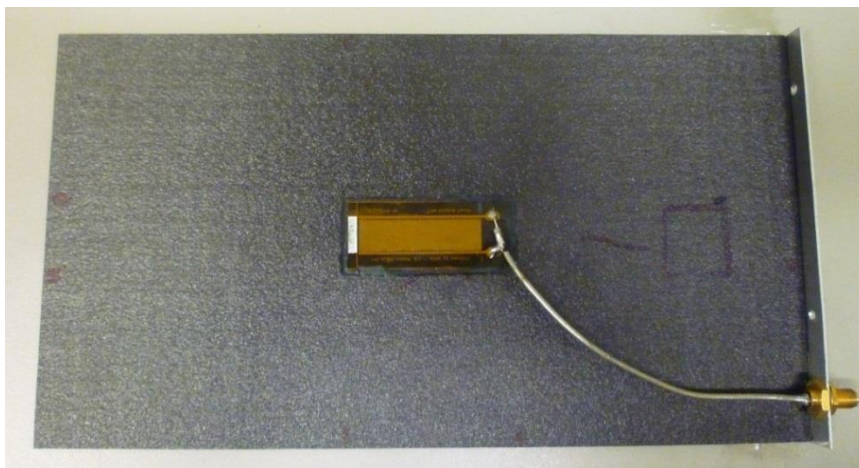
Figure 8-17: Final coaxial cable port connection setup

8.5.2.3. Damage induction during the test

In order to compare the healthy and damaged transducer, the samples with the damaged transducer are initially used and the measurements are made by placing the healthy sample and the sample with damaged transducer in the chamber separately before comparing the s-parameters accordingly. While the measurements show different s-parameters for the healthy and damaged transducer, it is also observed that swapping the samples is not a consistent process as the measurements are sensitive to the location of the sample in the chamber.

To address this issue, the sample with the healthy transducer is placed in the chamber and the S-parameters are measured and stored as the baseline. Following this, the damage is introduced to the MFC transducer while it is inside the chamber (Figure 8-18). This process is repeated 3 times and measurements are compared. The comparison of these results confirms the consistency and repeatability of the measurements.
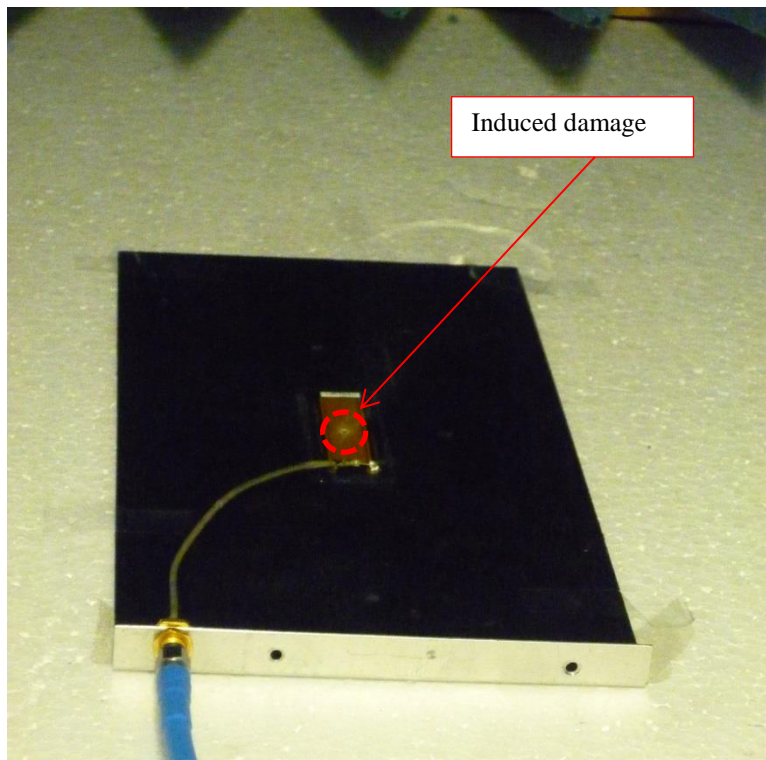
Induced damage

Figure 8-18: Damage induction in the MFC transducer

8.5.2.4. Experimental Process and Measurements

The MFC transducers as well as Horn antenna are connected to the network analyser using coaxial cables. The Horn is connected to Port 1 and the MFC transducer is connected to Port 2. The frequency range of 0.04-8 GHz is selected for this experiment. The network analyser sends the signal to the Horn which then transmits it to the MFC transducer. The scattering parameters are

measured for the healthy and damaged MFC transducers by the network analyser. A total of 3 scattering parameters, namely S_{11}, S_{22} and S_{12} are measured. This setup is shown in Figure 8-20.

8.5.2.4.1. Scattering Parameters

Scattering parameter or S-Parameter is a measurement of the reflection coefficient and transmission coefficient in a 1-port or 2-port network (Equation 8-3) (Huang & Boyle, 2008).

Equation 8-3

$$[S] = \begin{bmatrix} S_{11} & S_{12} \\ S_{21} & S_{22} \end{bmatrix}$$

Scattering parameter links the input to the output by the following equation to the equivalent 2-port network of a transmitting-receiving antenna system as shown in Figure 8-19.
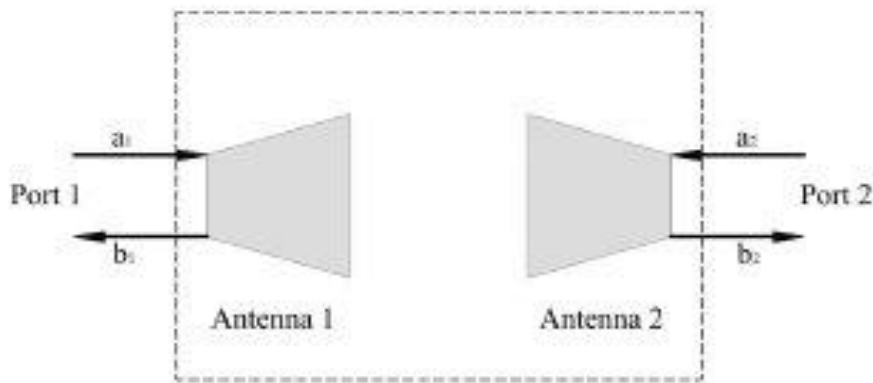
Figure 8-19: The equivalent 2-port network of transmitting - receiving antenna systems (Huang & Boyle, 2008)

Equation 8-4

$$\begin{bmatrix} b_1 \\ b_2 \end{bmatrix} = \begin{bmatrix} S_{11} & S_{12} \\ S_{21} & S_{22} \end{bmatrix} \begin{bmatrix} a_1 \\ a_2 \end{bmatrix}$$

Where

S_{11} is port 1 reflection coefficient (b_1/a_2)

S_{12} is port 2 to part 1 transmission coefficient (b_1/a_2)

S_{21} is port 1 to port 2 transmission coefficient (b_2/a_1)

S_{22} is port 2 reflection coefficient (b_2/a_2)
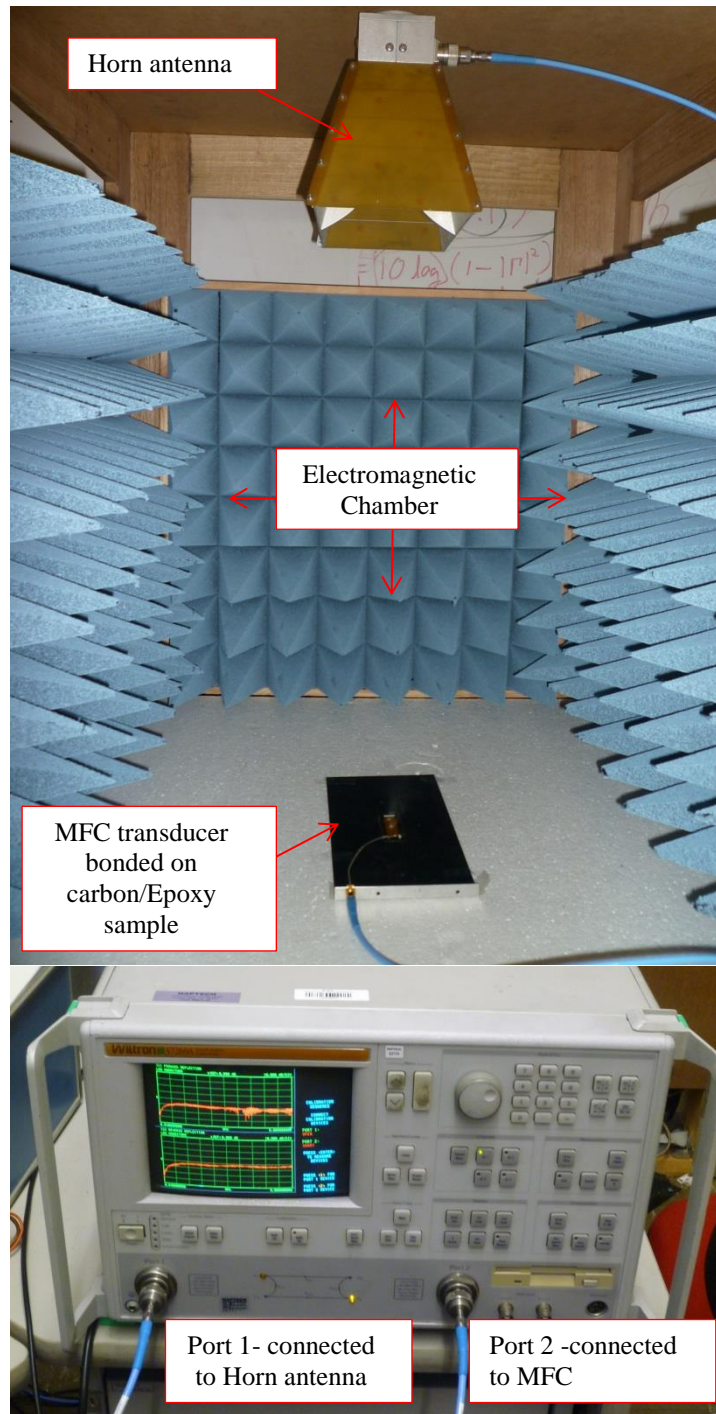
Figure 8-20: Setup for s-parameter measurement using horn antenna

8.6. Results

The measurements are taken for the healthy and damaged transducer and the scattering parameters are plotted against the designated frequency range. In this test configuration, the horn antenna acts as the transmitter and the MFC transducer acts as the receiver. The resonant frequencies of the MFC are measured by connecting the coaxial cable to the network analyser. The resonance frequencies are used as a reference to assess whether the damage in the transducer modifies these resonant frequencies. As mentioned earlier, 3 s-parameters are measured in these experiments,

namely S_{11}, S_{12} and S_{22}. S_{11} is the Horn`s reflection coefficient or return loss and shows how much power is reflected from the horn antenna. S_{12} represents the power received by the horn antenna relative to the power input to MFC transducer. Finally, S_{22} would be the power received by the MFC transducer relative to power input to the MFC transducer.

As the aim of this experiment is to investigate the possibility of using the sensitivity of an MFC transducer to EMF to detect the transducer damage, the S_{11} and S_{12} parameters are more informative and therefore measured. These scattering parameters of horn antenna and MFC transducer are saved by the network analyser on a disk using *.CSV format (Comma-Separated Values). The measurements are repeated 5 times to ensure that the process is repeatable and results are consistent. The S_{11} is compared for the healthy and damaged transducer in Figure 8-21. It can be seen from this figure that the resonance frequency of the MFC transducer measured by horn antenna is decreased for the damaged transducer, especially at around 2.2 GHz with near 10 dB. This is because of the reduction in the damaged transducer's ability to absorb the energy in the piezo-fibres, meaning that it reflects more than the healthy transducer.
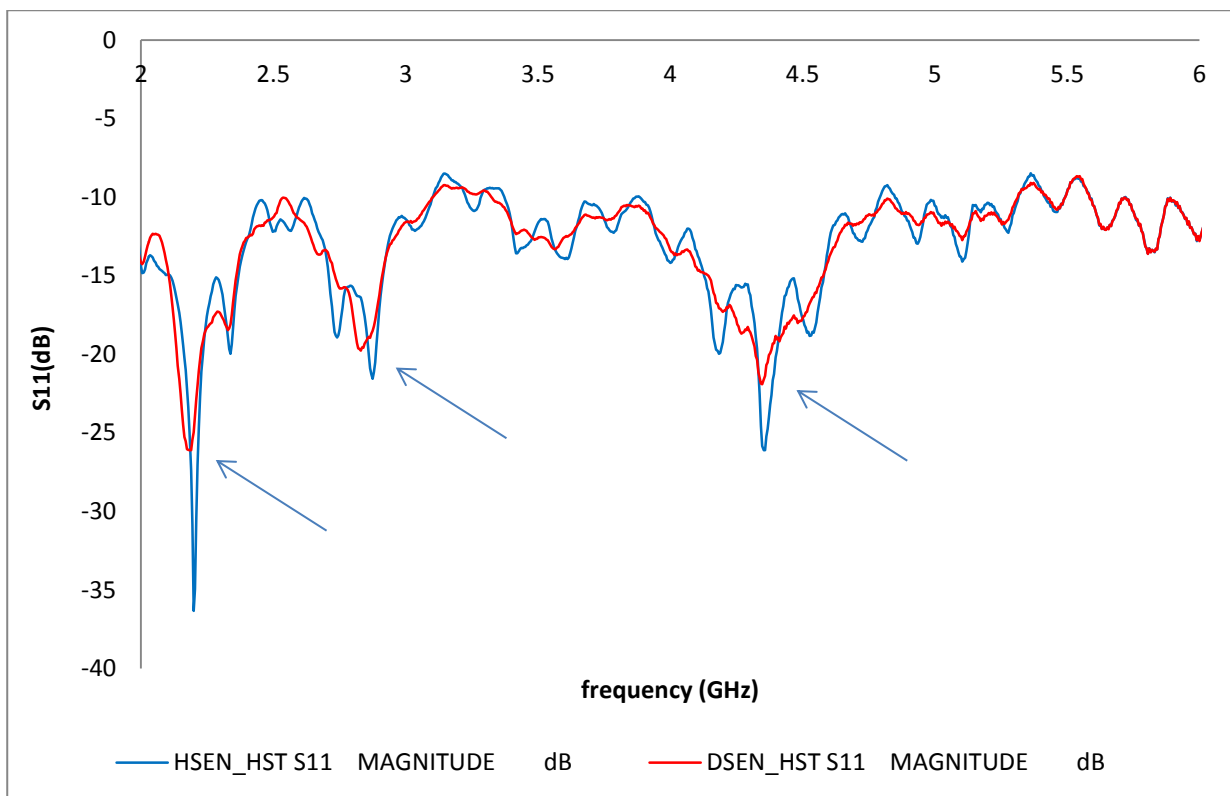
Figure 8-21: Return Loss (S_{11}) for horn antenna

Based on the above discussion, it is shown that the reduction in the s_{11} resonance frequency of the transducer can be considered as a sign of damage. However, as one of the main goals of this project is to delineate the structural damage from transducer damage, the sensitivity of the S_{11} to the structural damage is also investigated. The damage was induced on the surface of the structure

258

inside the chamber and S_{11} parameter was measured. The comparison of the measured S_{11} for healthy sample, sample with damaged transducer and sample with damaged structure is presented in Figure 8-22.
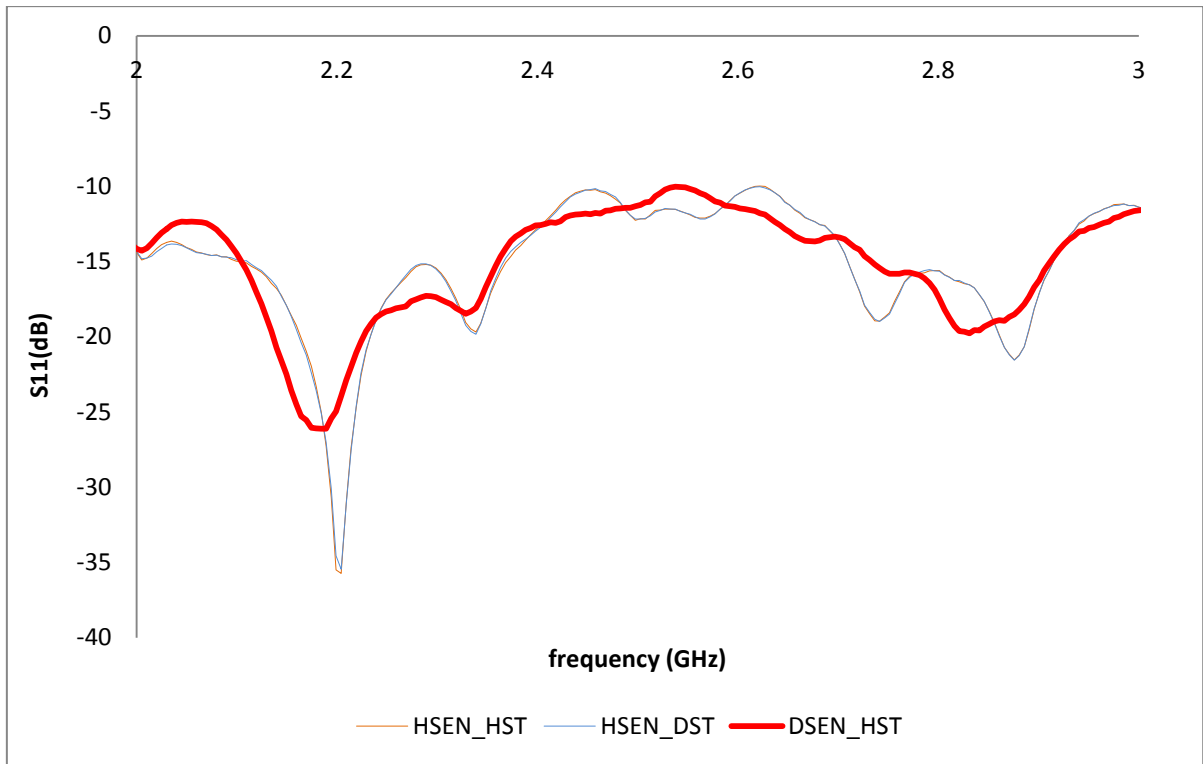
Figure 8-22: Comparison of Return Loss of Horn antenna for damaged transducer and damaged structure
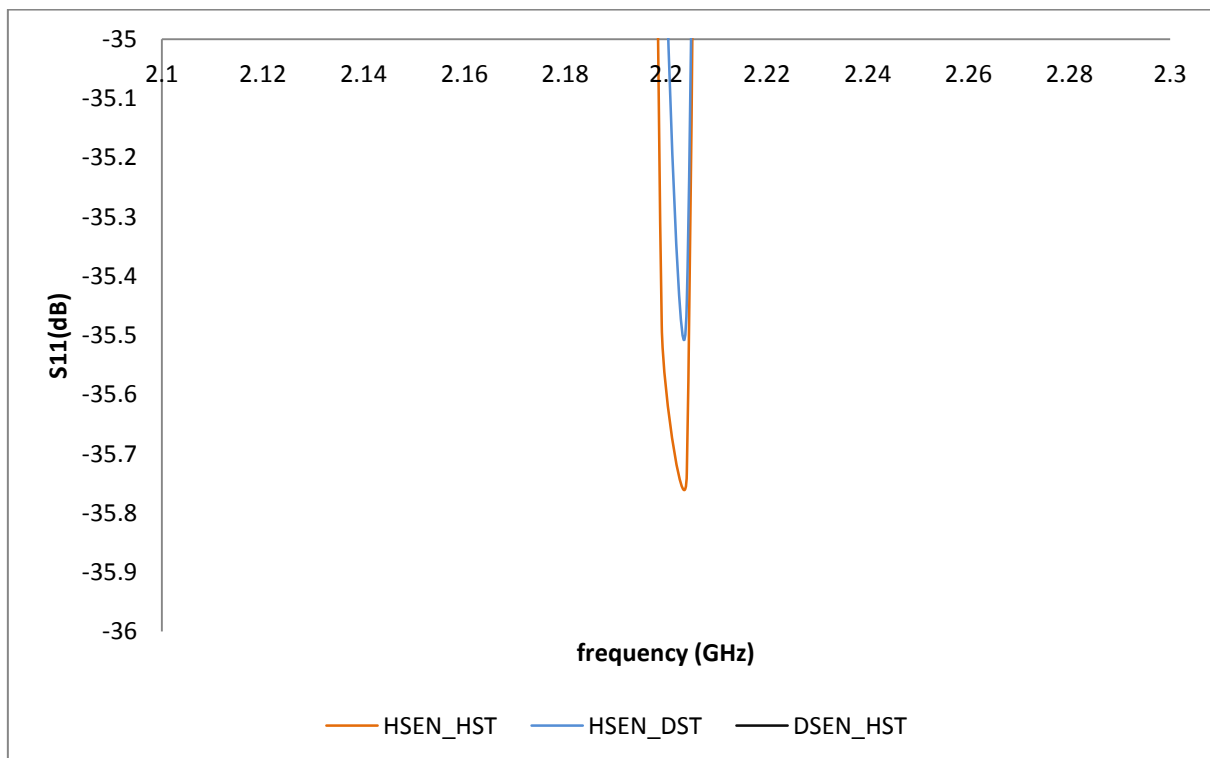
Figure 8-23: S_{11} comparison for sample with damaged structure and healthy sample

259

It is observed that the damage in the transducer reduces the return loss by approximately 10dB as described before while the structural damage causes less than 0.3dB further loss as shown in the magnification of the resonance frequency in Figure 8-23. By comparing these two figures, it can be said that the damage in the transducer considerably reduces the S_{11} at resonance frequency while the damage in the structure increases the S_{11}. However, this increase is very insignificant and negligible.

The next s-parameter to be measured, as previously described, is S_{12}. This measurement shows how much power the transducer (port2) gains from the power which is sent from the horn antenna (port 1). In other words, how much power the transducer can store in itself which has a direct relation to the integrity of piezo-fibres. Therefore, it is expected that a higher S_{12} will be observed for the healthy transducer compared to the damaged transducer. This is because of the damage in the piezo-fibres within the transducer which reduces its ability to store power. This expectation is satisfied through experimental results as shown in Figure 8-24. At approximately 2.2 GHz, which is close to the resonance frequency of the transducer, a reduction of approximately 15 dB can be observed. This parameter is irrelevant to structural damage and therefore can be purely indicative of transducer damage.
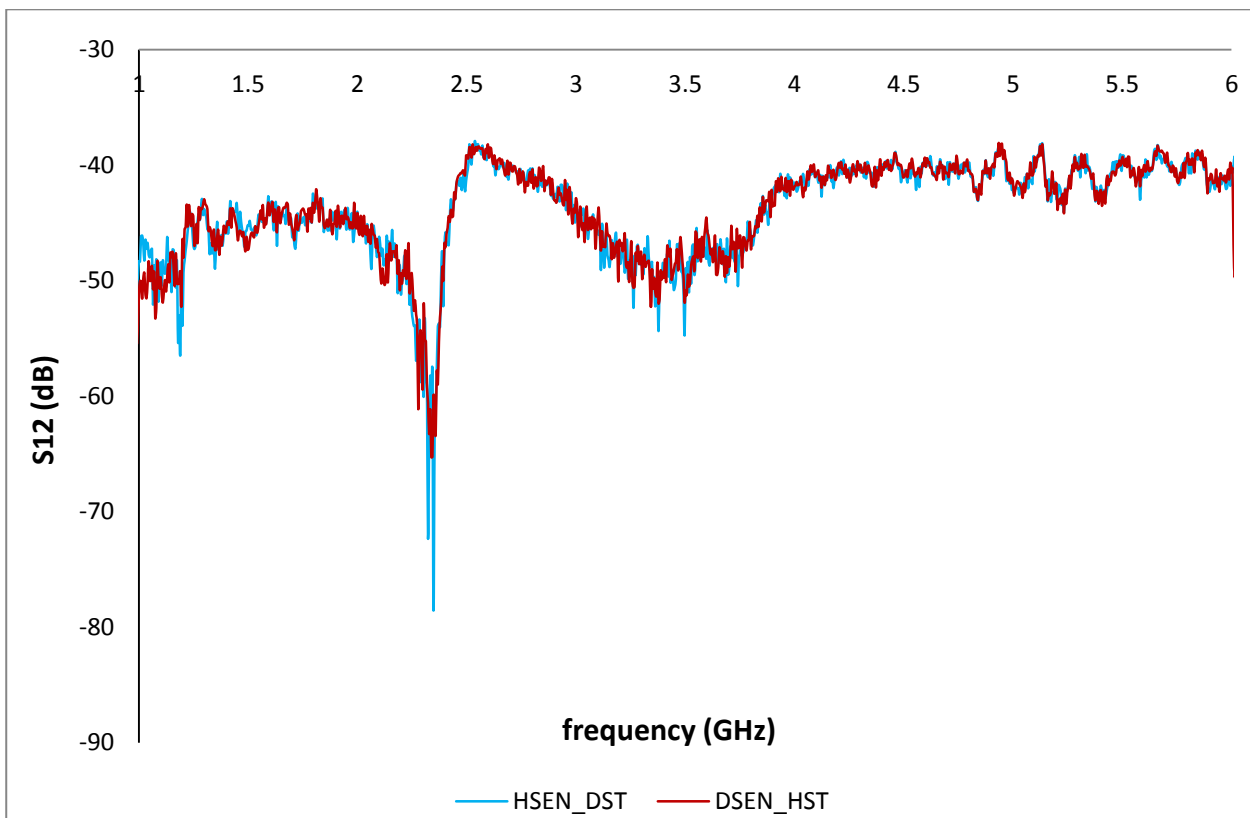
Figure 8-24: S12 measurements for healthy and damaged transducer

8.7. Summary

In this chapter, the effect of electromagnetic interference on the performance of the MFC transducer has been investigated. This effect was not previously mentioned in the literature, and therefore requires an in-depth investigation. Various shielding and insulation techniques were used to eliminate the EM interference and also to determine the main recipient of the interference within the designated test configuration. The comparison of the behaviour of traditional PZT and MFC illustrated that the EM interference does not affect the PZT responses. It was determined that the interdigitated electrodes and the shape of piezoceramics, which are poled fibres, are the causes behind the interference in MFC. The shielding of the MFC transducer with high-conductive material like Aluminium has shown better results in terms of filtering the electromagnetic interference on the MFC output voltage. Furthermore, the feasibility of using the sensitivity of the MFC transducer to the electromagnetic field as a basis for the damage detection technique was investigated. It was observed that the responses of intact and damaged transducers to an identical electromagnetic field differ. This statement was investigated by placing the sample in the electromagnetic chamber and using the Horn antenna and Network analyser to transmit the power and measure the scattering parameters of S_{11} and S_{12} respectively. The process of inducing the damage to the transducer was carefully completed while the sample was in the chamber. This was done to ensure that the only variable was the damage induced to the transducer.

The results show that the damage in the transducer reduces the magnitude of the dips in the S_{11} graph at resonant frequencies while the structure damage does not affect this parameter significantly. However, a very minor increase was observed in the magnitude of the dip in the S_{11} trend. The S_{12} parameter was also measured for the MFC transducer before and after the damage induction. It was observed that the magnitude of dip at the resonance frequency in the S_{12} curve reduced due to the transducer damage. This parameter did not show any sensitivity to structural damage as was expected based on the nature of this parameter. The outcomes of this chapter are important findings as the electromagnetic field is fairly common in the usual operation environment of piezo-fibre-based transducers and this effect must be considered in future investigations. Moreover, the proposed technique is a novel solution to detect and diagnose the damage occurring in the piezo-fibre-based transducers while they are in operation.

CHAPTER 9   Conclusion

The overall aim of this research is to address one key issue, within the context of structural health monitoring (SHM). This aim is to ascertain structural damage from measurements of transducers that may concurrently incur damage and degradation. The ability to attribute changes in sensor response to either structural damage or sensor damage is critical to the ultimate certification of SHM systems.

9.1.   Computational Modelling (Finite Element Analysis)

To evaluate the performance of the bonded MFC transducer, a Finite Element Method Analysis (FEA) is conducted using ABAQUS software. To justify the need for accurate micro-scale simulation, a macro-scale simplified model of MFC is also simulated, which is similar to existing MFC simulations available in literature, and the results are compared with micro-scale analysis values. The comparison of these two sets of results with experimental measurements confirms that micro-scale simulation is necessary for determining the performance of MFC. It was observed that while the strain calculation by MFC simulation exhibited an accuracy of approximately 90% of compared to experimental results, the accuracy of the simplified approach was less than 20% compared to experimental strain measurements. Furthermore, FEM calculations of generated electric potential in MFC had over 90% accuracy compared to experimental measurements, while the accuracy of the simplified simulation was around 60%.

Two approaches are investigated in terms of simulating the MFC transducer and it is observed that the complex approach, which is based on the actual structure of the MFC and not the simplified one, is the most reliable approach for piezo-fibre-based transducers as it validated the experimental results. It is shown that the electromechanical coupling of bonded MFC transducer and carbon/epoxy structure can be successfully simulated using the coupled-field FEM analysis. A FEM–based method to calculate the real and imaginary parts of electromechanical impedance (admittance) is proposed using the coupled-filed method. It is established that to numerically induce and propagate damage in the MFC transducer and/or composite structure, the extended finite element method (XFEM) tool can be employed. A comparison of FEM results, which are based on the investigation in this chapter, with the experimental results is presented in relevant chapters. The strain measurements were validated by FEM simulation. The similar mechanical loading and boundary conditions were defined and the results show a greater than 90% match with

experimental measurements. Also, similar electromechanical loading and poling conditions were applied on the FEM model and the results show less than 5% variation as compared to experimental measurements. However, the comparison of the FEM calculations with the experimental measurements confirms the accuracy of FEM simulations.

9.2. The Fatigue Performance of MFC and PFC transducer

By comparing these measurements, it is observed that the proper bonding process will not have any considerable effect on the integrity of the transducer and the structure. The voltage responses of MFC and PFC sensors are shown to have a substantial sensitivity to damage. The monitoring of key electrical properties of PFC and MFC sensors, such as capacitance, resistance, inductance and voltage coefficient, during the fatigue test emphasises that the capacitance has greater sensitivity to sensor degradation as compared to other electrical properties. The visual investigation of the damaged sensor using an optical microscope confirms that the drops in capacitance measurements are due to sensor damage. It is noticed that the MFC sensor has a much better performance under fatigue loading when compared to the PFC sensor. The PFC shows signs of degradation after approximately 45,000 cycles while the MFC shows significantly better robustness even after approximately 300,000 cycles. In addition, the measurements of the key electrical properties show that the degradation of the sensor starts prior to damage in the structure, thus resulting in 'false positive' readings from the sensors. The changes in the local measurements show that the capacitance is more sensitive to the properties of the sensor components, such as piezoelectric coefficient and voltage coefficient, rather than misalignments caused by micro-cracking. The results from the SEM technique show that the local misalignment of fibres and/or electrodes has less impact on capacitance reduction when compared to piezoelectric coefficients, which is caused by fibre breakage and debonding between sub-layers of the sensor.

9.3. Strain-based Delineation Technique

The strain-based technique is presented in Chapter 6. This technique is based on the comparison of three sets of strain values, namely strain gauge measurements, MFC strain measurements and the theoretically calculated strain. By deriving the constitutive equations for MFC and applying the relevant geometrical and electrical properties to these equations, an equation is presented that is capable of calculating the strain level based on MFC voltage responses. The MFC strain calculations are validated with the strain gauge readings. The theoretical strain, which is calculated, based on the configuration of the three-point-bend test, as well as numerical strain values that are calculated using an FEM-based software package called ABAQUS, both have greater than 95% similarity to the experimental measurements, thus validating the accuracy of the simulated model.

The results illustrate that the difference between theoretically calculated strain and the strain gauge measurements ($\Delta_{\text{structure}}$) is close to zero as long as the structure is intact, while structural damage causes this difference to increase significantly. The comparison between the MFC strain measurements and the calculated strains from theoretical equations (Δ_{sensor}) is also used to monitor the status of the sensor itself. The difference between these two values was close to zero as long as the sensor was intact. The increase in this difference is shown to be a sign of structural damage. From these results, it is observed that the continuous monitoring of $\Delta_{\text{structure}}$ and Δ_{sensor} can be used to delineate structural damage from sensor damage.

9.4. Electromechanical Impedance-based Delineation Technique

The electromechanical coupling between the electrical impedance of the active MFC and mechanical impedance of the structure is used as a tool to delineate structural damage from MFC actuator damage (CHAPTER 7). It is shown that the interaction between MFC and a carbon/epoxy structure can be modelled through dynamic equilibrium between a thin vibrating bar and a system of mass/spring/damper, which represents mechanical impedance. It is concluded from the equivalent circuit of MFC-Structure that the change in the mechanical impedance, which may stem from structural damage, can also affect the impedance value. In the equivalent circuit, the MFC is modelled with a capacitor with similar capacitance as the MFC and V_{IN}, while the structure is modelled with a resistor. It is determined that the AD5933 impedance analyser, which is a light-weight, low-cost and low energy consumption device, is a proper solution for SHM systems and is successfully used in this project to automatically send the signal to the transducer and collect the required responses from the actuator. The comparison of this device with other more popular impedance analysers, which are relatively bulky and expensive, confirms its functionality. The real and imaginary components of the electromechanical impedance (admittance) are used for delineation purposes.

Five electromechanical impedance and admittance parameters are selected based on the analytical and theoretical investigations to delineate various damage scenarios, namely real impedance (Resistance), imaginary impedance (Reactance), real admittance (Conductance), imaginary admittance (Susceptance) and Imaginary magnitude. The experimental measurements of electromechanical impedance have been validated with FEM numerical results from CHAPTER 4. The outcome shows a very good match between the numerical and experimental results.

The aforementioned electromechanical impedance parameters are measured for six samples with various structure/actuator damage scenarios. Furthermore, the sequence of MFC actuator damage

to structural damage and its effect on the impedance/admittance parameters is also investigated. It is observed that the sequence of each damage scenario, such as actuator damage and structural damage, to the other damage scenario affects the results differently. The four main situations in terms of MFC actuator/structure damage statuses are investigated. These include: the generation of damage in the structure when the MFC actuator is still intact, the generation of damage in the MFC actuator when the structure is still intact, the generation of damage in the structure while the MFC actuator is already damaged and the generation of damage in the MFC actuator when the structure is already damaged. It was concluded from the experimental investigations, as well as FEA results, that the imaginary impedance is the most suitable parameter for pure actuator damage (intact structure) as it shows consistent and measurable changes after the damage occurred. It was also found that the real admittance is a reliable parameter to control when the actuator is degraded. It has quantifiable sensitivity to structural damage and is capable of identifying the location of structural damage with regards to actuator location. Furthermore, the imaginary admittance has shown robust sensitivity to structural damage when the structure is already degraded. In other words, this is a proper parameter to be used to detect actuator damage when one knows the structure is already damaged. Finally, the detection of structural damage when the actuator is intact was proved to be possible by the continuous monitoring of real impedance.

9.5. Investigating the Effect of Electromagnetic Interference on Piezo-Fibre-based Transducers

The effect of electromagnetic interference on the performance of the MFC transducer is investigated in CHAPTER 8. Various shielding and insulation techniques were used to eliminate the EM interference and it was observed that shielding of the MFC transducer with a high-conductive material, such as aluminium, gave better results in terms of filtering the electromagnetic interference on the MFC output voltage. The comparison of the behaviour of traditional PZT and MFC illustrated that the EM interference does not affect the PZT responses. It was determined that the interdigitated electrodes and the shape of piezoceramics, which are poled fibres, are the causes of the interference in MFC. It was observed that the responses of intact and damaged transducers to an identical electromagnetic field differ. It is shown that inducing damage in the MFC causes the reduction of 10 dB at resonance frequency, which accounts for a 60% increase of return loss as compared to the intact MFC. Furthermore, the feasibility of using the sensitivity of the MFC transducer to the electromagnetic field as a basis for a damage detection technique was investigated. It can be concluded that the difference in the behaviour of intact and

damaged transducers towards the identical electromagnetic field was a reliable factor in detecting damage within the transducer itself.

9.6. Original Contributions

The original contributions of this thesis can be summarised as follows:

(1) A practical micro-scale FEM simulation of MFC transducers was proposed. The approach is based on the detailed structure of MFC transducers with all the components of MFC, such as interdigitated electrodes, piezoceramic fibres, epoxy layers and gaps, being considered in the simulation. While the complex structure of MFC components and scale of the modelling make the simulation process considerably difficult and time consuming, the outcome of this simulation allows for a proper understanding of the behaviour of MFC, especially when the MFC becomes degraded. The numerical calculations by detailed FEM simulation of the MFC show much better accuracy compared to simplified simulation with over 90% of matching with strain and voltage experimental results. This is one aspect of MFC transducer technology, and piezo-fibre-based transducers in general, that has not been properly explored in previous studies. (CHAPTER 4)

(2) An extensive new study regarding the topology of damage in the subcomponents of piezo-fibre-based transducers and especially the MFC was conducted. A series of destructive and non-destructive evaluations were performed using techniques such as Scanning Electron Microscopy (SEM) and Microprobe to: (a) visualise the effect of transducer damage on the integrity and shape of subcomponents, such as piezoceramic fibres and interdigitated electrodes (IDE), (b) determine the effect of transducer damage on the local properties of the transducer (comparison of the electrical properties of damage and undamaged zones of transducer), (c) distinguish the root cause of the degradation of electrical and mechanical properties of the damaged transducer. It was concluded that for damaged transducers, the voltage reduction is due to the internal debonding of piezo-fibres from the epoxy layer, the capacitance reduction is caused by the breakage or crack within the piezo-fibres and the changes of relative permittivity is due to the generation of a crack in the epoxy layer. This study can be used as a very useful tool with which to understand the root cause of the disadvantages of existing piezo-fibre-based transducers and to make the necessary improvements in future generations of this type of transducer. (CHAPTER 5)

(3) A practical solution was devised with which to delineate the sensor damage from structural damage for SHM systems. The novelty of this approach is that this method can be employed in any existing SHM system that uses the piezo-fibre-based sensors, and especially MFC, as the

sensor of preference. The bases of this method are: (a) voltage-strain relation that is specifically derived in this project for the MFC sensor to calculate the strain based on voltage responses of the sensor, (b) the accurate numerical calculation of the strain using the novel FEM model of MFC, the $\Delta_{structure}\,(\varepsilon_T - \varepsilon_{SG})$ parameter, which is the difference of strain gauge measurements and the numerical strain calculations from FEM simulation, showed significant sensitivity even to small (6%) strain changes caused by, structural fatigue damage while the $\Delta_{sensor}(\varepsilon_T - \varepsilon_{MFC})$ parameter, which is the difference of MFC strain measurements and the numerical strain calculations from FEM simulation, performed well in detecting MFC strain changes of only 4% caused by fatigue loading. (CHAPTER 6)

(4) A very unique and novel delineation technique was presented based on the electromechanical impedance readings of the actuator. This technique is capable of delineating various actuator-structure damage situations and providing an accurate and reliable feedback on the actual status of not only the structure but also the actuator itself. A novel technique is proposed with unique abilities to: (a) delineate actuator damage from structural damage regardless of which damage occurs first, (b) compensate the responses of the degraded actuator to continue the monitoring task and also avoid false positive or false negative readings, (c) use the responses of the actuator, as the only available source of information in real life conditions, for all damage detection purposes, thus making it a practical technique for actual projects, (d) employs a low-power, portable and cheap impedance analyser with similar accuracy and sensitivity to the popular impedance analysers, which are bulky, expensive and require large amounts of power to run. It was determined that the real impedance is a suitable parameter to detect structural damages, while the imaginary impedance is a reliable parameter to detect pure actuator damages. The imaginary admittance parameter proved to be capable of extracting measurable responses from the degraded actuator to detect structural damages. Also, the real admittance performed well for detecting actuator damage when the responses were already degraded due to structural damage. (CHAPTER 7)

(5) The sensitivity of piezo-fibre based transducers was also reported, an example of which is the sensitivity of MFC to electromagnetic interference. Indeed, this has not been previously reported in the literature. This is a very important discovery as it may significantly affect the quality and reliability of the responses received from the transducer, thus reducing the functionality of the SHM techniques that use piezo-fibre-based or similar transducers. A novel diagnostic technique for piezo-fibre-based transducers was proposed in accordance with the responses of the transducer to electromagnetic fields. It is shown that the behaviour of the intact and degraded transducer differs when they receive interference from an identical

electromagnetic source. It was demonstrated that this difference in the responses can be used as a parameter to delineate the transducer damage from structural damage. The measurement of S_{11} scattering parameter showed a 60% increase of return loss due to a damaged transducer, while this change was only 2% for structural damage. This difference was employed as an indicator to detect transducer damage. (CHAPTER 8)

9.7. Future Work

The results from this study open new areas of research that require profound multidisciplinary input. Some of the ideas that could be developed further in the future include:

- The capability of the proposed techniques to detect and delineate other types of damage, such as impact and corrosion as well as combined damage situations. Moreover, other types of transducers rather than Macro Fibre Composite (MFC) could be used to evaluate the functionality of the proposed techniques for other transducer types.

- The relationship between the severity of transducer damage and the effective zone that the damaged transducer can still sense in terms of structural damage should also be investigated. In addition, the proposed techniques should be used to characterise the effect of the propagation of induced damage in the transducer, as well as in the structure, on the monitoring parameters.

References

AD, A. N. (2005). *MSPS, 12-Bit Impedance Converter*. Analog Devices.

Altenbach, H., and Becker, W. (2003). *Modern trends in composite laminates mechanics.* Springer.

Ansede Pena, A. (2010). A Feasibility Study of the Suitability of an AD5933-based Spectrometer for EBI Applications, (Doctoral dissertation), School of Engineering. Sweden Electrical Engineering Specialization In Communications & Signal Processing.University of Boras.Sweden..

Annamdas, V. G. M., and Annamdas, K. K. K. (2010). *Impedance based sensor technology to monitor stiffness of biological structures. SPIE Defense, Security, and Sensing* (pp.76730V-76730V). International Society for Optics and Photonics.

Anton, S. R., and Sodano, H. A. (2007). A review of power harvesting using piezoelectric materials (2003–2006). *Smart Materials and Structures 16*(3): R1-R21

Aoki, Y. B. O. I. (2001). Damage Detection of CFRP pipes and shells by using Localized Flexibility Method. *Advanced Composite Materials 10*, pp. 189-198

Azzouz, M. S., and Hall, C. (2010). *Nonlinear Finite Element Analysis of a Rotating MFC Actuator*. Proceeding of 51ST AIAA/ASME/ASCE/AHS/ASC Structures, Structural Dynamics, And Materials Conference. Orlando, USA:

Baker, A. (2008). *Structural Health Monitoring of a Bonded Composite Patch Repair on a Fatigue-Cracked F-111C Wing*. (No. DTSO-RR-0335). Defence Science and Technology Organisation Victoria (Australia) Air Vehicles Div.

Baker, A. A. A., and Dutton, S., et al. (2004). *Composite materials for aircraft structures.* AIAA.

Balanis, C. A. (2012). *Antenna theory: analysis and design*. John Wiley & Sons.

Banks, W. M., and Dumolin, et al. (2000). Dielectric and mechanical assessment of water ingress into carbon fibre composite materials. *Computers & Structures 76*(1). pp. 43-55.

Beard, S. J., A., and Kumar, et al. (2005). *Practical issues in real-world implementation of structural health monitoring systems Smart Structures and Materials* (pp. 196-203). International Society for Optics and Photonics.

Beckert, W., and Kreher, W. S. (2003). Modelling piezoelectric modules with interdigitated electrode structures. *Computational materials science 26*. pp. 36-45

Belytschko, T., and Black, T. (1999). Elastic crack growth in finite elements with minimal remeshing. I*nternational Journal for Numerical Methods in Engineering 45*(5). pp. 601-620

Bent, A. A., and Hagood, N. W. (1997). Piezoelectric fibre composites with interdigitated electrodes. *Journal of Intelligent Material Systems and Structures 8*(11). pp. 903-919

Bhalla, S., and Soh, C. K. (2004). Structural health monitoring by piezo-impedance transducers. I: modeling. *Journal of Aerospace Engineering 17*. p. 154

Bhalla, S., and Soh, C. K. (2008). Electro-mechanical impedance technique for structural health monitoring and non-destructive evaluation. *National workshop on structural health monitoring, non-destructive evaluation and retrofitting of structures. Indian Institute of Technology Delhi*.

Bilgen, O., and Kochersberger, K., et al. (2009). Macro-fibre composite actuators for a swept wing unmanned aircraft. *Aeronautical Journal 113*(1144). pp. 385-395

Blackshire, J. L., and Cooney, A. (2006). Evaluation and improvement in sensor performance and durability for structural health monitoring systems. Nondestructive Evaulation for Health Monitoring and Diagnostics. *International Society for Optics and Photonics*. pp. 61790K-61790K

Bois, C., and Hochard, C. (2004). Monitoring of laminated composites delamination based on electro-mechanical impedance measurement. *Journal of Intelligent Material Systems and Structures 15*(1). pp. 59-67

Born, M., and Wolf, E. (1999). Principles of optics: electromagnetic theory of propagation, interference and diffraction of light. *CUP Archive*.

Bray, D. M. D. (1992). *Non-Destructive Testing Techniques*. (1st ed.).

Brunner, A. J., and Birchmeier, M., et al. (2009). Piezoelectric Fibre Composites as Sensor Elements for Structural Health Monitoring and Adaptive Material Systems. *Journal of Intelligent Material Systems and Structures 20*(9). pp. 1045-1055

Bystricky, P. (2012). *Smart Structures*. Wiley Encyclopedia of Composites..

Cady, W. G. (1964). *Piezoelectricity: an introduction to the theory and applications of electromechanical phenomena*.pp. 333-334.

Callus, P. J. (2008). *Novel concepts for Conformal Load-bearing Antenna Structure*. (No. DSTO-TR-2096). Defence Science And Technology Organisation Victoria (Australia) Air Vehicles Div.

Chambers J. T. W. B. L., and Kessler, S. S. (2007). *Lessons Learned from a Broad Durability Study of an Aerospace SHM System. Structural Health Monitoring—Quantification, Validation, and Implementation, Chang FK (ed). DEStech Publications: Lancaster, PA*, 247-255.

Chamis, C. C., and Center, N. G. R. (2010). *Probabilistic Methods for Structural Reliability and Risk.* Glenn Research Center.

Chaudhry, Z. A., and Joseph, T., et al. (1995). Local-area health monitoring of aircraft via piezoelectric actuator/sensor patches.. *International Society for Optics and Photonics., Smart Structures & Materials' 95 (pp. 268-276)*.

Chen, Q. C. Y. W., and Worden, K. (2003). Structural Fault Diagnosis and Isolation Using Neural Networks based on Response-only Data. *Computers & Structures 81*(22). pp. 2165-2172

Coowar, F. A., French, M. A., Mepsted, G. O., & Spooner, C. D. J. (2009). *U.S. Patent Application 13/139,854.*

Chou, J. H. G. J. (2001). Genetic Algorithm in Structural Damage Detection. *Computers & Structures Vol.?* (79). pp. 1335-1353

Cook, A. C., and Vel, S. S. (2012). Multiscale analysis of laminated plates with integrated piezoelectric fibre composite actuators. *Composite Structures 94*(2). pp. 322-336

Crawley, E. F., and De Luis, J. (1987). Use of piezoelectric actuators as elements of intelligent structures. *AIAA Journal 25*(10). pp. 1373-1385

Cunningham, M., and Jenkins, D., et al. (1997). Experimental investigation of optimum thickness of a piezoelectric element for cantilever actuation. *Science, Measurement and Technology,* IEE Proceedings- (Vol. 144, No. 1, pp. 45-48). IET.

Curie, J., and Curie, P. (1880). Développement, par pression, de l'électricité polaire dans les cristaux hémièdres à faces inclinées. *Comptes Rendus 91*. pp. 291-295.

Standard, A. S. T. M. D3039M-08 (2008) Standard test method for tensile properties of polymer matrix composite materials. *Annual Book of ASTM Standards*.
Dargie, W. and Poellabauer, C. (2010). *Fundamentals of wireless sensor networks: theory and practice*. John Wiley & Son..

Deraemaeker, A., Benelechi, S., et al. (2007). *Analytical and numerical computation of homogenized properties of MFCs: Proceedings of the III ECCOMAS thematic conference on Smart Structures and Materials.*

Deraemaeker, A., and Nasser, H. (2010). Numerical evaluation of the equivalent properties of Macro Fibre Composite (MFC) transducers using periodic homogenization. *International Journal of Solids and Structures 47*(24). pp. 3272-3285

Deraemaeker, A., and Nasser, H. et al. (2009). Mixing Rules for the Piezoelectric Properties of Macro Fibre Composites (MFC). *Journal of Intelligent Material Systems and Structures, 20(12), 1475-1482.*

Eaton, M., Pullin, R., et al. (2009). Use of Macro Fibre Composite Transducers as Acoustic Emission Sensors. *Remote Sensing 1*(2). pp. 68-79

Farrar, C. R., Hemez, F. M., Shunk, D. D., Stinemates, D. W., Nadler, B. R., & Czarnecki, J. J. (2004). *A review of structural health monitoring literature: 1996-2001* (p. 303). Los Alamos, NM: Los Alamos National Laboratory.

Figueiredo, E., Park, G., et al. (2012). Use of time-series predictive models for piezoelectric active-sensing in structural health monitoring applications. *Journal of vibration and acoustics 134*(4). pp.?

Gade, J., Korhonen, I., et al. (2000). Technical description of the IBIS Data Library. *Computer Methods and Programs in Biomedicine 63*(3). pp. 175-186

Ghasemi-Nejhad, M. N. (2005). Manufacturing and Testing of Active Composite Panels with Embedded Piezoelectric Sensors and Actuators. *Journal of Intelligent Material Systems and Structures 16*(4). pp. 319-333

Gibson, R. F. (2010). A review of recent research on mechanics of multifunctional composite materials and structures. *Composite Structures 92*(12). pp. 2793-2810

Gigliotti, L. (2012). *Assessment of the applicability of XFEM in Abaqus for modeling crack growth in rubber.* KTH. (Doctoral dissertation, KTH Royal Institute of Technology).

Giurgiutiu, V. (2009). Piezoelectricity principles and materials. *Encyclopedia of Structural Health Monitoring*.

Giurgiutiu, V., and Rogers, C. A. (1998). *Recent advancements in the electro-mechanical (E/M) impedance method for structural health monitoring and NDE. 5th Annual International Symposium on Smart Structures and Materials*(pp. 536-547). International Society for Optics and Photonics.

Giurgiutiu, V., Zagrai, A. et al. (2004). Damage identification in aging aircraft structures with piezoelectric wafer active sensors. *Journal of Intelligent Material Systems and Structures 15*(9-10). pp. 673-687

Giurgiutiu, V., Zagrai, A. et al. (2002). Piezoelectric wafer embedded active sensors for aging aircraft structural health monitoring. *Structural Health Monitoring 1*(1). pp. 41-61

Glushkov, E., Glushkova, N., et al. (2010). Guided Wave Generation and Sensing in an Elastic Beam Using MFC Piezoelectric Elements: Theory and Experiment. *Journal of Intelligent Material Systems and Structures 21*(16). pp. 1617-1625

Goddu, G., McDowell, D., et al. (2000). Adaptive control of radiated noise from a cylindrical shell using active fibre composite actuators. SPIE's 7th Annual International Symposium on Smart Structures and Materials, *International Society for Optics and Photonics. pp. 95-102.*

Golubović-Bugarski, V., and Blagojević, D. (2010). *An approach to damage detection in a beam like structures from experimentally measured FRF data.*

Hannah, R. L., & Reed, S. E. (Eds.). (1992). *Strain gage users' handbook*. Springer.

Hartl, D., Mooney, J., et al. (2010). Use of a Ni60Ti shape memory alloy for active jet engine chevron application: II. Experimentally validated numerical analysis. *Smart Materials and Structures 19*(1), 015021.

Hassan, J. M., Brown, T. J., et al. (2011). Design Field Bending Moment Coefficients for Interior Reinforced Concrete Flat Plates. *Practice Periodical on Structural Design and Construction 16*(1). pp. 34-45

Hibbitt, D., Karlsson, B., & Sorensen, P. (2002). Getting Started with ABAQUS/Explicit–Interactive Version. *Hibbitt, Karlsson and Sorensen Inc., Rhode Island*.

Hibbit, K. (2007). Sørensen, Abaqus standard user's manual version 6.7. 1, *Providence, Rhode Island*.

High, J. W., Wilkie, W. K., et al. (2003). Method of fabricating NASA-standard macro-fibre composite piezoelectric actuators *National Aeronautics and Space Administration*, Langley Research Center, USA.

Hirsch, C. (2007). *Numerical computation of internal and external flows: The fundamentals of computational fluid dynamics.*Vol. 1, Butterworth-Heinemann.

Huang, Y. a. Boyle, K. (2008). *Antennas from theory to practice* (1st ed.). England: John Wiley & Sons, Ltd.

Inman, D. J. and Ruggiero, E. J. (2000). Concept Paper A07*Composite Materials with Embedded Sensing*.

Jha, A. K. and Inman, D. J. (2003). Vibration control of a gossamer toroidal structure using smart material actuators and sensors. *Smart Structures and Materials*., International Society for Optics and Photonics, pp. 475-486.

Kent, R. M. and Murphy, D. A. (2000). *Health monitoring system technology assessments: Cost benefits analysis.* National Aeronautics and Space Administration, Langley Research Center.

Kessler, S. S. (2005, November). Certifying a structural health monitoring system: Characterizing durability, reliability and longevity. In *Proceedings of the 1st International Forum on Integrated Systems Health Engineering and Management in Aerospace, Napa, CA* (pp. 7-10).

Kessler, S. S., Amaratunga, K., & Wardle, B. L. (2005, September). An assessment of durability requirements for aircraft structural health monitoring sensors. In *Proceedings of the 5th International Workshop on Structural Health Monitoring, Stanford, CA* (pp. 12-14).

Kessler, S. S. (2002). *Piezoelectric-based in-situ damage detection of composite materials for structural health monitoring systems* (Doctoral dissertation, Massachusetts Institute of Technology).

Khoo, L. M. M. P. R., and Jadhav, P. (2004). Structural damage assessment using vibration modal analysis. *Structural Health Monitoring 3*. pp. 177-194

Kim, R. Y. (1979). Fracture of composite laminates by three-point bend. *Experimental Mechanics 19*(2). pp. 50-55

Konka, H. P. (2010). *Characterization of composite piezoelectric materials for smart joint applications* (Doctoral dissertation, Faculty of the Louisiana State University and Agricultural and Mechanical College in partial fulfillment of the requirements for degree of Master of Science in Mechanical Engineering In The Department of Mechanical Engineering by Hari Prasad Konka B. Tech, Jawaharlal Nehru Technological University).

Kothari, R. M. (2008). *Design and analysis of multifunctional structures for embedded electronics in unmanned aerial vehicles*.

Kulkarni, S. S., and Achenbach, J. D. (2008). Structural Health Monitoring and Damage Prognosis in Fatigue. *Structural Health Monitoring 7*(1). pp. 37-49

Lalande, F., Rogers, C. A., Childs, B. W., & Chaudhry, Z. A. (1996, May). High-frequency impedance analysis for NDE of complex precision parts. In *1996 Symposium on Smart Structures and Materials*, International Society for Optics and Photonics, pp. 237-243.

Lee, J.-R., Chong, S. Y., et al. (2011). A lasing wavelength stabilized simultaneous multipoint acoustic sensing system using pressure-coupled fibre Bragg gratings. *Optics and Lasers in Engineering 49*(1). pp. 110-120

Lee, J.-R., and Tsuda, H. (2005). A novel fibre Bragg grating acoustic emission sensor head for mechanical tests. *Scripta materialia 53*(10). pp. 1181-1186

Lehmann, M., Büter, A., Frankenstein, B., Schubert, F., & Brunner, B. (2006). Monitoring System for Delamination Detection–Qualification of Structural Health Monitoring (SHM) Systems. In *Conference on Damage in Composite Material CDCM*, pp. 1-10.

Liang, C., Sun, S., et al. (1994). Coupled electro-mechanical analysis of adaptive material systems—determination of the actuator power consumption and system energy transfer. *Journal of Intelligent Material Systems and Structures 5*(1). pp. 12-20

Lin, B., Giurgiutiu, V., et al. (2010). Durability and survivability of piezoelectric wafer active sensors on metallic structure. *AIAA Journal 48*(3). pp. 635-643

Lin, Y., and Sodano, H. A. (2008). Concept and model of a piezoelectric structural fibre for multifunctional composites. *Composites Science and Technology 68*(7-8). pp. 1911-1918

Lindvall, P., Bergstrom, P. et al. (2005). Hypofractionated conformal stereotactic radiotherapy alone or in combination with whole-brain radiotherapy in patients with cerebral metastases. *International Journal of Radiation Oncology Biology Physics 61*(5). pp. 1460-1466

Lingyu, Y., and Giurgiutiu, V. (2008). Multi-mode Damage Detection Methods with Piezoelectric Wafer Active Sensors. *Journal of Intelligent Material Systems and Structures 20*(11). pp. 1329-1341

Lloyd, J. M. (2004). *Electrical properties of macro-fibre composite actuators and sensors*, (doctoral dissertation), Virginia Polytechnic Institute and State University.

Loh, K. J., and Lynch, J. P. (2006). Miniaturized Sensors Employing Micro-and Nanotechnologies. *Encyclopedia of Structural Health Monitoring*.

Loh, K. J. H. (2008). *Development of Multifunctional Carbon Nanotube Nanocomposite Sensors for Structural Health Monitoring* (Doctoral dissertation, The University of Michigan).

Lynch, J. P., Huo, T.-C., et al. (2012). *Electrical impedance tomography of nanoengineered thin films.* U.S. Patent No. 8,159,235. 17 Apr. 2012.

Lynch, J. P., Kamat, V., Li, V. C., Flynn, M., Sylvester, D., Najafi, K. & Ozdemir, T. (2009, March). Overview of a cyber-enabled wireless monitoring system for the protection and management of critical infrastructure systems. In *SPIE Smart Structures and Materials+ Nondestructive Evaluation and Health Monitoring* . International Society for Optics and Photonics, pp. 72940L-72940L

Lynch, J. P. and Loh K. J. (2006). A summary review of wireless sensors and sensor networks for structural health monitoring. *Shock and Vibration Digest 38*(2). pp. 91-130

Mahdi, S. (2005). Structural Repair of Composite Structural Armor. *Journal of Composite Materials 39*(19). pp. 1695-1717

Mallick, P. (1993). *Fibre-reinforced composites: materials, manufacturing, and design,* CRC press.

Mascarenas, D. D. L. (2006). *Development of an impedance method based wireless sensor node for monitoring of bolted joint preload*, (doctoral dissertation),University of California, San Diego.

Matveenko, V. P., Kligman, E., et al. (2012). Simulation and optimization of dynamic characteristics of piezoelectric smart structures. *Physical Mesomechanics 15*(3-4). pp. 190-199

Mehdizadeh, M. (2009). *Curvature mode shape analyses of damage in structures*. (Master thesis), RMIT University, Melbourne, Australia.

Mehdizadeh, M., John, S., et al. (2012). Delineation of structural damage from piezo-fibre-based sensor degradation. I*nternational Journal of Engineering Science 4(1)*.

Mehdizadeh, M., John, S., et al. (2011). Characterization of Piezo Fibre-Based Sensors Responses in Multifunctional Composites. *Advanced Materials Research 409*. pp. 633-638

Mieloszyk, M., Skarbek, L. et al. (2011). Application of fibre Bragg grating sensors for structural health monitoring of an adaptive wing. *Smart Materials and Structures 20*(12),125014

Moheimani, S. O. R., and Fleming, A. J., (2006). *Piezoelectric transducers for vibration control and damping*. Location: Springer.

Moslem, K. N. R. (2002). Structural Damage Detection by Genetic Algorithm. *AIAA Journal Vol* (40). pp. 1395-1401

Mouritz, A., Townsend, C., et al. (2000). Non-destructive detection of fatigue damage in thick composites by pulse-echo ultrasonics. *Composites Science and Technology 60*(1). pp. 23-32

Moutier, J., Fois, M., et al. (2009). Characterization of carbon/epoxy materials for structural repair of carbon/BMI structures. *Composites Part B: Engineering 40*(1). pp. 1-6

Mudarri, T. C. (2003). *A Novel Use for Ionic Polymer Transducers for Ionic Sensing in Liquid*, (doctoral dissertation), Virginia Polytechnic Institute and State University. Location and publisher?

Mudupu, V., Trabia, M., et al. (2008). Design and validation of a fuzzy logic controller for a smart projectile fin with a piezoelectric macro-fibre composite bimorph actuator. *Smart Materials and Structures 17*(3). page? 035034

Murri, G. B. (2006). *Effect of Embedded Piezoelectric Sensors on Fracture Toughness and Fatigue Resistance of Composite Laminates Under Mode I Loading*.

Murthy, P., and Phoenix L. (2009). *Composite overwrap pressure vessels: mechanics and stress rupture lifing philosophy*,

Nagata, Y., Park, S., & Ming, A. (2006, December). Structural Sensing and Actuation Utilizing Macro Fiber Composite. In *Robotics and Biomimetics, 2006. ROBIO'06. IEEE International Conference on*, pp. 1275-1280, IEEE.

Natarajan, S., Bordas, S., et al. (2009). Numerical integration over arbitrary polygonal domains based on Schwarz–Christoffel conformal mapping. *International Journal for Numerical Methods in Engineering 80*(1). pp. 103-134

Nguyen, C. H. (2006). A Comparison of Dynamic Piezoactuation of Fibre-based Actuators and Conventional PZT Patches. *Journal of Intelligent Material Systems and Structures 17*(1). pp. 45-55

Nokes, J., and Cloud, G. (1993). The application of interferometric techniques to the nondestructive inspection of fibre-reinforced materials. *Experimental Mechanics 33*(4). pp. 314-319

Oishi, R., and Nagai, H. (2005). Strain sensors of shape memory alloys using acoustic emissions. *Sensors and Actuators A: Physical 122*(1). pp. 39-44

Overly, T. G., Park, G., et al. (2007). *Compact hardware development for SHM and sensor diagnostics using admittance measurements*. SEM International Modal Analysis Conference.

Overly, T. G. S., Park, G., et al. (2008). Development of an extremely compact impedance-based wireless sensing device. *Smart Materials and Structures 17*,065011

Pandey, A., Biswas, M., et al. (1991). Damage detection from changes in curvature mode shapes. *Journal of Sound and Vibration 145*(2). pp. 321-332.

Paradies, R., and Melnykowycz, M. (2007). Numerical Stress Investigation for Piezoelectric Elements with a Circular Cross Section and Interdigitated Electrodes. *Journal of Intelligent Material Systems and Structures 18*(9). pp. 963-972

Paradies, R., and Schläpfer, B. (2009). Finite element modeling of piezoelectric elements with complex electrode configuration. *Smart Materials and Structures 18*(2). 025015

Park, G., Farrar, C. R., Rutherford, A. C., & Robertson, A. N. (2006). Piezoelectric active sensor self-diagnostics using electrical admittance measurements. *Journal of Vibration and Acoustics*, *128*(4), pp. 469-476.

Park, G., Ruggiero, E. et al. (2002). Dynamic testing of inflatable structures using smart materials. *Smart Materials and Structures 11*(1). pp. 147

Park, G., Sohn, H., et al. (2003). Overview of piezoelectric impedance-based health monitoring and path forward. *Shock and Vibration Digest 35*(6). pp. 451-464

Park, S., Grisso, B. L., et al. (2007). MFC-Based Structural Health Monitoring Using a Miniaturized Impedance Measuring Chip for Corrosion Detection. *Research in Nondestructive Evaluation 18*(2). pp. 139-150

Patnaik, P. C., & Chen, W. R. (2006). *Advanced materials and multifunctional structures for aerospace vehicles*. National Research Council Of Canada Ottawa (Ontario) Inst For Aerospace Research.

Pavelko, V., Ozolinsh, I., et al. (2011). *Structural Health Monitoring of Aircraft Structure by Methods of Electromechanical Impedance*. Proceedings of the 6th NDT in Progress 2011, International Workshop of NDT Experts. \

Peairs, D. M., Inman, D. J., et al. (2007). Circuit analysis of impedance-based health monitoring of beams using spectral elements. *Structural Health Monitoring 6*(1). pp. 81-94

Piefort, V. (2001). *Finite element modelling of piezoelectric active structures*(Doctoral dissertation, Université Libre de Bruxelles).

Preumont, A. (2011). *Vibration control of active structures: an introduction* (Vol. 179). Springer.

Qu, F. Z. Z. D. L., and Wang X. (2004). Substcutural Damaged Detection using Neural Network and ICA. *Advances in Neural Network 3173*. pp. 750-754

Raich, A. L. T. (2003). Benefits of Implicit Redundant Geneti Algirithm for Structural Damage Detection in Noisy Environment. *Genetic and Evolutionary Computation 2724*. pp. 319-339

Ren, P., & Du, Z. (Eds.). (2013). *Manufacture Engineering and Environment Engineering (set)* (Vol. 84). WIT Press.

RTCA (Firm). SC-135. (2010). *Environmental Conditions and Test Procedures for Airborne Equipment*. RTCA.

Rhodes, M. L., and Robertson, D. D. (1996). Computers in surgery and therapeutic procedures. *Computer 29*(1). pp. 20-23

Rosiek, M., Martowicz, A., et al. (2010). Electromechanical impedance method for damage detection in mechanical structures. *Proceedings of 11th IMEKO TC 10*. pp. 18-20.

Rossetti Jr, G. A., Pizzochero, A., & Bent, A. A. (2000). Recent advances in active fiber composites technology. In *Applications of Ferroelectrics, 2000. ISAF 2000. Proceedings of the 2000 12th IEEE International Symposium,* (Vol. 2, pp. 753-756). IEEE.

Santoni, G. (2010). *Fundamental studies in the Lamb-wave interaction between piezoelectric wafer active sensor and host structure during structural health monitoring* (Doctoral dissertation, University of South Carolina).

Schijve, J. (2009). Fatigue damage in aircraft structures, not wanted, but tolerated? *International Journal of Fatigue 31*(6). pp. 998-1011

Schwartz, M. (2009). *Smart Materials*. USA: CRC Press.

Shen, M.-H., and Grady, J. (1992). Free vibrations of delaminated beams. *AIAA Journal 30*(5). pp. 1361-1370

Shi, Z. Y. L. S. S. (2000). Structural Damaged Detection From Modal Strain Energy Change. *Journal Of Engineering Mechanics 126*(12). pp. 1216-1223

Shiraki, K., Sagawa, S., et al. (1988). Independence of brain and tympanic temperatures in an unanesthetized human. *Journal of Applied Physiology 65*(Copyright 1989, IEE). pp. 482-486

Shirui, W., and Chao, Y. (2008). A circuit design for impedance-based structural health monitoring. *Journal of Intelligent Material Systems and Structures 19*(9). pp. 1029-1040

Shull, P. J. (2002). *Nondestructive evaluation: theory, techniques, and applications*. CRC press.
Sirohi, J., and Chopra, I. (2000). Fundamental understanding of piezoelectric strain sensors. *Journal of Intelligent Material Systems and Structures 11*(4). pp. 246-257

Sittler, F., Brunel, D., et al. (2013). Process and Apparatus for Reducing EMI in the RF Subsystem of a Wireless Communication System, U.S. Patent Application 13/574,965.

Sodano, H. A. (2003). *Macro-fibre composites for sensing, actuation and power generation.* Virginia Polytechnic Institute and State University,, USA.

Sodano, H. A., Inman, D. J., et al. (2005). Comparison of piezoelectric energy harvesting devices for recharging batteries. *Journal of Intelligent Material Systems and Structures 16*(10). pp. 799-807

Sodano, H. A., Park, G., et al. (2004). An investigation into the performance of macro-fibre composites for sensing and structural vibration applications. *Mechanical Systems and Signal Processing* **18**(3): pp. 683-697.

Soh, C. K. (2008). Damage Prognosis For Aerospace, Civil And Mechanical Systems. *Journal of Sound and Vibration 309*(3-5). pp. 898-899

Sohn, H., Park, G., et al. (2004). Wavelet-based active sensing for delamination detection in composite structures. *Smart Materials and Structures 13*(1). pp. 153

Sue, M. K. (2011). Radio frequency interference at the geostationary orbit. *Jet Propulsion Lab. Report*, reterived.

Sun, F., Roger, C. A., & Liang, C. (1995, April). Structural frequency response function acquisition via electric impedance measurement of surface-bonded piezoelectric sensor/actuator. In *Proceedings of 36th AIAA/ASME/ASCE/AHS/ASC Structures, Structural Dynamics, and Materials Conference*, pp. 3450-3461

Systèmes, D. (2010). *Abaqus 6.10: Analysis user's manual*. Providence, RI: Dassault Systèmes Simulia Corp.

Takeda, N., & Minakuchi, S. (2012, January). Smart aircraft composite structures with embedded small-diameter optical fiber sensors. In *Asia Pacific Optical Sensors Conference* International Society for Optics and Photonics, pp. 835101-835101.

Takeda, N., Okabe, Y. et al. (2005). Development of smart composite structures with small-diameter fibre Bragg grating sensors for damage detection: Quantitative evaluation of delamination length in CFRP laminates using Lamb wave sensing. *Composites Science and Technology 65*(15). pp. 2575-2587

Tang, L., Yang, Y., et al. (2008). Optimizing efficiency of energy harvesting by macro-fibre composites. Vol 726, pp. 808-809.

Thomas, J. P., Baucom, J. N. et al. (2012). Autophagous multifunction structure-power system, *U.S. Patent No. 8,141,822*, Washington, DC: U.S. Patent and Trademark Office.

Trindade, M. A., & Benjeddou, A. (2012). Parametric analysis of effective material properties of thickness-shear piezoelectric macro-fibre composites.*Journal of the Brazilian Society of Mechanical Sciences and Engineering*,*34*(SPE), 352-361.

Vepa, R. (2010). *Dynamics of smart structures.* John Wiley & Sons.

Wait, J. R., & Todd, M. D (2006). *Validation of Macro Fibre Composites as Strain Sensors.* Department of Structural Engineering, University of California, San Diego.

Wang, Y., Ye, Z., et al. (2012). New trends in impedimetric biosensors for the detection of foodborne pathogenic bacteria. *Sensors 12*(3). pp. 3449-3471

Warminski, J., Bochenski, M., et al. (2011). Active suppression of nonlinear composite beam vibrations by selected control algorithms. *Communications in Nonlinear Science and Numerical Simulation 16*(5). pp. 2237-2248

Wilbur, M. L., Mirick, P. H., et al. (2002). Vibratory loads reduction testing of the NASA/Army/MIT active twist rotor. *Journal of the American Helicopter Society 47*(2). pp. 123-133

Wildschek, A., Havar, T., et al. (2010). An all-composite, all-electric, morphing trailing edge device for flight control on a blended-wing-body airliner. *Proceedings of the Institution of Mechanical Engineers, Part G: Journal of Aerospace Engineering 224*(1). pp. 1-9

Wilkie, W., Bryant, R., et al. (2012). Piezoelectric macro-fibre composite actuator and manufacturing method, EP Patent 1,983,584.

Wilkie, W. K., High, J., & Bockman, J. (2002, June). Reliability testing of NASA piezocomposite actuators. In *Proceedings of the 8th International Conference on New Actuators, Bremen, Germany*, pp. 10-12.

Wilkie, W. K., Bryant, R. G., High, J. W., Fox, R. L., Hellbaum, R. F., Jalink Jr, A., ... & Mirick, P. H. (2000, June). Low-cost piezocomposite actuator for structural control applications. In *SPIE's 7th Annual International Symposium on Smart Structures and Materials*. International Society for Optics and Photonics, pp 323-334.

Williams, R. B. (2004). *Nonlinear mechanical and actuation characterization of piezoceramic fiber composites* (Doctoral dissertation, Virginia Polytechnic Institute and State University).
Williams, R. B. (2006). Nonlinear Response of the Macro Fibre Composite Actuator to Monotonically Increasing Excitation Voltage. *Journal of Intelligent Material Systems and Structures 17*(7). pp. 601-608

Williams, R. B., Grimsley, B. W., et al. (2002). Manufacturing and mechanics-based characterization of macro fibre composite actuators. *Adaptive Structures and Materials Systems 22*. pp. 79-89

Xu, B., & Giurgiutiu, V. (2005, May). Efficient electromechanical (E/M) impedance measuring method for active sensor structural health monitoring. In *Smart Structures and Materials* (pp. 271-280). International Society for Optics and Photonics.

Yan, A. M. G. J. C. (2005). Structural Damage Localization by Combining Flexibility and Stiffness Methods. *Engineering Structures* (27). pp. 1752-1761

Yan, Y., L. Cheng, et al. (2007). Development in vibration-based structural damage detection technique. *Mechanical Systems and Signal Processing 21*(5). pp. 2198-2211

Yang, Y., B. S. Divsholi, et al. (2010). Strain Transfer Models for Macrofibre-Composite Strain Actuators. *Materials and Manufacturing Processes 25*(4). pp. 237-242

Yang, Y., Liu, H., Annamdas, V. G. M., & Soh, C. K. (2009). Monitoring damage propagation using PZT impedance transducers. *Smart Materials and Structures*, *18*(4), 045003.

Yarlagadda, S. (2003). *Multifunctional Materials and Structures*. Delaware Univ Newark Center For Composite Materials.

Yeates, K., Lynch, S. B., & Dabov, T. (2013). *U.S. Patent No. 8,457,333*. Washington, DC: U.S. Patent and Trademark Office.

Zhang, X. P., Ye, L., Mai, Y. W., & Galea, S. (2004). Fatigue Crack Growth And Piezoelectric Property Decay Induced By Cyclic Electric Fields For An Actuation Piezoceramic. In *Structural Integrity and Fracture International Conference (SIF'04).*, pp. 395-400).

Zhao, Z., Wang, S., & You, C. (2008). A circuit design for remote structural health monitoring. In *Proceedings of IMAC-XXVI, A Conference & Exposition on Structural Dynamics* pp. 4-7.

Zou, Y., L. Tong, et al. (2000). Vibration-based model-dependent damage (delamination) identification and health monitoring for composite structures — a review. *Journal of Sound and Vibration 230*(2). pp 357-378

APPENDIX A: FEM Simulation Codes

As it was mentioned in chapter 4, the ABAQUS software package was used to model simulate and analyse the composite structure and MFC transducer. This software package has the ability to visualise the pre-processing, solving and post-processing steps. However, some of the advanced features of FEM are still code-based and cannot be applied directly through ABAQUS or other software packages. Furthermore, as the analysis of the detailed MFC simulation presented in Chapter 4 required HPC (High-Performance-Computer), the FEM simulations codes which has all the details of geometric, loading and boundary conditions should be submitted to the HPC cluster. These FEM codes which were used in this project to simulate the MFC transducer as well as carbon/epoxy structure in both intact and damaged statuses are presented in this section. These codes are also presented for different damage scenarios which were investigated in this research.

A.1 ABAQUS Codes for Healthy MFC Sensor

*Heading

*Node

*Element, type=C3D8R

*Element, type=C3D8E

*Element, type=C3D8R

*Element, type=C3D8E

*Element, type=C3D8R

*Element, type=C3D8E

*Element, type=C3D8R

*Element, type=C3D8E

*Element, type=C3D8R

*Element, type=C3D8E

*Element, type=C3D8R

*Element, type=C3D8E

*Element, type=C3D8R

*Element, type=C3D8E

*Element, type=C3D8R

*Element, type=C3D8E

*Element, type=C3D8R

*Element, type=C3D8E

*Element, type=C3D8R

*Element, type=C3D8E

*Element, type=C3D8R

*Element, type=C3D8E

*Element, type=C3D8R

*Element, type=C3D8E

*Element, type=C3D8R

*Element, type=C3D8E

*Element, type=C3D8R

*Element, type=C3D8E

*Element, type=C3D8R

*Element, type=C3D8E

*Element, type=C3D8R

*Element, type=C3D8E

*Element, type=C3D8R

*Element, type=C3D8E

*Element, type=C3D8R

*Element, type=C3D8E

*Element, type=C3D8R

*Element, type=C3D8E

*Element, type=C3D8R

*Element, type=C3D8E

*Element, type=C3D8R

*Element, type=C3D8E

*Element, type=C3D8R

*Element, type=C3D8E

*Element, type=C3D8R

*Element, type=C3D8E

*Element, type=C3D8R

*Element, type=C3D8E

*Element, type=C3D8R

*Nset, nset="ASSEMBLY_SENSOR-1_ELECTRODE SIDE"

*Nset, nset="ASSEMBLY_SENSOR-1_SENSOR BOTTIM SIDE"

*Nset, nset=ASSEMBLY_SENSOR-1_ELECTRODEN

*Nset, nset=ASSEMBLY_SENSOR-1_ELECTRODEP

*Nset, nset=ASSEMBLY_SENSOR-1_ELN_M

*Nset, nset=ASSEMBLY_SENSOR-1_ELP_M

*Nset, nset=ASSEMBLY_SENSOR-1_EPOXY

*Nset, nset=ASSEMBLY_SENSOR-1_FIBERS

*Nset, nset=ASSEMBLY_SENSOR-1_SENSOR

*Elset, elset="ASSEMBLY_SENSOR-1_ELECTRODE SIDE"

*Elset, elset="ASSEMBLY_SENSOR-1_SENSOR BOTTIM SIDE"

*Elset, elset=ASSEMBLY_SENSOR-1_ELECTRODEN

*Elset, elset=ASSEMBLY_SENSOR-1_ELECTRODEP

*Elset, elset=ASSEMBLY_SENSOR-1_EPOXY

*Elset, elset=ASSEMBLY_SENSOR-1_FIBERS

*Elset, elset=ASSEMBLY_SENSOR-1_SENSOR

*Elset, elset=ASSEMBLY_SENSOR-1__SENS-BOT_S1

*Elset, elset=ASSEMBLY_SENSOR-1__SENS-BOT_S2

*Elset, elset=ASSEMBLY_SENSOR-1__SENS-BOT_S4

*Node

*Element, type=C3D20

*Nset, nset="ASSEMBLY_STRUCTURE-1_STRUCTURE TOP"

*Nset, nset="ASSEMBLY_STRUCTURE-1_SUPPORTING PIN"

*Nset, nset=ASSEMBLY_STRUCTURE-1_LOADLINE

*Nset, nset=ASSEMBLY_STRUCTURE-1_STRUCTURE

*Elset, elset="ASSEMBLY_STRUCTURE-1_STRUCTURE TOP"

*Elset, elset="ASSEMBLY_STRUCTURE-1_SUPPORTING PIN"

*Elset, elset=ASSEMBLY_STRUCTURE-1_LOADLINE

*Elset, elset=ASSEMBLY_STRUCTURE-1_STRUCTURE

*Elset, elset=ASSEMBLY_STRUCTURE-1__STR_TOP_S4

*Elset, elset=ASSEMBLY_STRUCTURE-1__STR_TOP_S6

*tie, name=CONSTRAINT-1, positiontolerance=1e-05, norotation, adjust=NO

*surface, type=ELEMENT, name=ASSEMBLY_SENSOR-1_SENS-BOT

*surface, type=ELEMENT, name=ASSEMBLY_STRUCTURE-1_STR_TOP

*tie, name=CONSTRAINT-1, positiontolerance=1e-05, norotation, adjust=NO

*surface, type=ELEMENT, name=ASSEMBLY_SENSOR-1_SENS-BOT

*surface, type=ELEMENT, name=ASSEMBLY_STRUCTURE-1_STR_TOP

*surface, type=ELEMENT, name=ASSEMBLY_SENSOR-1_SENS-BOT

*surface, type=ELEMENT, name=ASSEMBLY_STRUCTURE-1_STR_TOP

*tie, name=CONSTRAINT-1, positiontolerance=1e-05, norotation, adjust=NO

*tie, name=CONSTRAINT-1, positiontolerance=1e-05, norotation, adjust=NO

*orientation, name=ASSEMBLY_SENSOR-1_ORI-1

*orientation, name=ASSEMBLY_STRUCTURE-1_ORI-1

*material, name=COMPOSITE

*density

*elastic, type=ENGINEERINGCONSTANTS

*material, name=EPOXY

*density

*elastic

*material, name=PIEZO

*density

*dielectric, type=ORTHOTROPIC

*elastic, type=ENGINEERINGCONSTANTS

*piezoelectric, type=E

*orientation, name=ASSEMBLY_SENSOR-1_ORI-1

*orientation, name=ASSEMBLY_STRUCTURE-1_ORI-1

*solidsection, elset=ASSEMBLY_SENSOR-1_EPOXY, orientation=ASSEMBLY_SENSOR-1_ORI-1, material=EPOXY

*solidsection, elset=ASSEMBLY_SENSOR-1_FIBERS, orientation=ASSEMBLY_SENSOR-1_ORI-1, material=PIEZO

*solidsection, elset=ASSEMBLY_STRUCTURE-1_STRUCTURE, layup=CARBON/EPOXY, composite,

*boundary

*boundary

*boundary

*tie, name=CONSTRAINT-1, positiontolerance=1e-05, norotation, adjust=NO

*tie, name=CONSTRAINT-1, positiontolerance=1e-05, norotation, adjust=NO

*tie, name=CONSTRAINT-1, positiontolerance=1e-05, norotation, adjust=NO

*equation

*equation

*solidsection, elset=ASSEMBLY_SENSOR-1_EPOXY, orientation=ASSEMBLY_SENSOR-1_ORI-1, material=EPOXY

*solidsection, elset=ASSEMBLY_SENSOR-1_FIBERS, orientation=ASSEMBLY_SENSOR-1_ORI-1, material=PIEZO

*solidsection, elset=ASSEMBLY_STRUCTURE-1_STRUCTURE, layup=CARBON/EPOXY, composite,

*surface, type=ELEMENT, name=ASSEMBLY_SENSOR-1_SENS-BOT

*surface, type=ELEMENT, name=ASSEMBLY_STRUCTURE-1_STR_TOP

*tie, name=CONSTRAINT-1, positiontolerance=1e-05, norotation, adjust=NO

285

*output, field, timeinterval=0.01

*output, history, variable=PRESELECT

*output, field, timeinterval=0.01

*output, history, variable=PRESELECT

*elementoutput, directions=YES

*elementoutput, directions=YES

*output, field, timeinterval=0.01

*output, history, variable=PRESELECT

*output, field, timeinterval=0.01

*output, history, variable=PRESELECT

*elementoutput, directions=YES

*elementoutput, directions=YES

*output, field, timeinterval=0.01

*output, history, variable=PRESELECT

*output, field, timeinterval=0.01

*output, history, variable=PRESELECT

*elementoutput, directions=YES

*elementoutput, directions=YES

*amplitude, name=AMP-1, definition=SMOOTHSTEP

*amplitude, name=AMP-2, definition=PERIODIC

*Step, name=Step-1, nlgeom=YES, inc=100000

*output, field, timeinterval=0.01

*output, history, variable=PRESELECT

*Step, name=Step-2, nlgeom=YES, inc=100000

*output, field, timeinterval=0.01

*output, history, variable=PRESELECT

*Step, name=Step-1, nlgeom=YES, inc=100000

*Step, name=Step-2, nlgeom=YES, inc=100000

```
*Step, name=Step-1, nlgeom=YES, inc=100000

*dynamic, haftol=400

*boundary

*output, field, timeinterval=0.01

*elementoutput, directions=YES

*contactoutput

*output, history, variable=PRESELECT

*endstep

*Step, name=Step-2, nlgeom=YES, inc=100000

*dynamic, haftol=400

*boundary, amplitude=AMP-2

*output, field, timeinterval=0.01

*elementoutput, directions=YES

*contactoutput

*output, history, variable=PRESELECT

*endstep


*boundary

*boundary

*Step, name=Step-1, nlgeom=YES, inc=100000

*dynamic, haftol=400

*boundary

*output, field, timeinterval=0.01

*nodeoutput

*output, history, variable=PRESELECT

*endstep

*Step, name=Step-2, nlgeom=YES, inc=100000

*dynamic, haftol=400
```

*boundary, amplitude=AMP-2

*output, field, timeinterval=0.01

*nodeoutput

*output, history, variable=PRESELECT

*endstep

A2. ABAQUS Codes for MFC actuator

*Heading

*Node

*Element, type=C3D8R

*Element, type=C3D8E

*Element, type=C3D8R

*Element, type=C3D8E

*Element, type=C3D8R

*Element, type=C3D8E

*Element, type=C3D8R

*Element, type=C3D8E

*Element, type=C3D8R

*Element, type=C3D8E

*Element, type=C3D8R

*Element, type=C3D8E

*Element, type=C3D8R

*Element, type=C3D8E

*Element, type=C3D8R

*Element, type=C3D8E

*Element, type=C3D8R

*Element, type=C3D8E

*Element, type=C3D8R

*Element, type=C3D8E

*Element, type=C3D8R

*Element, type=C3D8E

*Element, type=C3D8R

*Element, type=C3D8E

*Element, type=C3D8R

*Element, type=C3D8E

*Element, type=C3D8R

*Element, type=C3D8E

*Element, type=C3D8R

*Element, type=C3D8E

*Element, type=C3D8R

*Element, type=C3D8E

*Element, type=C3D8R

*Element, type=C3D8E

*Element, type=C3D8R

*Element, type=C3D8E

*Element, type=C3D8R

*Element, type=C3D8E

*Element, type=C3D8R

*Element, type=C3D8E

*Element, type=C3D8R

*Element, type=C3D8E

*Element, type=C3D8R

*Element, type=C3D8E

*Element, type=C3D8R

*Element, type=C3D8E

*Element, type=C3D8R

*Element, type=C3D8E

*Element, type=C3D8R

*Nset, nset="ASSEMBLY_SENSOR-1_ELECTRODE SIDE"

*Nset, nset="ASSEMBLY_SENSOR-1_SENSOR BOTTIM SIDE"

*Nset, nset=ASSEMBLY_SENSOR-1_ELECTRODEN

*Nset, nset=ASSEMBLY_SENSOR-1_ELECTRODEP

*Nset, nset=ASSEMBLY_SENSOR-1_ELN_M

*Nset, nset=ASSEMBLY_SENSOR-1_ELP_M

*Nset, nset=ASSEMBLY_SENSOR-1_EPOXY

*Nset, nset=ASSEMBLY_SENSOR-1_FIBERS

*Nset, nset=ASSEMBLY_SENSOR-1_SENSOR

*Elset, elset="ASSEMBLY_SENSOR-1_ELECTRODE SIDE"

*Elset, elset="ASSEMBLY_SENSOR-1_SENSOR BOTTIM SIDE"

*Elset, elset=ASSEMBLY_SENSOR-1_ELECTRODEN

*Elset, elset=ASSEMBLY_SENSOR-1_ELECTRODEP

*Elset, elset=ASSEMBLY_SENSOR-1_EPOXY

*Elset, elset=ASSEMBLY_SENSOR-1_FIBERS

*Elset, elset=ASSEMBLY_SENSOR-1_SENSOR

*Elset, elset=ASSEMBLY_SENSOR-1__SENS-BOT_S1

*Elset, elset=ASSEMBLY_SENSOR-1__SENS-BOT_S2

*Elset, elset=ASSEMBLY_SENSOR-1__SENS-BOT_S4

*Node

*Element, type=C3D20

*Nset, nset="ASSEMBLY_STRUCTURE-1_STRUCTURE TOP"

*Nset, nset="ASSEMBLY_STRUCTURE-1_SUPPORTING PIN"

*Nset, nset=ASSEMBLY_STRUCTURE-1_LOADLINE

*Nset, nset=ASSEMBLY_STRUCTURE-1_STRUCTURE

*Elset, elset="ASSEMBLY_STRUCTURE-1_STRUCTURE TOP"

*Elset, elset="ASSEMBLY_STRUCTURE-1_SUPPORTING PIN"

*Elset, elset=ASSEMBLY_STRUCTURE-1_LOADLINE

*Elset, elset=ASSEMBLY_STRUCTURE-1_STRUCTURE

*Elset, elset=ASSEMBLY_STRUCTURE-1__STR_TOP_S4

*Elset, elset=ASSEMBLY_STRUCTURE-1__STR_TOP_S6

*tie, name=CONSTRAINT-1, positiontolerance=1e-05, norotation, adjust=NO

*surface, type=ELEMENT, name=ASSEMBLY_SENSOR-1_SENS-BOT

*surface, type=ELEMENT, name=ASSEMBLY_STRUCTURE-1_STR_TOP

*tie, name=CONSTRAINT-1, positiontolerance=1e-05, norotation, adjust=NO

*surface, type=ELEMENT, name=ASSEMBLY_SENSOR-1_SENS-BOT

*surface, type=ELEMENT, name=ASSEMBLY_STRUCTURE-1_STR_TOP

*surface, type=ELEMENT, name=ASSEMBLY_SENSOR-1_SENS-BOT

*surface, type=ELEMENT, name=ASSEMBLY_STRUCTURE-1_STR_TOP

*tie, name=CONSTRAINT-1, positiontolerance=1e-05, norotation, adjust=NO

*tie, name=CONSTRAINT-1, positiontolerance=1e-05, norotation, adjust=NO

*orientation, name=ASSEMBLY_SENSOR-1_ORI-1

*orientation, name=ASSEMBLY_STRUCTURE-1_ORI-1

*material, name=COMPOSITE

*density

*elastic, type=ENGINEERINGCONSTANTS

*material, name=EPOXY

*density

*elastic

*material, name=PIEZO

*density

*dielectric, type=ORTHOTROPIC

*elastic, type=ENGINEERINGCONSTANTS

*piezoelectric, type=E

*orientation, name=ASSEMBLY_SENSOR-1_ORI-1

*orientation, name=ASSEMBLY_STRUCTURE-1_ORI-1

*solidsection, elset=ASSEMBLY_SENSOR-1_EPOXY, orientation=ASSEMBLY_SENSOR-1_ORI-1, material=EPOXY

*solidsection, elset=ASSEMBLY_SENSOR-1_FIBERS, orientation=ASSEMBLY_SENSOR-1_ORI-1, material=PIEZO

*solidsection, elset=ASSEMBLY_STRUCTURE-1_STRUCTURE, layup=CARBON/EPOXY, composite,

*boundary

*boundary

*boundary, op=NEW, real

*boundary, op=NEW, real

*boundary, op=NEW, real

*tie, name=CONSTRAINT-1, positiontolerance=1e-05, norotation, adjust=NO

*tie, name=CONSTRAINT-1, positiontolerance=1e-05, norotation, adjust=NO

*tie, name=CONSTRAINT-1, positiontolerance=1e-05, norotation, adjust=NO

*equation

*equation

*solidsection, elset=ASSEMBLY_SENSOR-1_EPOXY, orientation=ASSEMBLY_SENSOR-1_ORI-1, material=EPOXY

*solidsection, elset=ASSEMBLY_SENSOR-1_FIBERS, orientation=ASSEMBLY_SENSOR-1_ORI-1, material=PIEZO

*solidsection, elset=ASSEMBLY_STRUCTURE-1_STRUCTURE, layup=CARBON/EPOXY, composite,

*surface, type=ELEMENT, name=ASSEMBLY_SENSOR-1_SENS-BOT

*surface, type=ELEMENT, name=ASSEMBLY_STRUCTURE-1_STR_TOP

*tie, name=CONSTRAINT-1, positiontolerance=1e-05, norotation, adjust=NO

*output, field

*output, history, variable=PRESELECT

*output, field

*output, history, variable=PRESELECT

*output, field

*output, history, variable=PRESELECT

*amplitude, name=AMP-1, definition=SMOOTHSTEP

*amplitude, name=AMP-2, definition=PERIODIC

*amplitude, name=AMP-3, definition=PERIODIC

*amplitude, name=AMP-4, definition=ACTUATOR

*Step, name=Step-3, perturbation

*steadystatedynamics, direct, realonly, frequencyscale=LINEAR, frictiondamping=NO

*output, field

*output, history, variable=PRESELECT

*Step, name=Step-3, perturbation

*Step, name=Step-3, perturbation

*steadystatedynamics, direct, realonly, frequencyscale=LINEAR, frictiondamping=NO

*boundary, op=NEW, real

*boundary, op=NEW, real

*boundary, op=NEW, real

*output, field

*output, history, variable=PRESELECT

*endstep

*boundary

*boundary

*Step, name=Step-3, perturbation

*steadystatedynamics, direct, realonly, frequencyscale=LINEAR, frictiondamping=NO

*steadystatedynamics, direct, realonly, frequencyscale=LINEAR, frictiondamping=NO

*boundary, op=NEW, real

*boundary, op=NEW, real

*boundary, op=NEW, real

*output, field

*nodeoutput

*output, history, variable=PRESELECT

*endstep

A3. ABAQUS code for damaged MFC actuator

*Heading

 *Node

 *Element, type=C3D8R

 *Element, type=C3D8E

 *Element, type=C3D8R

 *Element, type=C3D8E

 *Element, type=C3D8R

 *Element, type=C3D8E

 *Element, type=C3D8R

 *Element, type=C3D8E

*Element, type=C3D8R

*Element, type=C3D8E

*Element, type=C3D8R

*Element, type=C3D8E

*Element, type=C3D8R

*Element, type=C3D8E

*Element, type=C3D8R

*Element, type=C3D8E

*Element, type=C3D8R

*Element, type=C3D8E

*Element, type=C3D8R

*Element, type=C3D8E

*Element, type=C3D8R

*Element, type=C3D8E

*Element, type=C3D8R

*Element, type=C3D8E

*Element, type=C3D8R

*Element, type=C3D8E

*Element, type=C3D8R

*Element, type=C3D8E

*Element, type=C3D8R

*Element, type=C3D8E

*Element, type=C3D8R

*Element, type=C3D8E

*Element, type=C3D8R

*Element, type=C3D8E

*Element, type=C3D8R

*Element, type=C3D8E

*Element, type=C3D8R

*Element, type=C3D8E

*Element, type=C3D8R

*Element, type=C3D8E

*Element, type=C3D8R

*Element, type=C3D8E

*Element, type=C3D8R

*Element, type=C3D8E

*Element, type=C3D8R

*Element, type=C3D8E

*Element, type=C3D8R

*Element, type=C3D8E

*Element, type=C3D8R

*Nset, nset="ASSEMBLY_SENSOR-1_ELECTRODE SIDE"

*Nset, nset="ASSEMBLY_SENSOR-1_SENSOR BOTTIM SIDE"

*Nset, nset=ASSEMBLY_SENSOR-1_ELECTRODEN

*Nset, nset=ASSEMBLY_SENSOR-1_ELECTRODEP

*Nset, nset=ASSEMBLY_SENSOR-1_ELN_M

*Nset, nset=ASSEMBLY_SENSOR-1_ELP_M

*Nset, nset=ASSEMBLY_SENSOR-1_EPOXY

*Nset, nset=ASSEMBLY_SENSOR-1_FIBERS

*Nset, nset=ASSEMBLY_SENSOR-1_SENSOR

*Elset, elset="ASSEMBLY_SENSOR-1_ELECTRODE SIDE"

*Elset, elset="ASSEMBLY_SENSOR-1_SENSOR BOTTIM SIDE"

*Elset, elset=ASSEMBLY_SENSOR-1_ELECTRODEN

*Elset, elset=ASSEMBLY_SENSOR-1_ELECTRODEP

*Elset, elset=ASSEMBLY_SENSOR-1_EPOXY

*Elset, elset=ASSEMBLY_SENSOR-1_FIBERS

*Elset, elset=ASSEMBLY_SENSOR-1_SENSOR

*Elset, elset=ASSEMBLY_SENSOR-1__SENS-BOT_S1

*Elset, elset=ASSEMBLY_SENSOR-1__SENS-BOT_S2

*Elset, elset=ASSEMBLY_SENSOR-1__SENS-BOT_S4

*Node

*Element, type=C3D20

*Nset, nset="ASSEMBLY_STRUCTURE-1_STRUCTURE TOP"

*Nset, nset="ASSEMBLY_STRUCTURE-1_SUPPORTING PIN"

*Nset, nset=ASSEMBLY_STRUCTURE-1_LOADLINE

*Nset, nset=ASSEMBLY_STRUCTURE-1_STRUCTURE

*Elset, elset="ASSEMBLY_STRUCTURE-1_STRUCTURE TOP"

*Elset, elset="ASSEMBLY_STRUCTURE-1_SUPPORTING PIN"

*Elset, elset=ASSEMBLY_STRUCTURE-1_LOADLINE

*Elset, elset=ASSEMBLY_STRUCTURE-1_STRUCTURE

*Elset, elset=ASSEMBLY_STRUCTURE-1__STR_TOP_S4

*Elset, elset=ASSEMBLY_STRUCTURE-1__STR_TOP_S6

*Nset, nset=ASSEMBLY__PICKEDSET10

*Elset, elset=ASSEMBLY__PICKEDSET10

*tie, name=CONSTRAINT-1, positiontolerance=1e-05, norotation, adjust=NO

*surface, type=ELEMENT, name=ASSEMBLY_SENSOR-1_SENS-BOT

*surface, type=ELEMENT, name=ASSEMBLY_STRUCTURE-1_STR_TOP

*tie, name=CONSTRAINT-1, positiontolerance=1e-05, norotation, adjust=NO

*surface, type=ELEMENT, name=ASSEMBLY_SENSOR-1_SENS-BOT

*surface, type=ELEMENT, name=ASSEMBLY_STRUCTURE-1_STR_TOP

*surface, type=ELEMENT, name=ASSEMBLY_SENSOR-1_SENS-BOT

*surface, type=ELEMENT, name=ASSEMBLY_STRUCTURE-1_STR_TOP

*tie, name=CONSTRAINT-1, positiontolerance=1e-05, norotation, adjust=NO

*tie, name=CONSTRAINT-1, positiontolerance=1e-05, norotation, adjust=NO

*orientation, name=ASSEMBLY_SENSOR-1_ORI-1

*orientation, name=ASSEMBLY_STRUCTURE-1_ORI-1

*material, name=COMPOSITE

*density

*elastic, type=ENGINEERINGCONSTANTS

*material, name=EPOXY

*density

*elastic

*material, name=PIEZO

*density

*dielectric, type=ORTHOTROPIC

*elastic, type=ENGINEERINGCONSTANTS

*piezoelectric, type=E

*orientation, name=ASSEMBLY_SENSOR-1_ORI-1

*orientation, name=ASSEMBLY_STRUCTURE-1_ORI-1

*solidsection, elset=ASSEMBLY_SENSOR-1_EPOXY, orientation=ASSEMBLY_SENSOR-1_ORI-1, material=EPOXY

*solidsection, elset=ASSEMBLY_SENSOR-1_FIBERS, orientation=ASSEMBLY_SENSOR-1_ORI-1, material=PIEZO

*solidsection, elset=ASSEMBLY_STRUCTURE-1_STRUCTURE, layup=CARBON/EPOXY, composite,

*boundary

*boundary

*boundary

*boundary, op=NEW, real

*boundary, op=NEW, real

*boundary, op=NEW, real

*boundary, op=NEW, real

*tie, name=CONSTRAINT-1, positiontolerance=1e-05, norotation, adjust=NO

*tie, name=CONSTRAINT-1, positiontolerance=1e-05, norotation, adjust=NO

*tie, name=CONSTRAINT-1, positiontolerance=1e-05, norotation, adjust=NO

*equation

*equation

*solidsection, elset=ASSEMBLY_SENSOR-1_EPOXY, orientation=ASSEMBLY_SENSOR-1_ORI-1, material=EPOXY

*solidsection, elset=ASSEMBLY_SENSOR-1_FIBERS, orientation=ASSEMBLY_SENSOR-1_ORI-1, material=PIEZO

*solidsection, elset=ASSEMBLY_STRUCTURE-1_STRUCTURE, layup=CARBON/EPOXY, composite,

*surface, type=ELEMENT, name=ASSEMBLY_SENSOR-1_SENS-BOT

*surface, type=ELEMENT, name=ASSEMBLY_STRUCTURE-1_STR_TOP

*tie, name=CONSTRAINT-1, positiontolerance=1e-05, norotation, adjust=NO

*output, field

*output, history, variable=PRESELECT

*output, field

*output, history, variable=PRESELECT

*output, field

*output, history, variable=PRESELECT

*amplitude, name=AMP-1, definition=SMOOTHSTEP

*amplitude, name=AMP-2, definition=PERIODIC

*amplitude, name=AMP-3, definition=PERIODIC

*amplitude, name=AMP-4, definition=ACTUATOR

*Step, name=Step-3, perturbation

*steadystatedynamics, direct, realonly, frequencyscale=LINEAR, frictiondamping=NO

*output, field

*output, history, variable=PRESELECT

*Step, name=Step-3, perturbation

*Step, name=Step-3, perturbation

*steadystatedynamics, direct, realonly, frequencyscale=LINEAR, frictiondamping=NO

*boundary, op=NEW, real

*boundary, op=NEW, real

*boundary, op=NEW, real

*boundary, op=NEW, real

*output, field

*output, history, variable=PRESELECT

*endstep

*boundary

*boundary

*boundary

*Step, name=Step-3, perturbation

*steadystatedynamics, direct, realonly, frequencyscale=LINEAR, frictiondamping=NO

*steadystatedynamics, direct, realonly, frequencyscale=LINEAR, frictiondamping=NO

*boundary, op=NEW, real

*boundary, op=NEW, real

*boundary, op=NEW, real

*boundary, op=NEW, real

*output, field

*nodeoutput

*output, history, variable=PRESELECT

*endstep

A4. ABAQUS code for Damaged Carbon/Epoxy Structure

*Heading

*Node

*Element, type=C3D8R

*Element, type=C3D8E

*Element, type=C3D8R

*Element, type=C3D8E

*Element, type=C3D8R

*Element, type=C3D8E

*Element, type=C3D8R

*Element, type=C3D8E

*Element, type=C3D8R

*Element, type=C3D8E

*Element, type=C3D8R

*Element, type=C3D8E

*Element, type=C3D8R

*Element, type=C3D8E

*Element, type=C3D8R

*Element, type=C3D8E

*Element, type=C3D8R

*Element, type=C3D8E

*Element, type=C3D8R

*Element, type=C3D8E

*Element, type=C3D8R

*Element, type=C3D8E

*Element, type=C3D8R

*Element, type=C3D8E

*Element, type=C3D8R

*Element, type=C3D8E

*Element, type=C3D8R

*Element, type=C3D8E

*Element, type=C3D8R

*Element, type=C3D8E

*Element, type=C3D8R

*Element, type=C3D8E

*Element, type=C3D8R

*Element, type=C3D8E

*Element, type=C3D8R

*Element, type=C3D8E

*Element, type=C3D8R

*Element, type=C3D8E

*Element, type=C3D8R

*Element, type=C3D8E

*Element, type=C3D8R

*Element, type=C3D8E

*Element, type=C3D8R

*Element, type=C3D8E

*Element, type=C3D8R

*Element, type=C3D8E

*Element, type=C3D8R

*Element, type=C3D8E

*Element, type=C3D8R

*Nset, nset="ASSEMBLY_SENSOR-1_ELECTRODE SIDE"

*Nset, nset="ASSEMBLY_SENSOR-1_SENSOR BOTTIM SIDE"

*Nset, nset=ASSEMBLY_SENSOR-1_ELECTRODEN

*Nset, nset=ASSEMBLY_SENSOR-1_ELECTRODEP

*Nset, nset=ASSEMBLY_SENSOR-1_ELN_M

*Nset, nset=ASSEMBLY_SENSOR-1_ELP_M

*Nset, nset=ASSEMBLY_SENSOR-1_EPOXY

*Nset, nset=ASSEMBLY_SENSOR-1_FIBERS

*Nset, nset=ASSEMBLY_SENSOR-1_SENSOR

*Elset, elset="ASSEMBLY_SENSOR-1_ELECTRODE SIDE"

*Elset, elset="ASSEMBLY_SENSOR-1_SENSOR BOTTIM SIDE"

*Elset, elset=ASSEMBLY_SENSOR-1_ELECTRODEN

*Elset, elset=ASSEMBLY_SENSOR-1_ELECTRODEP

*Elset, elset=ASSEMBLY_SENSOR-1_EPOXY

*Elset, elset=ASSEMBLY_SENSOR-1_FIBERS

*Elset, elset=ASSEMBLY_SENSOR-1_SENSOR

*Elset, elset=ASSEMBLY_SENSOR-1__SENS-BOT_S1

*Elset, elset=ASSEMBLY_SENSOR-1__SENS-BOT_S2

*Elset, elset=ASSEMBLY_SENSOR-1__SENS-BOT_S4

*Node

*Element, type=C3D20

*Nset, nset="ASSEMBLY_STRUCTURE-1_STRUCTURE TOP"

*Nset, nset="ASSEMBLY_STRUCTURE-1_SUPPORTING PIN"

*Nset, nset=ASSEMBLY_STRUCTURE-1_LOADLINE

*Nset, nset=ASSEMBLY_STRUCTURE-1_STRUCTURE

*Elset, elset="ASSEMBLY_STRUCTURE-1_STRUCTURE TOP"

*Elset, elset="ASSEMBLY_STRUCTURE-1_SUPPORTING PIN"

*Elset, elset=ASSEMBLY_STRUCTURE-1_LOADLINE

*Elset, elset=ASSEMBLY_STRUCTURE-1_STRUCTURE

*Elset, elset=ASSEMBLY_STRUCTURE-1__STR_TOP_S2

*Elset, elset=ASSEMBLY_STRUCTURE-1__STR_TOP_S3

*Elset, elset=ASSEMBLY_STRUCTURE-1__STR_TOP_S4

*tie, name=CONSTRAINT-1, positiontolerance=1e-05, norotation, adjust=NO

*surface, type=ELEMENT, name=ASSEMBLY_SENSOR-1_SENS-BOT

*surface, type=ELEMENT, name=ASSEMBLY_STRUCTURE-1_STR_TOP

*tie, name=CONSTRAINT-1, positiontolerance=1e-05, norotation, adjust=NO

*surface, type=ELEMENT, name=ASSEMBLY_SENSOR-1_SENS-BOT

*surface, type=ELEMENT, name=ASSEMBLY_STRUCTURE-1_STR_TOP

*surface, type=ELEMENT, name=ASSEMBLY_SENSOR-1_SENS-BOT

*surface, type=ELEMENT, name=ASSEMBLY_STRUCTURE-1_STR_TOP

*tie, name=CONSTRAINT-1, positiontolerance=1e-05, norotation, adjust=NO

*tie, name=CONSTRAINT-1, positiontolerance=1e-05, norotation, adjust=NO

*orientation, name=ASSEMBLY_SENSOR-1_ORI-1

*orientation, name=ASSEMBLY_STRUCTURE-1_ORI-1

*material, name=COMPOSITE

*density

*elastic, type=ENGINEERINGCONSTANTS

*material, name=EPOXY

*density

*elastic

*material, name=PIEZO

*density

*dielectric, type=ORTHOTROPIC

*elastic, type=ENGINEERINGCONSTANTS

*piezoelectric, type=E

*orientation, name=ASSEMBLY_SENSOR-1_ORI-1

*orientation, name=ASSEMBLY_STRUCTURE-1_ORI-1

*solidsection, elset=ASSEMBLY_SENSOR-1_EPOXY, orientation=ASSEMBLY_SENSOR-1_ORI-1, material=EPOXY

*solidsection, elset=ASSEMBLY_SENSOR-1_FIBERS, orientation=ASSEMBLY_SENSOR-1_ORI-1, material=PIEZO

*solidsection, elset=ASSEMBLY_STRUCTURE-1_STRUCTURE, layup=CARBON/EPOXY, composite,

*boundary

302

*boundary

*boundary, op=NEW, real

*boundary, op=NEW, real

*boundary, op=NEW, real

*tie, name=CONSTRAINT-1, positiontolerance=1e-05, norotation, adjust=NO

*tie, name=CONSTRAINT-1, positiontolerance=1e-05, norotation, adjust=NO

*tie, name=CONSTRAINT-1, positiontolerance=1e-05, norotation, adjust=NO

*equation

*equation

*solidsection, elset=ASSEMBLY_SENSOR-1_EPOXY, orientation=ASSEMBLY_SENSOR-1_ORI-1, material=EPOXY

*solidsection, elset=ASSEMBLY_SENSOR-1_FIBERS, orientation=ASSEMBLY_SENSOR-1_ORI-1, material=PIEZO

*solidsection, elset=ASSEMBLY_STRUCTURE-1_STRUCTURE, layup=CARBON/EPOXY, composite,

*surface, type=ELEMENT, name=ASSEMBLY_SENSOR-1_SENS-BOT

*surface, type=ELEMENT, name=ASSEMBLY_STRUCTURE-1_STR_TOP

*tie, name=CONSTRAINT-1, positiontolerance=1e-05, norotation, adjust=NO

*output, field

*output, history, variable=PRESELECT

*output, field

*output, history, variable=PRESELECT

*output, field

*output, history, variable=PRESELECT

*amplitude, name=AMP-1, definition=SMOOTHSTEP

*amplitude, name=AMP-2, definition=PERIODIC

*amplitude, name=AMP-3, definition=PERIODIC

*amplitude, name=AMP-4, definition=ACTUATOR

*Step, name=Step-3, perturbation

*steadystatedynamics, direct, realonly, frequencyscale=LINEAR, frictiondamping=NO

*output, field

*output, history, variable=PRESELECT

*Step, name=Step-3, perturbation

*Step, name=Step-3, perturbation

*steadystatedynamics, direct, realonly, frequencyscale=LINEAR, frictiondamping=NO

*boundary, op=NEW, real

*boundary, op=NEW, real

*boundary, op=NEW, real

*output, field

*output, history, variable=PRESELECT

*endstep

*boundary

*boundary

*Step, name=Step-3, perturbation

*steadystatedynamics, direct, realonly, frequencyscale=LINEAR, frictiondamping=NO

*steadystatedynamics, direct, realonly, frequencyscale=LINEAR, frictiondamping=NO

*boundary, op=NEW, real

*boundary, op=NEW, real

*boundary, op=NEW, real

*output, field

*nodeoutput

*output, history, variable=PRESELECT

*endstep

APPENDIX B: Configuration of AD5933 Impedance Analyser

The AD5933 impedance analyser is one of the key tools in developing the novel electromechanical impedance-based SHM technique presented in Chapter 7. This impedance analyser made the in-situ measurement and analysis of the real and imaginary components of electromechanical impedance possible. In this appendix, more details on the operation, performance and calibration of AD5933 will be presented to provide a valid instruction on how to employ this impedance analyser which will be a valuable insight for future researches.

B1. Basis of operation

Over this section it will be explained the operation of the AD5933 Impedance Converter Network Analyser and the way the original software from Analog Devices operates with it in order to perform the measurements. It will also be explained the Changes that the Analog Front-End added in the system has caused in the original software.

B2. Frequency Sweep

The impedance spectroscopy measurement is done frequency by frequency. Figure below shows the operation flow of the impedance sweep performed by the AD5933 Impedance Converter Network Analyser.

B3. Impedance Estimation Procedure

For the impedance estimation, the AD5933 Analyser performs a Discrete Fourier Transform (DFT) over the sampled current signals and the reference sinusoidal signals from the DDS on the DSP core. The DSP calculates a 1024 points- DTF transform for each frequency point contained in the frequency sweep, obtaining the real and imaginary components. Since the sinusoidal signals from the DDS represent the voltage applied on the load and the sampled signals represent the corresponding current to such a voltage excitation, the impedance can be directly estimated by applying Ohm's law in the frequency domain:

Equation 1

$$\frac{V(\omega)}{I(\omega)} = Z(\omega) = \frac{1}{Y(\omega)} = (V_{out}(\omega) - V_{in}(\omega))/\ I_{load}(\omega)$$

Notice that with such a current measurement it has been used the 2-Electrode method, what means that the estimated impedance corresponds to the load between the exciting leads. Finally, the DFT transform provides with the Fourier coefficients of the relationship between the voltage signal controlling the excitation and the current signal through the load. From each pair of Fourier coefficients, the magnitude and phase can be calculated at each frequency point. It is doing using the following equations:

Equation 2

$$Magnitude = \sqrt{R^2 + I^2}$$

Equation 3

$$Phase = Tan^{-1}(\frac{i}{R})$$

The magnitude represents the ratio between the voltage generated by the DDS and the current through the load, and the phase the time delay between both signals.

B3. Calibration

The calibration process is a mechanism applied on the impedance measurement process to compensate for systematic errors caused by the electronic components in the injection and measurement channels, i.e. time delays, attenuation, differences between the frequency response of the measurement channels, etc.

In the AD5933 circuit, the voltage signal used as a reference is transmitted to the DSP straight from the DDS, while the exciting voltage applied on the load, and true responsible for the current flow through the load, is the signal at the Vout output. Such pin is after a DAC converter and a voltage buffer and it is most likely that from the DDS to the Vout pin the signal has suffered certain delay scaling. Therefore the signals used as reference in the DSP core are not exactly representing the value of Vout. If the DSP did not consider this situation, the impedance calculation would have a systematic error due to the scaling and phase shifting that occur in the electronics building the exciting stage.

In order to obtain the correct impedance value, this scaling and delay must be compensated and removed from the final calculation. The AD5933 Analyser does it by a calibration process. The AD5933 circuit allows two different calibration modes: Single Frequency Point calibration mode and Multi Frequency Point calibration mode.

B4. Single Frequency Point Calibration

In this calibration process, a load with a known impedance value is placed between the exciting leads. The AD5933 Impedance Network Analyser chooses the frequency value that is just at the middle point of the measurement frequency range as the single calibration frequency. Then a voltage signal excites the calibration load, and the corresponding current is sensed. This way, the calibration impedance value can be estimated. Since the calibration impedance is known, it can be calculated a calibration factor in order to compensate the difference between the estimated impedance and the real calibration impedance value. This calibration factor is represented by two Fourier complex components, representing a scaling and a phase adjustment, and is denominated Gain Factor. Further impedance measurement over unknown loads will be corrected with this factor in order to obtain their correct values.

B5. Multi Frequency Point Calibration

In this mode the calibration process is done in the same manner as in the previous mode, but with one exception. The excitation is done at every single frequency point contained in the spectroscopy measurement. This way the Gain Factor is calculated at each frequency. In both modes the Gain Factor is obtained using the following equation:

Equation 4

$$GAIN\ FACTOR = \frac{CALIBRATION\ ADMITTANCE}{CALIBRATION\ MAGNITUDE}$$

And the measured impedance is shown by the next equation:

Equation 5

$$UNKNOWN\ IMPEDANCE = \frac{1}{GAIN\ FACTOR\ MAGNITUDE}$$

The Analog Front-End adds electronic components at the output of the Impedance Network analyser in both the injection channel and the measurement channel. This extra electronic stage introduces more systematic errors, but fortunately the calibration through the Gain Factor calculation also compensates for them. Since the scaling and delay produced by the DAC and the buffer are frequency dependent and the Single Frequency Point calibration only calculates the Gain Factor at one frequency, this calibration mode only performs an appropriate compensation at the calibration frequency. For a proper compensation in a multi-frequency measurement, the

calibration prior the measurement must be done using the Multi Frequency Point calibration mode. Furthermore, considering the nature of the electronics in the Analog Front-End, i.e. active components with non-ideal frequency response, the decision taken was ruling out the Single Frequency Point calibration mode from the measurements, and not including this option in the new software application.

B6. Changes introduced by the Analog Front-End circuit

The Analog Front-End circuit introduces new elements in the impedance network that influence the impedance calculation method implemented by the Impedance Network Analyser. The software provided by Analog Devices to process the impedance measurements must be adapted to the new operation conditions. The mentioned differences between the calculation process used with the AFE (four-electrode technique) and the one used with the original configuration (two-electrode technique) are explained in the following lines:

The DSP core provides Fourier components of the injecting signal and the measured signal to evaluate the unknown load. With the original configuration X reference is the applied voltage and Xmeasured is the resulting current. And the ratio between them provides the impedance value according to Ohm's Law:

Equation 6

$$X(f) = \frac{X_{reference}}{X_{measured}} = \frac{V_{out}}{I_{load}} = Z(f)[\Omega]$$

But the AFE modifies such relationship. Now Xreference refers to the injected current into the load provided by the voltage to current converter while Xmeasured refers to the resulting voltage drop in the load sensed by the instrumentation amplifier in the AFE. Since the function of the DSP core in the Impedance Network analyser cannot be modified, the impedance estimation implementation with the AFE changes to

Equation 7

$$X_{reference} = I_{load} \times R_{current\ source}$$

$$X_{measured} = \frac{V_{load}}{R_{out\ front-end}}$$

Where the units continue being Ohms corresponding to impedance, but X (f) corresponds to the admittance value of the load instead. This change forced to modify the software provided by Analog Devices in order to process correctly the coefficients provided by the Impedance Network

analyser and this way obtain the correct impedance value of the load. The original software executed the following two actions in order to calculate the Impedance under measurement:

Equation 8

$$GAIN\ FACTOR = \frac{CALIBRATION\ ADMITTANCE}{CALIBRATION\ MAGNITUDE}$$

$$UNKOWN\ IMPEDANCE = \frac{1}{GAIN\ FACTOR \times UNKOWN\ MAGNITUDE}$$

Now, the calculation method with the Front-End is:

Equation 9

$$UNKONW\ IMPEDANCE = GAIN\ FACTOR \times UNKONWN\ MAGNITUDE$$

$$GAIN\ FACTOR = \frac{1}{CALIBATION\ ADMITTANCE \times CALIBRATION\ MAGNITUDE}$$

So this characteristic has been taken into account in the software application when treating the real and imaginary values obtained from the DFT transform.